AMPLITUDE VARIATION WITH OFFSET (AVO) ATTRIBUTE ANALYSIS FOR SEISMIC RESERVOIR CHARACTERIZATION AND SEISMOFACIES STUDY OF KUYOLO FIELD, NIGER DELTA BASIN

OZOR, CHUKWUMA CHRISTIAN
REG.NO.PG/Ph.D/09/51382

A RESEARCH SUBMITTED TO THE DEPARTMENT OF GEOLOGY, FACULTY OF PHYSICAL SCIENCES, UNIVERSITY OF NIGERIA, NSUKKA, IN PARTIAL FULFILLMENT OF THE REQUIREMENTS FOR THE AWARD OF THE DEGREE OF DOCTOR OF PHILOSOPHY (Ph.D) IN APPLIED GEOPHYSICS

NOVEMBER, 2016

CERTIFICATION

Ozor Chukwuma Christian, a Postgraduate student in the Department of Geology with Registration No: PG/PhD/09/51382 has satisfactorily completed the requirements for course and research work for the degree of Doctor of Philosophy in Geology with emphasis on Applied Geophysics. The work is original and has not been submitted in part or full thereof for any diploma or degree or professional qualification of the University or any other University.

__________________	__________________
Prof. K.M. Onuoha	Dr. Smart C. Obiora
(Project Supervisor)	(Head of Department)

DEDICATION

To Almighty God the giver of life, our blessed mother Virgin Mary, my wife and daughter, Uche and Zimife, my parents Chief and Mrs. William Ozor, and my sisters Ndidiamaka, Kelechi, Nkechi, Uche and Theodora.

ACKNOWLEDGEMENT

The journey to get a Ph.D degree from the University of Nigeria Nsukka has been the most wonderful, enriching and delightful experience for my family and myself. I am very grateful to the people that have made this possible.

First of all, I wish to express my sincere appreciation to my supervisor Professor Mosto Onuoha. During all these years, Prof. Onuoha has been a supportive and assertive supervisor, an example of excellence in teaching, an open-minded dynamic researcher, and a source of wise advice. I have been honoured with and fortunate of having the opportunity to work with him.

I especially thank my two great friends Christian Longis and Pascal Desegaulx for arranging my coming to Total E & P Port-Harcourt as a research intern. I thank Pascal for the countless scientific discussions that not only helped me to complete my Ph.D but also to increase my knowledge in a broad set of interesting topics. It has been an honour to work with Pascal.

I have no words to thank enough Evans Owah my Total Project Advisor for his unselfish and continuous help, support, and encouragement, for all the patience listening to my problems (not few), for being a great companion. It will never be sufficient to send my sincere appreciation to Evans. I couldn't ask for a better Project Advisor. I learned a lot from him. Thank you Evans!

I feel honoured to have worked and interacted with all members of the Geosciences and Reservoir (GSR) team in Port-Harcourt. I am so grateful to my Lines Manager Oluremi, Chukwudum, Jean, Glory, Victor, Cyril, Paul Gibbson, Uche, Doris, Patrick, Thierry, Olagundoye, Paul Duke, Caroline, Victor Bamdele, Yetunde…for all the support and great time we had together.

I am very thankful to my cousin Onyeka Manu, Okey Attah and their family for their continuous support, extraordinary patience and constant encouragement.

I would like to thank all professors, staff members, and students in the Geology Department who made my stay at University of Nigeria Nsukka a most exceptional and pleasant experience. The list is large, but some of the names that come right now to my mind are Prof. O. P. Umeji, Dr. Ugbor C.C., Dr. Ekwe, Dr. S. C. Obiora, Dr. Igwe, Dr. Mamah, Dr. Mode, Dr. Amobi, Dr. Anyiam, Dr. Onwuka, Ikenna, Dim, Okey, Ezim, Chidi, Chiamaka, Mrs Aroh, Obi…

I would also like to thank my friends, the list is large, but some of the names that come right now to my mind are Barr. & Mrs Ekowu, Okechukwu, Chikwe, Chidiebere, Nnaemeka, Edu … for their support and encouragement.

I am indebted to my loving parents, Chief and Mrs. William Ozor, and my sisters, Ndidiamaka, Kelechi, Nkechi, Uche and Theodora, for their love, care, unstinting support and encouragement. They were always together with me and shared all difficulties and happiness every day.

Finally, I deeply thank my wife Uche Ozor for having the patience and consideration that allowed me to steal hours and days from the time she deserved. Without her at my side, there is no way I would be able to finish my Ph.D. This doctorate owes much to Uche's companionship, perseverance, and love over the years.

ABSTRACT

Amplitude variation with offset (AVO) attributes analysis, based on integration of geophysical and petrophysical data has become an important and innovative tool for the detection of hydrocarbons in many exploration provinces of the world, including the Niger Delta Basin. The method has been demonstrated to be effective when seismic data processing is carefully done with detailed petrophysical modeling from complete well log suites. However, routine application of the method has from time to time yielded disappointing results largely due to poor or non-availability of shear wave data. Considering the need for reduced risk and enhanced productivity in today's petroleum industry, a new and more efficient technique that ameliorates the problem of poor or non-availability of shear wave data is required. AVO Seismofacies methodology is one of such techniques and this approach was adopted for this study. It accounts for expected Amplitude Variation with Angle (AVA) effects, uses information from angle substacks, and effectively takes care of problems arising from the absence of data on shear waves, missing well log sections, and difficult well-to-seismic ties. The objectives of the study were to: (i) delineate (ii) map and (iii) characterize reservoirs in the Kuyolo field using the AVO Seismofacies approach. This approach involves quality control analysis of data, seismic data interpretation, shear wave data generation, reservoir fluid substitution via Gassmann technique, crossplots of elastic parameters and finally AVO Seismofacies analysis. The result of the quality control (QC) analysis shows that it was sufficient for the analysis of the Kuyolo field AVO anomalies. The result of the seismic data interpretation showed excellent tie of the well and seismic data with the R11 reservoir clearly delineated and mapped with high confidence. The result of the comparison of the actual well log measurements with the modelled well logs showed that the logs were relatively similar over all wells, with the trends and variations of density and velocities correctly modelled, especially in clean reservoirs. The analysis of the crossplots of modelled density (ρ) versus P-wave velocity (V_p) and Poisson's Ratio (PR) versus acoustic impedance (IP) generated after water substitution over all the wells, showed overall good separation of water saturated sands and shales giving confidence that AVO Seismofacies methodology could be used to characterize the reservoirs. Cross-correlation analysis showed that substack pairs of Near – Mid and Mid – Far offsets were suitable for AVO analysis. The study revealed that cross-correlation between Near and Far offset substack were too low to allow an

AVO analysis using this pairing of substacks. Substack pairs of Mid – Far were then selected to be used for this study. Average lambda and slope in degrees values of 0.24 and 37 degrees (37^0) extracted from the crossplots of filtered Mid and Far offset substacks at several locations and depths where there was no hydrocarbon were used to compute the AVO Seismofacies cube. All analyzed AVO anomalies gave fair responses fitting rather well on the AVO maps with the structural, sedimentary and stratigraphic interpretation, with anomaly shut-off at their base that could be interpreted as water/hydrocarbon contacts. Results of crossplot analysis of the amplitude values extracted at the top of R11 reservoir from filtered Near and Far substacks above the presumed Oil-Water-Contact (OWC) suggested Class II Reservoir sands. Thus the analysis carried out in the study area enhanced the identification and delineation of the hydrocarbon reservoir with high confidence. Additionally, the study has demonstrated that crossplot analysis such as those developed and analyzed in this work has helped to characterize the AVO Class of reservoir sands.

TABLE OF CONTENTS

CHAPTER THREE: WELL AND SEISMIC DATA QUALITY CONTROL ANALYSIS

CHAPTER FOUR: HORIZONS AND FAULT INTERPRETATIONS

CHAPTER FIVE: PETROELASTIC STUDY

CHAPTER SIX: AVO SEISMOFACIES STUDY

CHAPTER SEVEN: AVO INTERPRETATION

CHAPTER EIGHT: CONCLUSION AND RECOMMENDATIONS

LIST OF FIGURES

\

LIST OF TABLES

CHAPTER ONE

INTRODUCTION

Over the years, global demands for oil and gas have continued to increase, resulting in intensified exploration efforts for new hydrocarbon reserves in reservoir rocks, onshore, offshore and in very deepwaters. The Niger Delta Basin is known to hold several giant oil accumulations and large gas fields with a lot of unexplored opportunities trapped in a variety of complex structural and stratigraphic units. Amplitude variation with offset (AVO) attributes analysis, based on integration of geophysical and petrophysical data has become an important and innovative tool for the detection of hydrocarbons. Careful processing, detailed petrophysical modeling from complete log suites, and AVO analyses closely calibrated to measured properties of target reservoir sands have demonstrated effectiveness of the method. However, routine application of AVO has not been without problems, and its misapplication has led to disappointing results. Many failures are largely due to poor or non-availability of shear wave data. Considering the need for reduced risk and enhanced productivity in today's petroleum industry, a new and more efficient technique is required. AVO Seismofacies attribute methodology is one of such techniques and this approach was adopted for this study. The AVO Seismofacies combines two angle sub-stacks to create a third cube, AVO Seismofacies cube showing the differences from a background/ reference trend. It is displayed with a specific colour scale or with values closely related to Poisson Ratio (PR) variations; the white zones generally correspond to shale or wet sand (background/reference), a blue event shows a PR (Poisson's Ratio) decrease which can be interpreted as possible onset of an hydrocarbon bearing reservoir, a yellow-red event shows a PR increase which can be interpreted as either the offset of an hydrocarbon reservoir or a fluid contact.

1.0 Objectives of this Study

The objectives of this study are to delineate, characterize and map reservoirs in the Kuyolo field using the AVO Seismofacies approach.

1.1 Study Location

Kuyolo field is located on Eastern Offshore area of the Niger Delta, 75km Southeast (SE) of Port-Harcourt and covers an area of approximately 4km × 5km with an average distance of 30km to shore. The water depth ranges from 15m (North) to 40m (South). See figure below

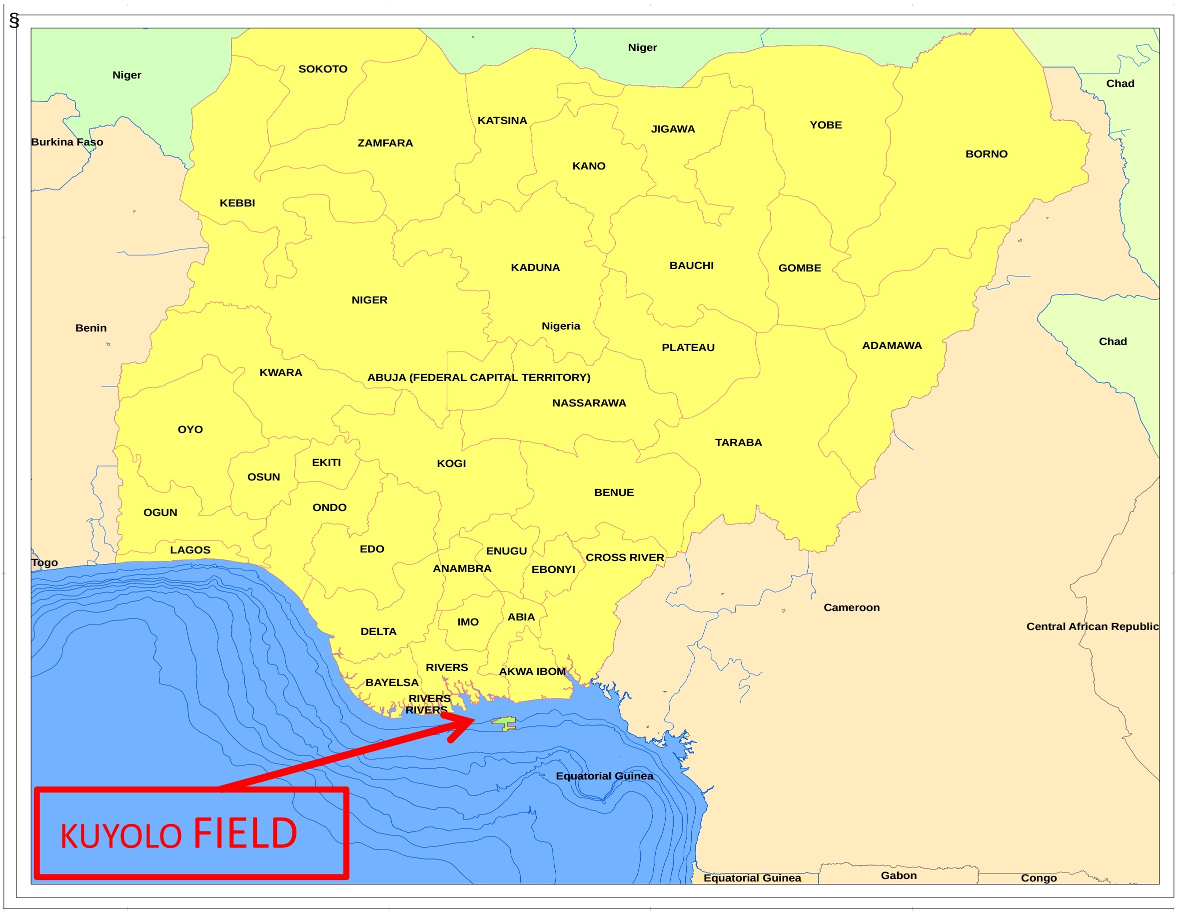

Figure 1.1: Location map of the study location

1.2 Regional Geology of the Niger Delta

The Niger Delta Oil Provinces is one of the basins initiated during the opening of the Atlantic in Albian times. It is situated at the Southern extremity of Nigeria bounded on the West by the Benin flank, on the north by the Anambra Basin, on the east by the Afikpo Syncline and Abakaliki Anticlinorium, on the South east by the Calabar flank and on the South by the Gulf of Guinea (Figure 1). The Niger Delta Basin is between lat.30 and 60N and long 50 and 80N situated on the continental margin of the Gulf of Guinea in Equitorial West Africa. The Niger Delta can be described as the centre of a triple junction with three arms of which are the Gulf of Guinea, South Atlantic and Benue Trough. By the phenomenon of Sea Floor Spreading and Plate Tectonics, the Gulf of Guinea and South Atlantic moved but the Benue Trough represented the failed trough (Aulacogen). Synrift marine and marginal marine clastics and carbonates accumulated during a series of transgressive-regressive phases between the Cretaceous to early Tertiary; the oldest dated sediments are Albian age (Doust and Omatsola, 1990). These Synrift phases ended with basin inversion in the Santonian (Late Cretaceous).

Renewed subsidence occurred as the continents separated and the sea transgressed the Benue Trough. The Niger Delta clastic wedge continued to prograde during Middle Cretaceous time into a depocenter located above the collapsed continental margin at the site of the triple junction. Sediment supply was mainly along drainage systems that followed two failed rift arms, the Benue and Bida Basins. Sediment progradation was interrupted by episodic transgressions during Late Cretaceous time.

During the Tertiary, sediment supply was mainly from the north and east through the Niger, Benue and Cross Rivers. Cross and Benue Rivers provided substantial amounts of volcanic detritus from the Cameroon volcanic zone beginning in the Miocene. The Niger Delta clastic wedge prograded into the Gulf of Guinea at a steadily increasing rate in response to the evolution of these drainage areas and continued basement subsidence. Regression rates increased in the Eocene, with an increasing volume of sediments accumulated since the Oligocene.

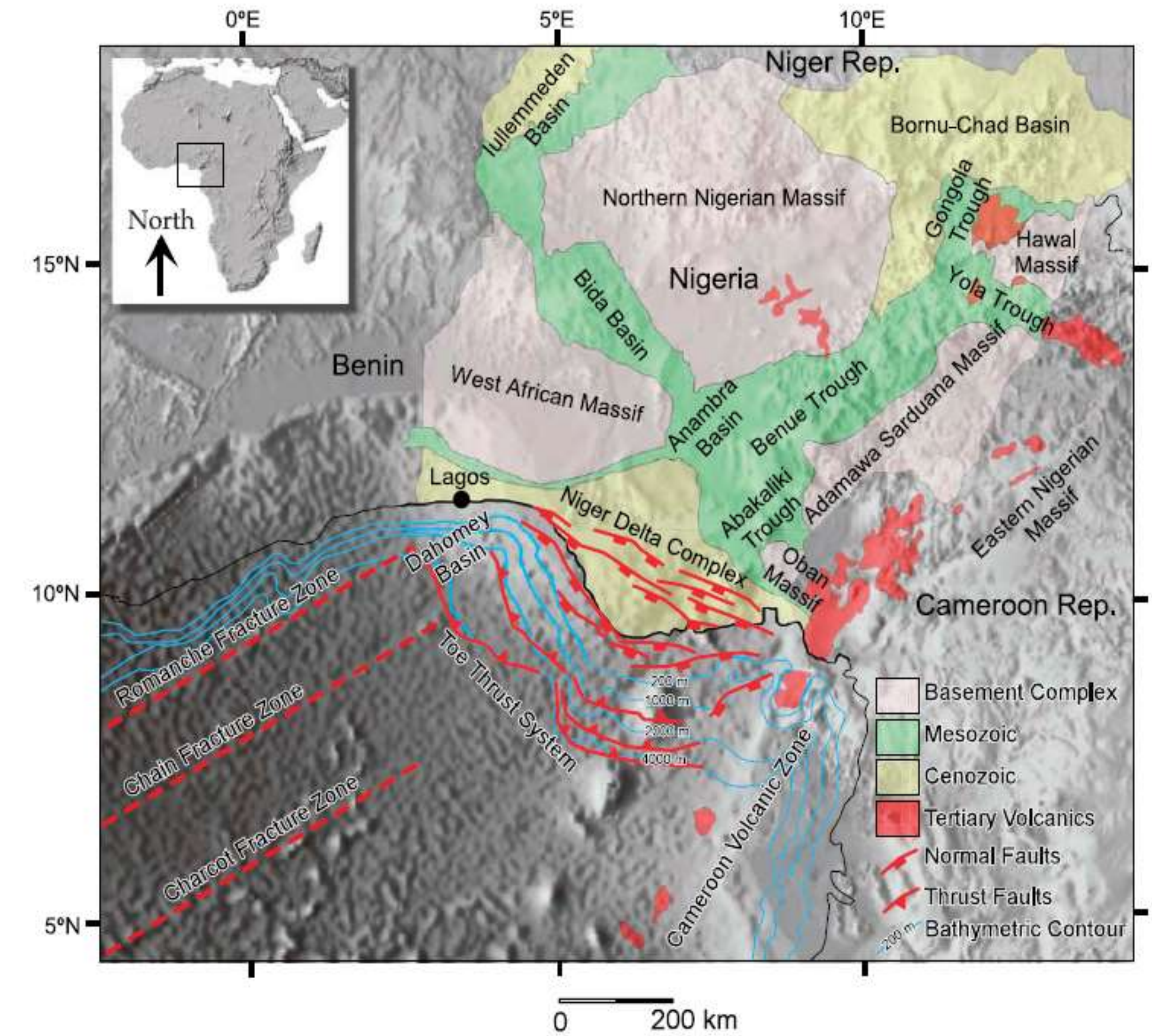

Figure 1.2: Location map of the Niger Delta region showing the main sedimentary basins and tectonic features. The delta is bounded by the Cameroon volcanic zone, the Dahomey basin, and the 4000-m (13,100-ft) bathymetric contour. The regional geology is modified from Corredor et al (2005). Topography and bathymetry are shown as a shaded relief gray-scale image.

1.2.1 Depositional Environments and Formations

The morphology of Niger Delta changed from an early stage spanning the Paleocene to early Eocene to a later stage of delta development in Miocene time. The early coastlines were concave to the sea and the distributions of deposits were strongly influenced by basement topography (Doust and Omatsola, 1990). Delta progradation occurred along two major axes, the first paralleled the Niger River, where sediment supply exceeded subsidence rate. The Second, smaller than the first, became active during Eocene to early Oligocene basinward of the Cross River where shorelines advanced into the Olumbe-1 area (Short and Stauble, 1965). This axis of deposition was separated from the main Niger Delta deposits by the Ihuo Embayment, which was later rapidly filled by advancing deposits of the Cross River and other local rivers (Short and Stauble, 1965). Late stages of deposition began in the early to middle Miocene, as these separate eastern and western depocenters merged. In Late Miocene the delta prograded far enough that shorelines became broadly concave into the basin. Accelerated loading by this rapid delta progradation mobilized underlying unstable shales. These shales rose into diapiric walls and swells, deforming overlying strata. The resulting complex deformation structures caused local uplift, which resulted in major erosion events into the leading progradational edge of the Niger Delta. Several deep canyons, now clay filled, cut into the shelf and are commonly interpreted to have formed during sea level lowstands. The best known are the Afam, Opuama, and Qua Iboe Canyon fills (Figure 1.1; Reijers et al., 1997).

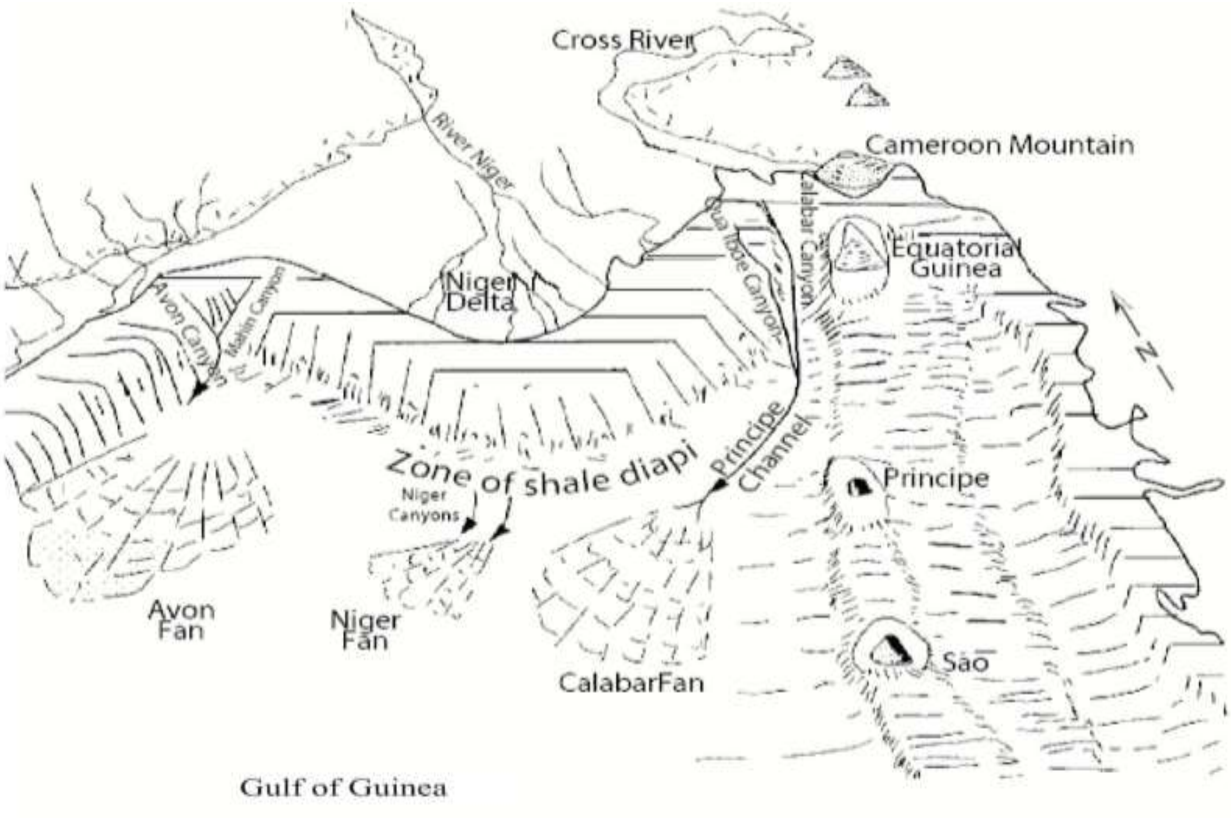

Figure 1.3: Physiographic sketch of the deep marine sediments in the Gulf of Guinea offshore Niger Delta (modified from Reijers et al., 1997).

1.2.2 Depobelts

Three major depositional cycles have been identified within Tertiary Niger Delta deposits (Short and Stauble, 1967; Doust and Omatsola, 1990). The first two, involving mainly marine deposition, began with a middle Cretaceous marine incursion and ended in a major Paleocene marine transgression. The second of these two cycles, starting in late Paleocene to Eocene time, reflects the progradation of a "true" delta, with an arcuate, wave- and tide-dominated coastline. These sediments range in age from Eocene in the north to Quaternary in the south (Doust and Omatsola, 1990). Deposits of the last depositional cycle have be divided into a series of six depobelts (Doust and Omatsola, 1990; also called depocenters or megasequences) separated by major synsedimentary fault zones. These depobelts formed when paths of sediment supply were restricted by patterns of structural deformation, focusing sediment accumulation into restricted areas on the delta. Such depobelts changed position over time as local accommodation was filled and the locus of deposition shifted basinward (Doust and Omatsola, 1990).

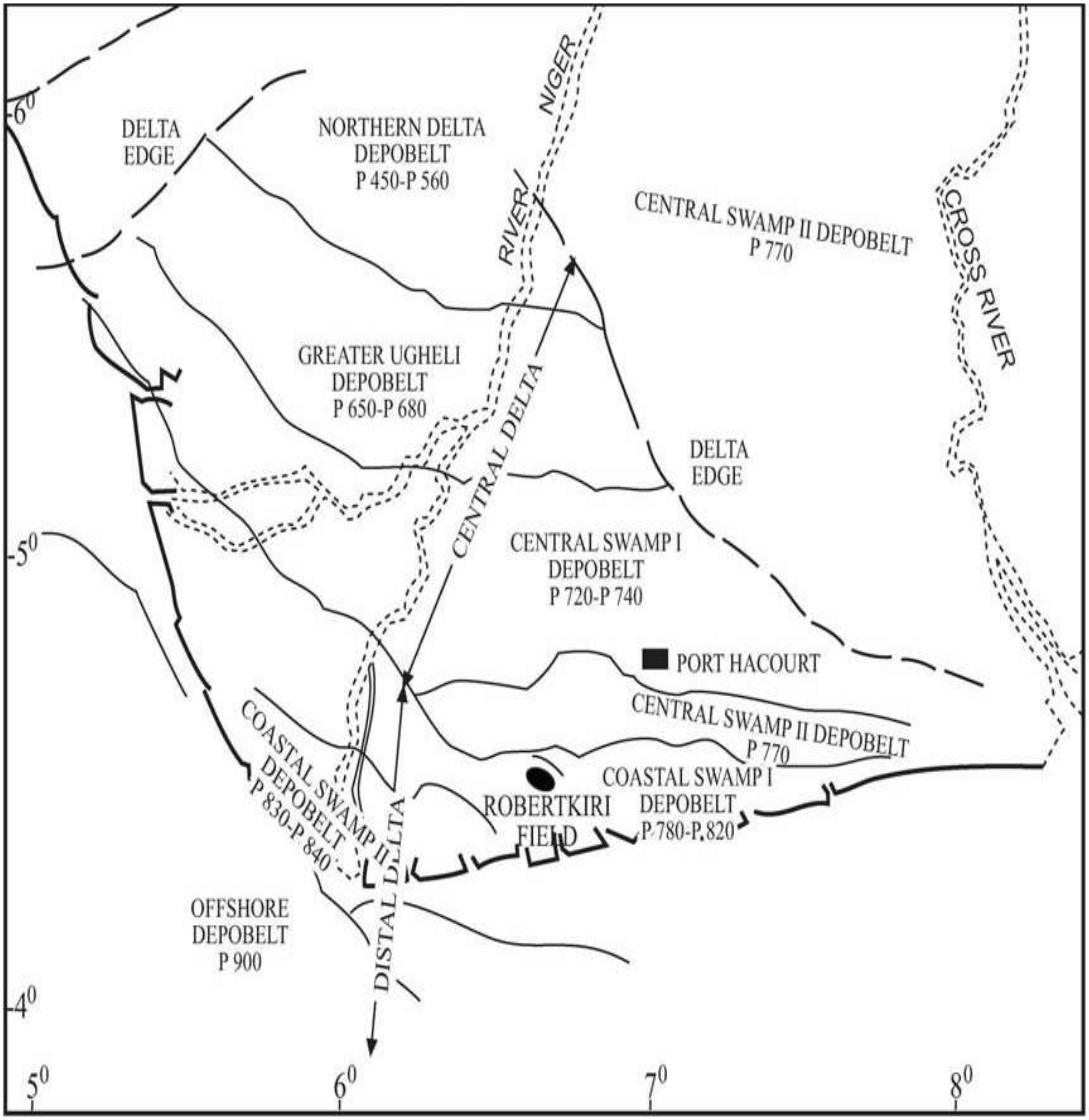

Figure 1.4: Depobelts with relative ages striking northwest- southeast. Depobelt are sub-parallel to the present coastlines and become successively younger basinward. Three broad areas are distinguished: the delta edge, central delta and distal delta. Modified from Doust and Omatsola (1990).

1.2.3 Structures

Normal faults triggered by the movement of deep-seated, overpressured, ductile, marine shale have deformed much of the Niger Delta clastic wedge (Doust and Omatsola, 1990). Many of these faults formed during delta progradation and were syndepositional, affecting sediment dispersal. Growth fault was also accompanied by slope instability along the continental margin. Faults flatten with depth onto a master detachment plane near the top of the overpressured marine shales at the base of the Niger Delta succession. Structural complexity in local areas reflects the density and style of faulting. Simple structures, such as flank and crestal folds, occur along individual faults. Hanging-wall rollover anticlines developed because of listric-fault geometry and differential loading of deltaic sediments above ductile shales. More complex structures, cut by swarms of faults with varying amounts of thrown, include collapsed-crest features with domal shape and strongly opposing fault dips at depth (Figure 3).

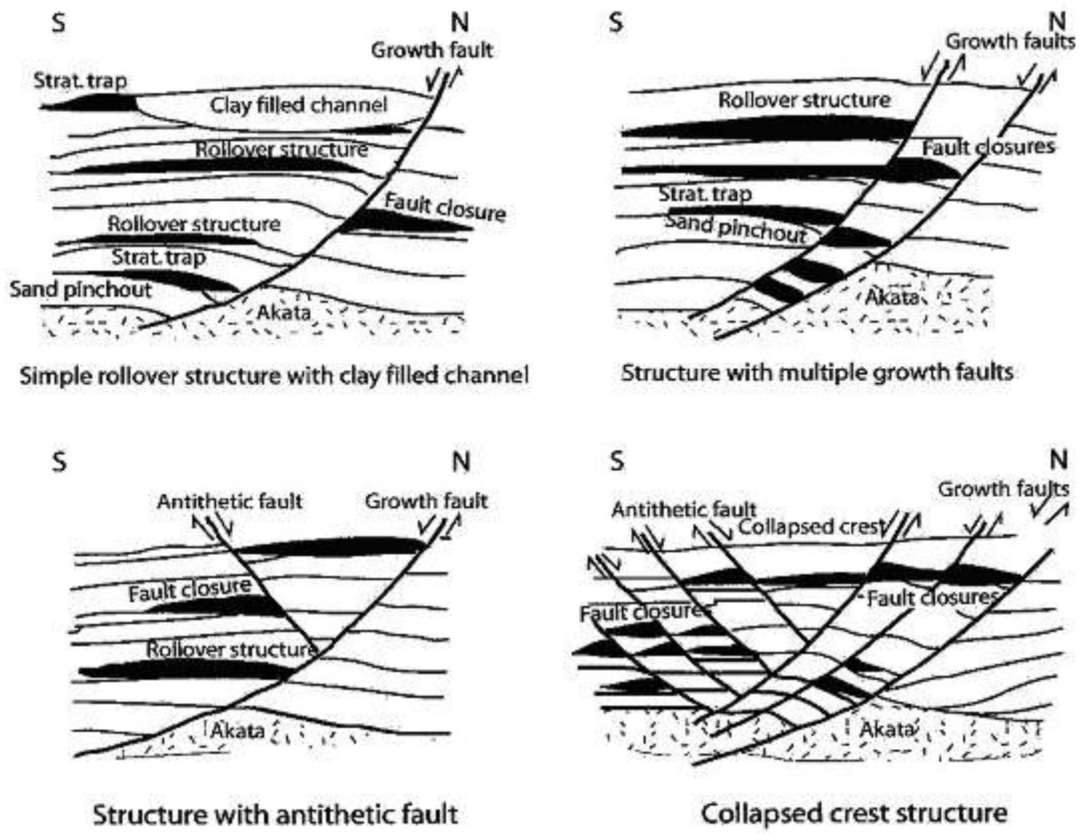

Figure 1.5: Niger Delta oil field structures and associated traps. Modified from Doust and Omatsola (1990) and Stacher (1995).

1.2.4 Stratigraphy

Although the stratigraphy of the Niger Delta clastic wedge has been documented during oil exploration and production, most stratigraphic schemes remain proprietary to the major oil companies operating concessions in the Niger Delta Basin. Stratigraphic evolution of the Tertiary Niger Delta and underlying Cretaceous strata is described by Short and Stauble (1965). Petroleum Geology of the Niger Delta is described in Evamy et al. (1978), Doust and Omatsola (1990). Stacher (1995) developed a hydrocarbon habitat model for the Niger Delta based on sequence stratigraphic methods. Short and Stauble (1965) described depositional environments, sedimentation and physiography of the modern Niger Delta. The three major lithostratigraphic units defined in the subsurface of the Niger Delta (Akata, Agbada and Benin Formations, Figure 4) decrease in age basinward, reflecting the overall regression of depositional environments within the Niger Delta clastic wedge. Stratigraphic equivalent units to these three formations are exposed in southern Nigeria (Table 1; Short and Stauble, 1965). The formations reflect a gross upward coarsening clastic wedge. These Formations were deposited in dominantly marine, deltaic, and fluvial environments respectively (Weber and Daukoru, 1975; Weber, 1987).

1.2.4.1 Akata Formation

The Akata Formation are dark gray shales and silts with rare streaks of sand of probable turbidite flow origin The formation is estimated to be 6,400 m thick in the central part of this clastic wedge (Doust and Omatsola, 1990). Marine planktonic foraminifera suggest a shallow marine shelf depositional setting ranging from Paleocene to Recent in age (Doust and Omatsola, 1990). The type section of the Akata Formation was defined in Akata 1 Well, 80 km east of Port Harcourt (Short and Stauble, 1967). A total depth of 11,121 feet (3, 680 m) was reached in the Akata 1 well without encountering the base of this formation. The top of the formation is defined by the deepest occurrence of deltaic sandstone beds (7,180 feet in Akata well). These shales are exposed onshore in the northeastern part of the delta, where they are referred to as the Imo Shale. This formation also crops out offshore in diapirs along the continental slopes. Where deeply buried, Akata shales are typically overpressured. Akata shales have been interpreted to be prodelta and deeper water deposits that shoal vertically into the Agbada Formation (Stacher, 1995, Doust and Omatsola, 1990).

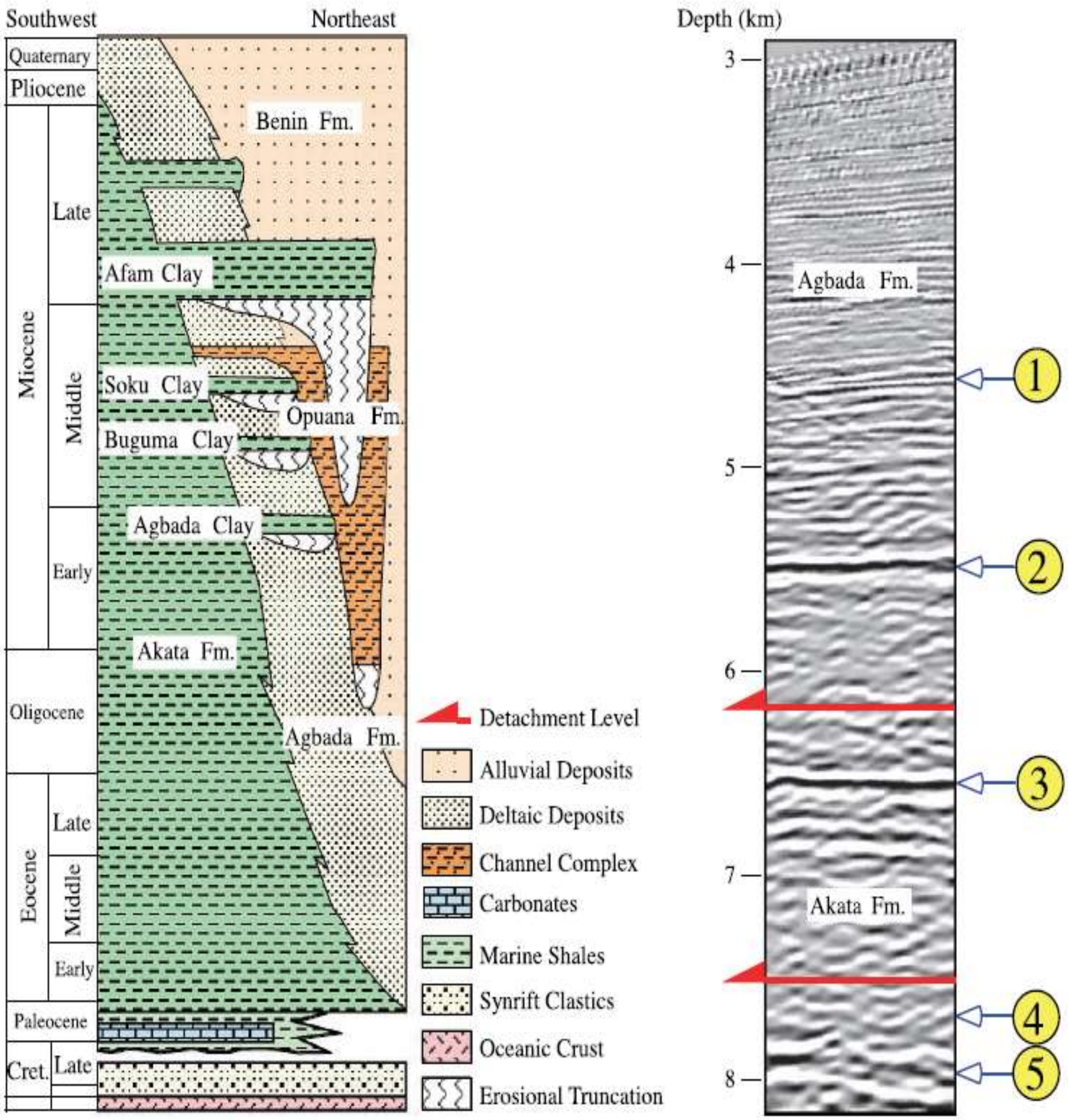

Figure 1.6: Stratigraphy column showing formations of the Niger Delta and variable density seismic display of the main stratigraphy units with corresponding reflections, including (1) top of the Agbada Formation, (2) top of the Akata Formation, (3) mid-Akata reflection, (4) speculated top of the synrift clastic deposits, and (5) top of the oceanic crust. Main detachment levels are highlighted with red arrows. Stratigraphy section is modified from Lawrence et al. (2002).

Table 1: Stratigraphic units of the Niger Delta area, Nigeria. Modified from Short and Stauble (1967).

Subsurface			**Surface Outcrops**		
Youngest known Age		**Oldest known Age**	**Youngest Known Age**		**Oldest Known Age**
Recent	Benin Formation (Afam clay member)	Oligocene	Plio/Pleistocene	Benin Formation	
Recent	Agbada Formation	Eocene	Miocene Eocene	Ogwashi-Asaba Formation Ameki Formation	Oligocene Eocene
Recent	Akata Formation	Eocene	lower Eocene	Imo shale Formation	Paleocene
	Unknown		Paleocene Maestrichtian Campanian Campanian/Maestrichtian Coniacian/Santonia Turonian Albian	Nsukka Formation Ajali Formation Mamu Formation Nkporo Shale Awgu Shale Eze Aku Shale Asu River Group	Maestrichtian Maestrichtian Campanian Santonian Turonian Turonian Albian

1.2.4.2 Agbada Formation

The Agbada Formation occurs throughout the Niger Delta clastic wedge and has a maximum thickness of about 3,962 m and ranges in age from Eocene to Pleistocene (Doust and Omatsola, 1990). Where it crops out in southern Nigeria (between Ogwashi and Asaba), it is called the Ogwashi-Asaba Formation (Doust and Omatsola, 1990). The lithologies consist largely of alternating sands, silts and shales with progressive upward changes in grain size and bed thickness. The strata are generally interpreted to have formed in fluvial-deltaic environments (Stacher, 1995, Doust and Omatsola, 1990). The Agbada Formation is defined in the Agbada 2 well, drilled about 11 km north-northwest of Port Harcourt (Short and Stauble, 1967). The well reached a total depth of 2896m without penetrating the base of the formation (the base was defined as the top of the Akata Formation in Akata 1 well).

1.2.4.3 Benin Formation

The Benin Formation comprises the top part of the Niger Delta clastic wedge, from the Benin-Onitsha area in the north to beyond the present coastline (Short and Stauble, 1967). Its type section is Elele 1 Well, drilled about 38 km north-northwest of Port Harcourt (Short and Stauble, 1967). The top of the formation is the recent subaerially-exposed delta top surface and its base extends to a depth of 1400m. The base is defined by the youngest marine shale. Shallow parts of the formation are composed entirely of non-marine sand deposited in alluvial or upper coastal plain environments during progradation of the delta (Doust and Omatsola, 1990). Although lack of preserved fauna inhibits accurate age dating, the age of the formation is estimated to range from Oligocene to Recent (Short and Stauble, 1967). The formation thins basinward and ends near the shelf edge.

1.2.5 Niger Delta Petroleum System

Petroleum occurs throughout the Agbada Formation in the Niger Delta clastic wedge. Although the distribution of hydrocarbons is complex, there is a general tendency for the ratio of gas to oil to increase southward within individual depobelts (Doust and Omatsola, 1990). Stacher (1995) developed a hydrocarbon habitat model based on sequence stratigraphy of some petroleum-rich belts within the Niger Delta area, and provides a short summary of basin, trap, reservoir, source rock and hydrocarbon character (Table 2). Gas to oil ratios within reservoirs were reported by Evamy et al. (1978), Ejedawe (1981) and Doust and Omatsola (1990). Reservoirs occur along northwest-southeast “oil rich belts” and along a number of north-south trends in the Port Harcourt area. Tuttle et al. (1999) suggest that belts roughly correspond to the transition between continental and oceanic crust within the axis of maximum sediment thickness. Other authors have related oil-rich belts to structural or depositional controls, to an increase in the geothermal gradient, and shifts in deposition basinward within Source rocks in the Niger Delta might include marine interbedded shale in the Agbada Formation, marine Akata Formation shales and underlying Cretaceous shales (Evamy et al, 1978; Ekweozor et al. 1979; Ekweozor and Okoye, 1980; Lambert- Aikhionbare and Ibe, 1984; Bustin, 1988; Doust and Omatsola, 1990). Reservoir intervals in the Agbada Formation have been interpreted to be deposits of highstand and transgressive systems tracts in proximal shallow ramp settings (Evamy et al, 1978). The reservoirs range in thickness from less than 45 feet to a few with thicknesses greater than 150 feet (Evamy et al, 1978). Kulke (1995) describes the most important reservoir units as point bars of distributary channels and coastal barrier bars intermittently cut by sand17 filled channels. Most primary reservoirs were thought to be Miocene-aged paralic sandstones with 40% porosity, 2 Darcy permeability, and thickness of about 300 feet. Reservoirs may thicken toward down-thrown sides of growth faults (Weber and Daukoru, 1975). Reservoir units vary in grain size; fluvial sandstones tend to be coarser than the delta front sandstones. Point bar deposits fine upward; barrier bar sandstones tend to have the best grain sorting. Kulke (1995) reported that most sandstone is unconsolidated with only minor argillaceous and siliceous cement. Potential reservoirs in the outer portion of the delta complex include deepchannel sands, lowstand sand bodies and proximal turbidite sandstones (Beka and Oti, 1995).

Structural traps formed during synsedimentary deformation of the Agbada Formation (Evamy et al, 1978; Stacher, 1995), and stratigraphic traps formed preferentially along the delta flanks (Beka and Oti, 1995), define the most common reservoir locations within the Niger Delta complex. The primary seal rocks are interbedded shales within the Agbada Formation. Three types of seal are recognized: (1) clay smears along faults, (2) interbedded sealing units juxtaposed against reservoir sands due to faulting, and (3) vertical seals produced by laterally continuous shale-rich strata (Doust and Omatsola, 1990). Major erosion events of early to middle Miocene age formed canyons which filled with shale; these fills provide top seals on the flanks of the delta for some important offshore fields (Doust and Omatsola, 1990).

Table 2: Hydrocarbon habitat table. Modified from Stacher (1995).

Geology	Tropical delta at passive continental margin of south Atlantic; Early Tertiary to recent age; Mostly shallow ramp depositional model; Shelf break locally mappable.
Traps	Dip closures (rollover anticline in growth faults); Fault bound traps; Stratigraphic traps (truncation Traps; Stratigraphic traps (truncation traps, tidal Deltas, channels etc.).
Reservoir	Deltaic sandstones (shoreface, beach, channel etc); Stacked sand/shale alternations; Multi-reservoir fields; Reservoir depth 5000-14000 ft.
Source rock	Marine shales (Akata shales) with land plant material (high potential); Type III/II, III vitrinite Liptinite, S.O.M; within well penetrations measured VR less than 0.7; Top oil window variable 9000-14000 ft.
Hydrocarbons	Oil/condensate/gas; Gravity 15-25 API biodegraded; Gravity 25-45 API non-bio-degraded; Low sulphur/nickel; Pristane/Phythane ratio 0.6-1.6; Rich in waxes/resins, other land plant material S.O.M.

CHAPTER TWO

BASIC THEORY OF ROCK PHYSICS AND AVO

2.0 Rapid Overview of Rock Physics Theory

Rock physics describes a reservoir rock by physical properties such as porosity, rigidity, compressibility; properties that will affect how seismic waves physically travel through the rocks. It aims to establish P-wave (v_p), S-wave velocity (v_s), density and their relationships to elastic moduli κ (bulk modulus) and μ (rigidity modulus), porosity, pore fluid, temperature, pressure, etc. for given lithologies and fluid types. Rock physics uses sonic logs, density logs and also dipole (shear velocity) logs if available. It may also use information provided by the petrophysicist, such as shale volume, saturation levels and porosity in establishing relations between rock properties or in performing fluid substitution analyses.

2.1 Basic Terms of Rock Physics

2.1.1 Density

Density (ρ) is the mass of the rock per unit volume. The bulk density of the rock is affected by the composition of the different minerals, the porosity of the rock, and the type of fluids which fill the pore space.

2.1.2 Porosity

Porosity (ϕ) is the percentage of the pore space per unit volume. Porosity can never reach 100% which would mean that the rock does not contain any minerals only pores. There is a point called critical porosity (ϕ_c) where the rock is considered to still be a rock. Above critical porosity the rock becomes a suspension.

2.1.3 Saturation

Saturation (S) defines the quantity of a specific fluid in the pore space. Saturation requires the specification of fluid type.

The overall elastic rock property is determined by the properties of the rock matrix, the porosity, and the composition of the fluids that fill the pore space.

2.1.4 Elasticity

The wave propagation process which occurs during a seismic experiment is controlled by the elastic properties of the rock – meaning how the rock deforms as a result of the force which is applied to it. Soft rock reacts to the strain differently than does a stiffer rock.

Elasticity theory deals with the deformation caused by the application of stress to a substance.

Strain (e) is the amount of deformation of the material per unit area.

Stress (σ) is the force per unit area.

When stress is applied to the material it deforms causing strain.

2.1.4.1 Hooke's Law

Hooke's law states that there is a linear relationship between stress and strain (between the force applied and the amount of deformation).

$$\sigma = C.\, e \qquad \text{.......................................}(1)$$

C is a constant relation. Strain (e) and Stress (σ) are tensors and C is a matrix (tensor) of constants (with 81 coefficients) which define the fundamental elastic properties of the rock.

For isotropic material, the 81 coefficients of matrix C are reduced to two independent elastic parameters which characterize the elastic properties of the rock. Some combinations of the two independent parameters are called the Elastic Moduli and can be measured in laboratory experiments.

2.1.4.2 Young's Modulus

Young's modulus (E) is an elastic modulus that can be measured in a laboratory experiment. Young's modulus measures the change in length (longitudinal strain) when a longitudinal stress is applied to it (Figure 1.7).

$$\sigma_l = E\frac{\Delta L}{L} \quad \text{……………………………………………..(2)}$$

2.1.4.3 Shear Modulus - Rigidity

Shear modulus – rigidity (μ) is another elastic modulus which can be measured in a laboratory. The shear modulus is the elastic constant which relates the shear strain to shear stress (Figure 1.7).

$$\sigma_s = \mu\frac{\Delta Y}{X} \quad \text{……………………………………………..(3)}$$

2.1.4.4 Bulk Modulus - Incompressibility

Bulk Modulus – Incompressibility (k) is another elastic modulus which measures the resistance to volumetric stress (a force that is applied uniformly in all directions-hydrostatic pressure).

$$P = K\frac{\Delta V}{V} \quad \text{……………………………………………….. (4)}$$

where:

P = hydrostatic pressure

$\frac{\Delta V}{V}$ = relative change in volume

Bulk modulus is the elastic modulus used mostly in AVO. The table in Figure 5 lists several typical values of bulk modulus for some rocks and fluids. The units are in 10^{10} Dynes/cm^2.

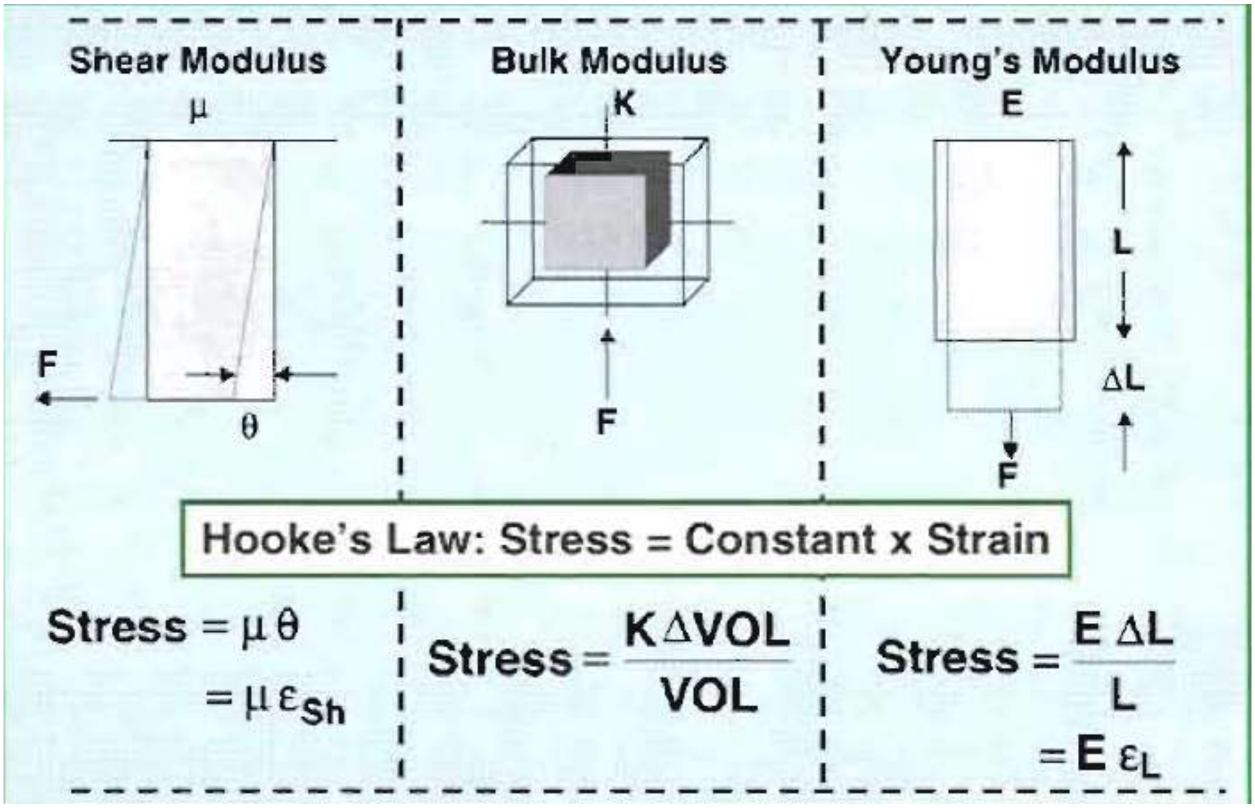

Figure 2.0: Computation of shear, bulk and young moduli

2.1.4.5 Lame's Constant

Lame Constant λ is another elastic modulus that is very often. It is not a property which is directly measured in the laboratory but is defined from other elastic moduli.

$$K = \lambda + 2/3\mu \ldots\ldots\ldots\ldots\ldots\ldots\ldots\ldots\ldots\ldots\ldots\ldots \text{(5)}$$

2.1.5 Wave Propagation Velocities

Two basic waves propagate in the subsurface. Pressure wave (P-wave) and shear (S-wave).

P-waves and S- waves propagate with different velocities, and those velocities are related to the elastic properties of the rocks. Shear waves do not propagate through fluids.

P-waves propagate with P-wave velocity (V_p). P-wave velocity (V_p) is given by:

$$(V_p) = \sqrt{\frac{k + 3/4\mu}{\rho}} \ldots\ldots\ldots\ldots\ldots\ldots\ldots\ldots\ldots\ldots\ldots\ldots \text{(6)}$$

S-waves propagate with S-wave velocity (V_s). P-wave velocity (V_s) is given by:

$$(V_s) = \sqrt{\frac{\mu}{\rho}} \ldots\ldots\ldots\ldots\ldots\ldots\ldots\ldots\ldots\ldots\ldots\ldots\ldots\ldots\ldots\ldots \text{(7)}$$

S-wave velocity is affected by density and shear modulus. P-wave velocity is affected by two elastic moduli, the bulk modulus and the shear modulus. In other words, the bulk modulus only affects the P-wave.

The relationship between P-wave velocity and S-wave velocity is a fundamental parameter in AVO analysis.

2.1.6 Possion's Ratio

Possion's Ratio (σ) is defined as the (minus of) ratio between longitudinal strain and axial strain.

$$\sigma = -\frac{Exx}{Ezz} \ldots\ldots\ldots\ldots\ldots\ldots\ldots\ldots\ldots\ldots\ldots\ldots\ldots\ldots \text{(8)}$$

In terms of velocities it is given by:

$$\sigma = \sigma = \frac{\left(\frac{V_P}{V_S}\right)^2 - 2}{2\left[\left(\frac{V_P}{V_S}\right)^2 - 1\right]} \ldots\ldots\ldots\ldots\ldots\ldots\ldots\ldots\ldots\ldots\ldots \text{(9)}$$

This means that Poisson's ratio is a measure of $\frac{V_p}{V_s}$. Poisson's ratio varies between 0 and 0.5.

σ = 0 when $\left(\frac{V_p}{V_s}\right) = \sqrt{2}$

σ = 0.5 when $V_s = 0$.

2.1.7 Impedance

Impedance (I_p; I_s) is the product of velocity and density. It is a fundamental property of the rock.

$$I_p = V_p .\rho \ldots\ldots\ldots\ldots\ldots\ldots\ldots\ldots\ldots\ldots\ldots\ldots\ldots\ldots\ldots \text{(10)}$$

$$I_s = V_s .\rho \ldots\ldots\ldots\ldots\ldots\ldots\ldots\ldots\ldots\ldots\ldots\ldots\ldots\ldots\ldots \text{(11)}$$

Impedance plays a major role in normal incidence reflectivity. At normal incidence, the reflection from an interface between two layers, with I_{ρ_1} representing impedance of the top layer, and I_{ρ_2}, the impedance of the bottom layer, is given by:

$$R = R = \frac{I_{P_2} - I_{P_1}}{I_{P_2} + I_{P_1}} \ldots\ldots\ldots\ldots\ldots\ldots\ldots\ldots\ldots\ldots\ldots\ldots\ldots \text{(12)}$$

The seismic experiment is controlled by the velocity of the waves in the subsurface. Because of the large wavelength of seismic waves in oil exploration, the velocity and density that we can measure from the seismic data reflects some average property of the rock. It is a combination of the parameters of the rock matrix (the grains) and the fluids that fill the pore spaces.

2.2 A Review of Relevant Literature on Rock Physics

Over the past two decades, amplitude-variation-with-offset (AVO) has evolved from a relatively new technology to increasingly mature applications. Particularly successful results have been achieved both offshore and onshore in many exploration provinces around the world including the Niger Delta. Careful processing, detailed petrophysical modeling from complete log suites, and AVO analyses closely calibrated to measured properties of target reservoir sands have demonstrated effectiveness.

Around 1900, Knott and Zoeppritz developed the theoretical work necessary for AVO theory (Knott, 1899; Zoeppritz, 1919). Given the P-wave and S-wave velocities along with the densities of the two bounding media, they developed equations for plane-wave reflection amplitudes as a function of incident angle. However, the exact mathematical expression of the reflection coefficient is exceptionally long, thus making it difficult to perceive how reflection amplitude varies if a rock property is changed slightly. Gassmann (1951) derived an equation using wave-propagation theories that relates the effective bulk-modulus of a fluid-saturated rock to that of the bulk moduli of the matrix material, the frame, pore fluid and porosity. Koefoed (1955) using the exact Zoeppritz's equation described the relationship of AVO to changes in Poisson's ratio across a boundary. Bortfeld (1961) introduced the fluid-fluid and rigidity terms which provided an insight in predicting how amplitude varies with offset as a function of rock properties.

Recognizing the significance of Koefoed's work for predicting lithology, Rosa (1976) investigated the elastic properties that could be extracted robustly from AVO inversion. His work tied very closely to the linear-approximation equation developed by Shuey (1985). Interestingly, Shuey also was inspired to examine AVO after learning of Koefoed's article.

However, it was 27 years after Koefoed's work that the relationship between AVO and lithology was dramatically brought into limelight by Ostrander (1982). Ostrander provided real data examples where the presence of gas caused reflection amplitudes to increase with offset. Since then, amplitude-variation-with offset (AVO) analysis has become common.

Shuey (1985) took the known linearization of compressional wave reflection coefficient and transformed variables from shear wave to Poisson's ratio to display analytically the effect of the contrast in Poisson's ratio. Shuey identified how various rock properties can be associated with Near-, Mid-, and Far-angle ranges.

Rutherford and Williams (1989) proposed a classification of gas-sand reflections based on their AVO characteristics and presented seismic data examples illustrating these characteristics. They classified gas-sand reflectors into three classes (I, II, &III) in terms of normal incidence reflection coefficient (R_0) at the top of the gas sand based on their AVO characteristics.

Fatti et al. (1994) evaluated the possibility of gas detection in sandstone reservoirs using the Geostack technique. The Geostack technique is a method of analyzing seismic amplitude variation with offset information. Preliminary results from their study on a 3D seismic dataset over the Mossel Bay gas field on the southern continental shelf of South Africa showed that anomalously amplitude fluid factor reflections occurred at the top and base of the gas- reservoir sandstone. Maps of the amplitude of the fluid factor reflections showed that the high amplitude values were restricted mainly to the gas field as determined by drilling. Their results further showed that the highest amplitudes were located in areas of best reservoir quality (highest porosity) and thickness.

Goodway et al. (1997) proposed the LMR (Lambda-Mu-Rho) method, where L, M, and R represent: the first Lame parameter; μ the shear modulus or coefficient of rigidity; and ρ the density. They showed that various combinations of λ, μ and ρ, such as $\lambda\rho$, $\mu\rho$ and λ/μ , show a better separation of gas sand from brine sands and shales than IP and IS where is IP P-impedance and IS is S-impedance.

Connolly (1999) derived the angle or offset equivalent of acoustic impedance, and used the term elastic impedance (EI). He noted that the elastic impedance (EI) is a function of p-wave velocity, s-wave velocity, density and incidence angle. The author demonstrated by using elastic impedance (EI) logs (which requires shear-wave logs) how to perform well calibration and inversion of Far (non-zero) offset data.

Omudu and Ebeniro (2005) in their study showed how hydrocarbon bearing reservoirs could be differentiated from non-hydrocarbon bearing reservoirs by using cross-plots of elastic rock parameters and their attributes. This they showed from cross-plots of elastic rock parameters from wells in offshore Niger Delta. Their results show that the crossplot of Vp/Vs versus depth is good for distinguishing sands from shales while the cross-plots of Lambda-Mu-Rho attributes and their combinations were more sensitive and robust for fluid discrimination in the study area.

Quakenbush et al. (2006) proposed the concept and calculation method of Poisson Impedance (PI). He defined Poisson Impedance (PI) as the difference between P-wave impedance and S-wave impedance with coefficient (C). They defined the coefficient (C) as the slope of line which can divide the points of P- and S- wave impedance crossplot into two different data types of points. The authors comparison of seismic attributes derived from log data over the North Sea well revealed the discriminatory properties of Poisson Impedance (PI).

Kathryn and Robert (2007) discussed an interesting case study wherein the evaluation of bright spot targets is carried out using the LMR attribute application and lowering risk in drilling prospects. The gas sands exhibiting bright spots in the Columbus Basin have lower acoustic impedance than the sealing shales, exhibiting class 3 AVO anomalies. Based on the LMR analysis, only nine of the 15 prospective intervals evaluated in this study proved gas-saturated and the other six were “false bright spots.”

Jeffery et al. (2007) presented a convincing AVO case study from Sacramento Basin, California, where the authors claimed 100% success in drilling subgorge traps. The approach followed was to identify and understand the amplitude anomalies associated with the subgorge traps within their sequence stratigraphic framework, followed by recognizing the AVO signatures of gas-charged sandstones and finally avoiding lithologic pitfalls. This approach was applied to identifying subcrop reservoirs associated with other gorges in Sacramento Basin as well as in the search for hydrocarbons trapped beneath submarine canyons in deepwaters basin worldwide.

Herbert (2007) introduced a novel idea of processing the Near and Far or Gradient and Intercept data, so that the background majority always lies within a predefined region in the data plane. AVO anomalies can then be detected by examining data at fixed locations that are separated from the fixed background region. In this way, large quantities of data can be quickly examined for AVO anomalies and so the method is suitable for reconnaissance AVO.

Necati et al. (2007) illustrated a method of flattening Prestack NMO-corrected gathers, which they refer to as a brute-force type method. Their method utilizes event tracking with a two-trace cross-correlation algorithm and Moveout functions that can be smoothed spatially as well as over time before applying corrections to the gathers. Spatial smoothing of Moveout functions is done in the inline and crossline directions. The authors demonstrated consistent flat gathers after application of this approach.

Yong and Satinder (2007) described the implementation of NMO stretching and thin-bed tuning corrections for production AVO analysis. Both synthetic and real data examples from Alberta showed that these corrections are necessary for reliable AVO analysis.

Yeshpal Singh (2007) demonstrated the application of principal component analysis on attributes derived from simultaneous inversion of seismic data from offshore peninsular Malaysia. Of the various attributes derived, the author showed how flat spot features could be observed on Poisson impedance and second principal component (PC2) attributes, and not seen on acoustic and shear impedance attributes and how in the study area the derivation of lithofacies and clay volumes derived from PC2 attributes led to improved reservoir characterization.

Charles et al. (2007) introduces the idea of spherical-wave AVO and present a way of calculating spherical-wave reflection coefficients. Their analysis show that spherical-wave effects are noticeable, not only near the surface, but even in deep reflections if there is a critical angle in the data. Also, the spherical wave reflection coefficients are only weakly dependent on the choice of the wavelet as long as the average frequency is specified correctly.

Ujuanbi et al. (2008) demonstrated the robustness of the Lambda-Mu-Rho technique for fluid and lithology discrimination in an oil sand reservoir in the Niger Delta. They used inverted data volumes from the area to derive volumes of Lamé’s impedances, Lambda-Rho and Mu-Rho. Cross-plots from the volumes of elastic rock parameters identified the oil sand reservoir and further demonstrated the viability of the Lambda-Mu-Rho technique in discriminating between hydrocarbons and lithology in the Niger Delta.

Ekwe and Onuoha (2014) used cross-plots of elastic rock properties Lambda (λ, incompressibility), Mu (μ, rigidity) and Rho (ρ, density) and their combinations ($\lambda\rho$,$\mu\rho$, λ/μ, etc.) to determine which combination of attributes depict characteristics that can be used to identify specific lithologies and pore fluid types in an old producing oilfield within the onshore Niger Delta basin. Their results show that the LambdaRho ($\lambda\rho$) versus MuRho ($\mu\rho$) cross-plot is a better indicator of fluids and lithology within the studied field in the Niger Delta Basin.

2.3 Empirical Relationship between Velocity and Density

There are several reasons for wanting empirical velocity-density relationships. Some of these reasons are generating missing well-log curves, estimating S-wave velocity for AVO analysis, quality controlling logs in questionable zones, and quantifying seismic amplitude variation for porosity changes to providing insight for screening anomalous lithologies at prospect.

With the advent of AVO, new empirical transforms have been advocated for predicting S-wave velocity from other logs and also for predicting velocity changes when pore fluid is varied. However, many of the transforms are not only dependent on lithology, but are also very dependent on local conditions and should not be extrapolated to other areas without recalibration.

2.3.1 Gardner's Velocity-Density Transform

Gardner et al. (1974) presented petrophysical principles for distinguishing gas-saturated sands from water-saturated sands using the seismic method.

$$\rho = 0.23V^{0.25}\ (gm/cm^3\ and\ ft/s) \ldots\ldots\ldots\ldots\ldots\ldots\ldots\ldots \text{(13)}$$

Castagna (1993) extended Gardner's work by developing velocity-density transforms for individual lithologies.

Sand $\rho = 0.200V_P^{0.261}$

Shale $\rho = 0.204V_P^{0.265}$

Limestone $\rho = 0.243V_P^{0.225}$

Dolomite $\rho = 0.226V_P^{0.243}$

Anhydrite $\rho = 0.600V_P^{0.160}$

As has been observed, the average transform, overestimates the density of sand and underestimates the density of shale. With the revised transforms there is a better correlation to the raw data.

2.3.2 Wyllie's Velocity – Porosity Transform

In 1956 and in subsequent publications, Wyllie 1958, proposed the empirical relationship between velocity and porosity for brine-filled porous media of

$$1/V = (1 - \phi)/V_{ma} + \phi/V_{fl} \text{……………….. ……} \quad (14)$$

where V = velocity of total rock, V_{ma} = velocity of matrix material, V_{fl} = velocity of pore fluid, and ϕ = porosity.

This is often expressed in terms of interval traveltime (μs/ft) as

$$\Delta t = (1 - \phi)/\ \Delta t_{ma} + \phi\Delta t_{fl} \text{ ………..} \quad (15)$$

where Δt's represent the respective traveltimes. When expressed in interval traveltimes, Wyllie's equation represents the total time it takes to pass through the porous material and matrix material individually.

Obviously, the variable Δt_{ma} is dependent on lithology. Commonly used values for Δt_{ma} (μs/ft) as reported by Schlumberger are

Sandstone	$55.5\ or\ 51.0$
Limestone	47.5
Dolomite	43.5
Anhydrite	50.0
Salt	67.0
Brine	$189.0(\Delta t_{fl})$

There are several assumption and limitations that are inherent in the application of Wyllie's time – average equation.

2.3.3 Raymer - Hunt - Gardner's (R-H-G) Velocity - Porosity Transform

In an effort to improve upon Wyllie's empirical time – average equation, Raymer et al. (1980) proposed the following Velocity – Porosity relationships (from Mavko et al., 1998):

$$V = (1-\phi)^2 V_{ma} + \phi V_{fl} \qquad \phi < 37\% \ \ldots\ldots\ldots\ldots (16)$$

$$1/V = (0.47-\phi)/(0.1V_{37}) + (\phi - 0.37)/(0.1\,V_{47}) \qquad 37 < \phi < 47\% \ \ldots\ldots\ldots (17)$$

$$1/\rho V^2 = (1-\phi)/(\rho_{ma} V_{ma}^2) + \phi/(\rho_{fl} V_{fl}^2) \qquad \phi < 47\% \ \ldots\ldots\ldots\ldots\ldots (18)$$

where V_{37} is calculated from low-porosity equation at $\phi = 0.37$ and V_{47} is calculated from high-porosity equation at $\phi = 0.47$.

Even though the R-H-G transform was developed to better estimate lower-porosity values from sonic readings, it is still not adequate for all areas.

2.3.4 Han's Velocity – Porosity – Clay Volume Transform

Han (1986) and Han et al. (1986) developed empirical relationships among velocity, porosity, and clay content, *c*, using ultrasonic measurements on 75 well-consolidated sandstones.

Measurements were conducted with variations of effective pressure and water saturation. Han's transforms are

Clean sandstones:

40MPa $V_p = 6.08 - 8.06\,\phi$ $V_s = 4.06 - 6.28\,\phi$ ……………… (19)

Shaly sandstones:

40MPa $V_p = 5.59 - 6.93\,\phi - 2.18c$ $V_s = 3.52 - 4.91\,\phi - 1.89c$ …….. (20)

5MPa $V_p = 5.26 - 7.08\,\phi - 2.02c$ $V_s = 3.16 - 4.77\phi - 1.64c$ ……….. (21)

With the conversion of 1MPa = 145psi and an effective pressure gradient ≈ 0.5 psi/ft, the measurements at 40MPa and 5MPa correspond to approximate depths of 12000ft and 1500ft, respectively.

2.3.5 Castagna V_p- V_s Transforms

Pickett (1963) introduced the concept that V_p/V_s ratios could be used for identifying lithology. This concept didn't receive much attention until Ostrander (1984) verified that V_p/V_s ratios could be inferred from seismic data.

Castagna (1985), published additional laboratory and in-situ measurements of V_p/V_s ratios for clastic silicate rocks composed primarily of clay – or silt-sized particles. Castagna called this relationship the Mudrock line and expressed the velocity relationship as

$$V_p = 1.16V_s + 1.36 \quad \text{……………………. (22)}$$

where the velocities are expressed in km/s.

Greenberg and Castagna (1992) published additional V_p- V_s transforms in their work on pore-fluid substitution techniques, based on the Gassmann equation. They assumed that a conventional suite of well-log curves would normally be available for modelling. As they noted, however, when no in-situ V_s information is available, additional empirical information is needed to solve Gassmann's equation for the fluid-substitution problem. Greenberg and Castagna provided this needed information in the form of V_p-to- V_s transforms for various water-saturated lithologies. Their transforms, in km/s, are:

Sandstones: $V_s = -0.856 + 0.804\ V_p$ …………………………….. (23)

Limestone: $V_s = -1.030 + 1.017\ V_p - 0.055V_p^2$ ……………………. (24)

Dolomite: $V_s = -0.078 + 0.583\ V_p$ ……………………………... (25)

Shale: $V_s = -0.867 + 0.770V_p$ ………………………………. (26)

The V_p-to- V_s transforms are more robust than velocity – density transforms.

2.4 Relationships for Bulk Moduli

Empirical transforms are often valuable not only for the direct estimates of a rock-property value, but for the functional relationship they provide between the variables.

2.4.1 Voigt, Reuss, and Hill's (V-R-H) Models – K_{ma} Estimate

In the late 1920s, Voigt (1928) and Reuss (1929) proposed two different mixing laws to compute effective moduli (K_{eff} and μ_{eff}) from the individual moduli of the composite material. Reuss's method provided the lower limit for the effective moduli, while Voigt's provided the upper limit. However, Hill (1952) suggested that an average taken from Voigt and Reuss models would yield a better estimate.

Wang and Nur (1992) tested the V-R-H model with laboratory data. As noted, the Voigt and Reuss models place upper and lower bounds on the effective moduli of the composite material. The Hill model comes close to matching the best-fit curve for the bulk modulus, but the Hill model should not be used to estimate the shear moduli. They also noted that the V-R-H model should not be used for gas-saturated rocks. These last two constraints limit the direct application of the V-R-H model for predicting V_p and V_s from a volumetric analysis of a rock. In short, the V-R-H model is used to estimate the effective bulk modulus of the mineral (grain) components, K_{ma}, not the total bulk modulus.

In order to estimate the effective bulk modulus of the various minerals with the V-R-H model, the volumetric percentage of each mineral and the porosity must be known. In addition, the bulk moduli of the minerals and pore fluid are required.

$$\left.\begin{aligned} 1/K_r &= N_1/K_1 + N_2/K_2 + \ldots\ldots + N_n/K_n \\ 1/\mu_r &= N_1/\mu_1 + N_2/\mu_2 + \ldots\ldots + N_n/\mu_n \end{aligned}\right\}$$

Reuss's Lower Limit

$$\left.\begin{aligned} K_v &= N_1K_1 + N_2K_2 + \ldots N_nK_n \\ \mu_v &= N_1\mu_1 + N_2\mu_2 + \ldots N_n\mu_n \end{aligned}\right\}$$

Voigt's Upper Limit

where N_1 is the volumetric percentage of component i

$$\left.\begin{aligned} k_{eff} &= (K_v + K_r)/2 \\ \mu_{eff} &= (\mu_r + \mu_v)/2 \end{aligned}\right\}$$

Hill's Average

2.4.2 Wood's Pore-fluid modulus Model – K_{fl} Estimate

There are two scenarios where Wood's model (1955) is of use to the geoscientist: for estimating the effective bulk modulus of pore-fluid K_{fl} and for estimating the effective bulk modulus of shallow-marine sediments that are essentially in suspension. Wood's velocity equation (equation…) employs the Ruess model to compute the effective bulk modulus and assigns a value of zero to the shear modulus.

One difficulty with Wood's model is that the shear modulus and thus V_s are assumed to be zero.

$$V = \sqrt{\frac{K_R}{\rho}} \ldots\ldots\ldots\ldots\ldots\ldots\ldots\ldots\ldots (27)$$

$$\frac{1}{K_R} = \frac{(1-\emptyset)}{K_{ma}} + \frac{(S_W)(\emptyset)}{K_{BR}} + \frac{(1-S_W)(\emptyset)}{K_{HYD}} \ldots\ldots (28)$$

$$\rho = (1-\emptyset)\rho_{ma} + (S_W)(\emptyset)\rho_{BR} + (1-S_W)\emptyset\rho_{HYD} \ldots\ldots\ldots\ldots (29)$$

K_R = K =the total bulk modulus or effective bulk modulus

2.4.3 Batzle and Wang's Estimate of Pore-Fluid Properties

In order to apply Wood's equation for estimating the bulk modulus of the pore fluid, the bulk moduli of water and hydrocarbons are required.

A more detailed and recommended approach for determining the pore-fluid bulk moduli and density has been given by Batzle and Wang (1992). Current pore-fluid modeling programs implement some version of their algorithms. In their procedure, the bulk moduli and density of a pore fluid component are expressed in terms of pore temperature, pressure, salinity, Gas-Oil-Ratio (GOR), API number, and specific gas gravity. After the bulk moduli of the pore fluid components are determined, the effective bulk modulus of the total fluid is determined using Wood's equation.

The bulk modulus (K) of a fluid or a gas is defined as

$$K = \frac{1}{\beta} = -\frac{\partial P}{(\partial V/V)} = \rho\,\frac{\partial P}{\partial \rho} \ldots\ldots\ldots\ldots\ldots (30)$$

where β is compressibility, P is pressure, and V is volume. For small pressure variations (typical for wave propagation), the pressure variation is related to the density variation through the acoustic velocity c_o (which is 1500 m/s for water at room conditions) as follows:

$$\partial P = C_o^2 \partial \rho \ldots\ldots\ldots\ldots\ldots\ldots\ldots\ldots\ldots\ldots (31)$$

Therefore,

$$K = \rho C_o^2 \ldots\ldots\ldots\ldots\ldots\ldots\ldots\ldots\ldots\ldots (32)$$

BRINE

The density of brine ρ_B of salinity S of sodium chloride is

$$\rho_B = \rho_w + S\{0.668 + 0.44S + 10^{-6}[300P - 2400PS + T(80 + 3T - 3300S - 13P + 47PS)]\} \ldots\ldots\ldots\ldots\ldots\ldots (33)$$

where the density of pure water (ρ_w) is

$$\rho_w = 1 + 10^{-6}(-80T - 3.3T^2 + 0.00175T^3 + 489PS - 2TP + 0.016T^2P - 1.3 \times 10^{-5}T^3P - 0.333P^2 - 0.002TP^2) \ldots\ldots\ldots (34)$$

In these formulas pressure P is in MPa, temperature T is in degrees Celsius, salinity S is in fractions of one (parts per million divided by 10^6), and density (ρ_B and ρ_W) is in g/cm^3.

The acoustic velocity in brine V_B in m/s is

$$V_B = V_W + S(1170 - 9.6T + 0.055T^2 - 8.5 \times 10^{-5}T^3 + 2.6P - 0.0029TP - 0.0476P^2) + S^{1.5}(780 - 10P + 0.16P^2) - 1820S^2 \ldots\ldots\ldots (35)$$

where the acoustic velocity in pure water V_W in m/s is

$$V_W = \sum_{i=0}^{4} \sum_{j=0}^{3} W_{ij} T^i P^j \ldots\ldots\ldots\ldots\ldots\ldots\ldots\ldots\ldots\ldots (36)$$

and coefficients W_{ij} are

W_{00} = 1402.85 $\qquad$ $W_{02} = 3.437 \times 10^{-3}$

W_{10} = 4.871 $\qquad$ $W_{12} = 1.739 \times 10^{-4}$

$W_{20} = -0.04783$ $W_{22} = -2.135 \times 10^{-6}$

$W_{30} = 1.487 \times 10^{-4}$ $W_{32} = -1.455 \times 10^{-8}$

$W_{40} = -2.197 \times 10^{-7}$ $W_{42} = 5.230 \times 10^{-11}$

$W_{01} = 1.524$ $W_{03} = -1.197 \times 10^{-5}$

$W_{11} = -0.0111$ $W_{13} = -1.628 \times 10^{-6}$

$W_{21} = 2.747 \times 10^{-4}$ $W_{23} = -1.237 \times 10^{-8}$

$W_{31} = -6.503 \times 10^{-7}$ $W_{33} = -1.327 \times 10^{-10}$

$W_{41} = 7.987 \times 10^{-10}$ $W_{43} = -4.614 \times 10^{-13}$

We define the gas-water ratio R_G as the ratio of the volume of dissolved gas at standard conditions to the volume of brine. Then, for temperatures below 250°C, the maximum amount of methane that can go into solution in brine is

$$\log_{10}(R_G) = \log_{10}(0.712P|T - 76.71|^{1.5} + 3676P^{0.64}) - 4$$

$$- 7.786S(T + 17.78)^{-0.306}$$

If K_B is the bulk modulus of the gas-free brine, and K_G is that of brine with gas-water ratio R_G, then

$$\frac{K_B}{K_G} = 1 + 0.0494R_G \quad \text{………………………………….. (37)}$$

As far as the density of the brine is concerned, experimental data are sparse, but the consensus is that the density is almost independent of the amount of dissolved gas.

The viscosity of brine ŋ in *cPs* for temperatures below 250°C is

$$ŋ = 0.1 + 0.333S + (1.65 + 91.9S^3)e^{-\left[0.42(S^{0.8} - 0.17)^2\right]T^{0.8}} \quad \text{…….. (38)}$$

Gas

Natural gas is characterized by its gravity G, which is the ratio of gas density to air density at 15.6^0C and atmospheric pressure. The gravity of methane is 0.56. It may be as large as 1.8 for heavier natural gases. Algorithms for calculating gas density and bulk modulus follow.

STEP 1: Calculate absolute temperature ***T,*** as

$$T_a = T + 273.15 \text{ ....} \quad (39)$$

where T is in degrees Celsius

STEP 2: Calculate pseudopressure P_r and pseudotemperature T_r as

$$P_r = \frac{P}{4.892 - 0.4048G}, \quad T_r = \frac{T_a}{94.72 + 170.75G}$$

where pressure is in MPa.

STEP 3: Calculate density ρ_G in g/cm^3 as

$$\rho_G \approx \frac{28.8GP}{ZRT_a} \text{ ....} \quad (40)$$

$$Z = a\,P_r + b + E, \qquad E = cd$$

$$d = exp\left\{-\left[0.45 + 8\left(0.56 - \frac{1}{T_r}\right)\right]\frac{P_r^{1,2}}{T_r}\right\}$$

$$c = 0.109(3.85 - T_r)^2, \quad b = 0.642T_r - 0.007T_r^4 - 0.52$$

$$a = 0.03 + 0.00527(3.5 - T_r)^3$$

$$R = 8.31441 \text{ J/g –mole deg (gas constant)}$$

STEP 4: Calculate the adiabatic bulk modulus K_G in MPa as

$$K_G \approx \frac{P\gamma}{1 - \frac{P_r}{Z}f}, \qquad \gamma = 0.85 + \frac{5.6}{P_r + 2} + \frac{27.1}{(P_r + 3.5)^2} - 8.7e^{-0.65(P_r + 1)}$$

$$f = cdm + a, \quad m = 1.2\left\{-\left[0.45 + 8\left(0.56 - \frac{1}{T_r}\right)^2\right]\frac{P_r^{0.2}}{T_r}\right\}$$

The preceding approximate expressions for ρ_G and K_G are valid as long as P_r, and T, are not both within 0.1 of unity.

Oil

Oil density under room conditions may vary from under 0.5 to 1 g/cm^3, and most produced oils are in the 0.7 to 0.8 g/cm^3 range. A reference (standard) density that can be used to characterize oil ρ_o is measured at 15.6^{0}C and atmospheric pressure. A widely used classification of crude oil is the American Petroleum Institute oil gravity (API gravity). It is defined as

$$\text{API} = \frac{141.5}{\rho_o} - 131.5 \quad \text{…………………..} (41)$$

where density is in g/cm^3. API gravity may be about 5 for very heavy oils and about 100 for light condensates.

Acoustic velocity in oil V_p may generally vary with temperature T and molecular weight *M:*

$$V_p(T, M) = V_o - b\Delta T - a_m\left(\frac{1}{M} - \frac{1}{M_o}\right) \text{……………………………} (42)$$

$$b = 0.306 - 7.6/M$$

In this formula, V_o is the velocity of oil of molecular weight $M_o$at temperature T_o; a_m is a positive function of temperature, and thus oil velocity increases with molecular weight. When components are mixed, velocity can be approximately calculated as a fractional average of the end components.

For dead oil (oil with no dissolved gas), the effects of pressure and temperature on density are largely independent. The pressure dependence is

$$\rho_p = \rho_0 + (0.00277P - 1.71 \times 10^{-7}P^3)(\rho_o - 1.15)^2 + 3.49 \times 10^{-4}P \text{……..…} (43)$$

where ρ_p is the density in g/cm^3 at pressure P in MPa. Temperature dependence of density at given pressure P is

$$\rho = \rho_p/[0.972 + 3.81 \times 10^{-4}(T + 17.78)^{1.175}] \text{ ……………………….. } (44)$$

where temperature is in degrees Celsius.

Acoustic velocity in dead oil depends on pressure and temperature as

$$V_p(m/s) = 2096\left(\frac{\rho_o}{2.6-\rho_o}\right)^{1/2} - 3.7T + 4.64P + 0.0115\left[4.12(1.08\rho_o^{-1})^{1/2} - 1\right]TP \text{ .... (45)}$$

or, in terms of API gravity as

$$V_p(ft/s) = 15450(77.1 + API)^{-1/2} - 3.7T + 4.64P + 0.0115\left[0.36API^{1/2} - 1\right]\mathrm{TP} \text{ ...(46)}$$

Live Oil

Large amounts of gas can be dissolved in oil. The original fluid in situ is usually characterized by R_G, the volume ratio of liberated gas to remaining oil at atmospheric pressure and 15.6^0C. The maximum amount of gas that can be dissolved in oil is a function of pressure, temperature, and the composition of both the gas and the oil:

$$R_G^{(max)} = 0.02123G\left[P_{exp}\left(\frac{4.072}{\rho_o} - 00.00377T\right)\right]^{1.025} \text{ .... (47)}$$

or, in terms of API gravity as

$$R_G^{(max)} = 2.03G\left[P_{exp}(0.02878API - 00.00377T)\right]^{1.025} \text{ .... (48)}$$

where R_G is in Liters/Liter (1 L/L = 5.615 ft^3/bbl) and G is the gas gravity. Temperature is in degrees Celsius, and pressure is in MPa.

Velocities in oils with dissolved gas can still be calculated versus pressure and temperature as follows by using the preceding formulas with a pseudodensity ρ' used instead of ρ_o:

$$\rho' = \frac{\rho_o}{B_o}(1 + 0.001R_G)^{-1} \text{ ....(49)}$$

$$B_o = 0.972 + 0.00038\left[2.4R_G\left(\frac{G}{\rho_o}\right)^{1/2} + T + 1.78\right]^{1.175} \text{ .... (50)}$$

The true density of oil with gas (in g/cm^3) can be calculated as

$$\rho_G = (\rho_o + 0.0012GR_G)/B_o \text{ .... (51)}$$

Viscosity of dead oil (ŋ) decreases rapidly with increasing temperature. At room pressure for gas-free oil we have

$$\log_{10}(\eta + 1) = 0.505y(17.8 + T)^{-1.163}$$

$$\log_{10}(y) = 5.693 - 2.863/\rho_o$$

Pressure has a smaller influence on viscosity and can be estimated independently of the temperature influence. If oil viscosity is η_o at a given temperature and room pressure, its viscosity at pressure P and the same temperature is

$$\eta = \eta_o + 0.145PI \qquad (52)$$

$$\log_{10}(y) = 18.6[0.1\log_{10}(\eta_o) + (\log_{10}\eta_o)^{-0.1} - 0.985]$$

Viscosity in these formulas is in centipoises, temperature is in degrees Celsius, and pressure is in MPa.

$$\log_{10}(0.712P[T - 76.71] + 3676P^{0.64}) - 4 - 7.786S(T + 17.78)$$

2.4.4 Biot Coefficient's Estimation of Dry Rock Bulk Modulus K_{dry}

The bulk modulus of the total rock K (effective rock bulk modulus) depends on the pore-fluid bulk modulus (K_{fl}), the matrix bulk modulus (K_{ma}) and the dry-rock bulk modulus (K_{dry}). As has been discussed above, two of these bulk moduli K_{fl} and K_{ma} can be estimated if the volumetric mineral and pore-fluid components of the rock are known. Numerous petrophysicists have developed empirical approximations to estimate K_{dry} based on other known properties of the rock. Many of the techniques are related to Biot's coefficient as expressed in equation 53.

Biot's coefficient, B, is a function of K_{ma}, which can be estimated, and K_{dry}, the desired dry-rock bulk modulus. B values range from 0 (well consolidated sediments) to 1 (unconsolidated sediments and suspended loads). One the most popular experimental approaches has been to approximate B as a function of porosity. The following have been suggested.

1. Geertsma (1961) $B = 1 - [1 - 50\phi]^{-1}$
2. Krief et al. (1990) $B = 1 - [1 - \phi]^{[3/(1-\emptyset)]}$
3. Nur etal. (1991) $B = \phi/\phi_{critical} \quad \phi < \phi_{critical}$

   $B = 1 \quad \phi \geq \phi_{critical}$

   Where (Mavko et al., 1998):

Material	Critical porosity ($\phi_{critical}$)
Sandstone	40%
Limestone	60%
Dolomite	40%
Pumice	80%
Chalk	65%

4. Polynomial expansion of $K_{dry}/K_{ma} = a_0 + a_1 (\phi/\phi_{critical}) + a_2 (\phi/\phi_{critical})^2$

leads to $B = 2 (\phi/\phi_{critical}) - (\phi/\phi_{critical})^2$

from the initial conditions of:

$$K_{dry}/K_{ma} = 1 \quad at\ (\phi/\phi_{critical}) = 0$$

$$K_{dry}/K_{ma} = 0 \quad at\ (\phi/\phi_{critical}) = 1$$

The Krief model incorporates the Raymer – Hunt – Gardner's (H-R-G) relationship. The Nur model is based on empirical observations from laboratory measurements and the introduction of the critical porosity term.

B = Biot Coefficient = $\left(1 - K_{dry}/K_{ma}\right)$ … … … … … … … … … … … … .53

therefore $K_{dry} = (1 - B)K_{ma}$

A. End member at $\phi = 0$

$K_{dry} = K_{ma}$

B. End member at $\phi = 1$

$K_{dry} = 0$

$$0 \leq K_{dry}/K_{ma} < 1$$

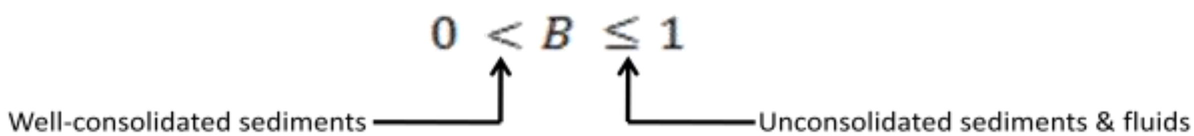

2.4.5 Gassmann's Theory

Of the many wave- propagation theories in the geophysical literature, Gassmann's (1951) has been the most widely applied by geophysicists. Gassmann's equation is popular because of the ease in providing values for the parameters in his equation. Basically, Gassmann derived an equation that relates the effective bulk-modulus of a fluid-saturated rock to that of the bulk moduli of the matrix material (K_{ma}), the frame (K_{dry}), pore fluid (K_{fl}) and porosity (ϕ). Methods to estimate K_{ma} and K_{fl} were discussed in the previous section.

Biot's (1955a) theory is an extension of Gassmann's (1951) theory. Biot included fluid viscosity and the fact that the pore fluid could move relative to the frame. With viscosity, Biot's model exhibited attenuation and the possibility of having two P-waves propagating at different velocities through the medium. However, values for the parameters required in Biot's equation are more difficult to derive, and to understand intuitively.

If only the conventional well-log suite of gamma, SP, resistivity, neutron, density, and p-wave sonic curves are available, none of the theoretical models mentioned above have enough information to estimate V_s. Thus, geophysicists need additional empirical models. The fact that Gassmann's equation only requires one additional piece of information and correlates fairly accurately to field measurements makes it obvious choice. In addition, the empirical models selected to provide the additional information needed to solve Gassmann's equation can be adjusted regionally.

2.4.5.1 Gassmann's Equation

Gassmann's Equation (Gassmann, 1951) is the most applicable model at seismic frequencies **(**equation 52). It is an approximation to real rocks (Wang and Nur, 1992) describing a rock in terms of the incompressibilities of a two-phase medium. It is applicable to rocks with intergranular porosity and more or less uniform grain size.

$$\frac{K_{sat}}{K_{ma}-K_{sat}} = \frac{K_{dry}}{K_{ma}-K_{dry}} + \frac{K_{fluid}}{\phi_{sand}(K_{ma}-K_{fluid})} \quad \ldots\ldots\ldots\ldots\ldots\ldots\ldots \text{(53)}$$

$$\mu_{sat} = \mu_{dry} \quad \ldots\ldots\ldots\ldots\ldots\ldots\ldots\ldots\ldots\ldots\ldots\ldots \text{(54)}$$

where:

K_{dry} = effective bulk modulus of dry rock;

K_{sat} = effective bulk modulus of the rock with pore fluid;

K_{ma} = bulk modulus of mineral material making up rock

K_{fluid} = effective bulk modulus of pore fluid;

ϕ_{sand} = sand porosity ($\varphi_{sand} = \frac{\varphi_e}{(1-V_{cl})}$)

μ_{sat}= effective shear modulus of rock with pore fluid;

μ_{dry}= effective shear modulus of dry rock.

Gassmann Assumptions

Importantly, key assumptions in the model are that (Wang and Nur 1992) (Figure 8.2)

1. The solid is homogenous and isotropic

2. All the pore space is in communication

3. There is limited coupling between fluid and matrix (low frequency assumption)

4. Fluid that fills the pore space is frictionless (ie low viscosity) and that the shear modulus is not affected by interaction with the pore filling fluid.

$$\mu = V_S^2 \rho_b \ldots\ldots\ldots\ldots\ldots\ldots\ldots \text{(55)}$$

$$K_{sat} = V_p^2 \rho_b - \frac{4}{3}\mu \ldots\ldots\ldots\ldots\ldots\ldots \text{(56)}$$

where:

V_p = compressional velocity

V_s = shear velocity

ρ_b = bulk density

The dry rock or frame bulk modulus is a key unknown and needs to be derived from other Gassmann parameters

$$K_{dry} = \frac{K_{sat}\left(\frac{\phi K_{ma}}{K_{fl}}+1-\phi\right)-K_{ma}}{\frac{\phi K_{ma}}{K_{fl}}+\frac{K_{sat}}{K_{ma}}-1-\phi} \ldots\ldots\ldots\ldots\ldots \text{(57)}$$

The mineral modulus is a function of the velocity, density and shear modulus of the minerals:

$$K_{ma} = V_{P_{ma}}^2 \rho_{ma} - \frac{4}{3}\mu_{ma} \ldots\ldots\ldots\ldots\ldots \text{(58)}$$

Given that shear velocities do not travel through fluids, the fluid modulus is a function of the fluid density and velocity:

$$K_{fluid} = V_{P_{fluid}}^2 \rho_{fluid} \ldots\ldots\ldots\ldots\ldots\ldots \text{(59)}$$

When calculating the effects of a change in fluid on the rock properties ('fluid substitution'), the change in density is readily calculated:

$$\rho_{b\_2} = \left(\rho_{fluid\_2} \times \phi\right) + \left((1-\phi) \times \rho_{ma}\right) \ldots\ldots\ldots\ldots (60)$$

Equally, given that the shear modulus has already derived the V_s for the rock with new fluid is also straightforward to calculate.

$$V_{s\_2} = \sqrt{\frac{\mu}{\rho_{b\_2}}} \ldots\ldots\ldots\ldots\ldots\ldots\ldots\ldots\ldots\ldots\ldots\ldots (61)$$

Calculation of fluid substituted V_p requires V_{sat} for the rock with new fluid.

$$K_{sat2} = K_{dry} + \frac{\left(1-\frac{K_{dry}}{K_{ma}}\right)^2}{\frac{\phi}{K_{fluid\_2}}+\frac{1-\phi}{K_{ma}}-\frac{K_{dry}}{K_{ma}^2}} \ldots\ldots\ldots\ldots\ldots\ldots\ldots\ldots (62)$$

$$V_{p\_2} = \sqrt{\frac{K_{sat}+{}^4/_3\mu}{\rho_{b\_2}}} \ldots\ldots\ldots\ldots\ldots\ldots\ldots\ldots\ldots\ldots\ldots\ldots (63)$$

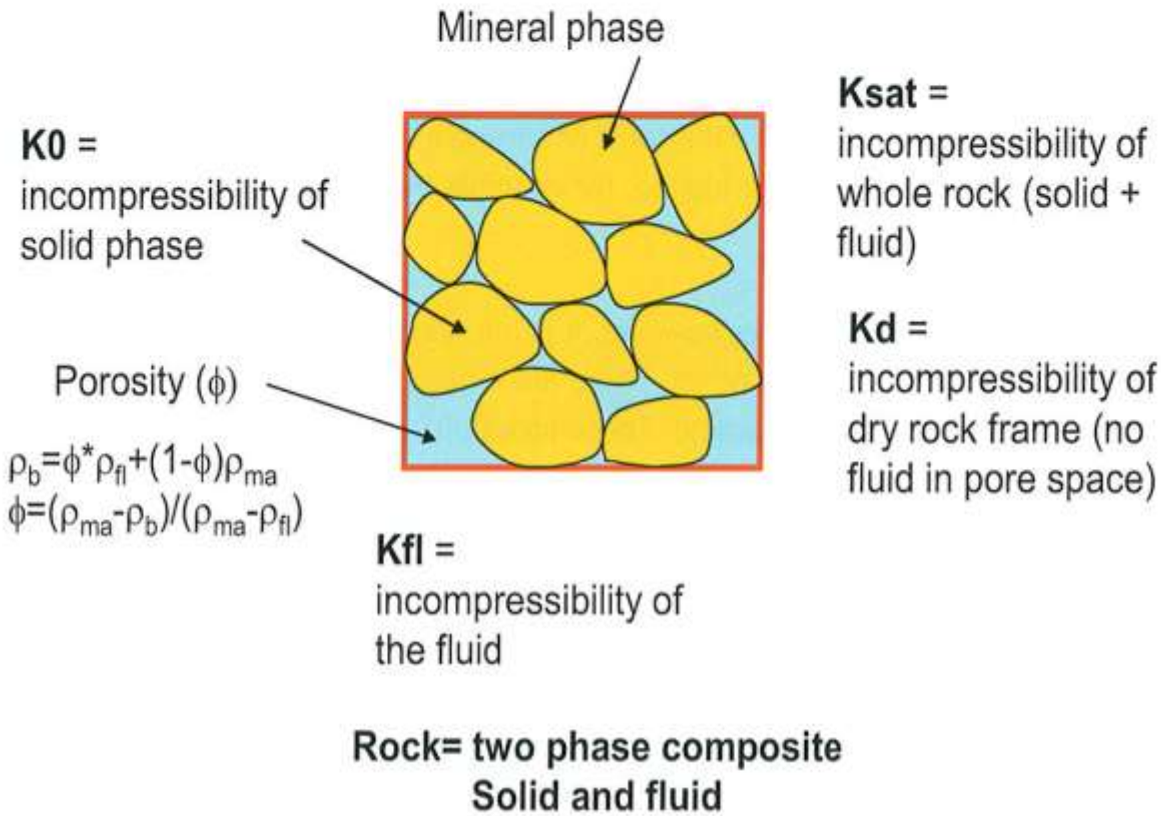

Figure 2.1: Gassmann rock parameters – incompressibility

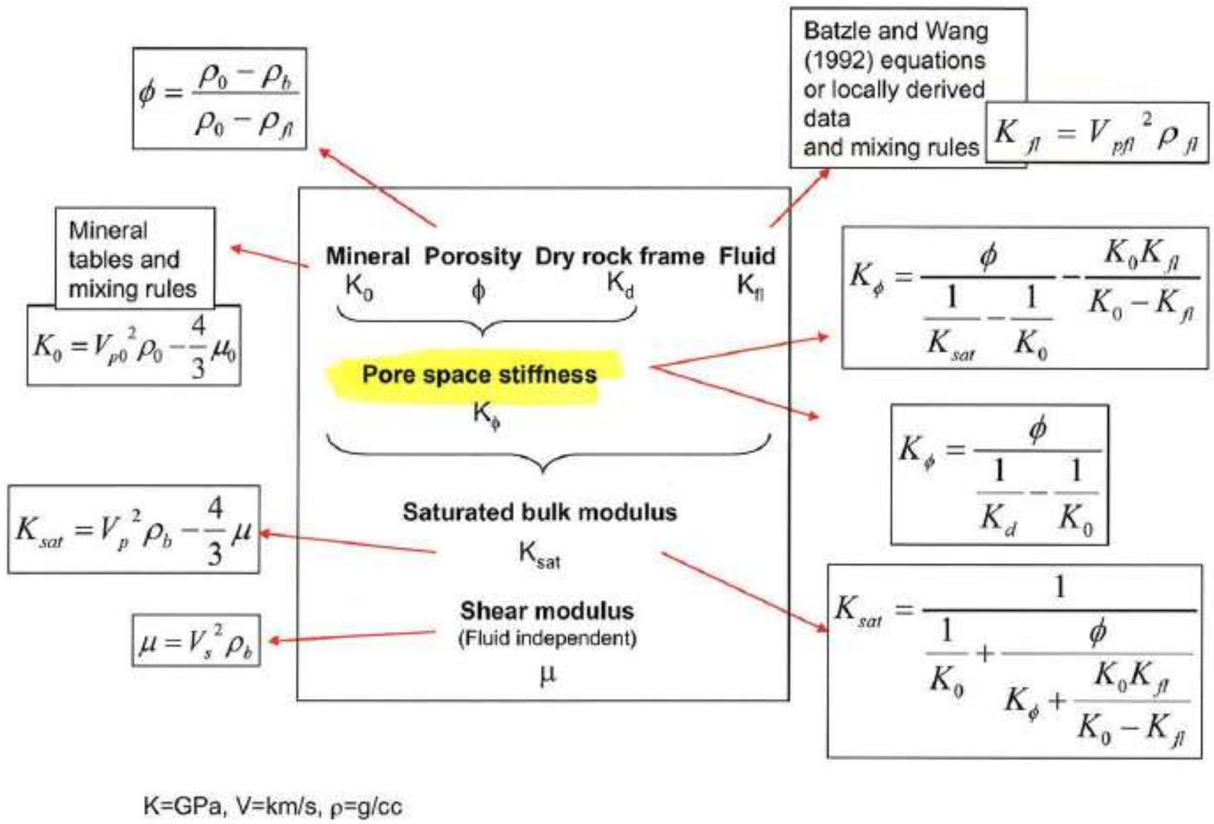

Figure 2.2: Gassmann rock components and practical equations (derived from Gassmann's relations) that can be used in log analysis.

Table 3: Gassmann and various rock types

<table>
<tr><td>Sandstones and Carbonates with moderate to high porosity</td><td>Gassmann OK</td><td>Considered that sonic log responses in these rocks are essentially low frequency and Gassmann is applicable</td></tr>
<tr><td>Tight Sands</td><td rowspan="2">Gassmann application requires care</td><td>At logging frequencies:
Velocities may be dispersive
Patchy saturation may characterise low saturation gas scenarios
At seismic frequencies:
uncertainty over fluid modulus</td></tr>
<tr><td>Shaley Sands and Laminated Sands</td><td>Common Gassmann pitfall of exaggerated fluid substitution effect
Gassmann needs to be 'fudged' to achieve intuitive result</td></tr>
<tr><td>Rocks with Fractures or Dual Porosity Systems</td><td>Other models required</td><td></td></tr>
</table>

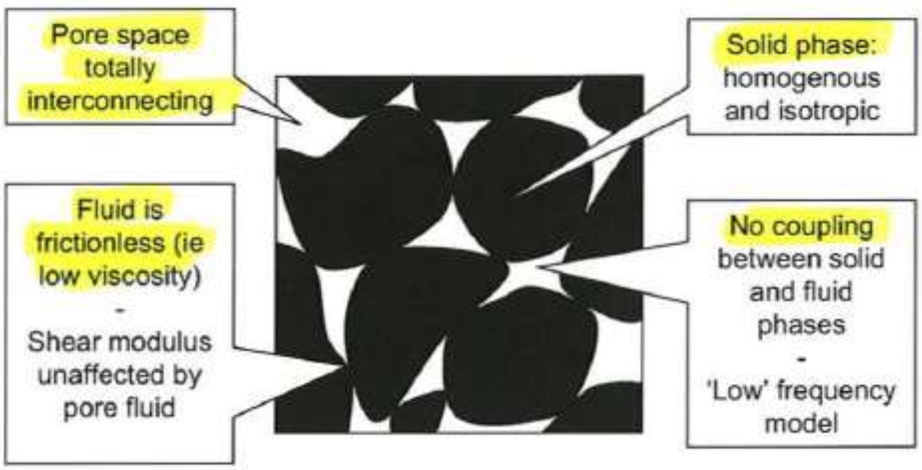

Figure 2.3: Gassmann Model - Assumptions

2.5 Overview of Amplitude Variation with Offset (AVO) Theory

AVO (Amplitude Versus Offset) is a powerful technique for analyzing prestack seismic data that can lead, sometimes, to the identification of hydrocarbon bearing reservoir potential.

Using the AVO technique seismic amplitudes and their variation as a function of offset are analyzed. This information is then used to predict lithology and fluid content.

The basic concept behind the AVO technique is the analysis of the reflection process. We take advantage of the fact that the measured amplitude is related to the strength of the reflection (reflection coefficient), and that the reflection coefficient depends on three parameters:

1. Change in P-wave velocity across the interface.
2. Change in S-wave velocity across the interface.
3. Change in density across the interface.

2.5.1 Reflectivities and Offset

When a P-wave arrives at an interface between two layers, some of the energy reflects back to the surface and some is transmitted. The amount reflected and the amount transmitted depends on the contrast in parameters of the two layers. The relevant parameters are:

V_{p_1}, V_{s_1}, ρ_1 – P − wave velocity, S − wave velocity, and density for layer 1

V_{p_2}, V_{s_2}, ρ_2 – P − wave velocity, S − wave velocity, and density for layer 2

At normal incidence the reflection coefficients depend only on V_p and ρ.

$$R_{NI} = \frac{\rho_2 V_{p_2} - \rho_1 V_{p_1}}{\rho_2 V_{p_2} + \rho_1 V_{p_1}} = \frac{\Delta I_P}{I_P} \quad \text{.............................. (64)}$$

Where I_P is the P-wave impedance

When the wave arrives at the interface at non-normal incidence, some of the P wave energy is converted to shear. Figure 2.0 describes these phenomena.

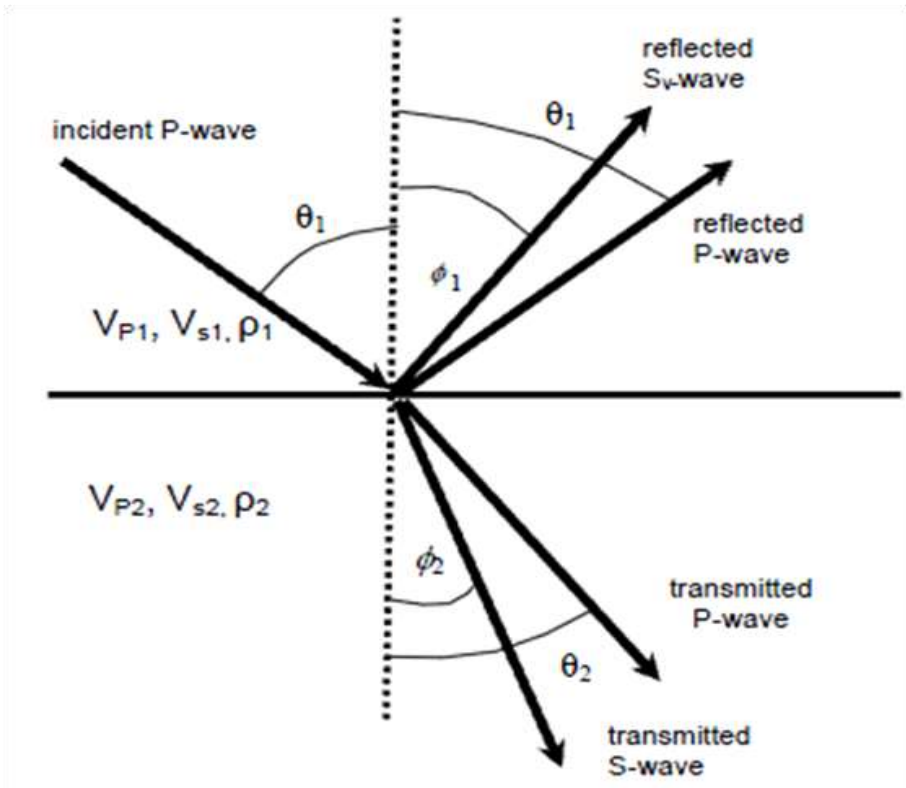

Figure 2.4: Reflection at the interface

2.5.2 Zoeppritz Equations

Zoeppritz Equations relate the reflection coefficients to the angle of incidence, $\Delta V_p, \Delta V_s$ *and* $\Delta\rho$.

Zoeppritz (1919) derived the particle motion amplitudes of the reflected and transmitted waves using the conservation of stress and displacement across the interface, which yields four equations with four unknowns:

$$\begin{bmatrix} R_P \\ R_S \\ T_P \\ T_S \end{bmatrix} = \begin{bmatrix} -\sin\theta_1 & -\cos\phi_1 & \sin\theta_2 & \cos\phi_2 \\ \cos\theta_1 & -\sin\phi_1 & \cos\theta_2 & -\sin\phi_2 \\ \sin 2\theta_1 & \frac{V_{P1}}{V_{S1}}\cos 2\phi_1 & \frac{\rho_2 V_{S2}^2 V_{P1}}{\rho_1 V_{S1}^2 V_{P1}}\cos 2\phi_1 & \frac{\rho_2 V_{S2} V_{P1}}{\rho_1 V_{S1}^2}\cos 2\phi_2 \\ -\cos 2\phi_1 & \frac{V_{S1}}{V_{P1}}\sin 2\phi_1 & \frac{\rho_2 V_{P2}}{\rho_1 V_{P1}}\cos 2\phi_2 & \frac{\rho_2 V_{S2}}{\rho_1 V_{P1}}\sin 2\phi_2 \end{bmatrix}^{-1} \begin{bmatrix} \sin\theta_1 \\ \cos\theta_1 \\ \sin 2\theta_1 \\ \cos 2\phi_1 \end{bmatrix}$$

R_P, R_S, T_P, and T_S, are the reflected P, reflected S, transmitted P, and transmitted S-wave amplitude coefficients, respectively. The Zoeppritz equations are complex. Inverting the matrix form of the Zoeppritz equations give the coefficients as a function of angle. Although the Zoeppritz equations are exact, the equations do not lead to an intuitive understanding of the Amplitude versus Offset (AVO) process. Modeling can be routinely done with the Zoeppritz equations but most Amplitude versus Offset (AVO) methods for analyzing real time seismic data are based on linearized approximations to the Zoeppritz equations.

2.5.2.1 Aki & Richards Approximation:

Main interest of this formulation is the expression of the reflection coefficient depending from relative contrasts of V_P, V_s and rho (respectively, P-wave, S-wave velocities and densities):

$$R(\vartheta) \cong \frac{1}{2}\left(1 - 4\frac{V_s^2}{V_p^2}Sin^2(\vartheta)\right)\frac{\Delta\rho}{\rho} + \frac{1}{2Cos^2(\vartheta)}\frac{\Delta V_p}{V_p} - 4\frac{V_s^2}{V_p^2}\frac{\Delta V_s}{V_s}Sin^2(\vartheta) \ldots\ldots\ldots\ldots (65)$$

with $\Delta V_p = V_{p2} - V_{p1}$ $\quad \Delta V_s = V_{s2} - V_{s1}$ $\quad \Delta\rho = \rho_2 - \rho_1$

and $V_p = \frac{1}{2}(V_{p2} + V_{p1})$ $\quad V_s = \frac{1}{2}(V_{s2} + V_{s1})$ $\quad \rho = \frac{1}{2}(\rho_2 + \rho_1)$ $\quad \vartheta = \frac{1}{2}(\vartheta_2 + \vartheta_1)$

It represents the variations in reflection coefficient with angle R (ϑ) as a function of three parameters:

1. Relative change in V_p - $\frac{\Delta V_p}{V_p}$
2. Relative change in V_s - $\frac{\Delta V_s}{V_s}$

3. Relative change in ρ - $\frac{\Delta\rho}{\rho}$

The basic form of this approximation is:

$$R(\vartheta) \approx a\frac{\Delta\rho}{\rho} + b\frac{\Delta V_p}{V_p} + c\frac{\Delta V_s}{V_s} \quad \text{……………………………..….. (66)}$$

Aki & Richards Approximation assumes that:

- It is a plane wave
- There is P wave to P wave reflection
- There are only precritical reflections
- There are only small changes in elastic parameters across the interface

2.5.2.2 Fatti Form of the Aki & Richards Equation

Fatti et al(1994) gave another form of Aki & Richards formulation, which does not account for the critical angle since it only computes with the incident angle (that is, it does not contain Snell's law):

$$R_{pp}(\theta)=(1+\ tan^2\theta)\frac{\Delta I_p}{2I_p} - 8\left(\frac{V_s}{V_p}\right)^2 sin^2\theta\ \frac{\Delta I_s}{2I_s} - \left[\frac{1}{2}\ tan^2\theta - \left(\frac{V_s}{V_p}\right)^2\ sin^2\theta\right]\frac{\Delta\rho}{\rho} \quad \text{…..(67)}$$

where R_{PP} is the P-wave reflectivity, θ is the incidence angle, I is the acoustic impedance for P and S waves (denoted by subscript), V is acoustic velocity, and ρ is bulk density. The deltas (Δ) indicate that the difference at each interface is to be used, and given as a proportion of the average of the quantity across the interface (so that these coefficients are positive).

Many people read the equation as three terms: the first driven principally by acoustic P-wave impedance, the second by shear wave impedance, and the third by density.

This equation is very useful for both independent and simultaneous prestack inversion of seismic data and provides a way to extract quantitative information about the P and S reflectivity which can be used for pre-stack inversion.

2.5.2.3 Wiggins Form of the Aki & Richards Equation

Wiggins et al. (1983) algebraically reformulated the Aki-Richards equation. They separated the equation into three reflection terms, each weaker than the previous term:

$$R_p\ (\theta) = \mathrm{A} + \mathrm{B}\ sin^2\theta + C\ tan^2\theta\ sin^2\theta \text{ ... ...(68)}$$

where: $\mathrm{A} = \frac{1}{2}\left[\frac{\Delta V_p}{V_p} + \frac{\Delta\rho}{}\rho\right]$, Intercept

$\mathrm{B} = \frac{1}{2}\frac{\Delta V_p}{V_p} - 4\left[\frac{V_s}{V_p}\right]^2\frac{\Delta V_s}{V_s} - 2\left[\frac{V_s}{V_p}\right]^2\frac{\Delta\rho}{\rho}$, Gradient

$\mathrm{C} = \frac{1}{2}\frac{\Delta V_p}{V_p}$, Curvation

2.5.2.4 Shuey Approximation:

Shuey (1985) chose a formula that underlines the role of the Poisson's ratio:

$$R\ (\theta_1) = R_0 + \left(A_0\, R_0 + \frac{\Delta\sigma}{(1-\sigma)^2}\right) sin^2\theta_1 + 1/2\,(tg^2\theta_1 - sin^2\theta_1\,)\,\frac{\Delta V_p}{V_p} \text{ .... (69)}$$

With:

$$,\sigma_i = \frac{\left(\frac{V_{Pi}}{V_{si}}\right)^2 - 2}{2\left(\left(\frac{V_{pi}}{V_{si}}\right)^2 - 1\right)} \text{ Poisson ratio of medium i.}$$

and:

$$\sigma = \frac{\sigma_{1} + \sigma_{2}}{2}$$

$$V_p = \frac{V_{p1} + V_{p2}}{2}$$

$$\Delta\sigma = \sigma_1 - \sigma_2$$

$$V_p = V_{p2} - V_{p1}$$

$$R_0 = \left(\frac{\Delta V_p}{V_p} + \frac{\Delta\rho}{\rho}\right) / 2 \qquad A_0 = B - 2(1+B)\frac{1-2\sigma}{1-\sigma}$$

$$\mathrm{B} = \frac{\frac{\Delta V_p}{V_p}}{\frac{\Delta V_p}{V_p} + \frac{\Delta\rho}{\rho}}$$

For angles less than 30°, the term $tg^2\theta_1 - \sin^2\theta_1$ of the above equation (69) is small and leads to the well known Shuey formulae:

$$R(\theta_1) = R_0 + Gr * sin^2(\theta_1) \ldots\ldots\ldots\ldots\ldots\ldots\ldots\ldots(70)$$

$$Gr = A_0 * R_0 + \frac{\Delta\sigma}{(1-\sigma)^2} \ldots\ldots\ldots\ldots\ldots\ldots\ldots\ldots\ldots\ldots\ldots\ldots(71)$$

It should be noted that further simplifications exist for the case where the average Poisson's ratio is 0.33 (equivalently Vp/Vs = 2). In such a case, A_0 equals to -1, irrespective of any relative density /velocity contrast ratio (i.e. term "B" of the above equation).

2.5.2.5. Hilterman Approximation:

Hilterman (1990) suggested another way to rearrange Shuey formulae assuming small angles and that $\sigma \approx \frac{1}{3}$.

$$R(\theta) \approx R_p \cdot \cos^2\theta + \frac{9}{4}\Delta\sigma sin^2\theta \qquad (72)$$

This formula shows that reflectivity at small angles is dominated by P-wave velocity and large angle reflectivity is dominated by $\Delta\sigma$ (change in Poisson's Ratio).

$$\Delta\sigma = \frac{9}{4}(R_p + G) \qquad (73)$$

where G is the gradient

2.6 Classification of AVO Anomalies.

To determine which seismic characteristics are pertinent for specific geologic trends, it is necessary to classify hydrocarbon-generated amplitude anomalies based on their geologic setting. Rutherford and Williams (1989) classified amplitude anomalies based on three classes of AVO responses from the top of gas sands. With the addition of Castagna's (1998) class 4, essentially all geologic settings are accounted for in clastic environments.

- Class I: Very consolidated sands (porosity <15%) that typically have gross interval velocities >12 500 ft/s (3650 m/s). These reservoir sands have higher impedance than the encasing shale with the density contrast having a greater effect on the AVO response. These reservoirs are usually found onshore in hard rock geologic settings (e.g., Mesozoic and Paleozoic rocks). On CMP gathers, Class I starts with a high amplitude and reduces with offset (see Figure 2.5)
- Class II: Less consolidated sands than class 1, but more consolidated than class 3. These

moderately compacted sands (porosity 15-25%) are found offshore and onshore. Gross interval velocities of the sands are typically between 8500 and 12 500 ft/s (2650-3650 m/s). The acoustic impedance of the gas sand and the encasing shale are about equal. On CMP gathers, this Class starts with low amplitude and increases with offset. There is a second Class II anomaly known as Class IIP. This Class IIP is similar to a standard class II anomaly but with a polarity reversal in the near offsets.

- Class III: This is the typical "bright spot" or "DHI" setting where unconsolidated reservoir sands are encased in higher impedance shales, usually of Tertiary age. These reservoirs commonly have porosities >25% and contain gas or high GOR oils. Gross interval velocity of these sands is usually <8500 ft/s (2650 m/s). Class 3 targets were initially found exclusively offshore but, due to higher quality seismic data, are now being observed more frequently onshore. This Class starts with high amplitude and increases further with offset.
- Class 4: Unconsolidated sand similar to class 3, but over-lain by high velocity hard shale, siltstone, or carbonate. Shear-wave velocity in this overlying hard interval is larger than that of the gas sand (this situation is opposite for all other classes). This Class starts with high amplitude and decreases with offset.

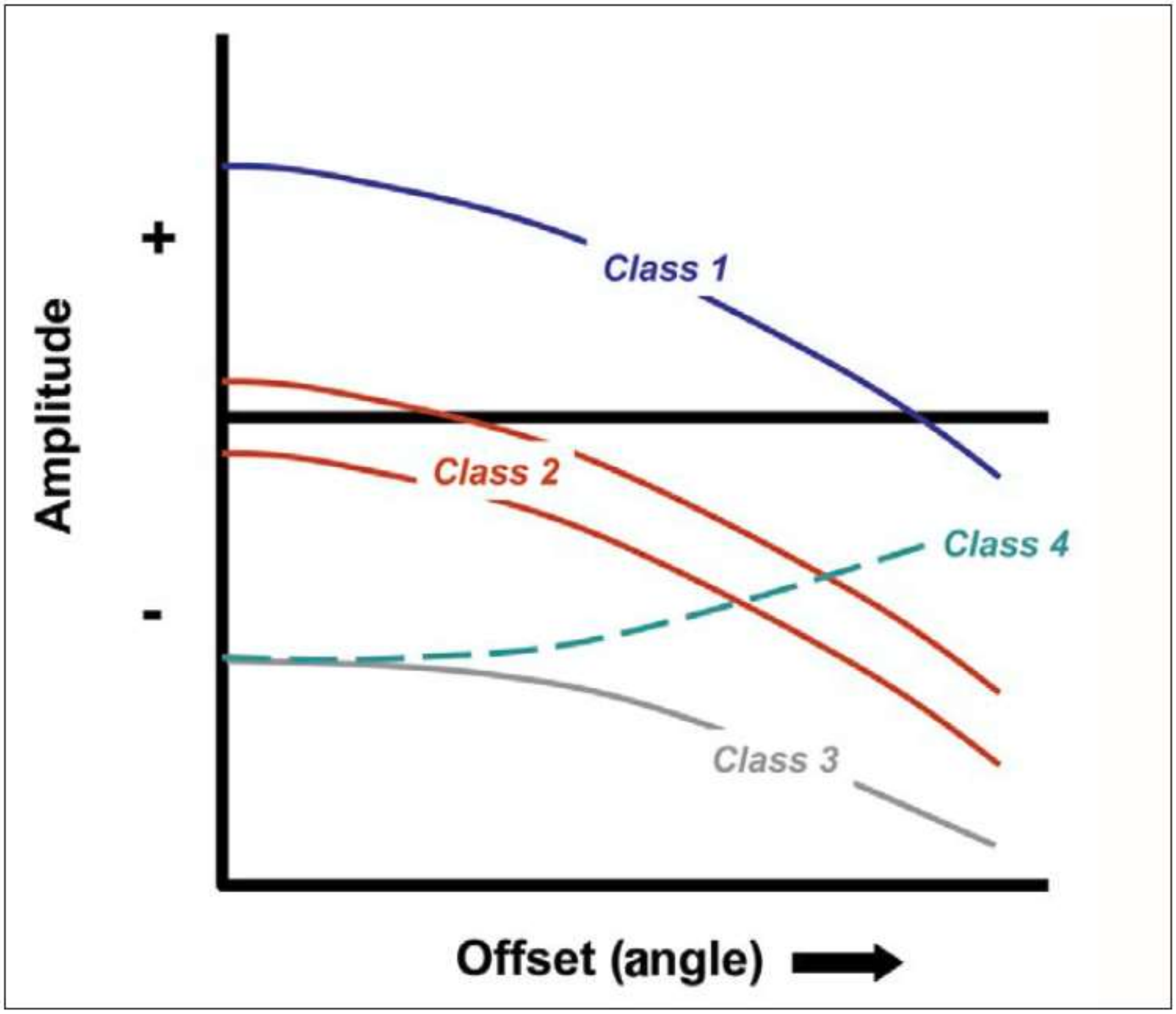

Figure 2.5: AVO classes based on amplitude change with offset from the top of gas sands (Rutherford and Williams, 1989; Castagna et al., 1998).

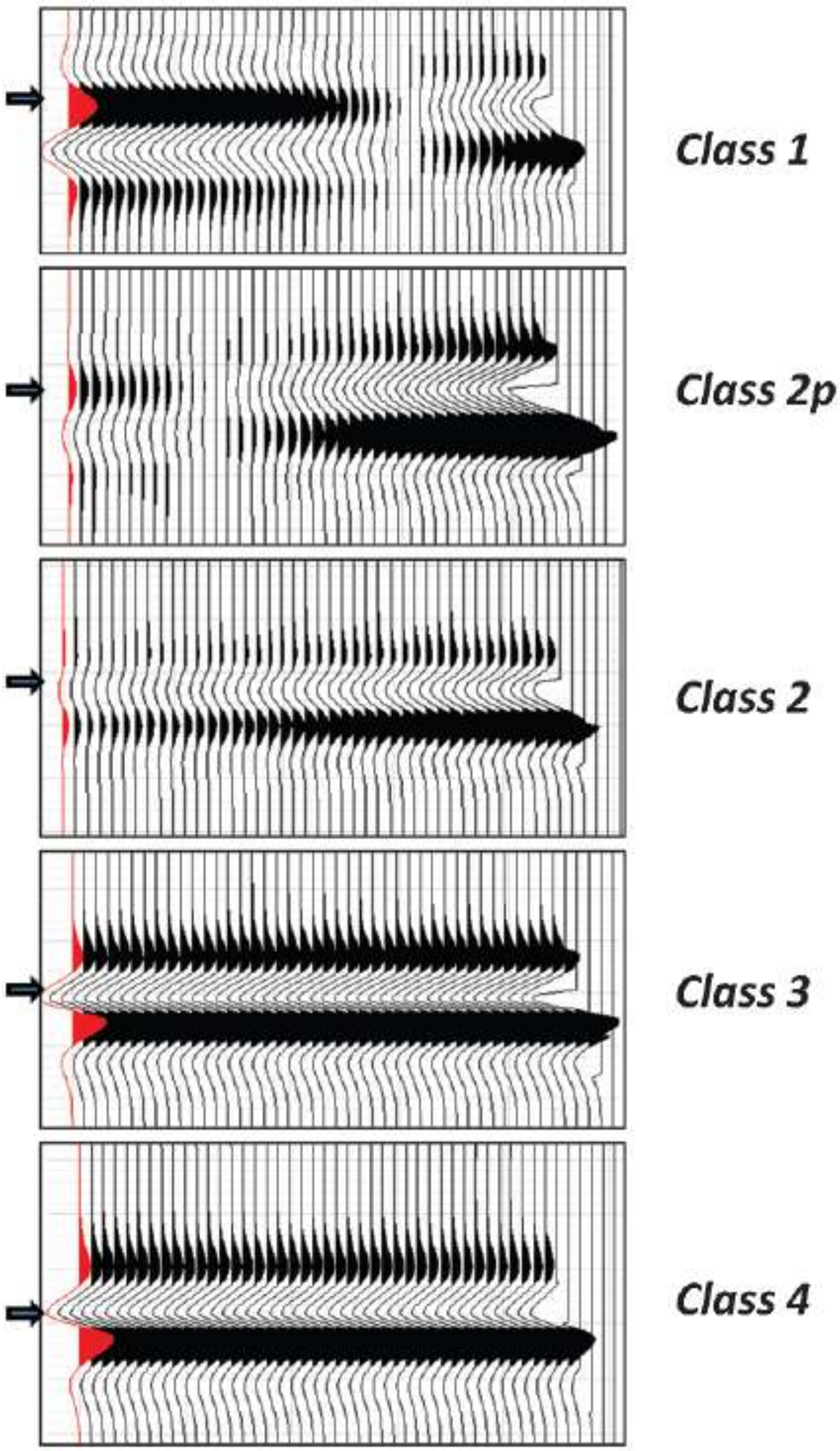

Figure 2.6: Modelled AVO curves and associated wiggle trace gather responses from AVO classes 1, 2, 2P, 3 and 4. The gather models represent a 50-foot sand with a 25-Hz Ricker wavelet applied.

CHAPTER THREE

METHODOLOGY, WORKFLOW AND DATA QUALITY CONTROL (QC) ANALYSIS

3.0 Methodology and Workflow

A detailed work using all the available data was carried out in the following steps listed in the order below:

1. Literature review: Initial review of existing literatures, reports and relevant information/data based on the research topic and on the study area.

2. Data Gathering for the research work: This consisted of extracting from well database, seismic database and archive database the most exhaustive information concerning the existing wells, well data, seismic data, studies and reports.

3. Well data and logs: An inventory was taken of the available log suites on each of the wells to check whether they have been corrected, edited and validated. Petroelastic study or a Petroelastic model is then carried out if shear sonic is available since this would allow building acoustic impedance versus Poisson's ratio (IP/PR) cross-plots at well or seismic scale which will tell if a lithological or fluid discrimination is possible.

4. Seismic data: The available seismic sub-stacks as designed by processing were analyzed in terms of consistency of amplitude, phase and time shift, by cross-correlating them by pair (Near/Mid, Mid/Far, Near/Far).Such a correlation was done after the sub-stack pairs are made to have the same spectral bandwidth. Afterwards a phase or a time shift may have to be applied to one of the sub-stacks. Upon the level of correlation a choice was made as to which ones to be used for the AVO analysis. Spatial consistency of Root Mean Square (RMS) amplitudes, resolution, stretch factor between sub-stacks produced from the

computation of the QC attribute maps was used as complementary information to assess the quality of the seismic sub-stacks. Analysis of the sea bed reflector phase was also done to access the quality of zero-phasing of each sub-stack.

5. Well to seismic tie: Comparison of a synthetic (modelled) seismic trace with the real seismic data was done to know whether if well data (reflectivities from impedance) could be linked to seismic reflectivities. Also the stability of the wavelet extracted between various wells and on the different sub-stacks was checked to determine the phase of the seismic as well as the spatial stability of the extracted wavelet and seismic amplitudes.

6. Determination of the background/reference trend: The background/reference trend represents the amplitude trend in a Near/Far domain corresponding to water sands and shales. This was computed from area on the seismic data where it was expected not to have any hydrocarbon and the values verified statistically on several areas at similar burial depth and within a similar stratigraphic interval as the potential zone of study.

7. AVO Seismofacies cube computation: The selection of a given background/reference trend gave a set of parameters (such as lambda, slope in degrees, scaling range etc) which was entered into the Sismage AVO Seismofacies building dialog box or Sismage volume calculator in order to derive an AVO Seismofacies cube from Near and Far sub-stacks.

8. AVO Seismofacies interpretation: The conformity between AVO anomalies and the structural closure, depositional system, the petroleum system and the migration was considered. The consistency between the AVO anomaly extinction and known water contacts will also be checked. Amplitudes from picked seismic events on the different sub-stacks was

cross plotted to better understand the AVO response. The coherency between the AVO attribute and the amplitude on each sub-stack will also be analyzed.

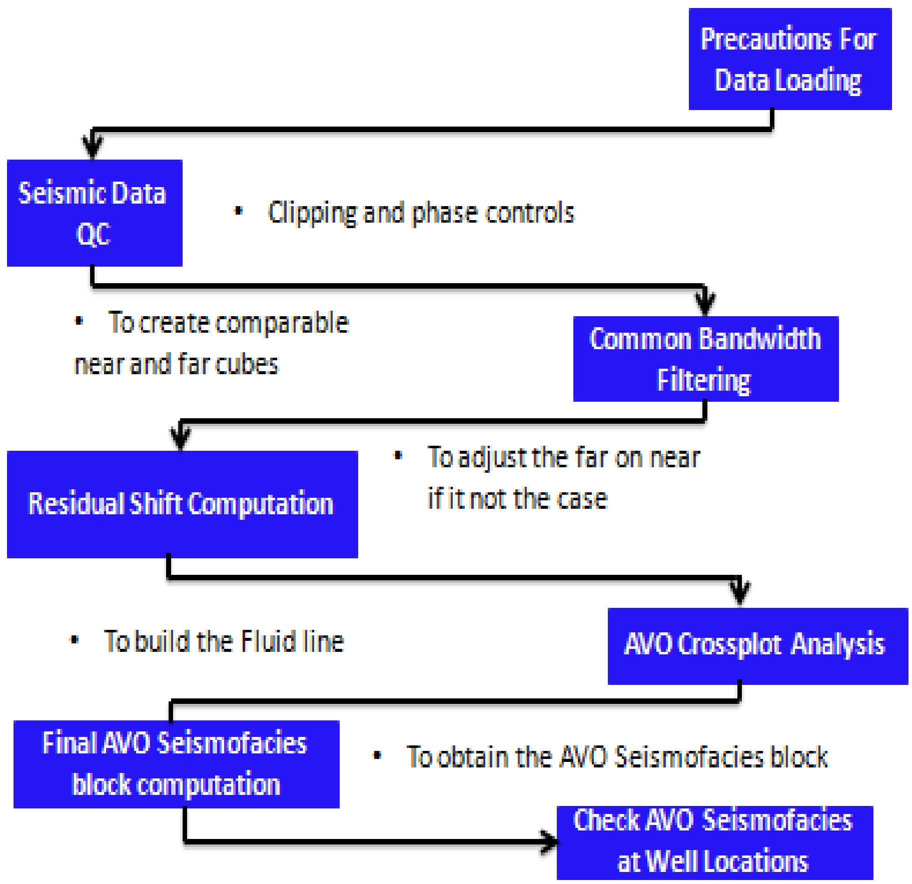

Figure 3.0: AVO Seismofacies workflow methodology.

3.1 Software Used

In this thesis, Total's proprietary software Sismage was used. The following packages were used to process and interpret the data in the order listed below:

- With the help of the seismic data QC tools, the quality of the two 3D seismic datasets were investigated by computing the frequency spectrum; the amplitude histogram; the resolution of the seismic data; search potential clipped samples on 3D seismic blocks; automatic phase analysis and statistical wavelet extraction.
- The well data display application was used to display and QC the well log data.
- The CAL 5D package, designed for well-to-seismic calibration was used to construct the synthetic seismogram, reflectivity curves and then correlate the well logs to seismic data.
- Using the horizon picking and horizon gridding/smoothing tools, the horizons were picked, gridded and then interpolated to generate the time maps.
- Depth conversion of the time maps were performed using Figaro/SuperDix package.
- Fault picking and estimation of fault boundaries was done using fault picking and automatic estimation of fault boundaries tools.
- The crossplot tools were used to analyze the relationships between the elastic rock properties and petrophysical parameters at well location and also the studied reservoir interval.
- Petroelastic Model/Rock Physics Model was performed using Numerical Interpreter.
- Finally, the AVOPAL package, designed for AVO Seismofacies studies, was the main tool to create the seismic attribute maps by comparing the sub-stack pair, filter the sub-stack pair so as to look at the same seismic bandwidth, recompute the filtered sub-stack cubes to see how it improved on the attribute maps, generate the scaling and dynamic

maps, compute the AVO Seismofacies cube, evaluate the AVO anomalies to determine the lithology and fluid content of the rocks and then interpret the AVO Seismofacies cube by integrating it with other interpretation data.

3.2 Available Dataset

The data provided for this study are as follows:

- 3D seismic cubes (pre and post - stacks) from 1986-88 and 2005 surveys with the processing report
- Borehole seismic data (Check-shots and VSPs)
- Suite of logs from OML’s 77, 99, 100 and 102 (GR, Resistivity, Caliper, Sonic, Density, Neutron, Dipmeter…etc) together with the interpreted logs (PHIE, VCL, SWE, PHIT, burial, SWE, SWT…etc).
- Suite of logs for 6 wells in Kuyolo field (GR, Resistivity, Caliper, Sonic, Density, Neutron, Dipmeter…) together with the interpreted logs (PHIE, VCL, SWE, PHIT, burial, SWE, SWT…etc).
- Formation tops, bases and contacts for all the 6 wells in Kuyolo field
- Core data and Sidewall core
- Pressure data
- Test data

Interpretation data such as time and depth maps, horizons and faults were derived as the work progressed.

3.3 Feasibility Study

Prior to the AVO analysis, a feasibility study was carried out to determine whether the available data quality is suitable for this study. The feasibility methodology used was adapted to suit the study objectives and was carried out in three steps namely well data QC, seismic data QC and seismic-to-well tie (Figure 3.1).

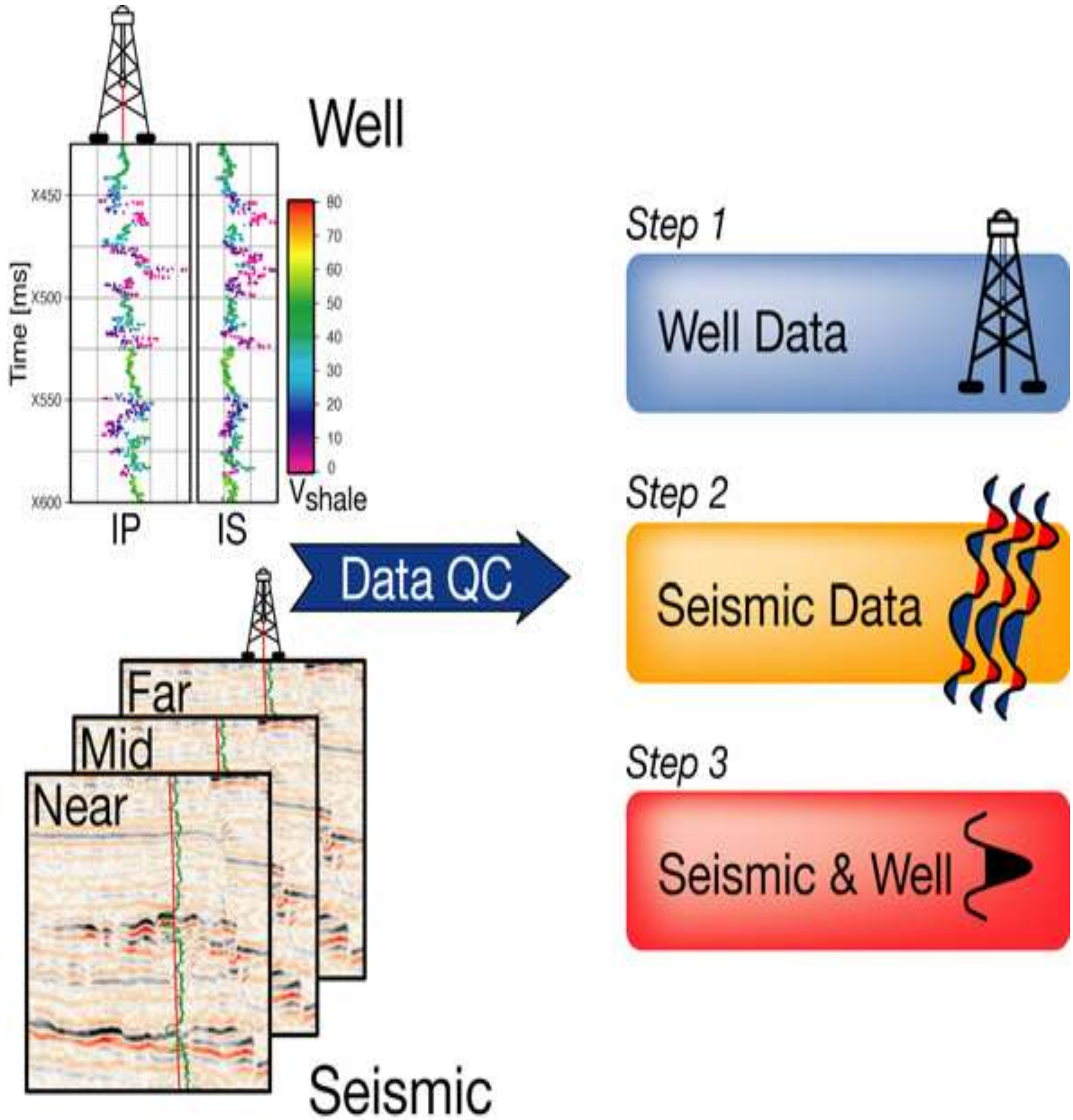

Figure 3.1: Three steps involved in the data assessment before the AVO analysis could be attempted. Both the seismic and well data were assessed before the well was intersected in the seismic data volume and a wavelet was obtained.

3.4 Well Data Quality Control (QC)

Six wells (KUY-1, KUY-2, KUY-3, KUY-4, KUY-5 and KUY-1E) were provided for this study. These wells were grouped into:

- “Old Wells” drilled in 70’s and 80’s (discovery & first appraisal), where large parts of logs like sonic or density, are missing. Furthermore checkshot (CKS) data are doubtful and some uncertainties exist on the exact locations and trajectories. Wells KUY-1, KUY-2 and KUY-3 are under this group.
- “Recent Wells” drilled in 90’s (appraisal) where log data is comprehensive and time-depth laws established by VSP. Wells KUY-4, KUY-5 and KUY-1E are under this group

Table 4 describes the available well data, highlighting potential issues for well-to-seismic calibration (QC of well trajectory, sonic, density, checkshot).

Table 4: General well status summary

Wells	Date	Well type/ Status	Log issues	Deviation status	Final HC status	RTE(m)/ Water Depth(m)	TD(m) MD-RT (driller)/ Log MSL
KUY-1	1977	Discovery	+ No density, except 50m in reservoir5 + Missing part of sonic (~100m) above reservoir11	Deviated	HC presence	23.5/22	3396/~3281
KUY-2	1980	Appraisal	+ Missing part of sonic (~275m) in levels 5,6,7 + Missing part of density (~300m) in levels 7 to 10	Deviated	HC mixed	21.3/21	3253/~3083
KUY-3	1981	Appraisal	+Log dataset questioned after very poor well-to-seismic calibration	Straight	HC presence	20.1/23.5	2522/~2502
KUY-4	1990	Appraisal	+ Gap from 2667 to 2686 (MD) due to borehole diameter change	Straight	HC/Oil(11levels)	31.0/20	3087/~3054
KUY-5	1991	Appraisal		Deviated	HC presence (2 levels)	22.5/21.5	3267/~2893
KUY-1E	1991	Exploration	+ Missing part of density (~200m) in the deep part (reservoir21)	Straight	HC presence	26.8/24	3784/~3757

Table 5: Kuyolo interpreted log – Petrolan quality check

KUYOLO Interpreted log quality check (Petrolan)									
Wells	Facies	VCL	PHIE	PHIT	SWE	SWT	K-Arith	K-Goe	Complete
KUY-1	Facies	VCL	PHIE	PHIT	SWE	SWT	K-Arith	K-Goe	
KUY-2	Facies	VCL	PHIE	PHIT	SWE	SWT	K-Arith	K-Goe	
KUY-3	Facies	VCL	PHIE	PHIT	SWE	SWT	K-Arith	K-Goe	
KUY-4	Facies	VCL	PHIE	PHIT	SWE	SWT	K-Arith	K-Goe	
KUY-5	Facies	VCL	PHIE	PHIT	SWE	SWT	K-Arith	K-Goe	
KUY- 1E	Facies	VCL	PHIE	PHIT	SWE	SWT	K-Arith	K-Goe	Missing

A Quality Control (QC) analysis of the six wells was done and the result showed that:

(1) Large uncertainties exist on old wells (70's, 80's), including issues of missing logs (e.g. sonic and density) and doubtful check-shots.

(2) No shear sonic information is available [this is an issue for Amplitude Variation with Angle (AVA) modeling and petroelastic studies].

(3) Core data is only available for reservoir R11 in kuy-1E well.

(4) Pressure data were acquired mainly in wells kuy-4, kuy-5 and kuy-1E.

(5) Sidewall cores are only available in kuy-5 well.

In summary, KUY 1E and KUY-4 wells were selected as the only representative wells for this study since they have a comprehensive log data and time-depth laws could be established using VSP.

3.5 Seismic Data Quality Control (QC)

In the seismic database provided for this study, there were two 3D seismic datasets. The 1986-88 seismic data acquired by CGG and 2005 acquired by Western-Geco (Figure 3.2). The 1986-88 survey covered an area of 170km^2 while 2005 covered an area of 250km^2.

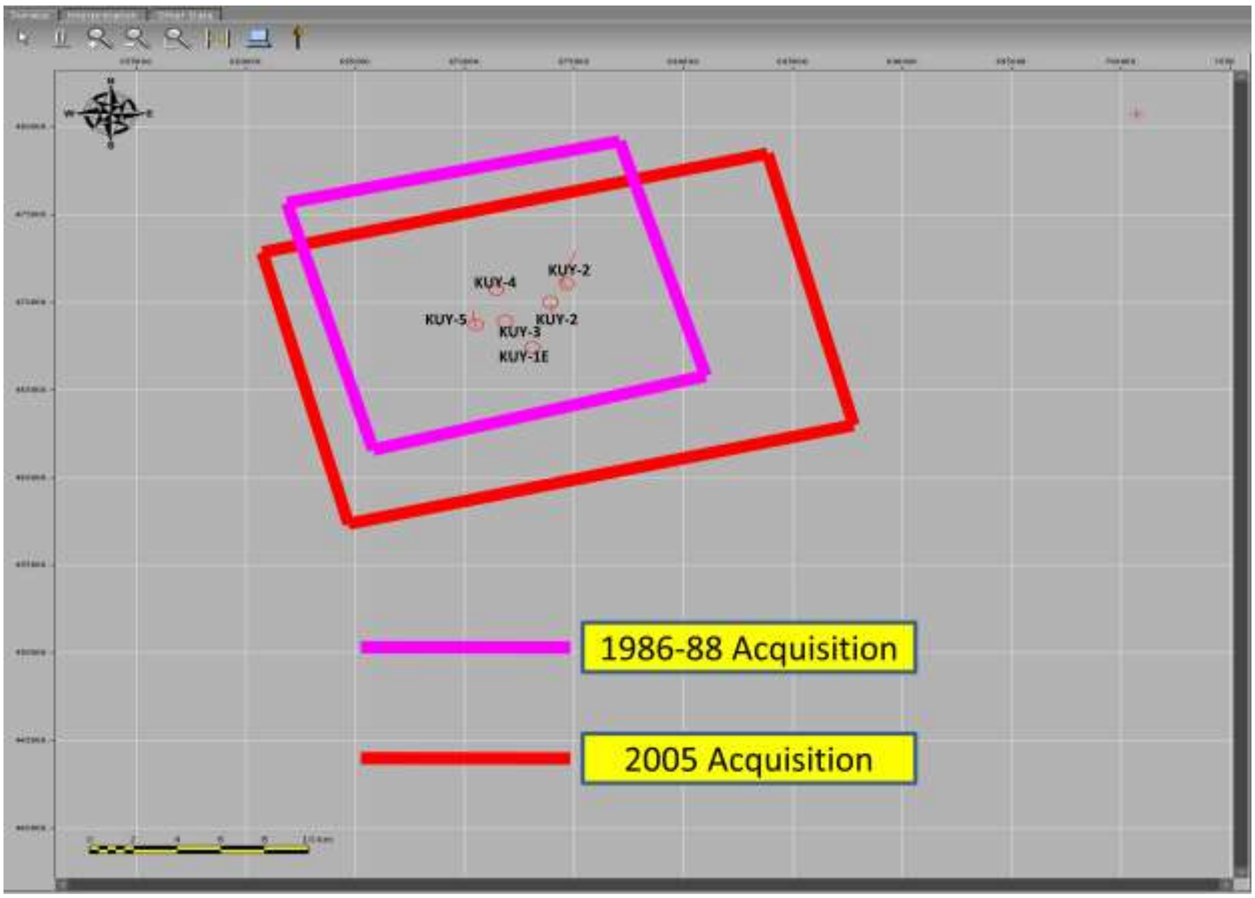

Figure 3.2: 3D seismic surveys acquired in Kuyolo field.

3.5.1 Comparison of Kuyolo 2005 and 1986-88 data sets

The 2005 dataset was compared to the 1986-88 dataset, in order to determine the dataset most appropriate for this study.

A quick comparison of images at first sight from both surveys showed that 2005 dataset has a better continuity of events, fault detection, amplitude preservation than 1986-88 dataset (Figure 3.3). The 1986-88 dataset suffered far more from large dimming areas below faults than 2005 dataset.

A spectral estimation was carried out within an interval of 500ms window which covers the reservoir of interest (R11) for the purpose of allowing the quantification in the improvement of the imaging. The result showed that 2005 has a wider bandwidth richer in lower and higher frequencies and more amplitude in the low frequency than the 1986-88 dataset (Figure 3.4).

A quick trace comparison was also done at KUY-1E well between 2005 and 1986-88 datasets (figure 3.5). It indicated that a time shift of approximately 10-15ms exists between the two dataset. Characteristics of these different surveys are explained in Table 6.

In conclusion, 2005 3D seismic dataset was then selected for this study because:

- It has better continuity of events, fault detection and amplitude preservation
- Larger fold
- Improved image below faults
- It has a wider bandwidth richer in lower and higher frequencies
- More amplitude in the low frequency

Table 6: 3D seismic data comparison between 2005 and 1986-88 surveys

3D Survey	Acquisition	Processing	Fold	Bin size	Sample time	Migration	Main processing status
KUYOLO 2005 (250km^2)	1986/CGG	1988/Elf	80	12.5 x 12.5	3ms	Pre-stack	One structural cube only
KUYOLO 1986-88 (170km^2)	2005/ Western-Geco	2005/ Western-Geco	60	12.5 x 50	4ms	Post-stack	Structural cube, angle sub-stacks and median stack from D3D

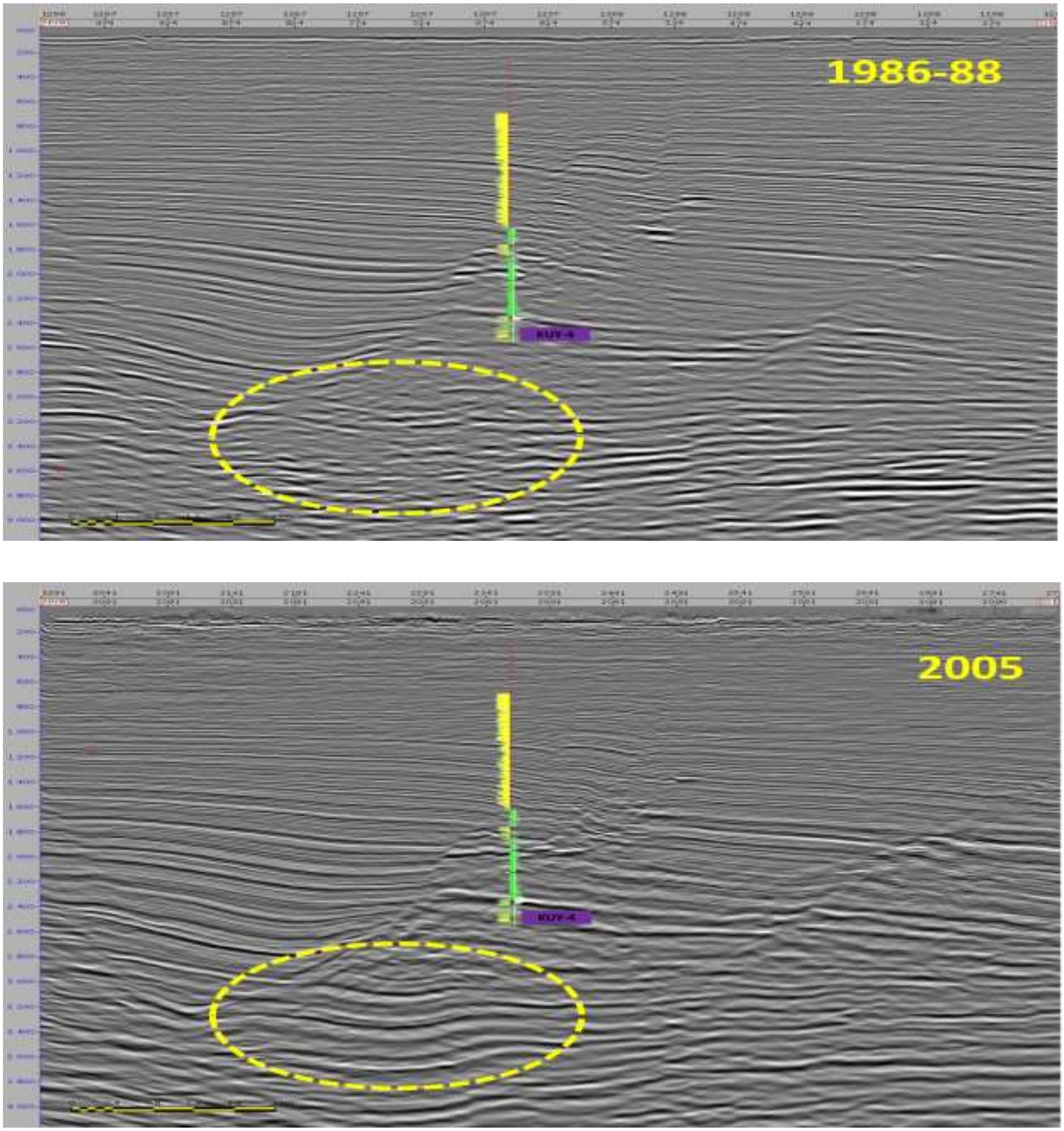

Figure 3.3: Comparison of images from both surveys. 2005 has a better quality than 1986-88.

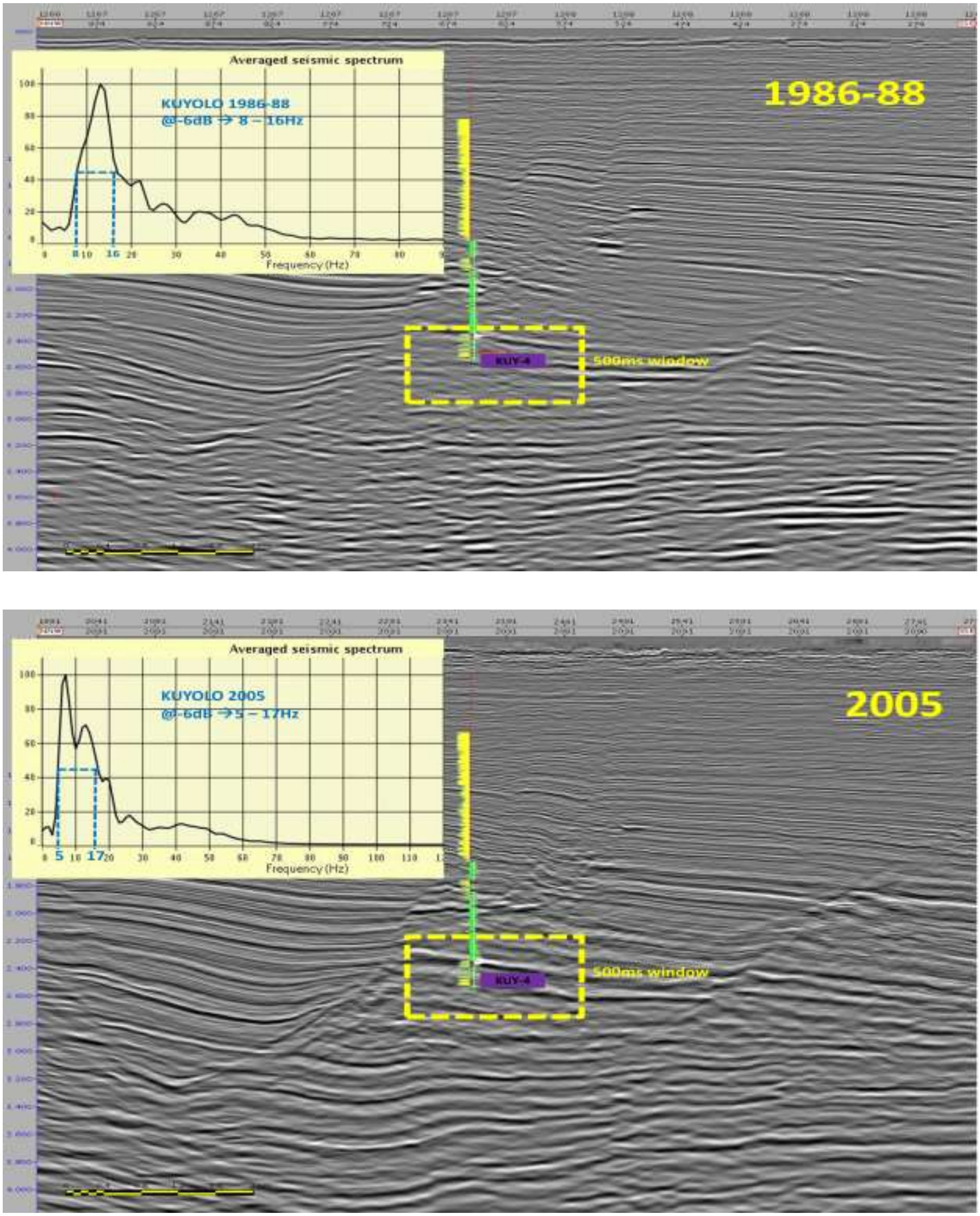

Figure 3.4: Spectral estimation done at 500ms window which covers the zone of interest (R11).

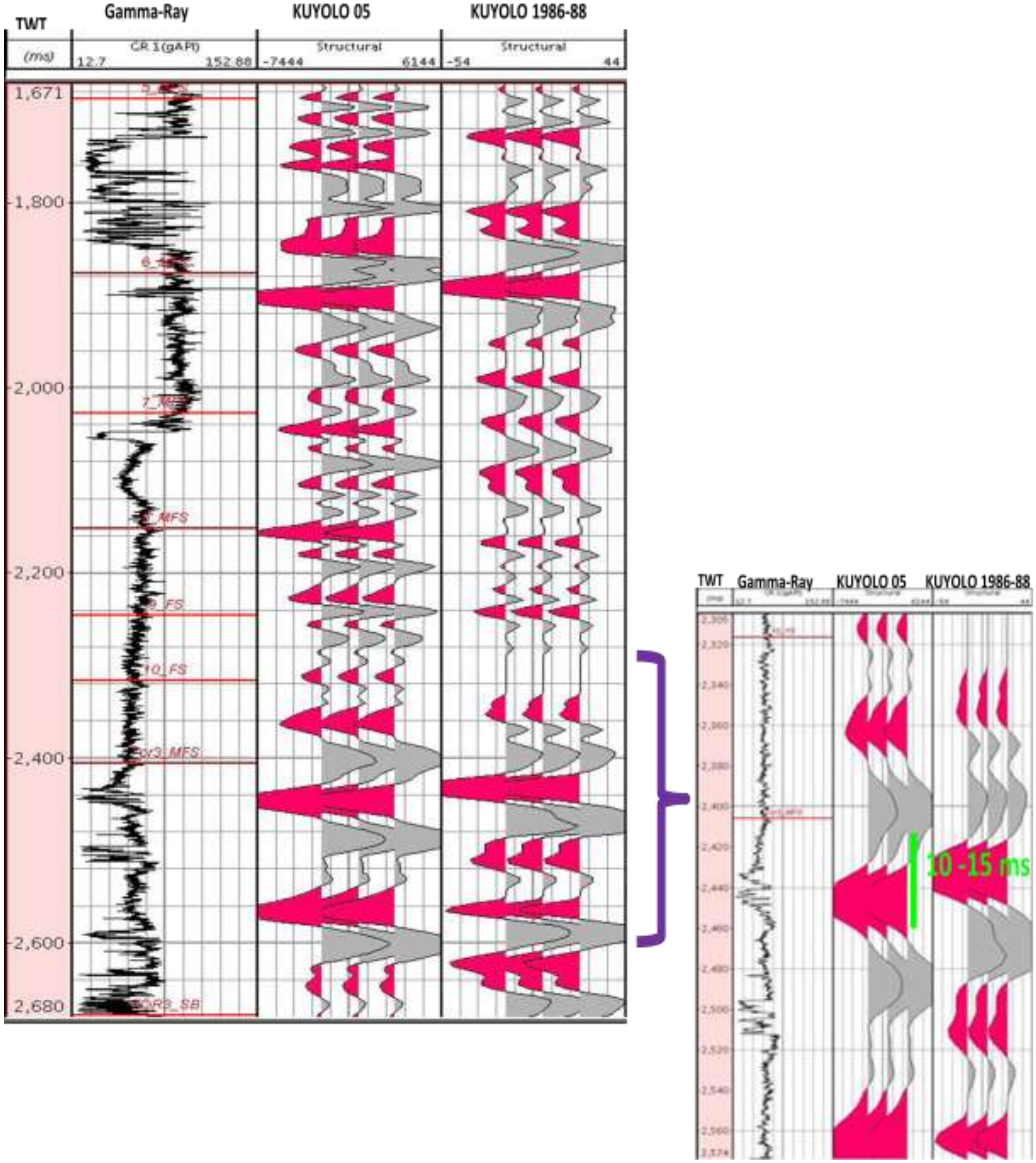

Figure 3.5: Comparison of extracted traces at KUY-1E well for both 2005 and 1986-88 datasets.

3.5.2 3D Kuyolo 2005

The data was acquired by WesternGeco, towing six 6000m long streamers and 3000CI airgun sources at a depth of approximately 7m in the East-West direction, covering an area of 250km^2.

The processing was done by WesternGeco. The processing sequence and the main facts are as follows:

- Least -square radon demultiple (before and after migration);
- PSTM (anisotropic Kirchoff migration algorithm);
- Automatic velocity analysis, SCVA (output velocity field 100mx100m);
- Full stack (Structural cube) and Angle sub-stacks generation

The main target of this survey was the Biafra series of Deltaic Sandstones. This series is between a depth of 1880 and 3000m over the survey area which equates to a two way time of between 1.7 and 2.5 seconds.

The secondary target was the Tortonian Sandstones which are between 3500 and 4500m depth. This equates to a two way time between 3.2 and 4.4 seconds.

Two different angle sub-stack designs requested and made available by Western-Geco are:

- Main target/Deltaic Sandstone objectives $\rightarrow$ Near (14-24^0), Mid (23-33^0), Far (32-42^0).
- Secondary target/Tortonian Sandstone objectives $\rightarrow$ Near (6-14^0), Mid (14-22^0), Far (22-30^0)

The angle sub-stack for the Main target/Deltaic Sandstone objectives was selected for this study since our R11 reservoir lies within 1880-3000m (1.7 -2.5s).

Acquisition Parameters

Table 7: Summary of the acquisition parameters

Seismic Source

Type of source	Sleeve Airgun
Number of sources	2(flip-flop mode)
Source center separation	50m
Shot interval per sources(same source)	37.5m(18.75m flip-flop)
Source Depth	6m +/-0.5m

Streamers

Number of streamers	6
Group interval	12.5m
Active length per cable	6000m
Streamer Depth	7m +/-1m
Crossline separation	100m (500m cross line-spread)
Number of groups per cable	480
Source to receiver offset	150m nominal

3.5.2.1 3D Kuyolo 2005 Data Quality Control (QC)

A QC analysis was done on both the structural and angle sub-stack cubes. The structural cube was divided into top, middle and reservoir sections respectively with spectral analysis done on each of them (Figure 3.6). On the top section, there was loss of low frequencies with some high frequency noise present. The middle section has multiples while the reservoir section contains high frequency rebound (Figure 3.7).

A spectral analysis was also done on the angle sub-stack datasets only at the reservoir section (R11) within an interval of 2250-2500ms. Within these reservoir sections there is good homogeneity of the frequency content between Near and Mid sub-stacks. Far stack shows a decrease in frequency. Near and Mid sub-stacks show larger frequency contents and visual resolution than the structural cube but they also contain more noise.

The seismic data quality was suitable for this study and the Near sub-stack was then selected to be used for the structural interpretation.

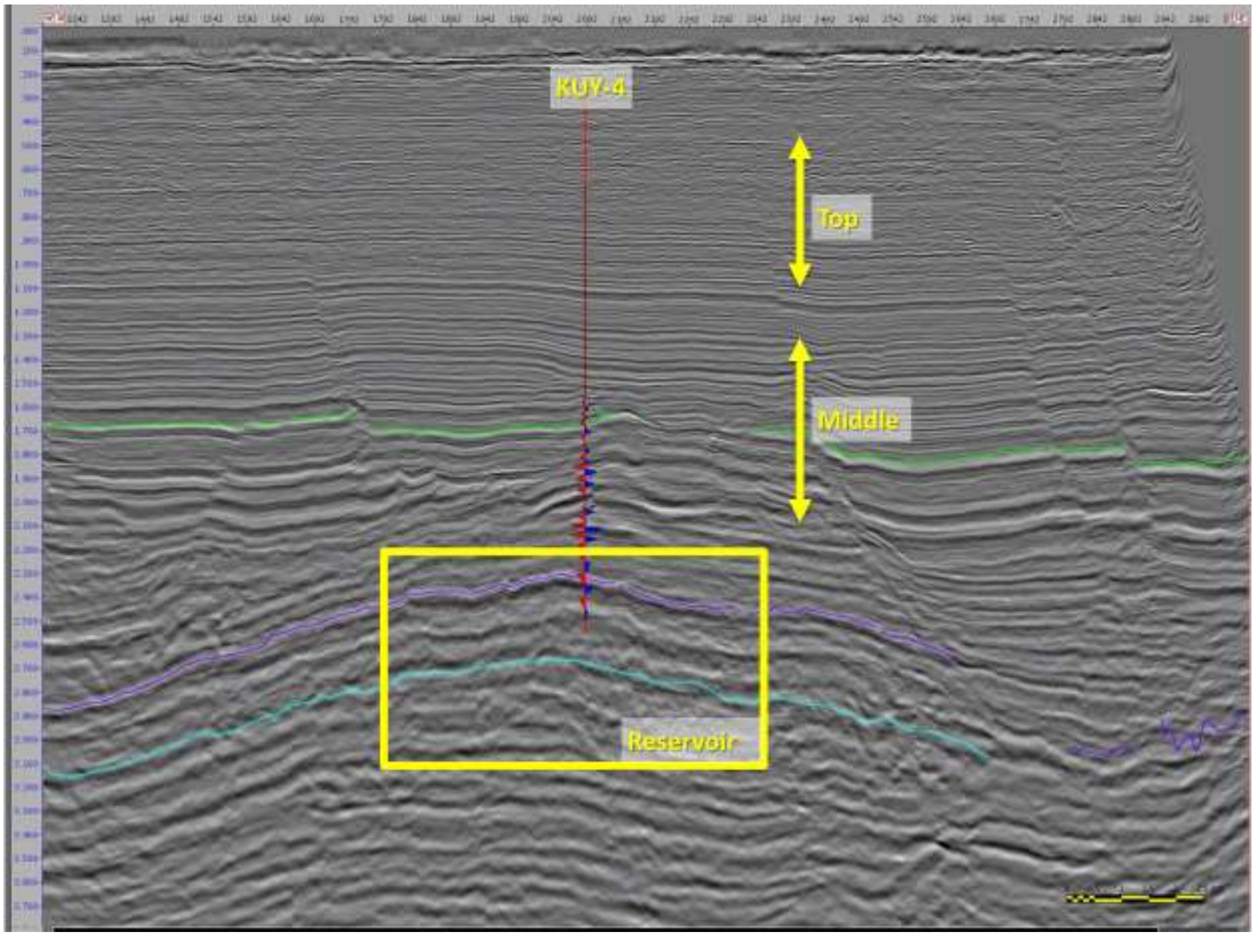

Figure 3.6: Structural cube divided into top, middle and reservoir sections

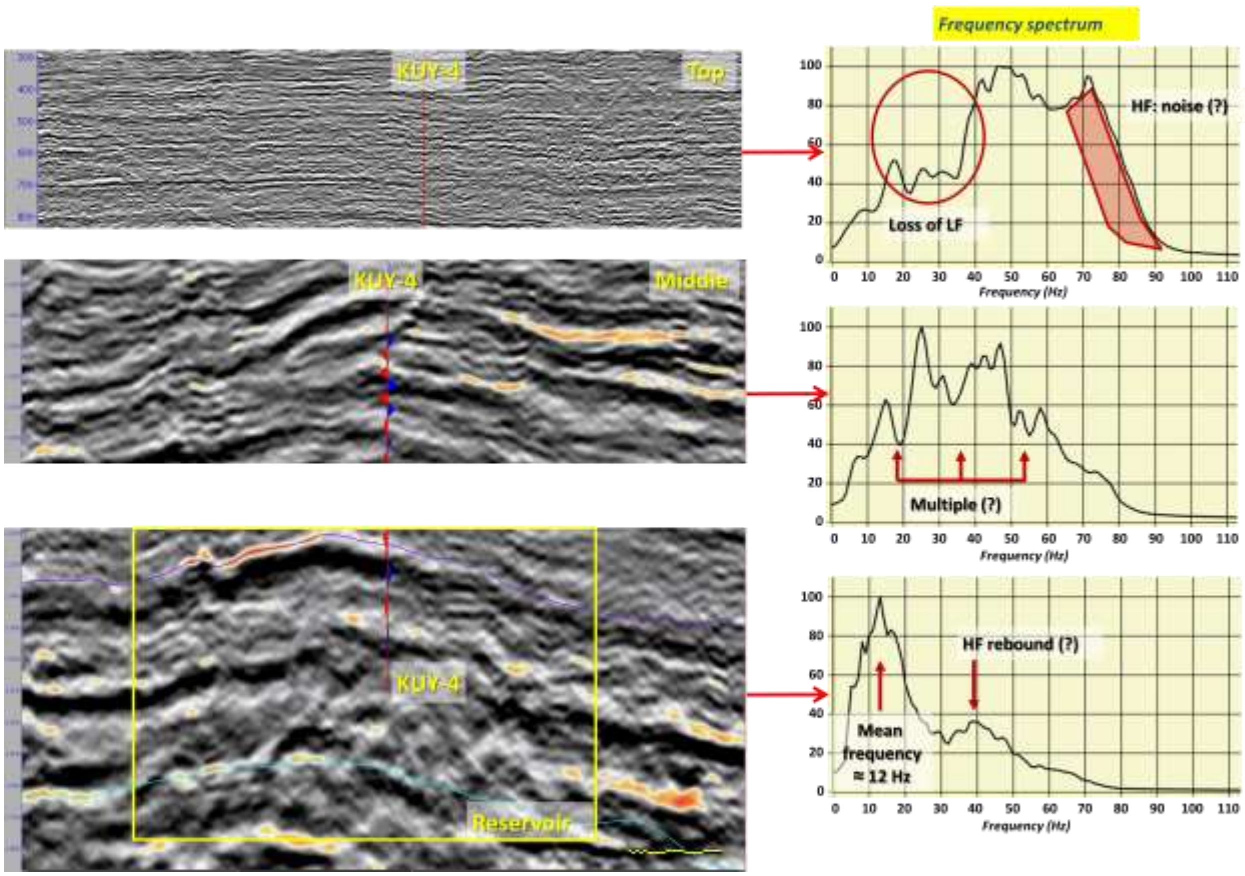

Figure 3.7: Spectral analyses of the top, middle and reservoir sections of the structural cube.

3.5.2.2 Kuyolo 2005 Tuning Thickness Analysis, Vertical Resolution and Depth Estimation.

Tuning thickness analysis was also carried out on R11 reservoir. The tuning thickness is fundamentally determined by the thickness and compressional velocity of the unit and the wavelength of the seismic pulse. A first order approximation appropriate for making quick calculations.

$$\textit{Tuning thickness} = \frac{Wavelength(\lambda)}{4} \ldots\ldots\ldots\ldots\ldots\ldots\ldots\ldots (74)$$

$$\lambda = V_p(m/s)\,/F_d(Hz) \ldots\ldots\ldots\ldots\ldots\ldots\ldots\ldots\ldots\ldots (75)$$

$$F_d(Hz) = {}^{1}/_{T} \ldots\ldots\ldots\ldots\ldots\ldots\ldots\ldots\ldots\ldots (76)$$

where:

λ = wavelength (m)

F_d = predominant frequency (Hz)

T = seismic period = peak-to-peak or trough-to-trough twt separation

The tuning thickness analysis done on R11 reservoir showed that the seismic resolution is 51m, seismic detectability is 26m and that R11 is not tuned (Figure 3.8 below).

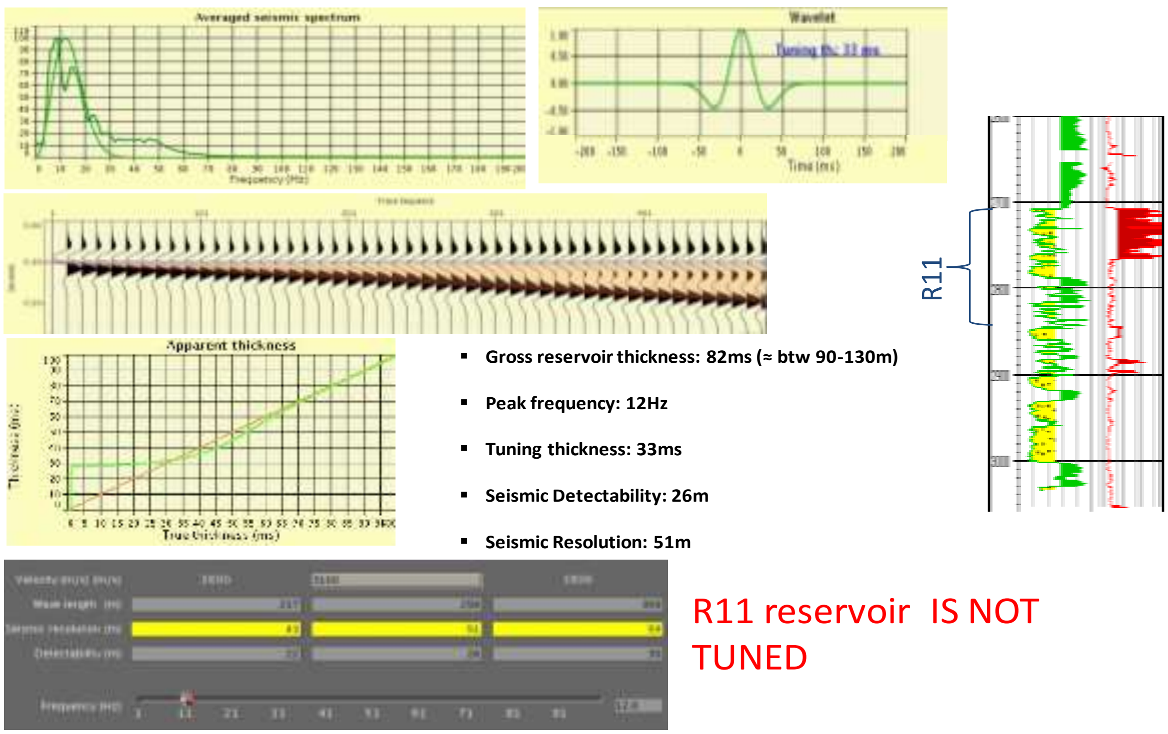

Figure 3.8: Tuning analysis result done on R11 reservoir.

3.6 Well-to-Seismic Calibration

The starting point of this geophysical interpretation is the correlation of the well logs to the seismic data. By convolving the reflectivity and wavelet at the well location, the synthetic traces are generated. Then each pick from the synthetic trace was correlated to each pick from real seismic data.

The well-to-seismic calibration was done using the CAL5D package of Sismage software. This step was challenging because:

- Old wells (Kuy-1, Kuy-2 and Kuy-3) have questionable check-shots and large sections of missing logs.
- Kuy-2 (deviated) and Kuy-4 go across faults into small panels where seismic imaging is clearly degraded by faults.
- Kuy-5 (highly deviated) shows a trajectory just below the main Kuyolo faults, in an area affected by pull-down and shadowing.

Eventually, kuy-4 was selected as the only representative well for this process because it has correct and relevant data.

After several tests, the Near sub-stack cube was selected to be used and the final calibration window was set at 1700-2420ms (large window which covers all the Kuyolo objectives, from R5-R11).

Figure 3.9 shows classic output maps from CAL5D software. Figure 3.10 gives the calibration plate of KUY-4 (calibration location toward N, time shift = 20ms, phase = -40^0) with interpreted horizon identification on it.

This calibration can be qualified as reliable (correlation coefficient around 60% but over a large window: 720ms) and allows a clear picking of seismic events. The wavelet has an acceptable shape.

Calibration of the other remaining Kuyolo wells follows the same CAL5D process.

KUY-1E and KUY-4 (recent straight wells with VSP data) show similar characteristics (Phase ~ -30 degrees, Time shift/lag ~ 15-20ms). -1 has been difficult to calibrate in a position consistent with other wells. KUY-1 check-shots were questioned and calibration was tried using a new time-depth function created with KUY-1E check-shots. However, an important drift (50ms) was seen with the sonic correction, but no better calibration was found using KUY-1E check-shots or raw sonic integration only. No proper calibration (in terms of synthetic versus seismic correlation) was found for KUY-3. Although a log problem was suspected, no clear reason was found after data checking. Table 8 synthesizes these results.

The different wavelets used for calibration are plotted in the Figure 3.14. They look quite similar however variations can be explained by the various seismic qualities in the different panels, close to the faults. The overall final proposed calibration is the better one, but nevertheless the majority of calibrations are fair to poor.

In spite of these difficulties, the geological events (main MFS) were recognized with confidence after a reliable calibration of Kuy-4 and after ensuring the global consistency between wells.

In conclusion, the well and seismic data tie properly and the extracted wavelet was stable within the studied area and also from one substack to the other.

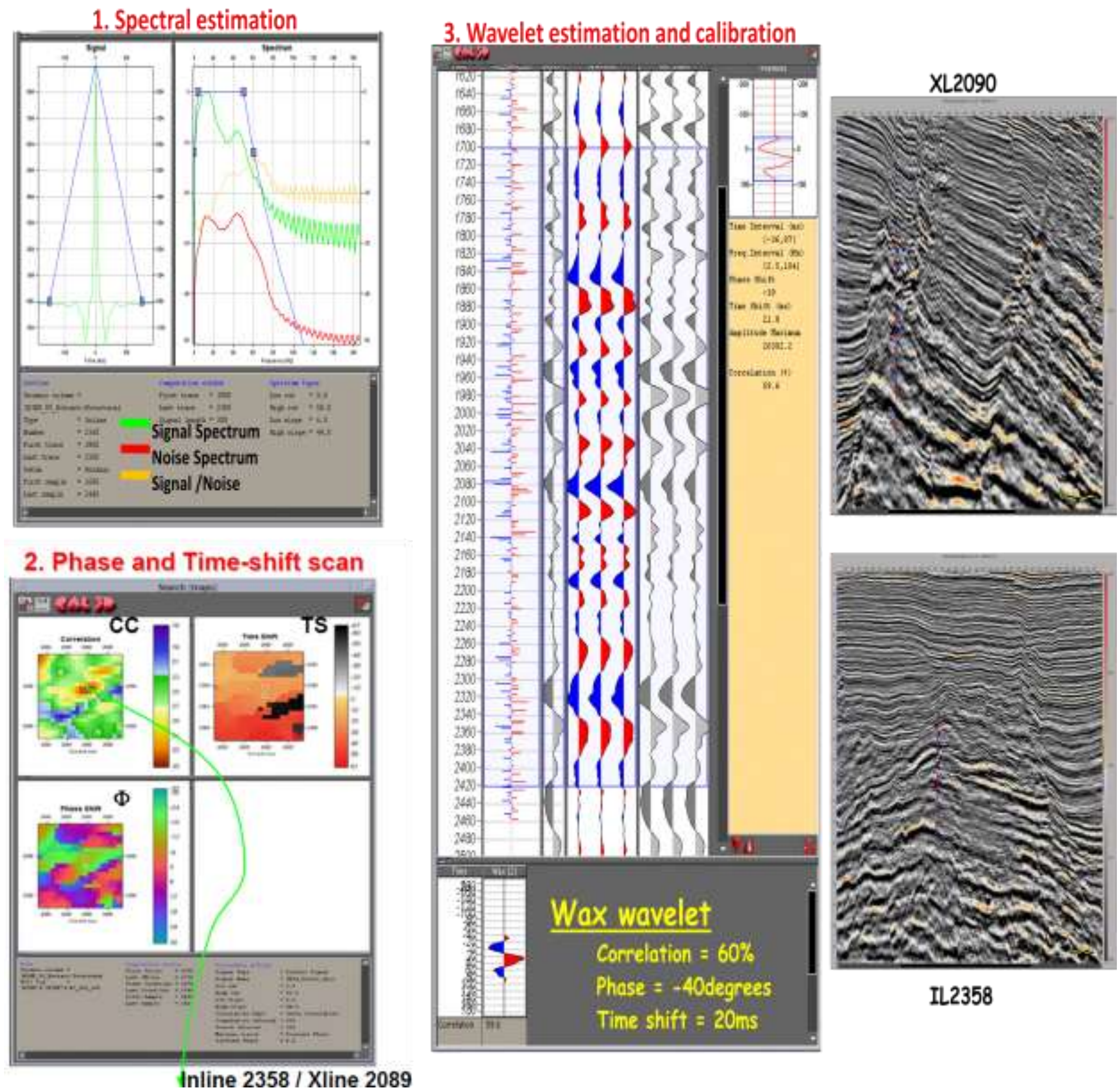

Figure 3.9: Well-to-seismic calibrations on Near angle sub stack cube.

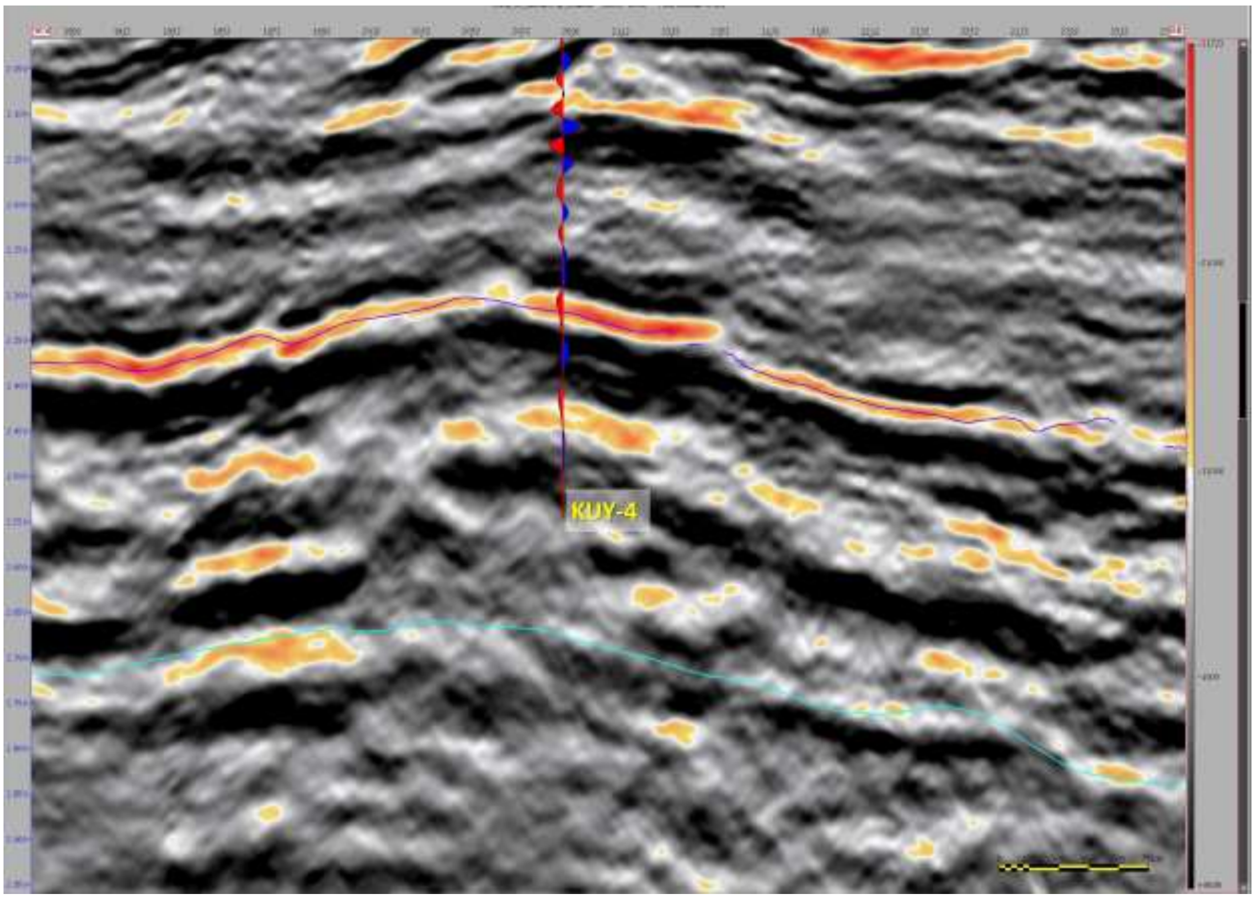

Figure 3.10: Zoomed seismic section with the synthetic on KUY-4 through R11 reservoir.

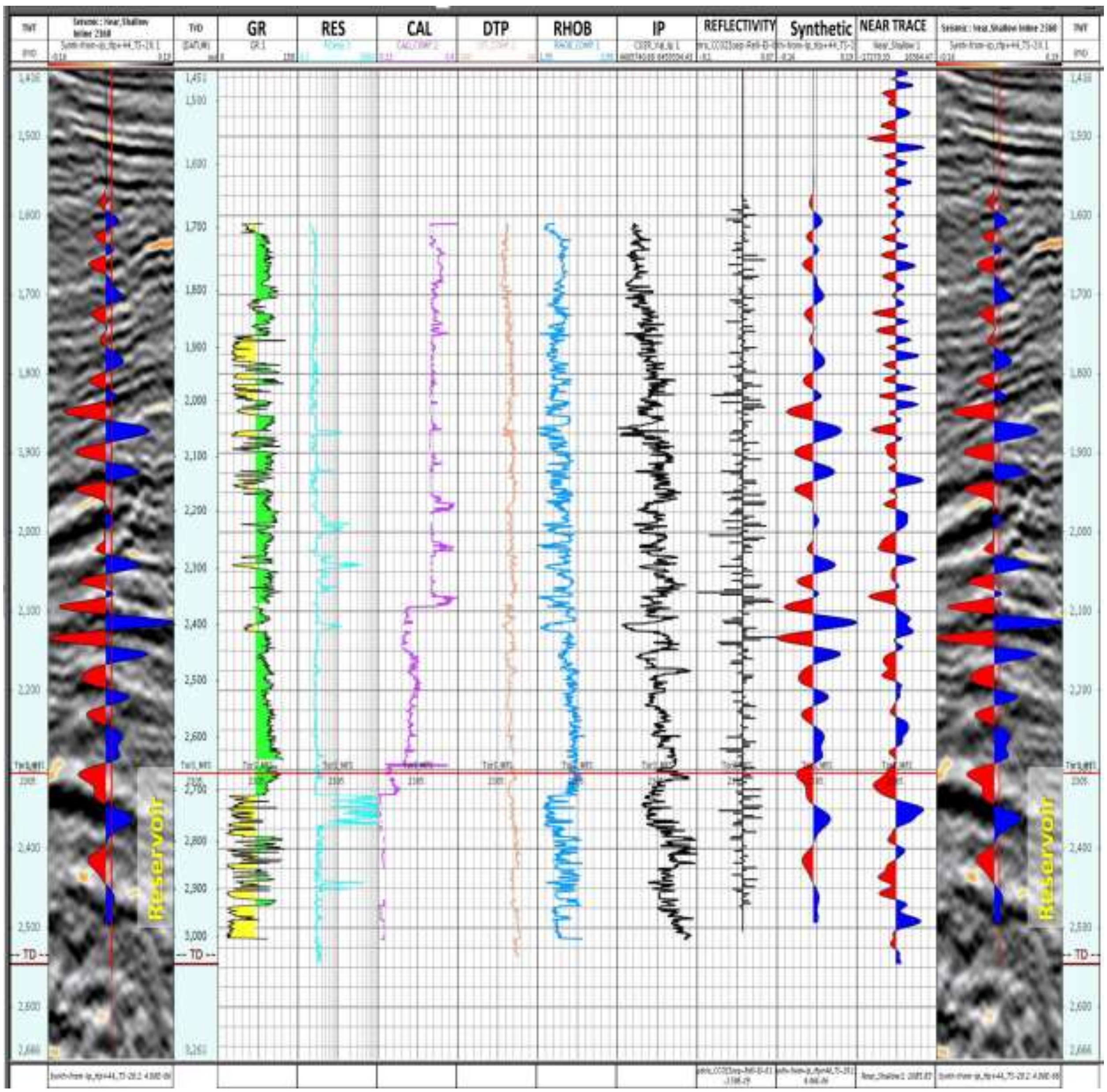

Figure 3.11: Calibration slide on Near angle sub-stack cube. R11 Top → red negative trough (decrease of IP), oil-water contact (OWC) → black positive peak and R11 Base → black positive peak (increase of IP).

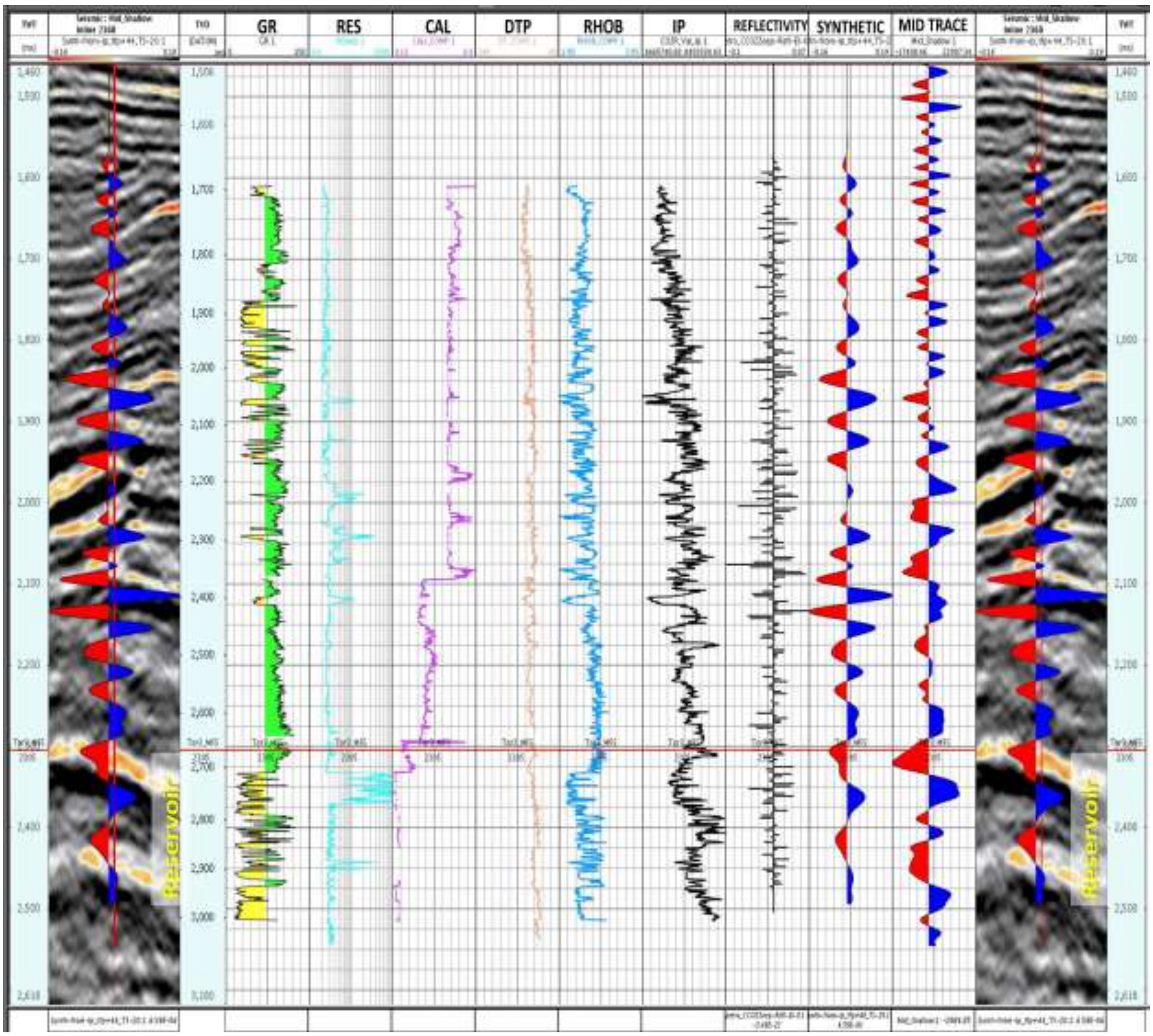

Figure 3.12: Calibration slide on Mid angle sub-stack cube. R11 Top → red negative trough (decrease of IP), oil-water contact (OWC) → black positive peak and R11 Base → black positive peak (increase of IP).

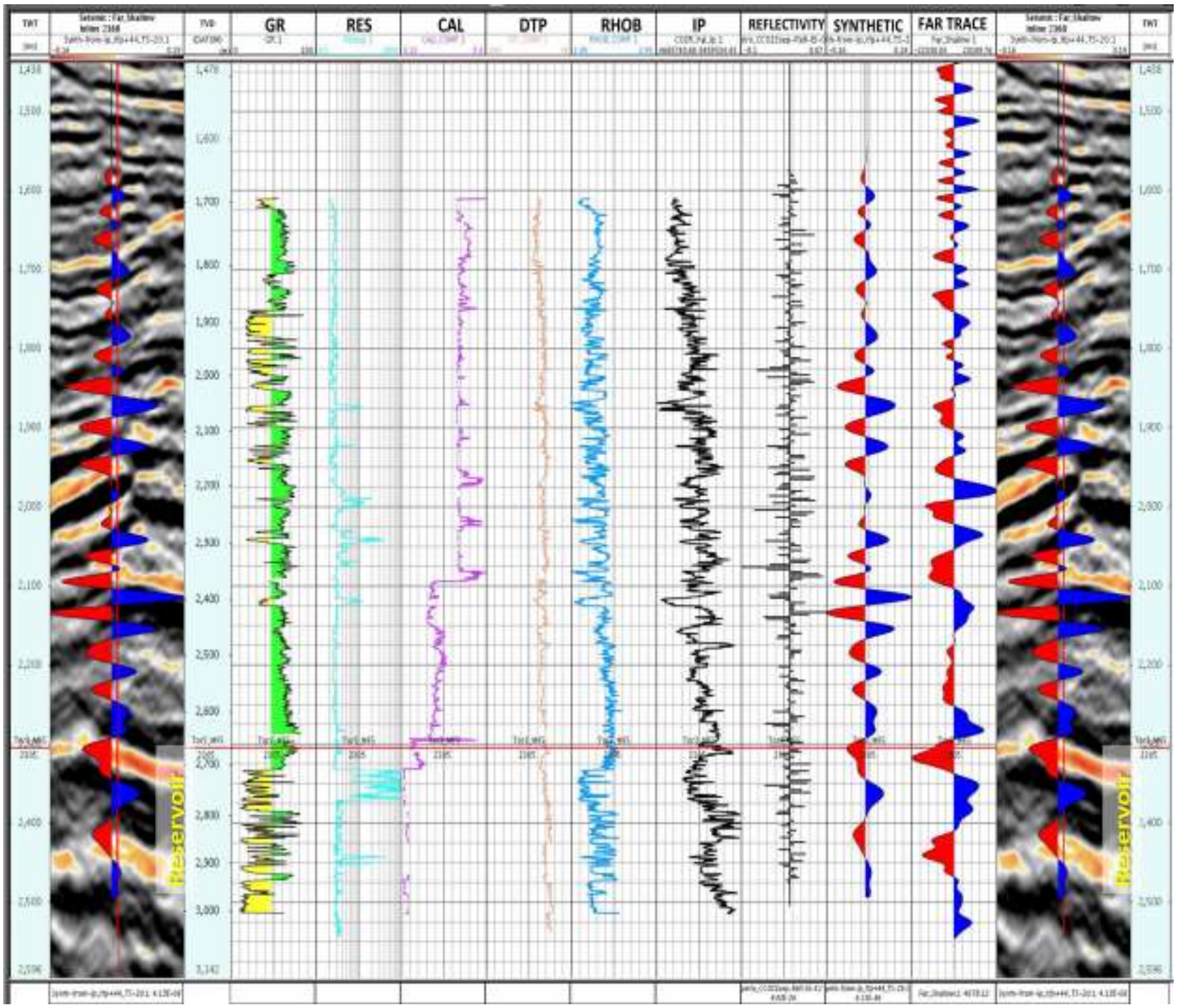

Figure 3.13: Calibration slide on Far angle sub-stack cube. R11 Top → red negative trough (decrease of IP), oil-water contact (OWC) → black positive peak and R11 Base → black positive peak (increase of IP).

Table 8: Summary table of well-to-seismic calibration on Near angle cube

Wells	**Inline/Xline location**	**Calibration window**	**Correlation coefficient**	**Estimated phase**	**Time shift (ms)**	**Inline/Xline calibration location**	**Remarks**
KUY-1E	2648/2150	1800-2700	57%	-20	16	2642/2148 84m toward NW	Time shift attested
KUY-4	2358/2090	1700-2420	60%	-25	22	2358/2090 20m toward North	Trajectory through Kuyolo faults
KUY-5	2464/2265	1750-2200	55%	20	25	2492/1970 89m toward West	Trajectory below Kuyolo fault
KUY-1	2464/2265	1750-2200	62%	35	22	2468/2262 64m toward South	Calibration with KUY-1E check-shots
KUY-2	2397/2345	2000-2430	71%	8	3	2402/2341 77m toward South	Only 300ms of reliable synthetic for levels 8 to 10

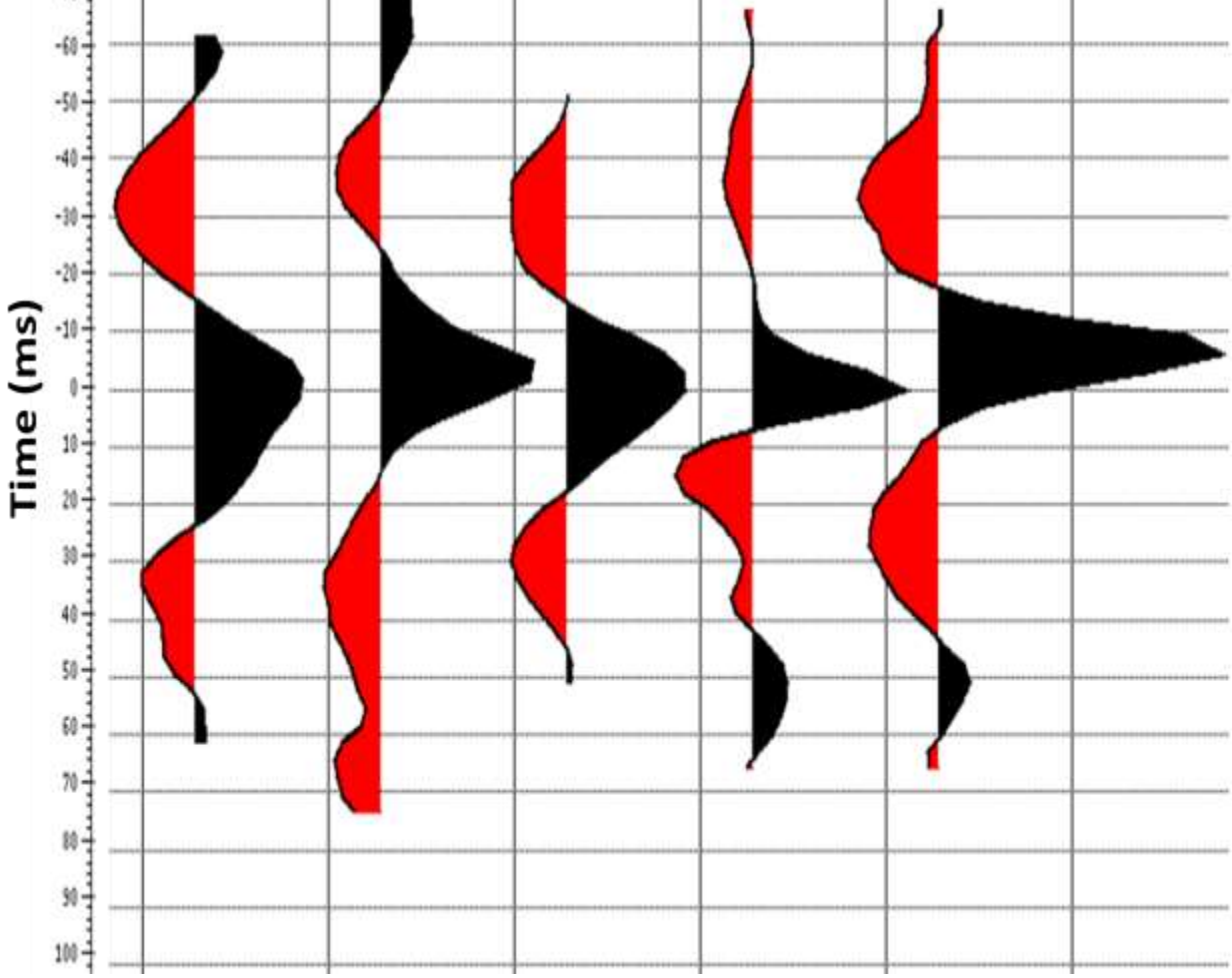

Figure 3.14: Estimated wavelet at each well.

CHAPTER FOUR

HORIZONS AND FAULT INTERPRETATIONS

4.0 Horizons Interpretation

Horizons were picked on Sismage workstation using the horizon picking tools. The shallowest interpreted horizon is the Base of Kwa Iboe formation (BKI) located around 700ms (at Kuy-4). It aims to define an intermediate level between seabed and the first important Kuyolo reservoir surface (5_MFS ~1600ms at Kuy-4). Base of Kwa Iboe formation (BKI) is easily recognizable as a conformable surface in the Kuyolo area. The final Base of Kwa Iboe (BKI) interpreted surface is fully consistent with the regional interpretation done on the entire East offshore area of the Niger Delta.

Since lithological contrasts are weak on the seismic, it was decided to pick Flooding Surfaces /Maximum Flooding Surfaces.

In total, seven surfaces were interpreted over Kuyolo field. They correspond to the MFS defined by the geologist. They were picked according to their acoustic impedance response (Table 9, Table 10 and Table 11). Correlated MFS correspond to a consistent Acoustic Impedance contrast type from one well to another.

The interpretation workflow used to achieve this process is as follows:

1. Horizons were interpreted on Inline/Crossline (approximately 5x5 each)
2. Propagation was done through Sismage algorithm
3. Interpolation was also done using “Directional gridding” algorithm
4. Interpolated horizon was smoothed (5x5) using “Classical Smoothing” algorithm to give the final time interpretation map

For the purpose of this study only the two-way-time maps of Tor3_MFS and Tor3_SB were interpreted since our reservoir of interest (R11) lies in-between these two horizons.

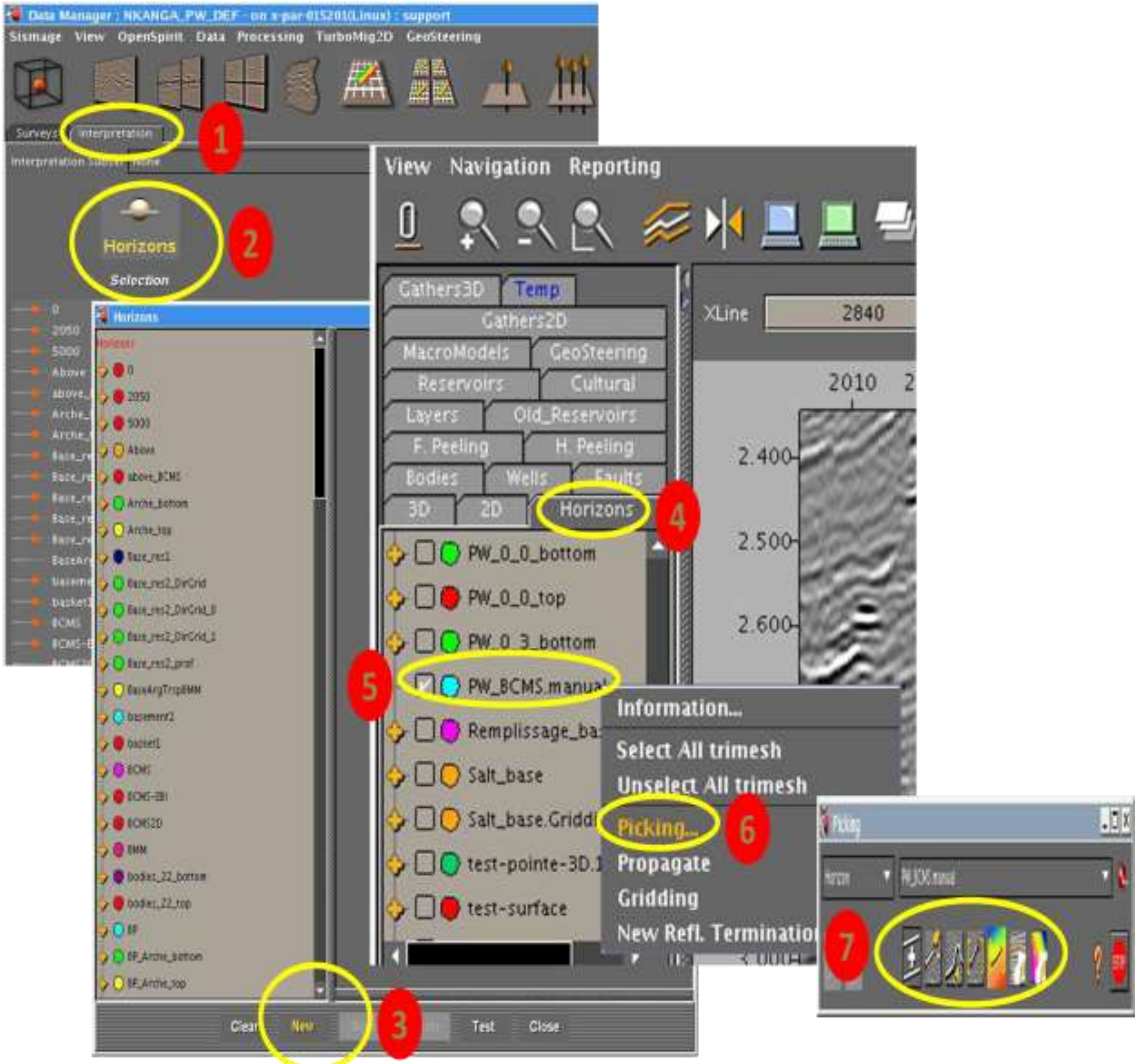

Figure 4.0: Sismage interface for horizon picking. The steps to pick horizons in Sismage are numbered from 1to 7.

Table 9: Horizon picking criteria (AI = Acoustic Impedance). Characterization of Kuyolo sands in terms of acoustic response was less easy and reflectivity at top or bottom sand can be weak. Kuyolo sands can be classified as class I to class II (IIa, IIb).

Horizons	Geological event	Picked on	Quality of the seismic event	Remarks
5 MFS	**AI Increase**	**>0 (peak)**	Subtle event picked on near angle dataset	Good interpretation
6 MFS		**<0 (trough)**	Clear event	6_MFS seismic event is more significant in seismic than expected from synthetic data and VSP data
7 MFS	**AI Decrease**	**<0 (trough)**		
8 MFS	**AI Decrease**	**<0 (trough)**	Subtle and sometimes less clear event	Less confident than other horizons
9 MFS	**AI Increase**	**>0 (peak)**	Clear event	Good interpretation
Tor3_ MFS (= R11)	**AI Decrease**	**<0 (trough)**	Clear event	Good interpretation
Tor3 SB	**Strong AI Decrease**	**<0 (trough)**	Clear event	Erosive surface Noisy result

Table 9: Horizon picking criteria (AI = Acoustic Impedance). Characterization of Kuyolo sands in terms of acoustic response was less easy and reflectivity at top or bottom sand can be weak. Kuyolo sands can be classified as class I to class II (IIa, IIb).

Horizons	**Geological event**	**Picked on**	**Quality of the seismic event**	**Remarks**
5 MFS	**AI Increase**	**>0 (peak)**	Subtle event picked on near angle dataset	Good interpretation
6 MFS		**<0 (trough)**	Clear event	6_MFS seismic event is more significant in seismic than expected from synthetic data and VSP data
7 MFS	**AI Decrease**	**<0 (trough)**		
8 MFS	**AI Decrease**	**<0 (trough)**	Subtle and sometimes less clear event	Less confident than other horizons
9 MFS	**AI Increase**	**>0 (peak)**	Clear event	Good interpretation
Tor3_ MFS (= R11)	**AI Decrease**	**<0 (trough)**	Clear event	Good interpretation
Tor3 SB	**Strong AI Decrease**	**<0 (trough)**	Clear event	Erosive surface Noisy result

Table 10: Acoustic impedance contrast at main flooding surfaces (Inc= Increase; Dec=Decrease; F/O = "Faulted out", X = not reached; AI= Acoustic Impedance; Vel = Velocity)

Horizons	**Kuy-1 (no density, except res5.1)**	**Kuy-2 (no sonic)**	**Kuy-3**	**Kuy-4**	**Kuy-5**	**Kuy-1E**
5 MFS	**Inc AI**	Inc Dens	**Inc AI**	**Inc AI**	**Inc AI**	**Inc AI**
6 MFS	Dec Vel Weak	F/O	**Dec AI Strong**	**Dec AI Weak**	**Not a clear AI contrast**	**Dec AI**
7 MFS	Not a clear Vel contrast	Dec Dens	**Dec AI Weak**	**F/O**	**Not a clear AI contrast**	**Dec AI**
8 MFS	Not a clear Vel contrast	F/O	**Not clear**	**Dec AI Weak**		**Dec AI**
9 MFS	Inc Vel Strong	Inc Dens	**X**	**Inc AI Strong**	**Not a clear AI contrast**	**Inc AI**
Tor3 MFS	Not a clear Vel contrast	Dec Dens	**X**	**Dec AI Weak**	**Dec AI Strong**	**Dec AI**
Tor3 SB	X	X	**X**	**X**	**X**	**Dec AI Strong**

Table 11: Reservoir 11 sands characteristics. It shows well by well that reservoir R11 sands are faster and with less density than surrounding shales. The resulting

Wells	Remarks	Sand characteristics	Top sand contrast
Kuy-1	No density	Fast	Increase in velocity
Kuy-2	No sonic	Less dense	Decrease in density
Kuy-4	Oil bearing	Fast/less dense	Low decrease in Acoustic Impedance (Oil)
Kuy-5		Fast / Very low density variation More impedant	Increase in Acoustic Impedance
Kuy-1E	Oil bearing	Fast/less dense	Low increase in Acoustic Impedance (Oil)

contrast in terms of acoustic impedance can be very low (>0 or <0) if oil-bearing but is expected positive if water-bearing.

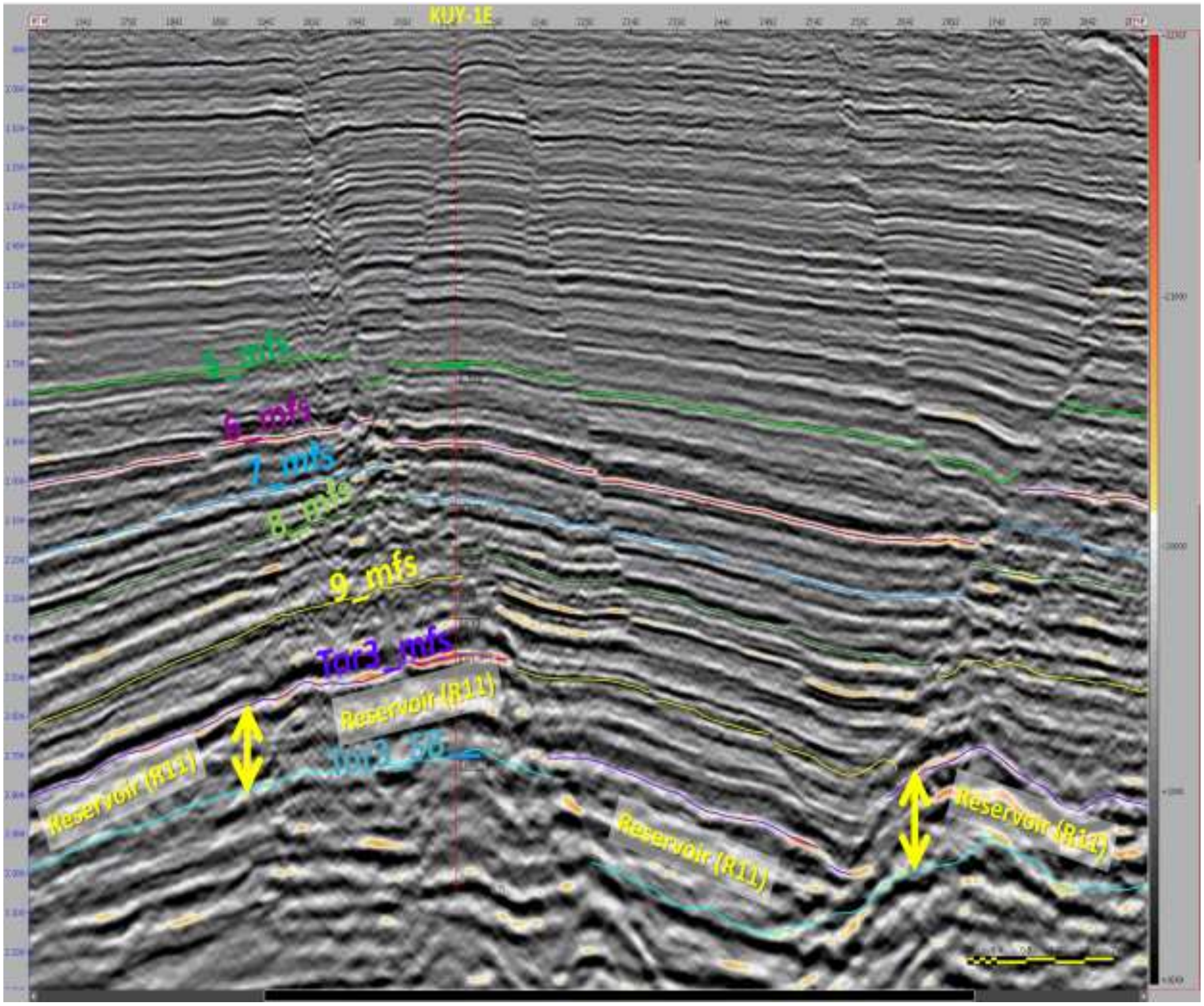

Figure 4.1: Interpreted horizons and well markers in time through KUY-1E along the Kuyolo field.

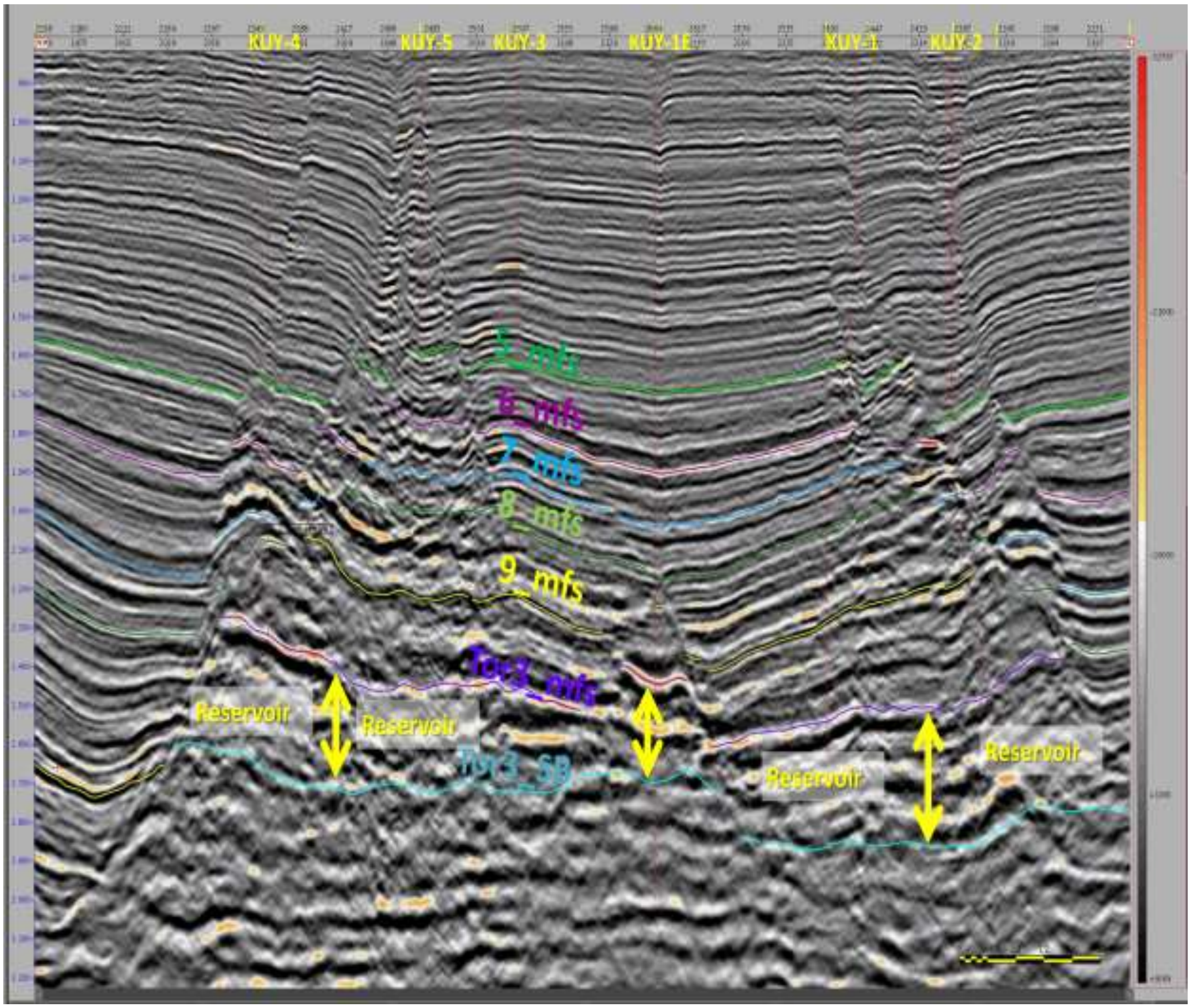

Figure 4.2: Interpreted horizons and markers in time along random line through all the wells.

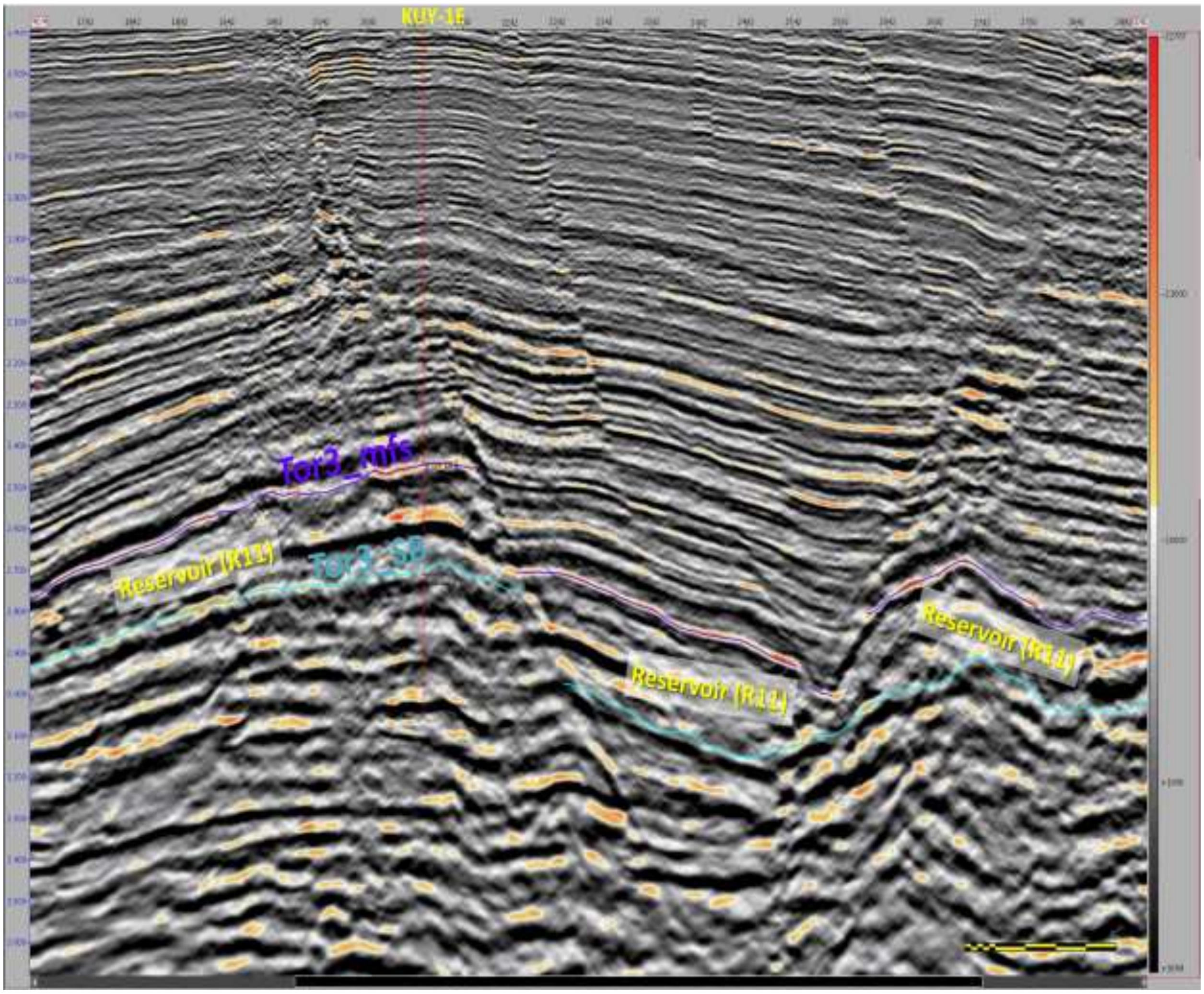

Figure 4.3: Interpreted horizons and well markers in time for the reservoir of interest (R11) which lays in-between Tor3_MFS and Tor3_SB.

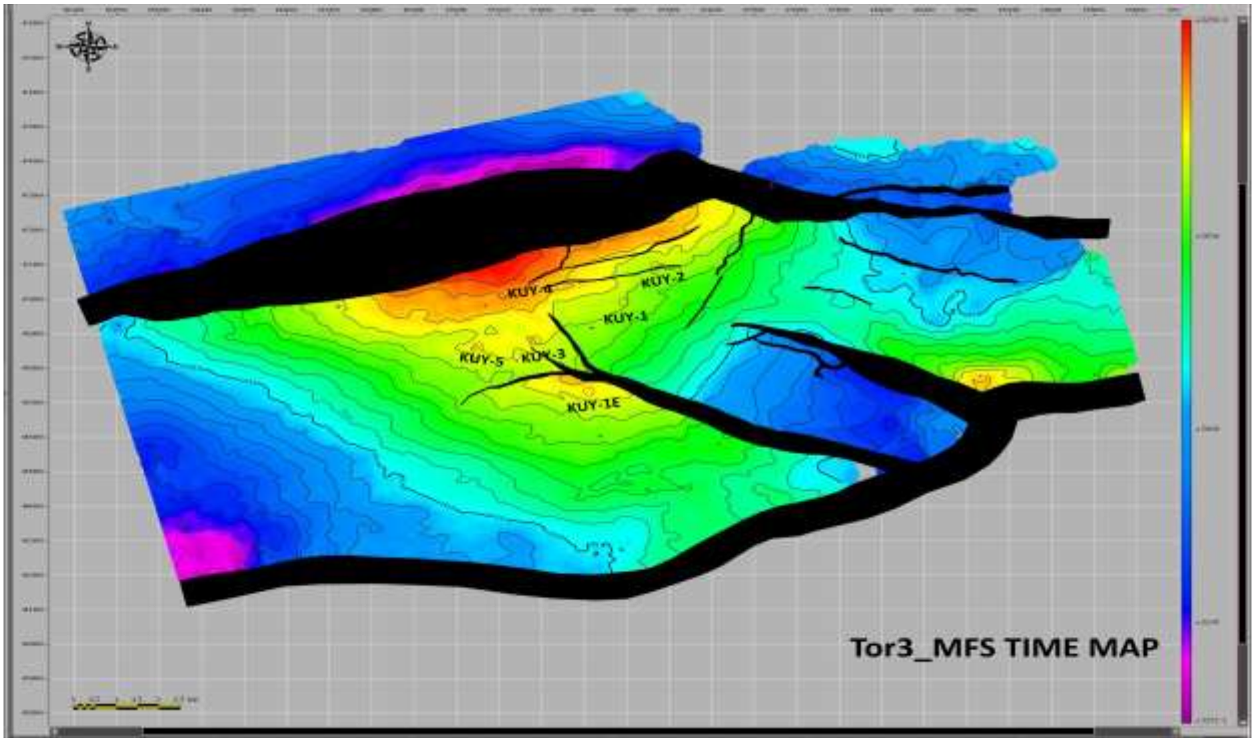

Figure 4.4A: Interpreted Tor3_MFS time map

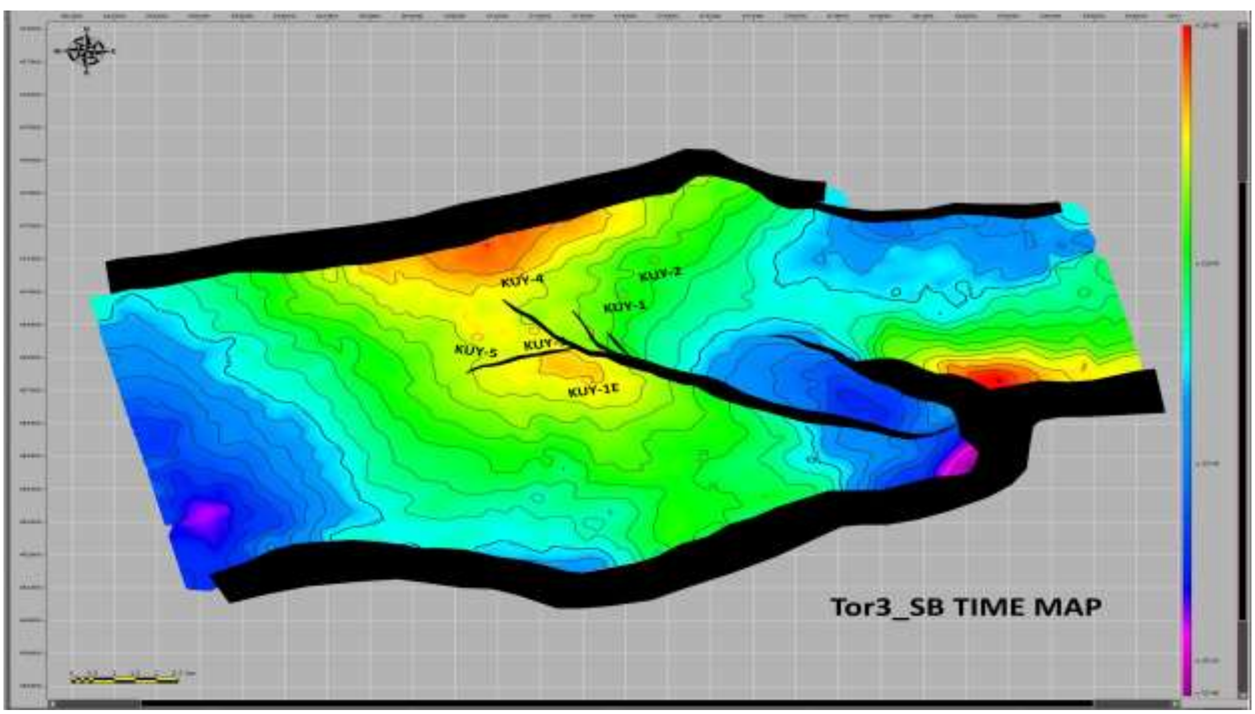

Figure 4.4B: Interpreted Tor3_SB time map

4.1 Time to depth conversion

As with well-to-seismic calibration, time-to-depth conversion has to account for the well database limitation: large missing part of sonic, doubtful check-shots. Furthermore, several levels are partly or totally faulted out (F/O) in some wells.

Table 12 summarizes the velocity parameters that can be extracted from wells (KUY-5 highly deviated is excluded from this table).

As can be seen from Table 12, it would have been difficult to build a representative velocity model based on well data alone; thus it has been decided to use Figaro/SuperDix methodology (stacking velocity inversion).

Table 12: Velocity parameters18 at wells from corrected sonic (F/O = “Faulted out”, X = not reached, K = velocity gradient).

	KUY-1	**KUY-2**	**KUY-3**	**KUY-4**	**KUY-1E**
SB to **BKI**	No sonic	No sonic	V_0 = 1600m/s K = 0.18/s V_{Mean} = 2120m/s (from extrapolated sonic)	No sonic	Too small part of sonic
BKI to **5_MFS**	No sonic	V_0 = 1500m/s K = 0.48/s V_{Mean} = 2120m/s	V_0 = 2100m/s K = 0.11/s V_{Mean} = 2120m/s	No sonic	V_0 = 1800m/s K = 0.46/s V_{Mean} = 2440m/s
5_MFS to **8_MFS**	V_0 = 250m/s K = 0.5/s V_{Mean} = 2480m/s **! deviated part of the well!**	No sonic	V_0 = 1200m/s K = 0.58/s V_{Mean} = 2475m/s	K = 0.05/s V_{Mean} = 2865m/s **! Fault = level 7** **Partly F/O!**	K = 0.09/s V_{Mean} = 2870m/s
8_MFS to **Tor3_MFS**	V_0 = 1500m/s K = 1/s V_{Mean} = 2860m/s **! part of log missing above Tor3_MFS!**	**! Level 8 F/O!** **! deviated part of the log!**	X	V_0 = 800m/s K = 0.6/s V_{Mean} = 2840m/s **! Levels 8 and 9 F/O!**	V_{Mean} = 2780m/s **Level 8 F/O!**
Tor3_MFS to **Tor3_SB**	X	X	X	X	V_0 < 0 m/s K = 1.25/s V_{Mean} = 3210m/s
Tor3_SB to **Tor2_TS**	X	X	X	X	Very high V_0 K = -1.90/s V_{Mean} = 2620m/s

4.1.1 Building an input model for Figaro/SuperDix

The model layering was mainly based on KUY-1E velocity profile (reliable well CKS and logs, no important part faulted-out, deepest well). The main velocity contrasts detected are (Figure 4.6):

- At 5_MFS where a clear velocity increase exists;
- Around 8_MFS from where a first light undercompaction trend is highlighted;
- At Tor3_MFS where a more normal trend returns;
- At Tor3_SB where the main undercompacted sequence starts (strong velocity drop).

A first layer (sea bottom to BKI) was created to have an additional control point (furthermore, BKI is known to be an important stratigraphic event).

Next, Figaro/SuperDix trials needs values of (V_0, k) in each layer as input for stacking velocities inversion.

The layer-cake a priori input for Figaro/SuperDix was constructed based on Table 12 results as follow (Figure 4.7):

SB to BKI: a_prioriV0 = 1700 m/s; k = 0.2 /s (~KUY-3).

BKI to 5_MFS: a_prioriV0 = 1700 m/s; k = 0.46 /s (~KUY-1E and KUY-2).

5_MFS to 8_MFS: a_prioriV0 = 2800 m/s; k = 0 /s (~KUY-1E and KUY-4).

8_MFS to Tor3_MFS: a_prioriV0 = 2780 m/s; k = 0 /s (~KUY-1E)

Tor3_MFS to Tor3_SB: a_prioriV0 = 2100 m/s; k = 1 /s (minored k from KUY-1E)

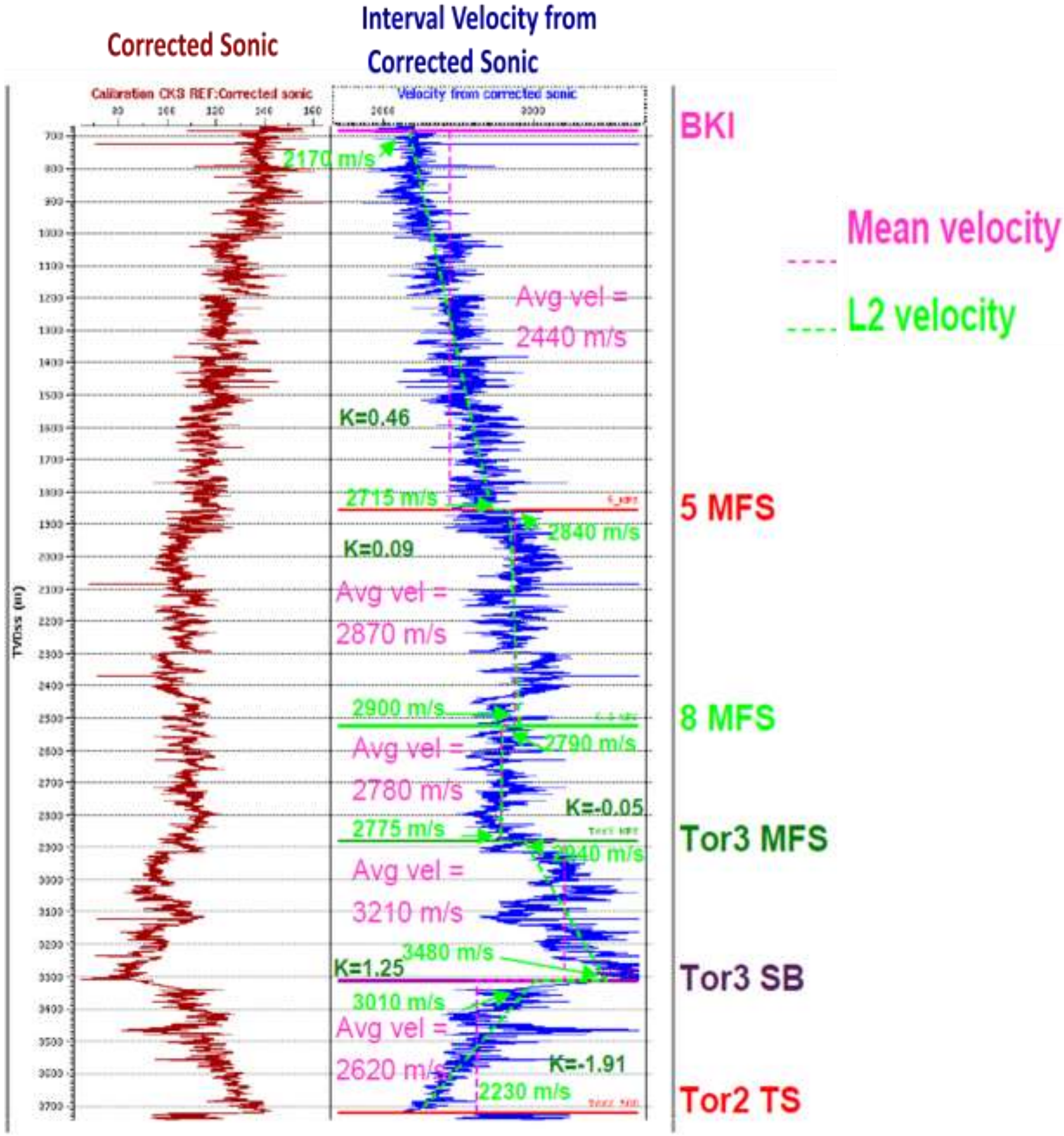

Figure 4.5: KUY-1E well velocity profiles from where the values of K and V_{mean} are derived for input into the Figaro/SuperDix.

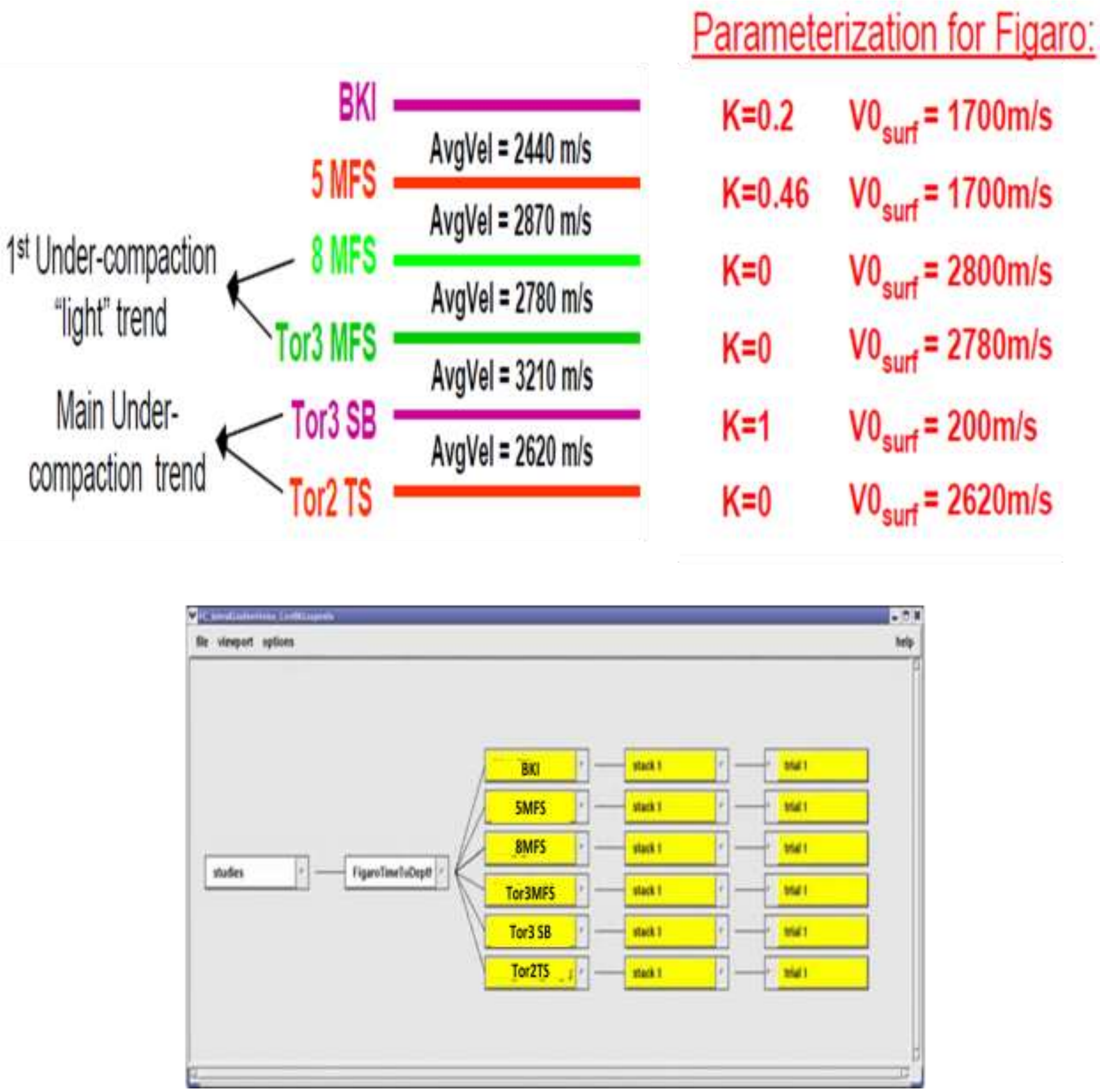

Figure 4.6: A priori velocity profiles for Figaro/SuperDix model interface

4.1.2 Stacking velocities inversion

Before starting the process, a geostatistical filtering of the seismic stacking velocities was done (Figure 4.7). Two filtering options (weak and strong filtering) were proposed, the “weak filtering” option was considered sufficient for input to SuperDix.

The approach used during Figaro/SuperDix tests was to increase step by step the complexity of the process, from the use of the isotropic version with a polynomial approximation of V_0 maps to the use of anisotropic version with a spline approximation of V_0 maps.

Confident well markers were used to constrain (softly) the inversion (anisotropic version).

The inversion was done using a straight ray approach for modeling; only the 2nd order stacking velocity was inverted. The final result was considered as a base case.

The results are globally satisfactory (Figure 4.8):

- Rms misfit was low: ~30m/s in average at Tor3_mfs level (~2500m);
- Vstack misfit was approximately 2% Vstack (or less) in the field area;
- Depth misfit was reasonably good: 10-15m at objective levels.
- KUY-1E log velocity profile was well recovered by the inversion.

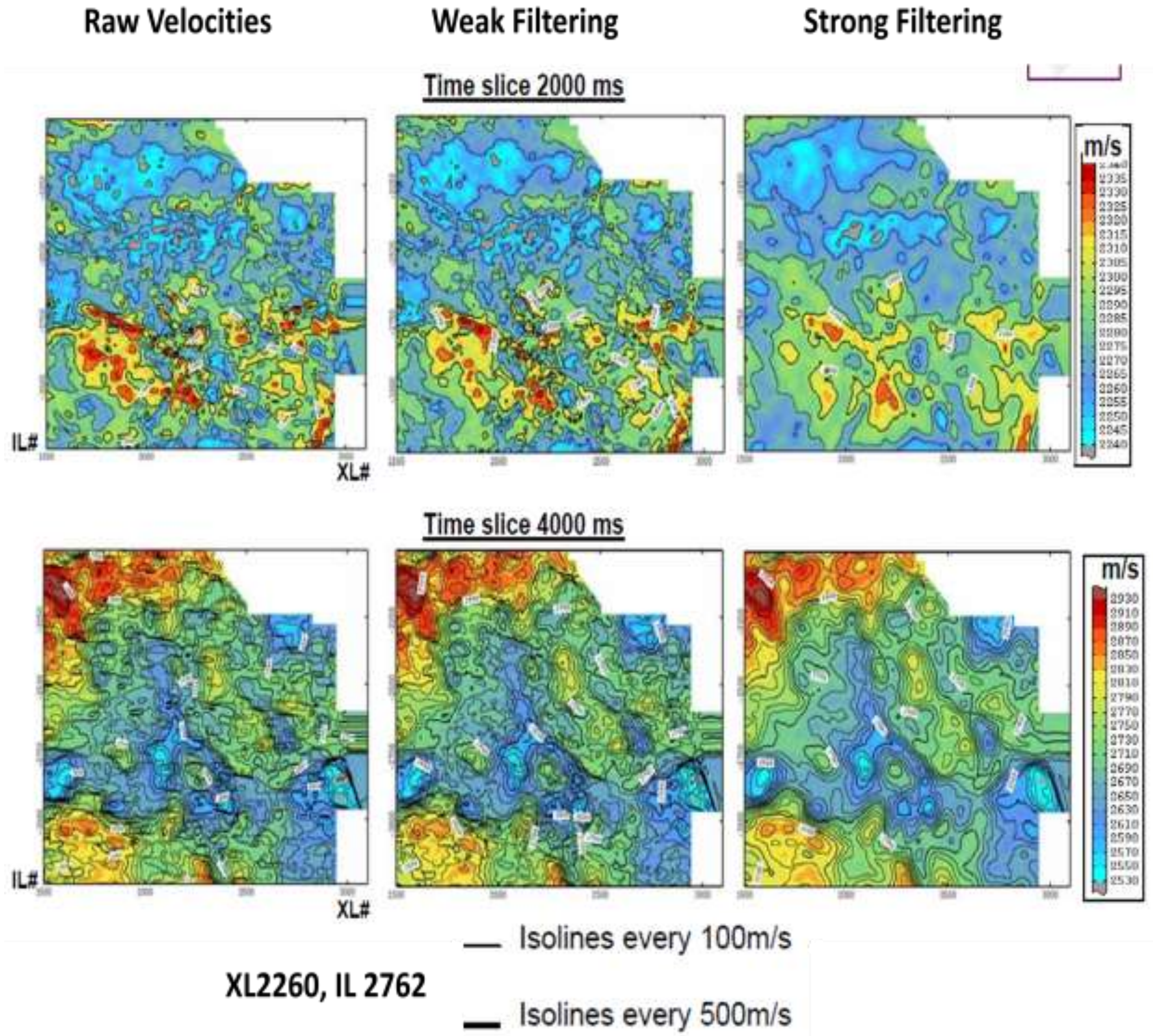

Figure 4.7: Geostatistical velocity filtering at 2000 and 4000ms through inline 2762 and Crossline 2260.

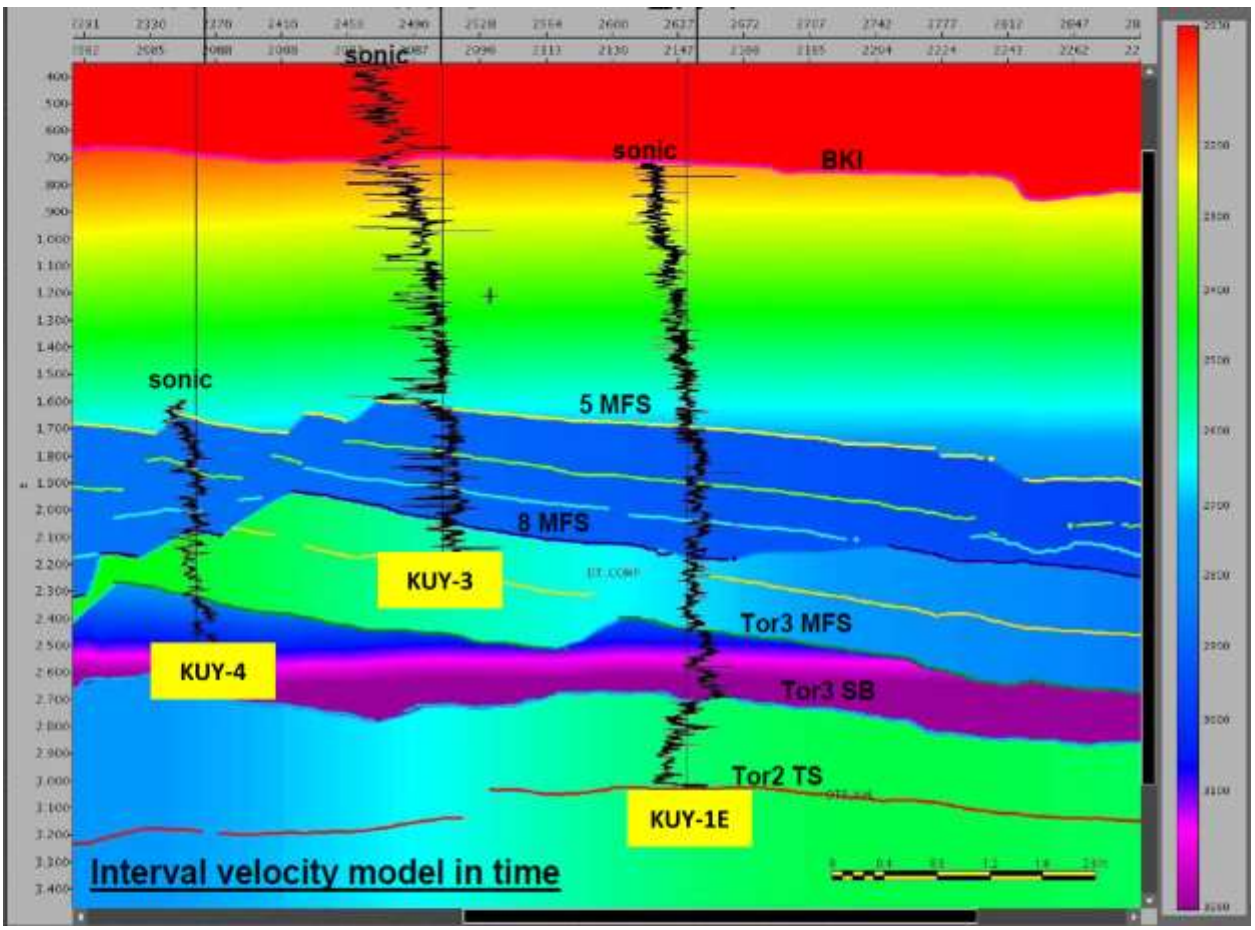

Figure 4.8: Cross section through the base case interval velocity model (straight ray spline)

4.1.3 Depth map correction (adjustment to well markers)

SuperDix model allows depth maps close to geological markers to be obtained. However some residuals must be corrected. This was done directly on depth maps with Sismage (universal kriging).

In summary, the interpretation was transformed to depth with the following workflow:

- Final interpretation was converted to depth using the base case velocity model
- This preliminary depth horizon was adjusted to well marker

Final depth maps are provided in the Figures 4.10A and 4.10B only for Tor3_MFS and Tor3_SB.

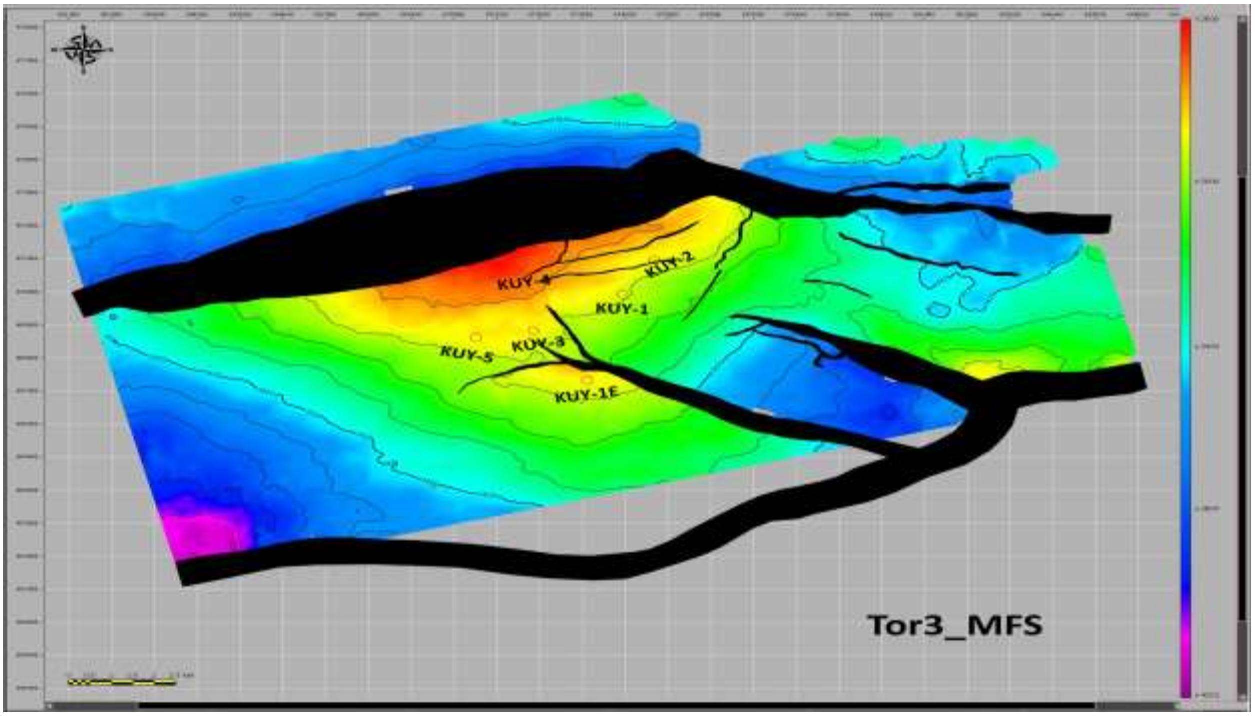

Figure 4.9A: Interpreted depth map Tor3_MFS

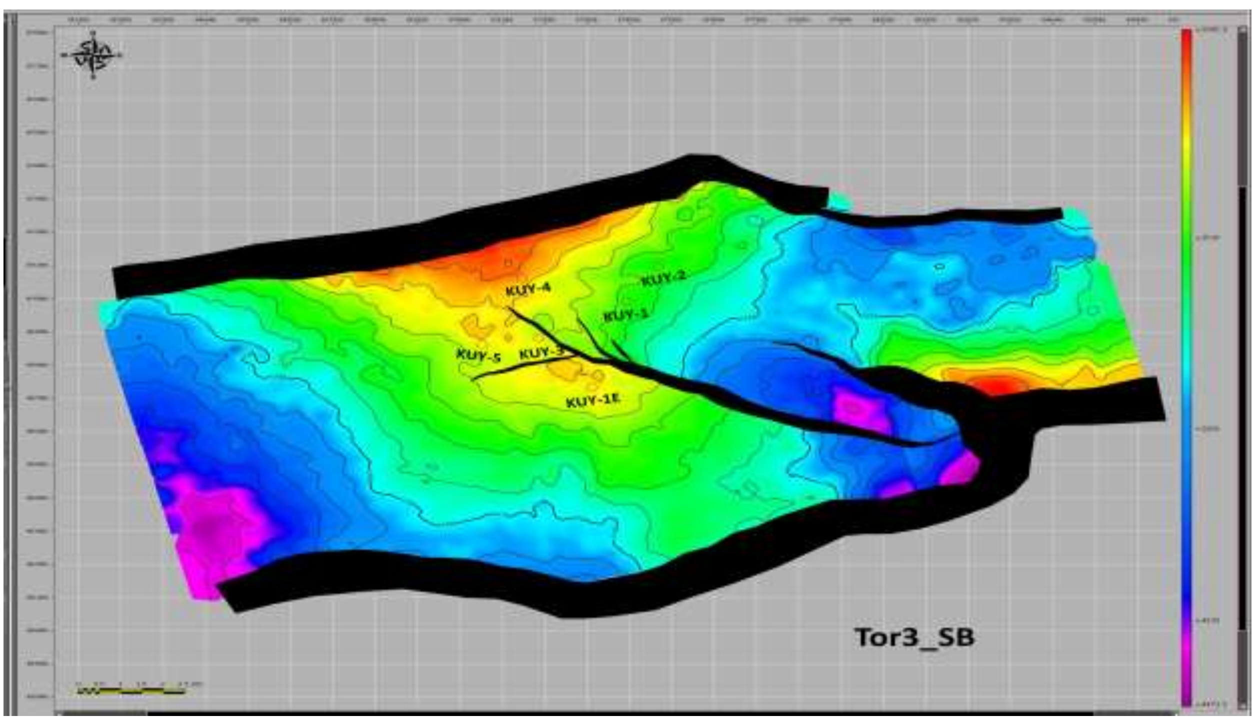

Figure 4.9B: Interpreted depth map Tor3_SB

4.2 Fault interpretation

Faults were also picked on Sismage workstation using the fault picking tools (Figure 4.12). Dipmeter was available on paper plot for all wells and was extensively used in deriving the fault picks. The faults consistency in 3D was checked using the 3D viewer.

From a structural point of view, the Kuyolo field corresponds to a complex structural trap in the upper-thrown compartment of down-to-the-North faults. These faults are normal growth faults. The structure is complex because the structure-forming faults are three branches merging below 2500-3000m and defining, above this merging point, thin and elongated compartments with several oil-bearing levels in each. These important faults are named F1, F2 and F3.

Furthermore, another fault F6 is crossing perpendicularly F2 and F3 (towards the West). So that the upper reservoirs are split up into seven compartments (A to F) with two major ones A and C.

The wells reached the compartments as follows (Table 13):

- Compartment A reached by KUY-4 and KUY-2
- Compartment B reached by KUY-2
- Compartment C reached by KUY-1, KUY-2, KUY-3, KUY-4 and KUY-1E
- Compartment D reached by KUY-1E
- Compartment E not reached
- Compartment F reached by KUY-5

The interpretation work flow used to achieve this process was as follows:

1. Faults were interpreted on Inline/Crossline (approximately 5x5 each)
2. Propagation was done through Sismage algorithm
3. The fault surface was then smoothed

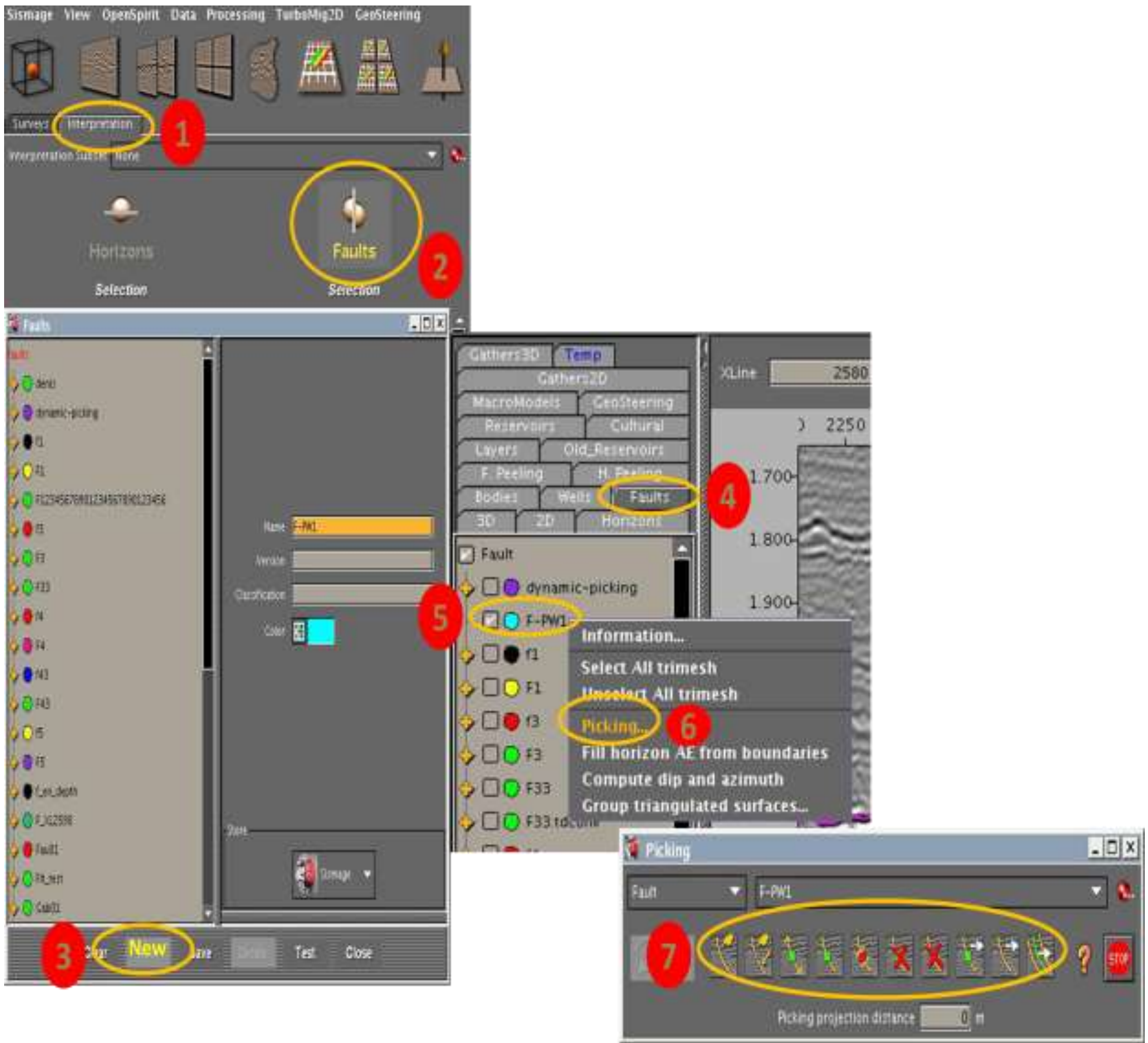

Figure 4.10: Sismage interface for fault picking. The steps to pick faults in Sismage are numbered from 1to 7.

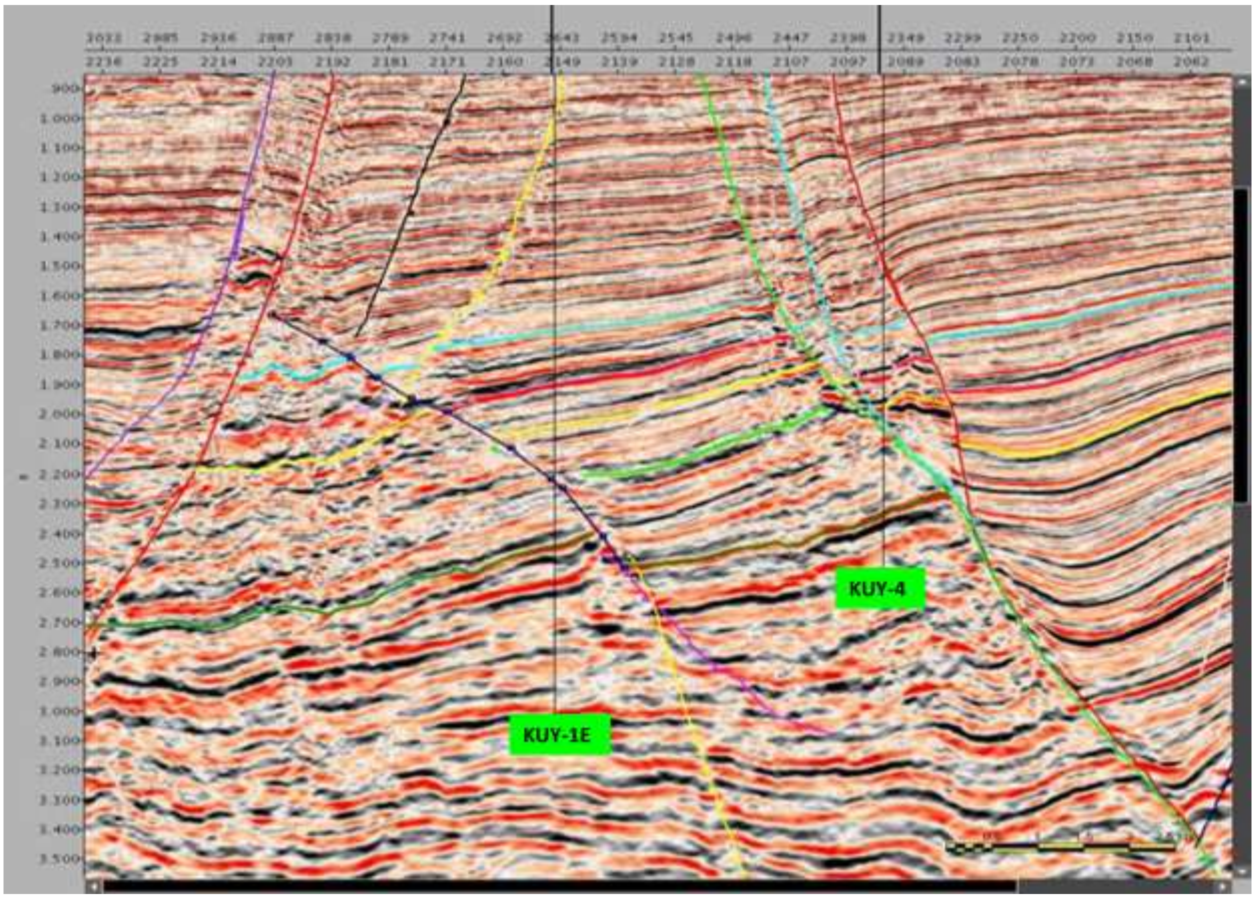

Figure 4.11: Seismic section through KUY-1E and KUY-4 showing fault picks.

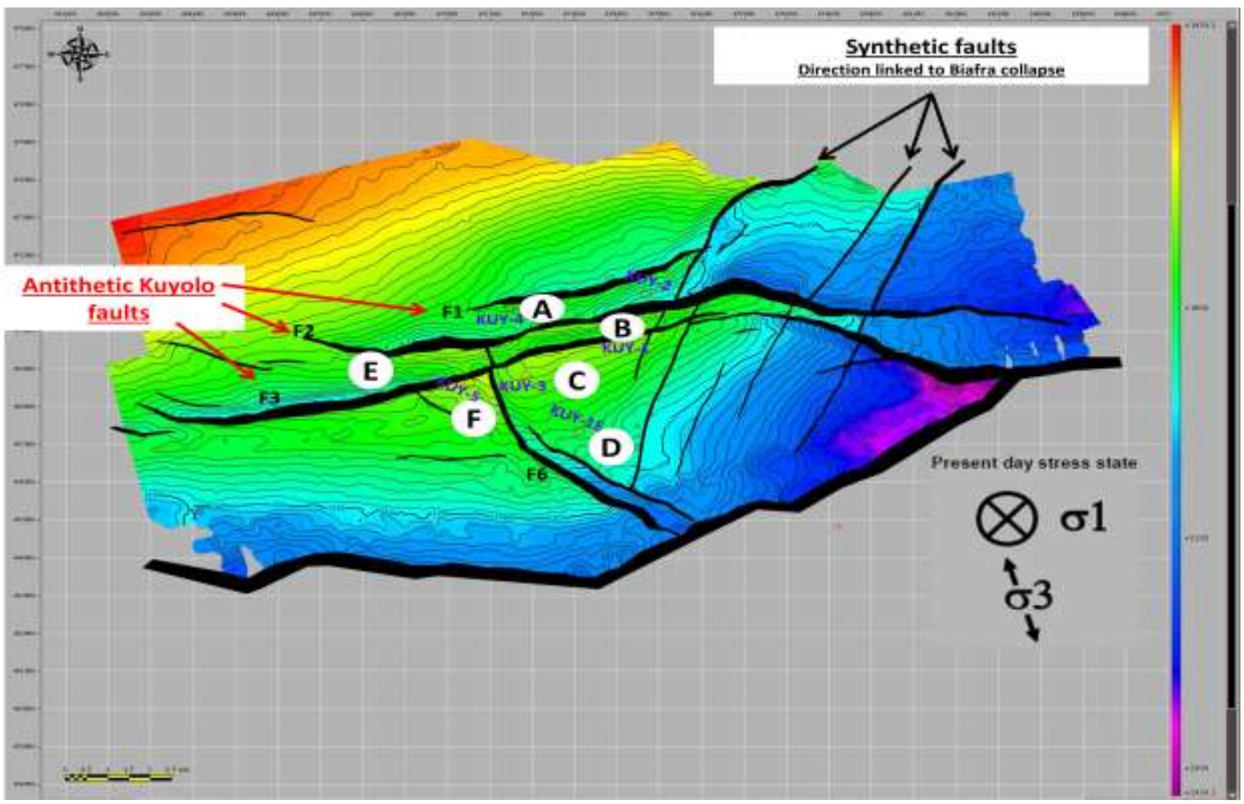

Figure 4.12: Structural schemes with the fault pattern (Time Map at R5)

	Panel A	Panel B/E	Panel C	Panel D	Panel F
KUY-1			R5 → R7		
KUY-2	R5	R7	R11		
KUY-3			R5 → R8		
KUY-4	R5 → R7	R8	R11 → R14		
KUY-5					R5 → R11
KUY-1E			R5 → R7	R11 → R23	

Table 13 Well penetration per compartment

CHAPTER FIVE

PETROELASTIC STUDY

5.0 General

The objective of this study was to characterize the elastic behaviour of the rock depending on the petrophysical parameters and to build a comprehensive Rock Physics Model (PetroElastic Model) of the Kuyolo field.

Since there was no shear sonic data at all in Kuyolo field, this study was carried out using data coming from numerous wells that contain shear sonic information in OML's 70, 99, 100 and 102 blocks to set up a general Rock Physics Model (PetroElastic Model) on Kuyolo field. A general Rock Physics Model (PetroElastic Model) based on the wells allowed us to model densities, velocities (V_p & V_s), impedances (I_p & I_s) and Poisson's ratio (PR). This Rock Physics Model (PetroElastic Model) was then applied on the representative well (KUY-1E) from the study area (Kuyolo-field) and the modelled densities, velocities, impedances and Poisson's ratio (PR) compared with the actual log measurements which allowed us to see how well they predicted each other and the possibility of characterizing the reservoirs using the AVO Seismofacies methodology.

The wells taken into account in this study are all located in OML's 70, 99,100 and 102 blocks (Figure 5.0). They are as follows:

- Two wells COC-4 and BOB-1 belong to a field located in the south-east part of OML 99 and both are vertical.

- Five wells ZOM-1, ZOM-5, ZOM-7, ZOM-11 pilot hole of the side track (ZOM-11ST-PH) and ZOM-26 are located in a field on OML 102 with the two last ones being deviated.
- One well KUY-1E (vertical) is situated south of the Kuyolo field, in OML 99. This well is the only representative well from Kuyolo field that will be used in this study because it has correct and relevant data.
- Another well EFE-2 (vertical) is situated a few kilometers east of the KUY-1E well, just outside of the OML 99 boundary, in the OML 70 block.
- The last one WOM-1(vertical) is situated in the Cameroon waters, but in a similar geological context.

Except wells COC-4, BOB-1, ZOM-1, ZOM-5, ZOM-7, ZOM-11ST-PH, ZOM-26, all others (KUY-1E, EFE-2 & WOM-1) had encountered strong overpressures.

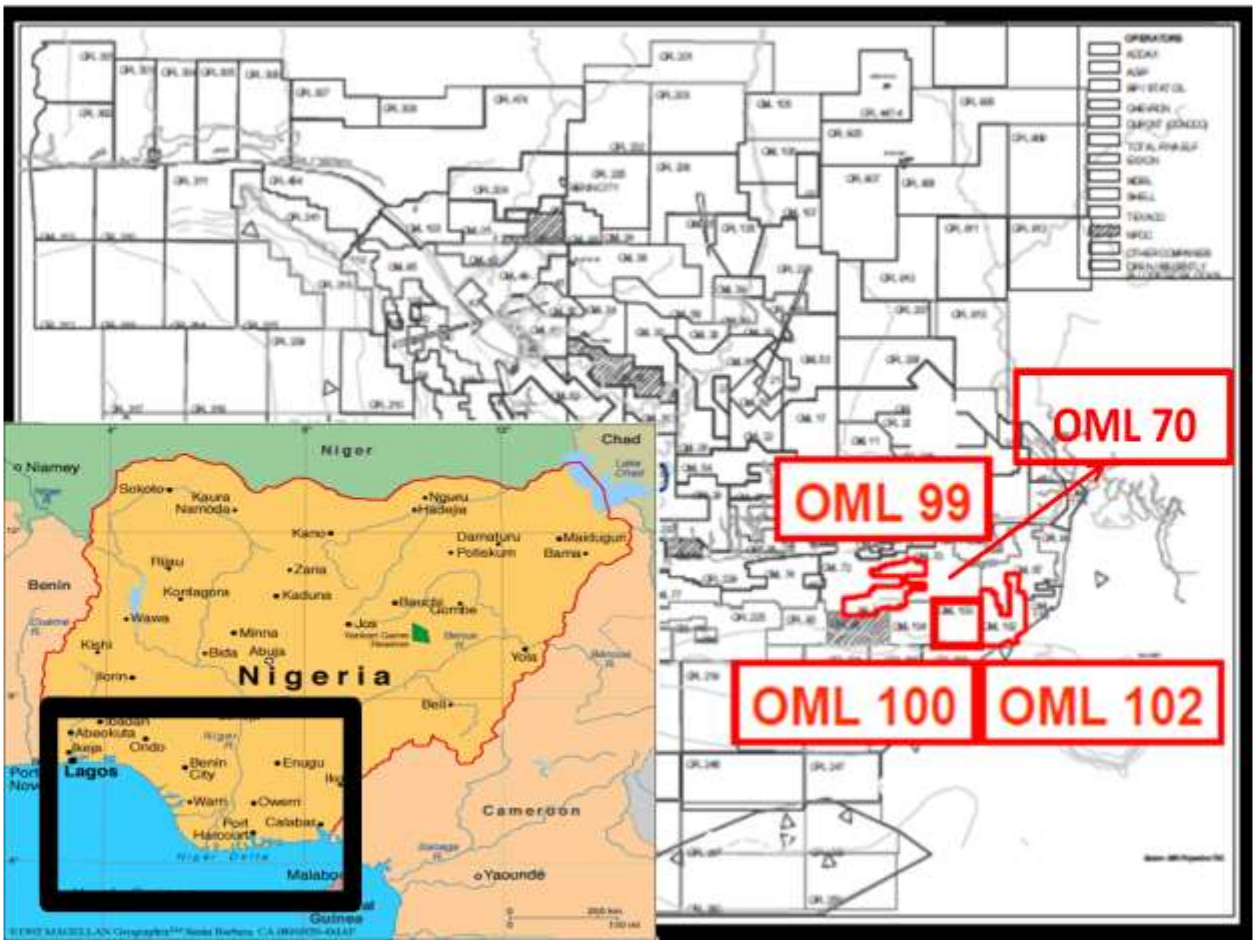

Figure 5.0: Situation maps of the wells in OML's 70, 99, 100 and 102 blocks where the Petroelastic study was carried out.

5.1 Feasibility study

Prior to this analysis, a feasibility study was first carried out to determine if some relations exist between seismic attributes and petrophysical parameters at well and also to determine the main factor driving the petroelastic behaviour (burial depth or effective pressure). To achieve the above, a quick cross-plots of acoustic impedance (IP) versus density (RhoB), P sonic (V_p) versus density (RhoB) colour coded by wells, volume of clay (VCL), effective porosity (PHIE), effective water saturation (SWE), burial depth and effective pressure was done using all the 10 wells, 5 shear sonic data and logs within the horizons (Tor3_MFS – Tor3_SB) that covered the reservoir (R11) of interest.

Figure 5.1A present acoustic impedance (IP) versus density (RhoB) crossplot for only the representative well (KUY-1E) of the Kuyolo field. This crossplot shows that there exists a linear relationship between acoustic impedance (IP) and density (RhoB). Acoustic impedance was obtained by multiplying velocity (V_p) log with the density (ρ) ($IP = V_p * \rho$) log.

Figure 5.1B represents the respective positions of sands (yellow ellipse) and shales (green ellipse). Crossplot is made with the acoustic impedance (IP) versus density (RhoB), colour coded by volume of clay (VCL) within the horizons (Tor3_MFS – Tor3_SB) that covered the reservoir (R11) of interest for only the representative well (KUY-1E) of Kuyolo field. In order to see clearly the reservoir and shale behavior, only points with VCL < 0.4 (reservoirs) and points with VCL >0.5 (shale) have been selected.

Figure 5.1C is a crossplot of acoustic impedance (IP) versus density (RhoB), colour coded by effective porosity (PHIE) within the same horizons (Tor3_MFS – Tor3_SB) that covered the reservoir (R11) of interest for only the representative well (KUY-1E) of Kuyolo field.

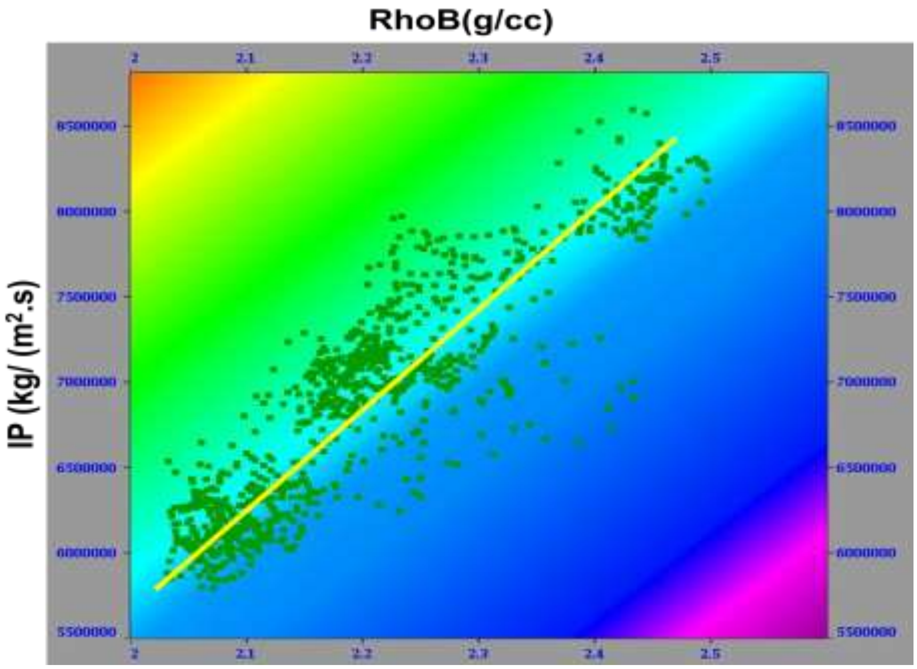

Figure 5.1A: Cross-plot of Acoustic impedance (IP) versus density (RhoB).

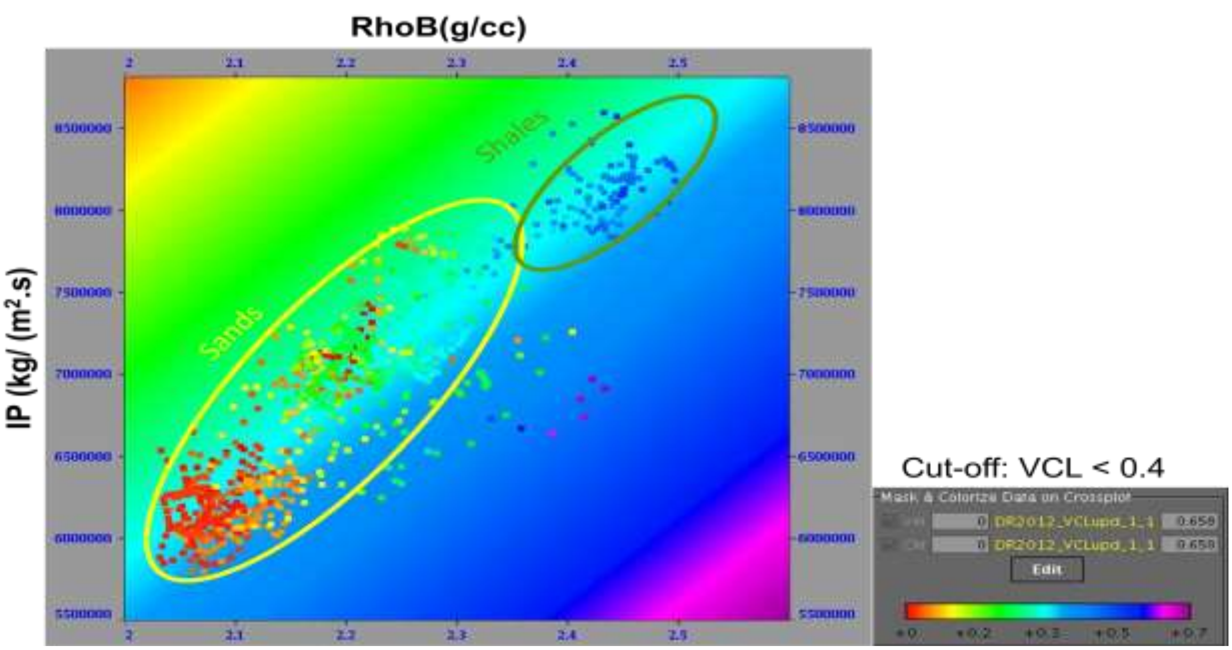

Figure 5.1B: Cross-plot of acoustic impedance (IP) versus density (RhoB) colour coded with the volume of clay or shale.

This crossplot highlights a normal porosity effect. Velocities and densities decrease as porosity increases

Figure 5.1D is a crossplot of acoustic impedance (IP) versus density (RhoB), colour coded by effective water saturation (SWE) within that same horizons (Tor3_MFS – Tor3_SB) that covered the reservoir (R11) of interest for only the representative well (KUY-1E) of Kuyolo field. Water saturation decreases as velocities and density decrease.

Figure 5.1E represents a crossplot made with P sonic (V_p) versus density (RhoB), colour coded by burial depth also within the horizons (Tor3_MFS – Tor3_SB) that covered the reservoir (R11) of interest for only the representative well (KUY-1E) of Kuyolo field. This crossplot reveals the overpressured zones: they are not aligned with a normal burial trend.

As a confirmation of the fact that burial depth is not the right value to consider for the PetroElastic analyze, Figures 5.2 and 5.3 present the crossplots of density, sonics (V_p & V_s), incompressibility modulus (*K*), shear modulus (*MU*), P-impedance and Poisson's ratio versus burial depth, colour coded by the 10 wells and 5 wells with shear data used in this study. Visible pressure effects on P-impedance, sonics (V_p & V_s) and shear modulus (*MU*) was observed (black circle): not in the same trend with the normal burial trend. This further confirms the presence of overpressured zones. Overpressured zones are not in the general trend, especially on wells like WOM-1.

Figures 5.4 is the crossplots of incompressibility modulus (*K*), shear modulus (*MU*), P-impedance and Poisson's ratio versus effective pressure, also colour coded by the 10 wells and 5 wells with shear data used in this study. These crossplots shows a much better organization of

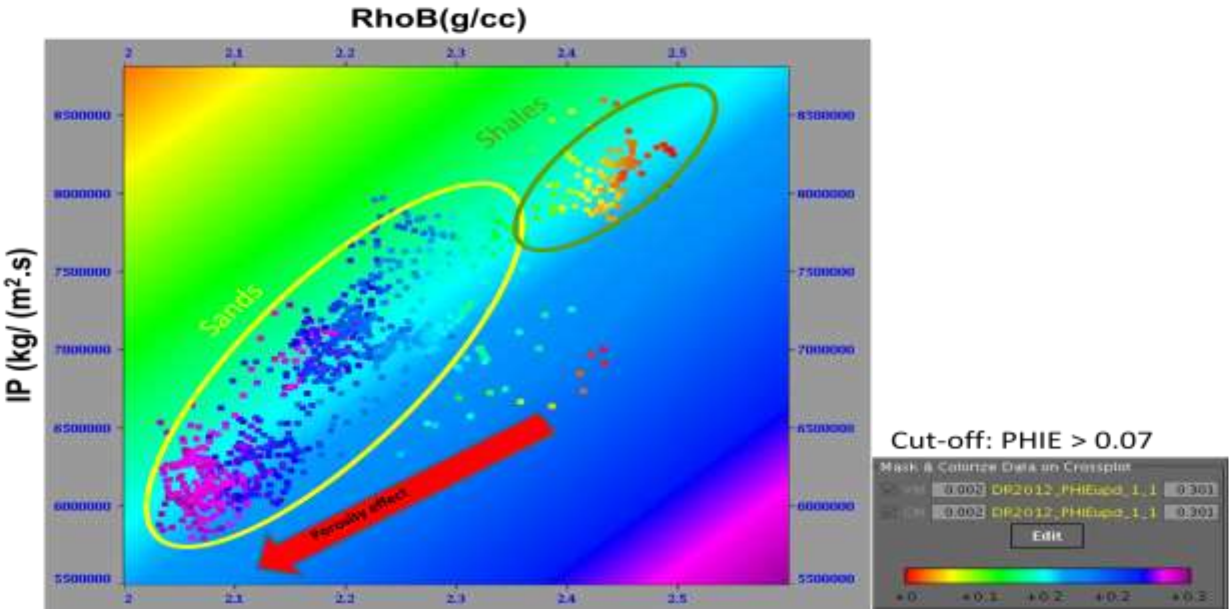

Figure 5.1C: Cross-plot of Acoustic impedance (IP) versus density (RhoB), colour coded by effective porosity (PHIE).

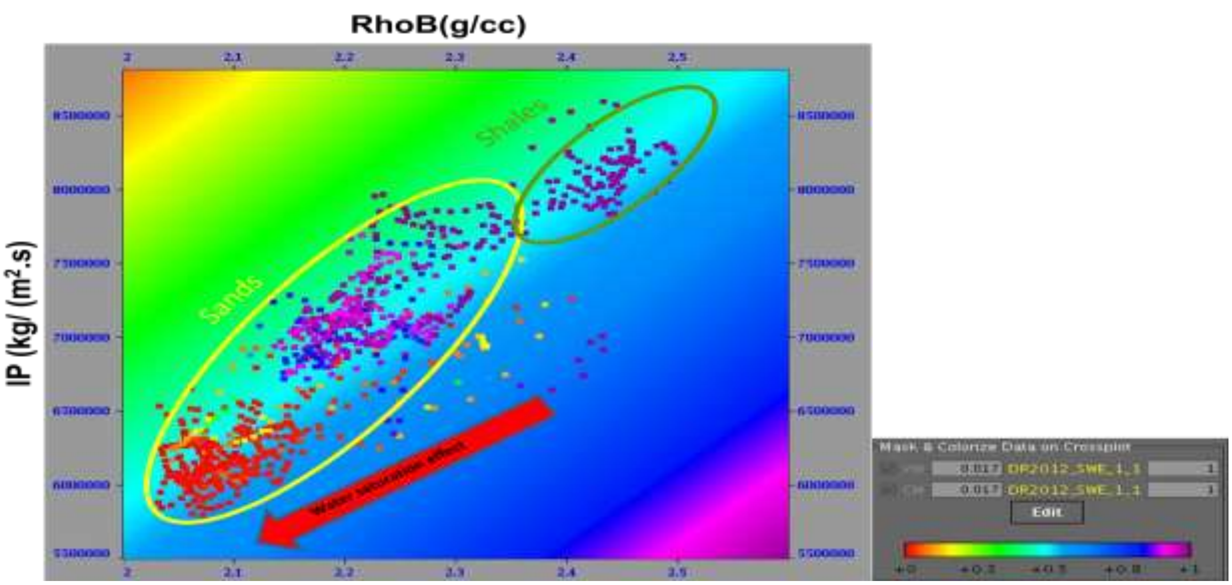

Figure 5.1D: Water saturation effect on acoustic impedance (IP) versus density (RhoB) cross-plot.

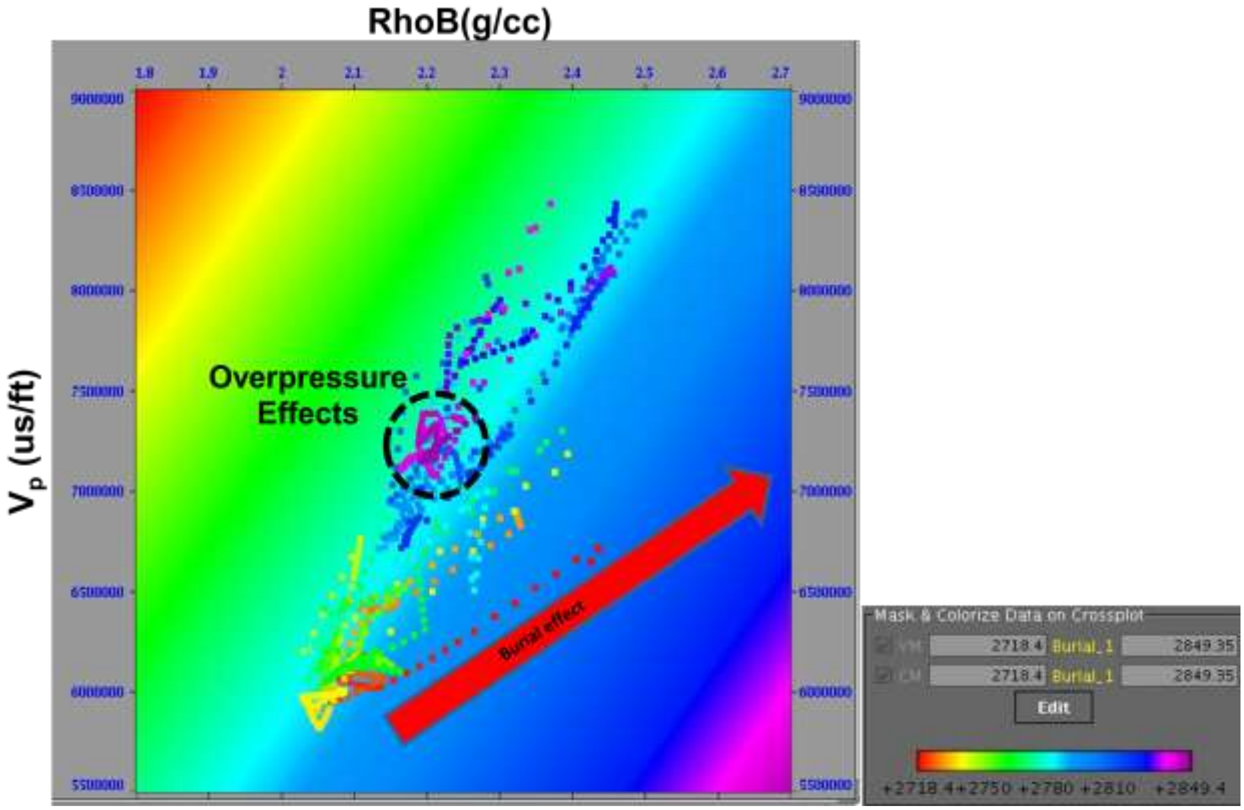

Figure 5.1E: P - sonic versus density (RhoB) cross-plot for the representative well KUY-1E on Kuyolo field revealing overpressured zones.

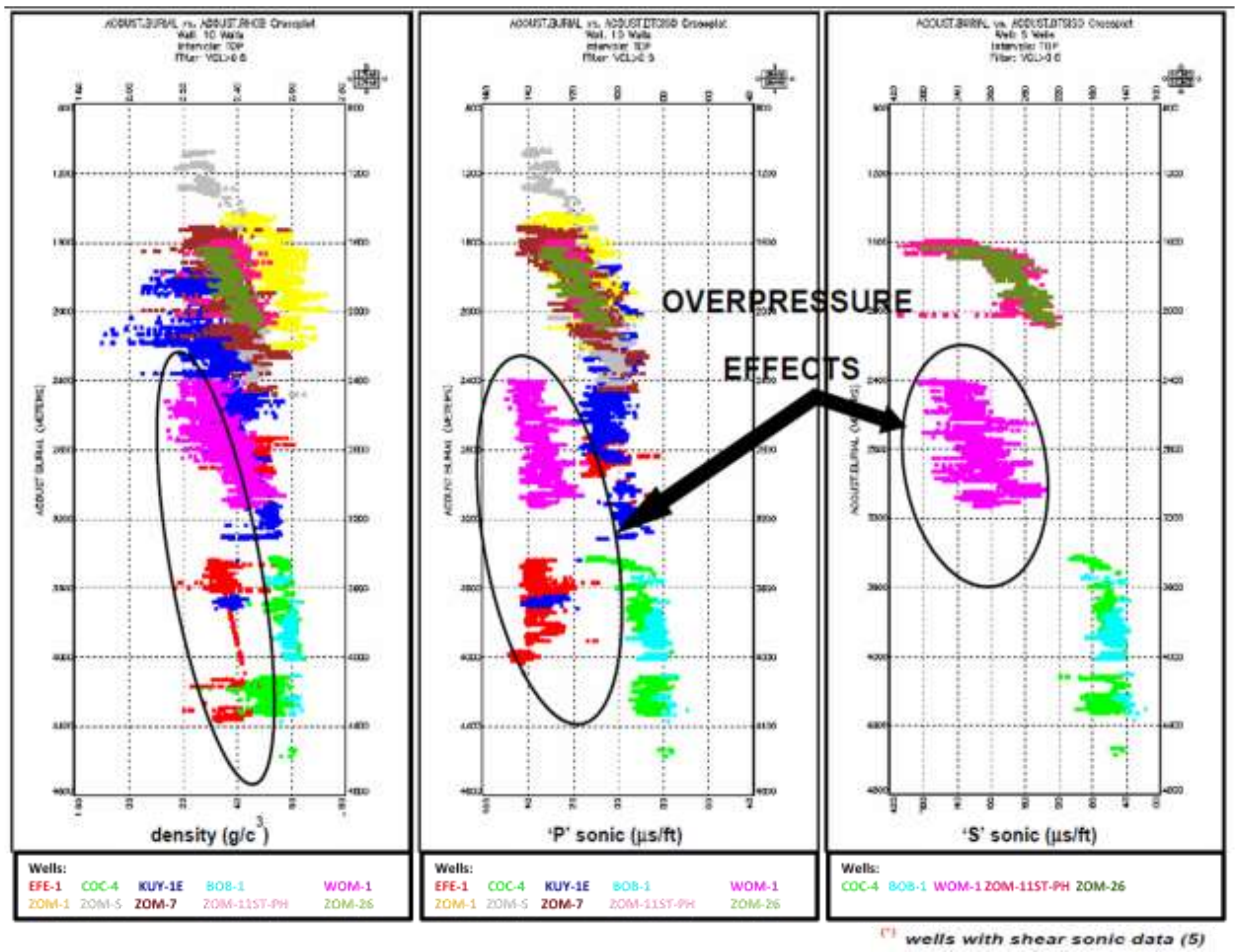

Figure 5.2: Cross-plots of density and sonics (V_p & V_s) versus burial depth, colour coded by the 10 wells and 5 wells with shear data used in this study. Overpressured effects are shown by the black circles.

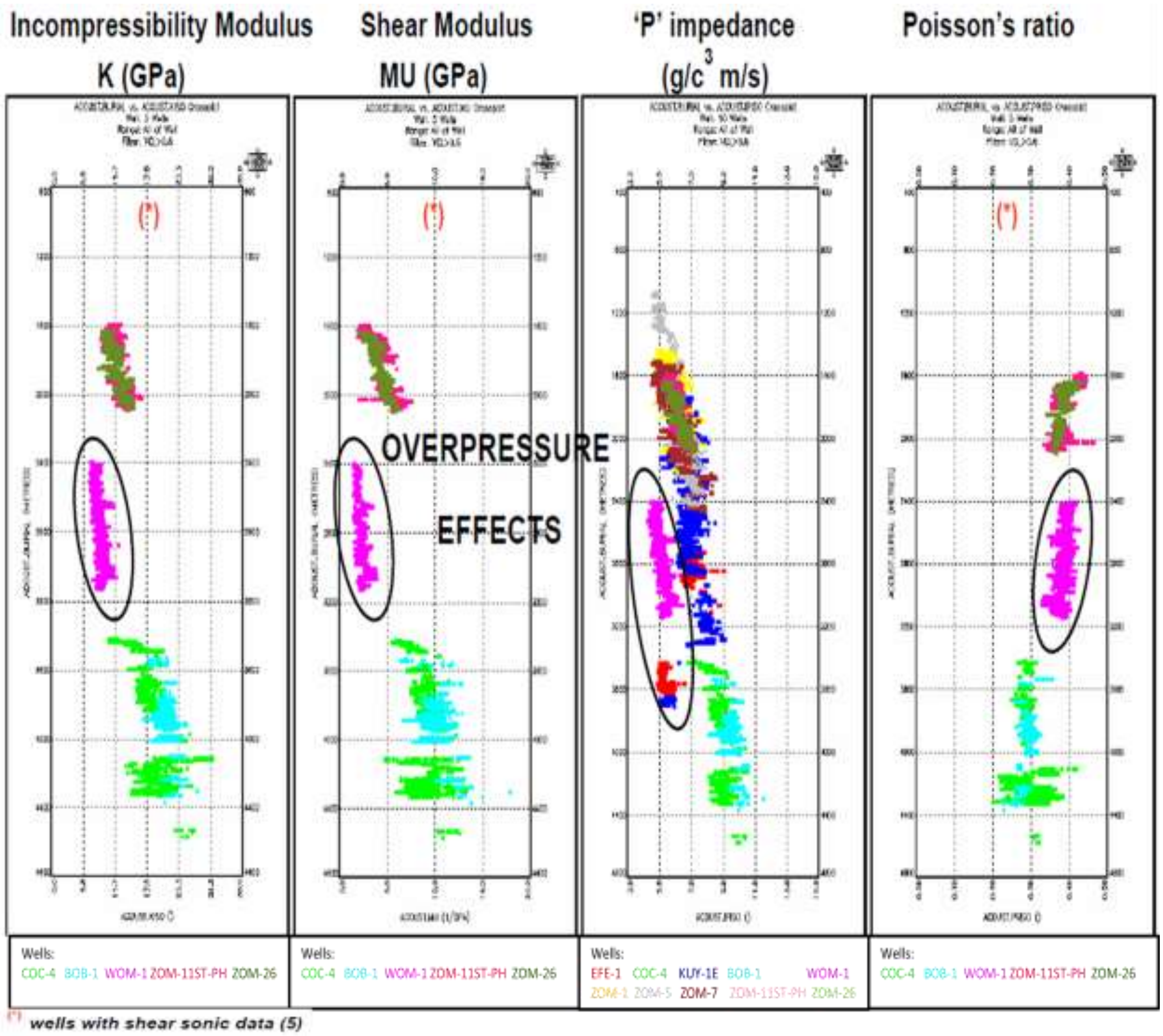

Figure 5.3: Cross-plots of incompressibility modulus (*K*), shear modulus (*MU*), P-impedance and Poisson's ratio versus burial depth, colour coded by the 10 wells and 5 wells with shear data used in this study. Overpressured effects are shown by the black circles.

the P-impedance, sonics (V_p & V_s) and shear modulus (*MU*): they are aligned with a normal burial trend.

As one can see, we cannot consider these variables as functions of the burial depth because of the overpressured zones that can be found on EFE-2, KUY-1E or WOM-1. Such overpressured zones are characterized by density and velocity drops, due to the clay porosity preservation. This increase of fluid pressure is itself caused by low permeabilities, preventing the fluid to flow and equilibrate pressure. By the way, these observations were confirmed by the Modular Formation Dynamic Testers (MDT) measurements we had at our disposal.

Due to overpressured zones, all laws and equations used in setting up this Rock Physics Model (PetroElastic Model) were established versus the effective pressure to take into account the pressure effect on the rock frame (effects of overpressures in shales and effect of pressure in sands).

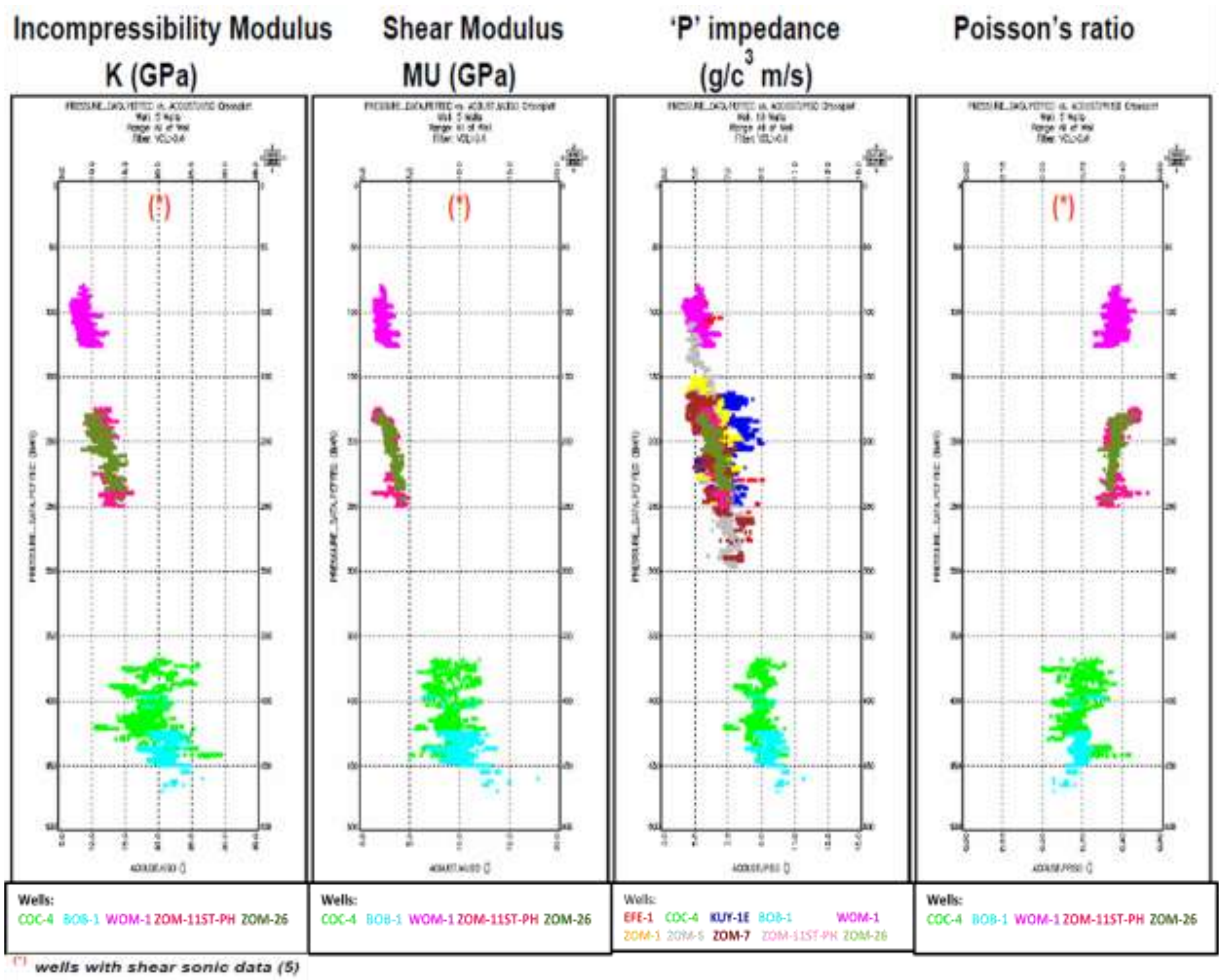

Figure 5.4: Cross-plots of incompressibility modulus (*K*), shear modulus (*MU*), P-impedance and Poisson's ratio versus effective pressure, colour coded by the 10 wells and 5 wells with shear data used in this study.

5.2 Main Steps

The employed methodology was as follows:

- The necessary data were first gathered in a unique study database. This database contains raw logs, composite logs and petrophysical interpretation.
- Anisotropy, editing and invasion of drilling fluids corrections were applied on all wells with the same methodology and parameters defined.
- Then, data from PVT studies were put together in order to characterize the elastic properties of fluids (such as density and incompressibility as a function of pressure and temperature). This phase of the study was carried out in parallel with the gathering of pressure and temperature data, since fluids are closely linked to these parameters (most of the time, these parameters come from Modular Formation Dynamic Testers (MDT) measurements).
- The initial in-situ elastic parameters for each well were calculated using density, P and S velocity logs. This phase led to a first description of the global elastic behaviour of the rocks, with the help of many crossplots. Clean reservoirs was considered as any facies whose clay content is less than 20% (VCL< 0.2), while shales were isolated with clay content greater than 60% (VCL >0.6).
- Fluid substitutions for each wells was performed. Fluid substitutions are based on Gassmann's theory, and make it possible to replace the in situ fluid by any other one, and to determine the associated petroelastic characteristics. Thus, water substitution for all wells was performed in order to simulate the behaviour of a rock saturated with brine and have a reference for the evaluation of the magnitude of the fluid effect.

- These fluid substitutions give the elastic characteristics of the brine saturated rock: density (RhoB), V_p, Vs, bulk modulus of brine saturated rock (K), from which we can easily obtain Petroelastic indicators such as Poisson's ratio (PR), or the acoustic impedance (AI, or P impedance).
- Fluid substitution are only valid for reservoir facies, isolated by a cut-off on the clay volume (VCL< 40%).

5.3 Data Validation and Data Consistency

Density, P and S sonic logs are the very first inputs of a Petroelastic study. Such raw data are a priori unusable, and that's why they must be validated to assure their coherency and accurateness.

5.3.1 Sonic Data Validation

"Modern" sonic acquisitions are thus delivered with coherency images: these images allow the interpreter to point wave arrivals on the sonic recording, since they are characterized by energetic maxima. Regarding the present study, we have corrected, edited and validated sonic data for 8 wells (COC-4, BOB-1 ZOM-1, ZOM-5, ZOM-7, ZOM-11ST-PH, ZOM-26 and WOM-1), except of the KUY-1E and EFE-2 wells on which data were collected from in-house database, corrected and validated from the subsidiary office in Port-Harcourt by the petrophysics team.

On Kuy-1E well, two different sets of data are stored in database. We took the one that was already used for the pressure prediction study. On EFE-2 well, the stored logs are incomplete, especially the density log. Moreover, validation of input density and sonics was impossible on those two wells

5.3.1.2 Anisotropy Correction

'P' and 'S' velocity measurements in shale intervals are potentially affected by the deviation of the well. This anisotropy effect is mainly observed on the highly deviated wells, while vertical wells are not affected. For instance, on the ZOM-11 ST-PH deviated well, because of the Dipole Sonic Imager (DSI) tool configuration and anisotropy of shales, the two shear slownesses is not equal.

In order to have comparable velocities, we computed anisotropy parameters and applied Thomsen's equations (function of angle of propagation and taking into account the clay volume).

Fully validated 'S' sonics are only recorded on wells ZOM-11 ST-PH and ZOM-26, both highly deviated. Another shear sonic with an incomplete data set was recorded on the BOB-1 well (vertical). This last one was taken as reference for anisotropy correction of shear velocities. Regarding 'P' velocities, we used data from ZOM-011STPH (deviated) and ZOM-5 (vertical), two wellheads being distant of about 700 meters. After matching deviated 'P' and 'S' velocities with vertical ones, we applied the same parameters on the ZOM-26 well, and compared corrected 'P' and 'S' velocities to ones recorded. Used anisotropy coefficients are:

$$\varepsilon = 0.1$$

$$\delta = 0.1$$

$$\gamma = 0.3$$

These corrections were then applied in all the 10 wells used for this study using the above anisotropy coefficients.

5.3.2 Density Data Validation

It rapidly appeared that density from studied wells were not homogeneous. A quick first check made on the wells ZOM-1, ZOM-7, ZOM-11ST-PH and ZOM-26 highlighted two different trends for density measurements (Figure 5.5). One corresponding to Wire Line (WL) acquisitions, the other corresponding to Logging While Drilling (LWD) acquisitions. Two wells ZOM-7 & ZOM-26 over the study area have validated densities from both acquisitions:

- On the ZOM-7 well (Figure 5.6), difference between both measurements are evaluated to 10% in change, Logging While Drilling (LWD) measurement being higher than WL one. On this particular well, the Wire Line (WL) density is affected by hole conditions and the LWD density is the correct one.
- On the ZOM-26 well (Figure 5.7), there is no difference between both measurements. This led us to choose LWD trend as the correct one for density modelling.

Densities recorded on vertical wells have been corrected in order to fit the Logging While Drilling (LWD) trend.

Remark: The input density and sonics on KUY-1E and EFE-2 wells were not properly validated by the petrophysics team. They were therefore not utilized in the study.

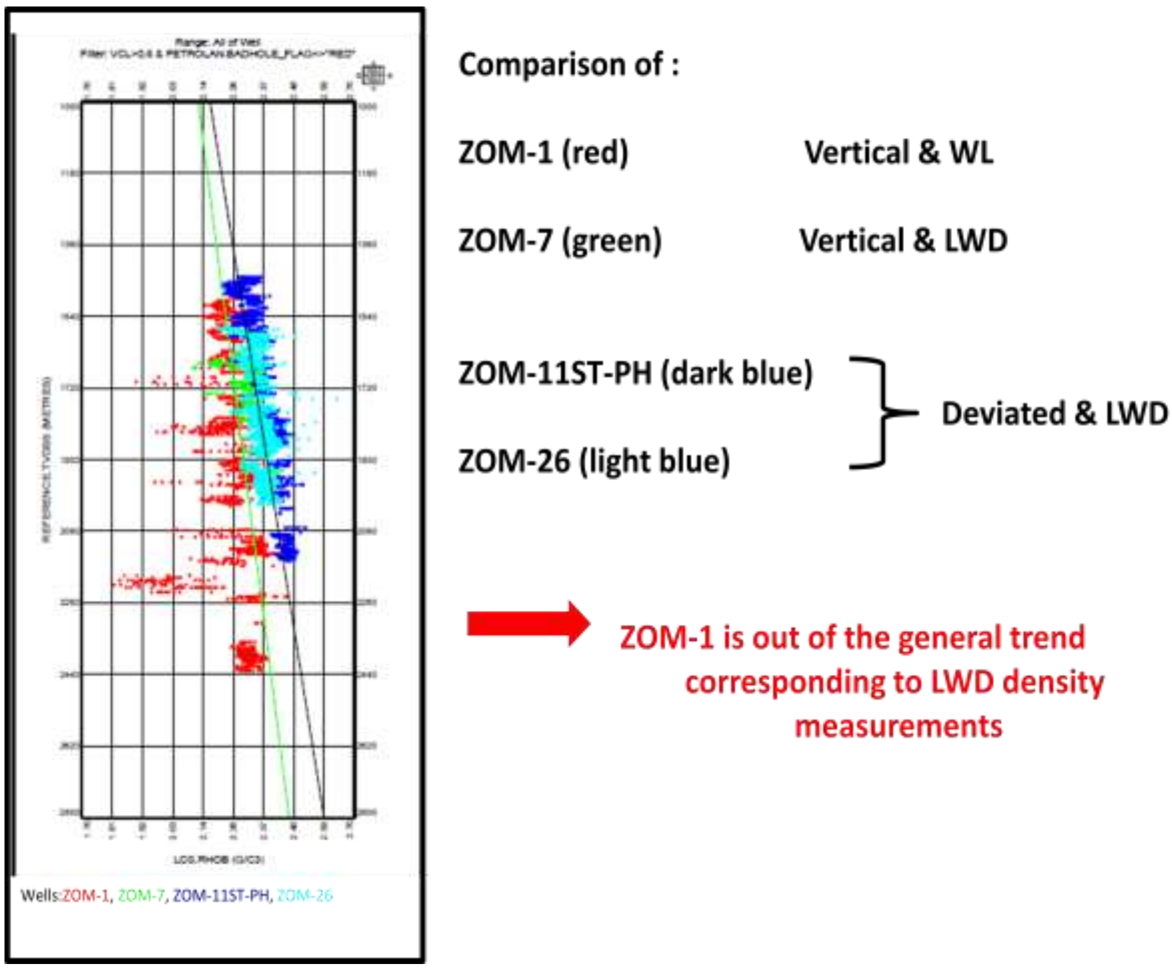

Figure 5.5 Density measurements (Wire Line and Logging While Drilling) from both acquisitions.

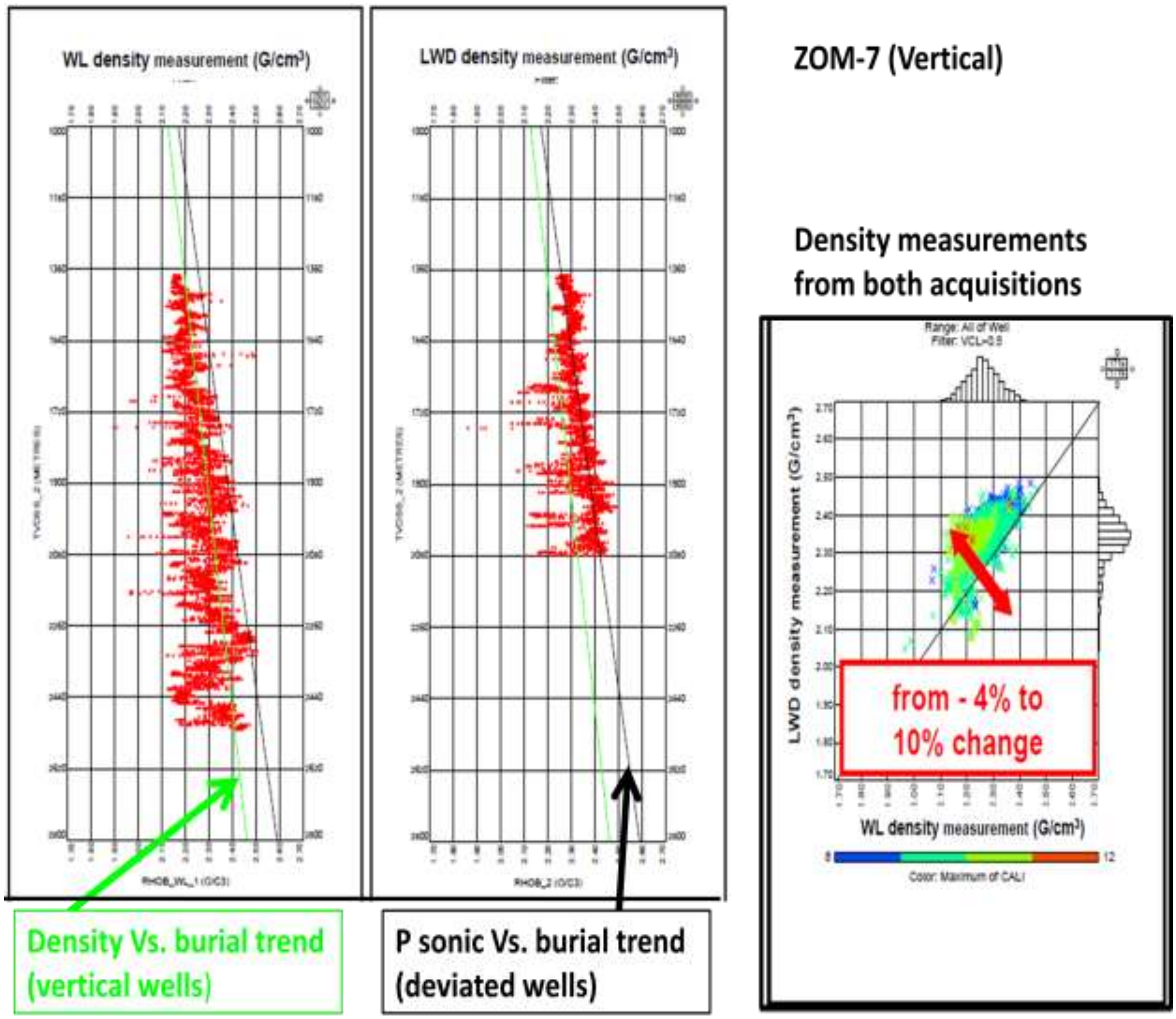

Figure 5.6: Density measurements (Wire Line and Logging While Drilling) from both acquisitions for well ZOM-7.

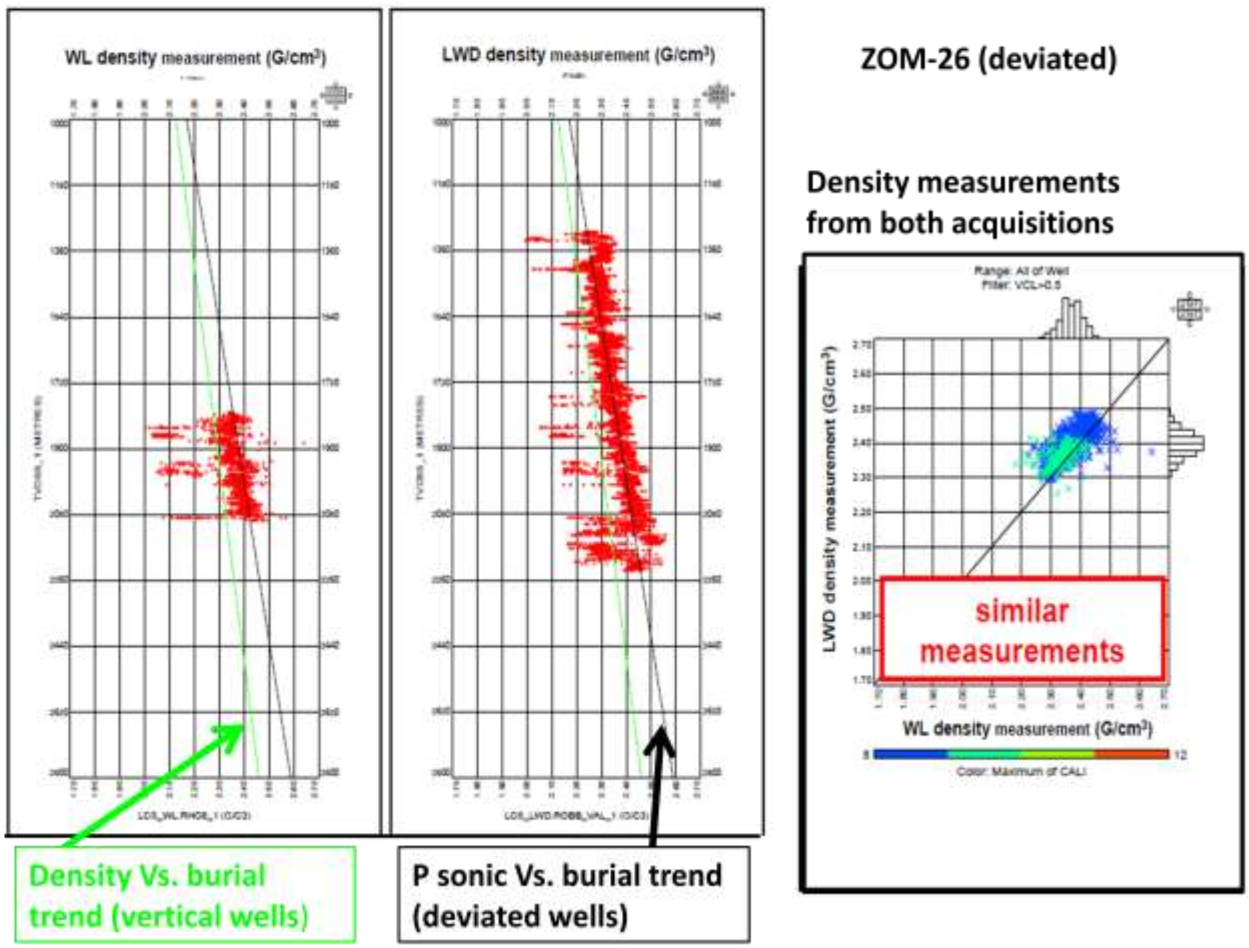

Figure 5.7: Density measurements (Wire Line and Logging While Drilling) from both acquisitions for well ZOM-26.

5.4 Pressure and Temperature Conditions

Temperature and pressure conditions are especially important in this study, since many wells are affected by fluid overpressure. It is therefore essential to give a description as precise as possible of pressure conditions in order to compute the effective pressure effect upon the rock frame. Pressure measurements are provided by Modular Formation Dynamic Testers (MDT), which are only used in reservoir facies. As a consequence, it is impossible for us to know the pressure in shaly environments, which another kind of uncertainty. To face this uncertainty, we have adopted the most natural way of determining the pressures in shales, that is to say linear interpolation between reservoirs where the pressure was known.

In many points, it appears that the effective pressure in shale can be different from that obtained from the linear interpolation between two consecutive Modular Formation Dynamic Testers (MDT) measurements from reservoir zones. A variation of the computed effective pressure in shales of plus or minus 30(+/- 30) bars was applied in order to fit with actual measurements.

For the current study, the effective pressure (directly linked to the effective stress) has been calculated by a difference between the geostatic and fluid pressures (Figure 5.8).

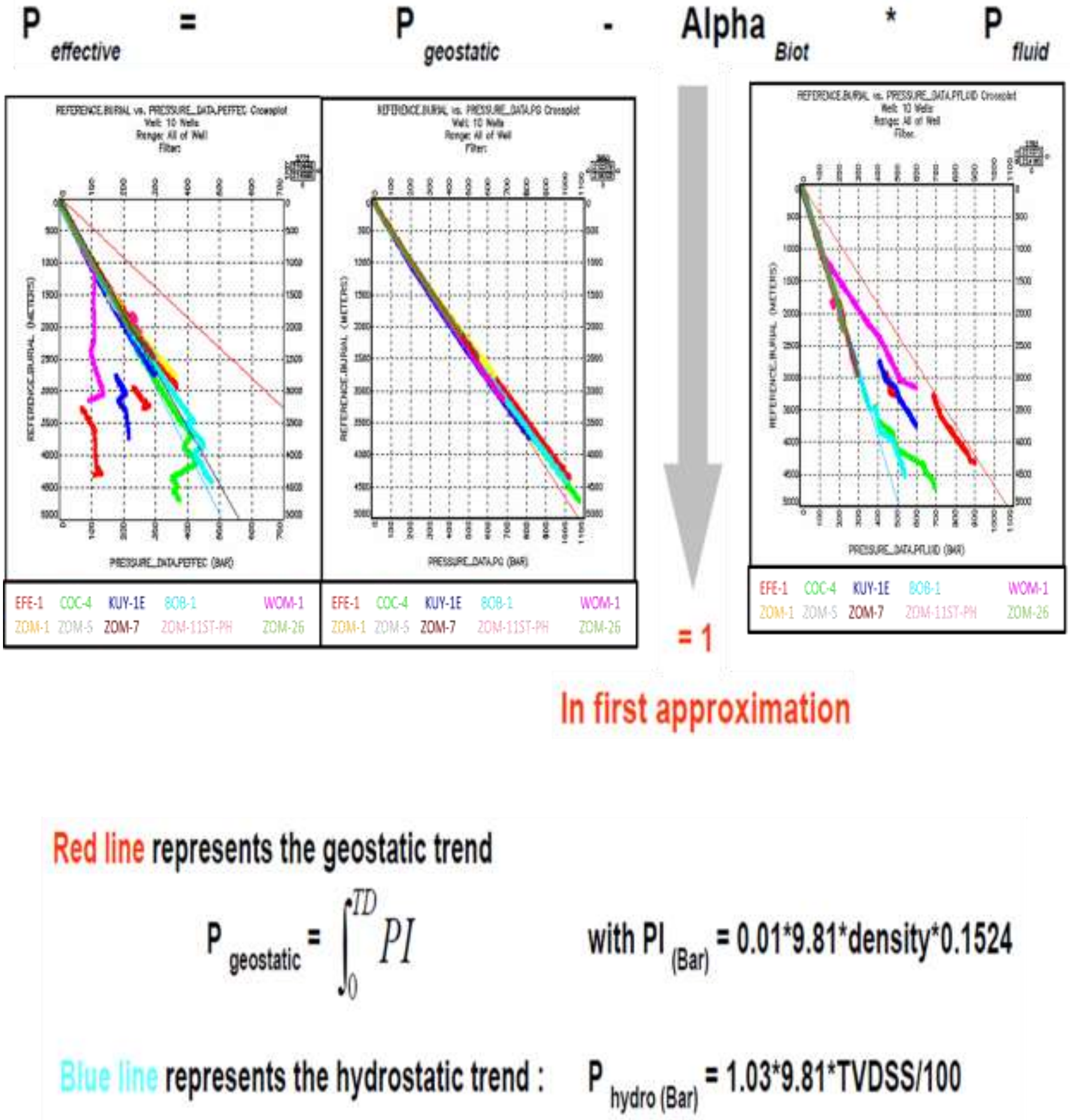

Figure 5.8: Effective pressure computations.

5.5 Fluid Description

Using the in-house software "BEST" the hydrocarbon elastic parameters have been computed with the PVT data.

The elastic parameters are the density, P velocity and thus compressibility modulus.

Connected to fluid pressure, temperature but also to hydrocarbon composition (which vary with depth), a constant value cannot be used for oil.

Knowing the water salinity (6-10g/l), fluid pressure and temperature, water elastic parameters have been computed using Baztle and Wang (1992). Because sensitivity of water incompressibility and water density to fluid pressure and temperature is not weak, a constant value cannot also be used for water (see section 2.3.3 for more details on how to compute elastic parameters using Baztle and Wang).

The inputs required for the Batzle and Wang (1992) calculation of fluid parameters are:

- Res. Temperature (C), Res. Pore Pressure (MPa)
- Brine salinity (ppm),
- Gas index for brine (0-1)
- Density of gas relative to air
- Oil gravity (API), Gas-oil-ratio (III).

The units of the calculated fluid parameters are *km/s* for velocities, GPa for moduli, and *g/cc* for density.

The computed elastic parameters of initial fluids have following values:

Brine incompressibility modulus: KWAT = 2.385 to 2.43 GPa (COC-4 & BOB-1)

= 2.534 to 2.556 GPa for all wells

Brine density: DWAT = 0.955 (g/c^3) (COC-4 & BOB-1)

= 0.984 to 0.991 g/c^3 for all other wells

HC incompressibility modulus: KHC = 0.065 to 0.663 GPa (ZOM-1)

= 0.431 GPa (ZOM-7)

= 0.1132 to 0.3621 GPa (COC-4)

= 0.1236 to 0.2293 GPa (BOB-1)

= 0.446 to 0.466 GPa (all others)

HC density: DHC = 0.198 to 0.701 g/c^3 (ZOM-1)

= 0.669 g/c^3 (ZOM-7)

= 0.3318 to 0.5276 GPa (COC-4)

= 0.3586 to 0.5189 GPa (BOB-1)

= 0.66 to 0.677 g/c^3 (all others)

Elastic parameters (water modelling-all wells): KWAT = 2.45 GPA

DWAT = 1.025 g/c^3

5.6 Fluid Effect Modelling with Gassmann's Equations

On Kuyolo field there are 2 lithologies (sand-shale) and 3 fluids (gas, light oil and water). In order to evaluate the fluid effect on elastic parameters, a fluid modelling has been done using Gassmann's equations (see chapter 2, section 2.3.5.1, and equations 53 - 63).

To obtain $K_{dry,}$ we first computed the in-situ effective bulk modulus of the rock with pore fluid, remembering that K = $\rho . V_p^2 - \frac{4}{3} . \mu$ and that μ= $\rho . V_s^2$, where V_p and V_s are the P and S velocities of the formation.

These values of K and μ are those of the rock saturated with initial pore fluid, a rock made of a mixture of sand and shale. To apply Gassmann's above equations, we only have to consider the sandy part of this mixture. Hence, it is necessary to know the distribution mode of shales (using crossplots such K-Vcl or Rhob-Nphi) in order to work on the effective bulk modulus of the sandy matrix.

Examination of crossplots on Figure 5.9 shows that all the wells of this study are characterized by laminated shales, what means that we pass from shales to sands through a system of less and less shaly laminas, and more and more sandy ones. To get the effective bulk modulus of the sandy part of the rock, we first have to "delaminate" sands from their clay content, using the fact that $K_{sand} = \frac{(1-V_{sh})}{\left[\left(\frac{1}{K}\right)-\left(\frac{V_{sh}}{K_{sh}}\right)\right]}$, V_{sh} being the clay content given by the petrophysicists, K_{sand} being the effective bulk modulus of the delaminated sands (which in this case is 38Gpa), and K_{sh} being the effective bulk modulus of shales calculated as a function of the effective pressure. Once the effective modulus of the delaminated sands is obtained, we then calculated the incompressibility of the initial in-situ fluid, which can be done using: $K_{fluid} = \frac{1}{\left(\frac{S_{we}}{K_w}+\frac{(1-S_{we})}{K_{Hc}}\right)}$,where S_{we} is the effective water saturation, K_w the effective bulk modulus of the in-situ water (used parameters are detailed in section 5.5 for water elastic parameters), and K_{hc} the effective bulk modulus of the in-situ hydrocarbon (used parameters are detailed in section 5.5 for hydrocarbon elastic parameters).

We then applied Gassmann's equation to find the effective bulk modulus of the dry rock:

$$K_{dry} = \frac{\left(\frac{K_{sand}}{K_{ma}-K_{sand}} - \frac{K_{fluid}}{\varphi_{sand}\times\left(K_{ma}-K_{fluid}\right)}\right)\times K_{ma}}{1+\frac{K_{sand}}{K_{ma}-K_{sand}} - \frac{K_{fluid}}{\left(\varphi_{sand}\times\left(K_{ma}-K_{fluid}\right)\right)}}$$

Having obtained the value of K_{dry}, we now substituted the initial in-situ fluids first by water and then calculated the associated effective bulk modulii, and thus obtained P and S velocities using Greenberg and Castagna equations of 1992 (section 2.3.5 of chapter 2 for details).

All the above procedures were carried out using in-house software known as Numerical Interpreter. The equations are set up by the successive subtraction of the effects from a first parameter then from the second parameters and so on (see appendix1: PEM equations for more details). It is necessary to have data at each step. Each parameter is subtracted in a precise order.

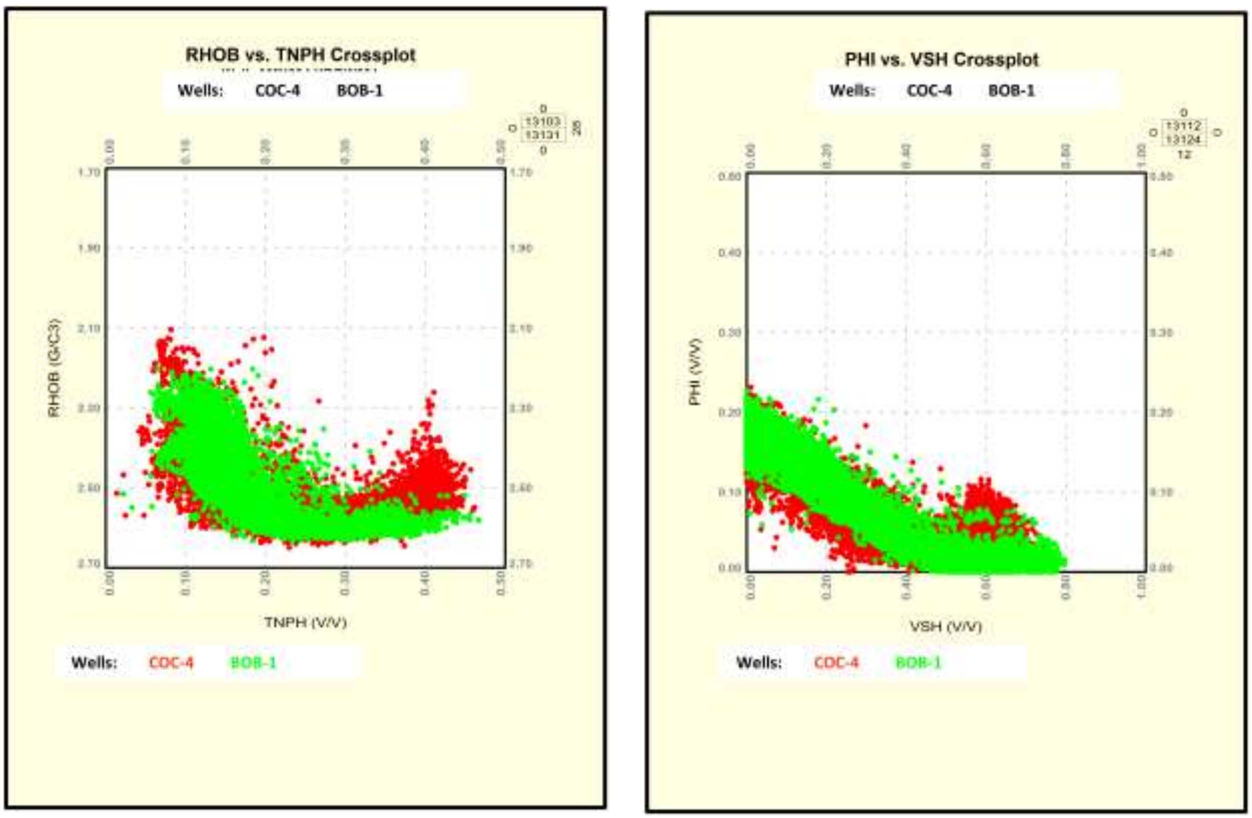

Figure 5.9: Sand – shale mixing model for wells COC- 4 and BOB - 1

5.7 Density Modelling and Comparison with Actual Measurements

RHOB is just an arithmetic average of the different individual constituents of the rock (clay, quartz) and fluid.

$$\text{RHOB} = V_{cl} \times RHOB_{clay} + \text{PHIE} \times [S_{we} \times RHOB_{water} + (1 - S_{we}) \times RHOB_{hc}] + (1 - V_{cl} - PHIE) \times RHOB_{quartz} \quad \text{.......} (77)$$

where:

$RHOB_{quartz}$ = 2.65 g/cm^3

$RHOB_{water}$ = refer to section 5.5 Fluid Description for fluid parameters

$RHOB_{hc}$ = hydrocarbon density provided by PVT analysis (refer to section 5.5 Fluid Description for fluid parameters)

$RHOB_{clay}$ = empirical law function of effective pressure

Remark: Assumption is made that shale is composed of 25% of quartz grains and 75% of clay.

5.8 Velocity Modelling and Comparison with Actual Measurements

P and S velocities are calculated with simulations of K and μ modulii and density by using equations 6, 7,53,54,55, 57,58,59,60,61,62,63 and 77.

The equations are set up by the successive subtraction of the effects from a first parameter then from the second parameter and so on. Each parameter is subtracted in a precise order.

Plates 1 to 9 illustrate the modelling results and measurements on all considered wells taken into account in this study. Actual measurements correspond to black curves, modelled logs with the Rock Physics Model (PEM) to red ones.

The relative deviations (modelling vs. measurement) are weak: About 6% for ‘P’ velocities, about 8% for ‘S’velocities and less than 3% on density.

5.9 Global Petroelastic Behaviour

This part aims at understanding, in a global manner, the connection between the petrophysical parameters of the rock (such as porosity, fluid saturation, etc.) and the way they are expressed through elasticity (P and S velocities, incompressibility modulus K etc.). Elastic quantities are particularly sensitive to porosity (volume, connectivity), fluid content (water, hydrocarbons), mineralogy (shaly part, diagenesis…), pressure and temperature (see above), texture of the mineral (arrangement of grains, porosity distribution), fracturation, seismic bandpass etc.

We first determined the global behaviours linking the different parameters listed above. To do so, we mainly focused on P and S velocities and on density (which are the main parameters involved in elastic calculations), which we considered as functions of effective pressure. From an elastic point of view, the global behaviour can be described through two fundamental variables, which are the incompressibility modulus (K) and the shear modulus (G). Considering density and velocities, we can compute the P impedance (IP) and the Poisson’s ratio (PR).

5.9.1 Density versus P sonic

Figures 5.10 to 5.12 represent, for each considered field, the respective positions of clean water sands and shales. Cross-plots are made with the modelled density after water substitution (RHOBSIMW) versus the modelled ‘P’ sonic (DTPSIMW), colour coded by well name or by lithology (sand in yellow, shales in green). Presented only are clean reservoirs (isolated by a cut-off applied on VCL<0.2) filled with 100% water in order to get rid of the fluid effect and shaly intervals (isolated by a cut-off applied on VCL>0.6). Straight lines represent the iso-impedance lines. For example, any point of the straight line located in the upper right hand corner of the crossplot, exhibits an impedance of 2. The more you move to the lower left hand corner, the higher the impedance. As a synthesis, Figure 5.13 shows the same cross-plots over all the 9 considered wells (except KUY-1E) colour coded by lithology (left hand side) and effective pressure (right hand side).

Results from the analysis of these cross-plots are:

- Generally good separation of shales and water sands.
- Shales globally present a homogeneous behaviour, their position being rather invariable over fields of OML 102 & 99, as well as isolated wells of EFE-2 & WOM-1.
- Clean reservoirs have also a comparable position over all considered well, whatever the fluid (all those cross-plots are made with actual density and sonics).
- Clean reservoirs and shales are aligned along two trends very close one from the other.

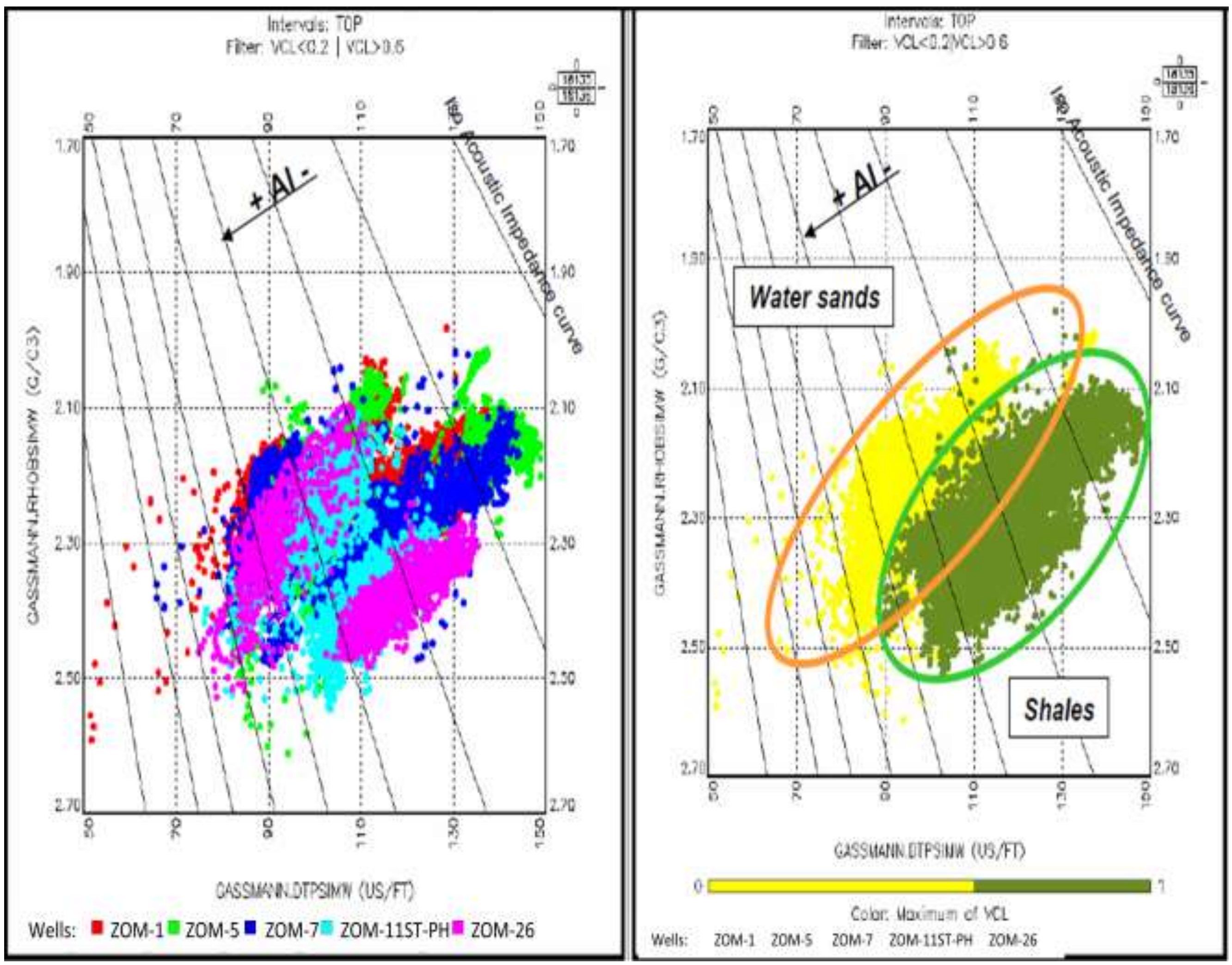

Figure 5.10: Petroelastic behaviour of density versus P sonic cross-plots for the field in OML 102 only. Water sands and shales are seen to be overlapping.

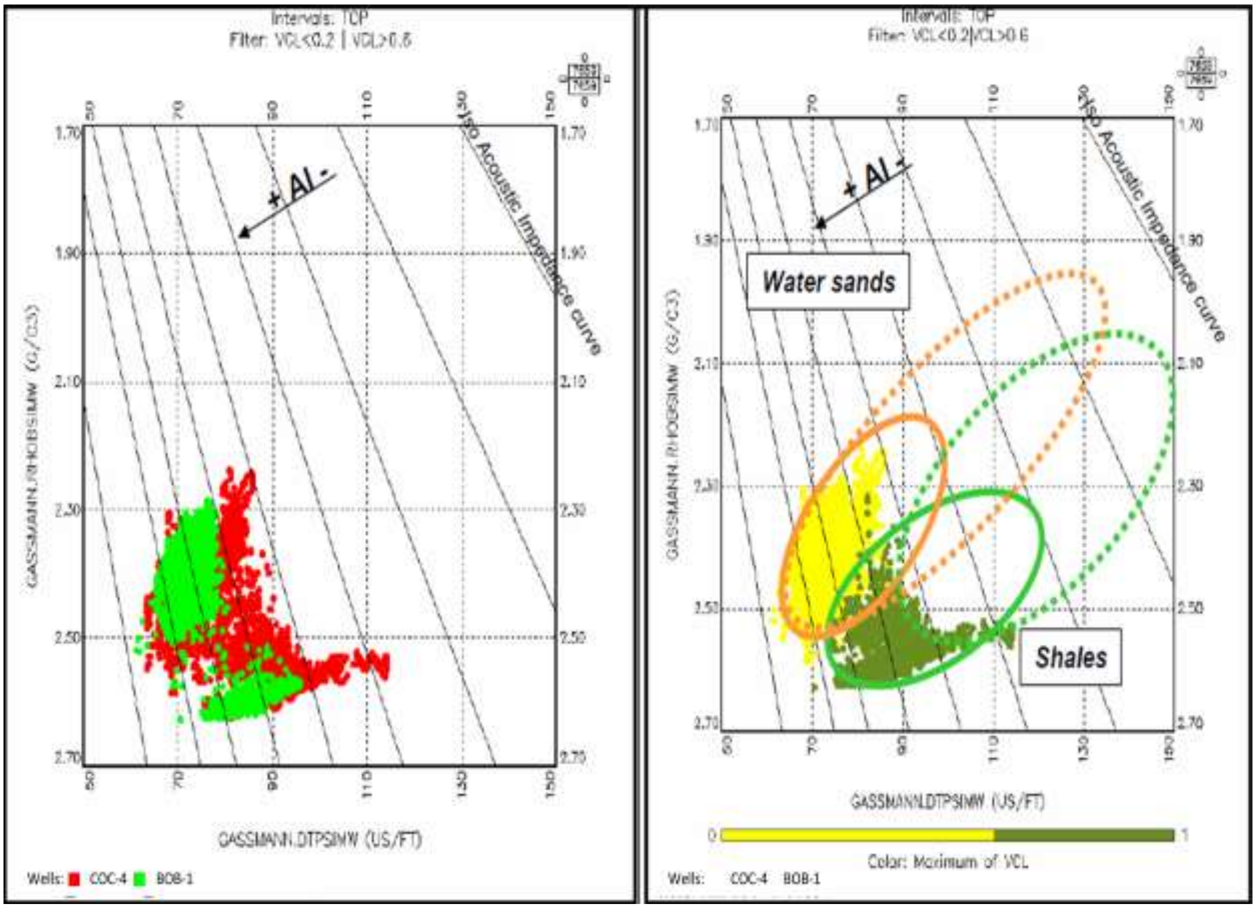

Figure 5.11: Petroelastic behaviour of density versus P sonic cross-plots for the field in OML 99 only. Good separation of water sands and shales. Water sands and shales are globally in the same trend than the field in OML 102 wells.

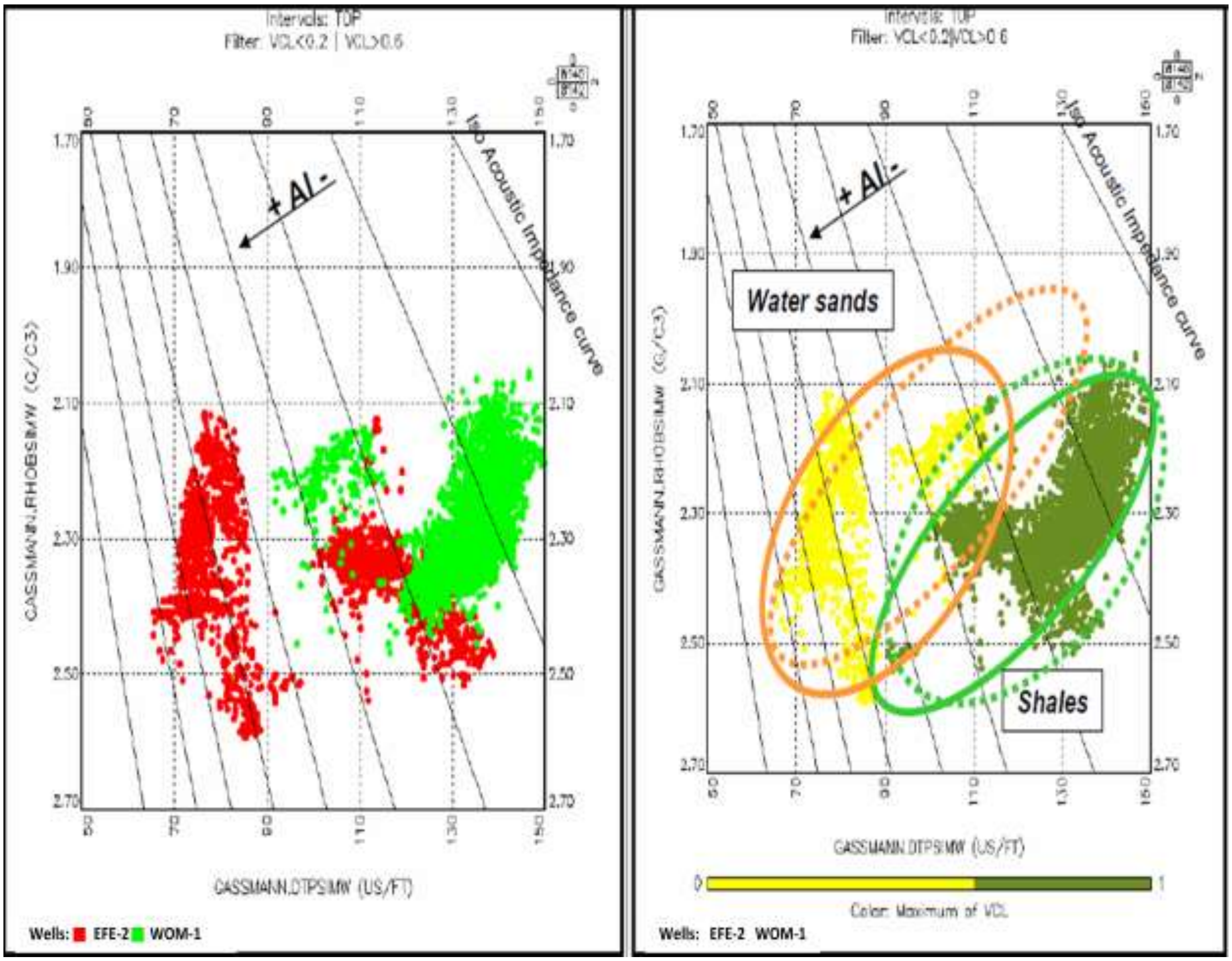

Figure 5.12: Petroelastic behaviour of density versus P sonic cross-plots for EFE-2 and WOM-1 wells. Good separation of water sands and shales. Water sands and shales are globally in the same trend than the field in OML's 102 and 99 wells.

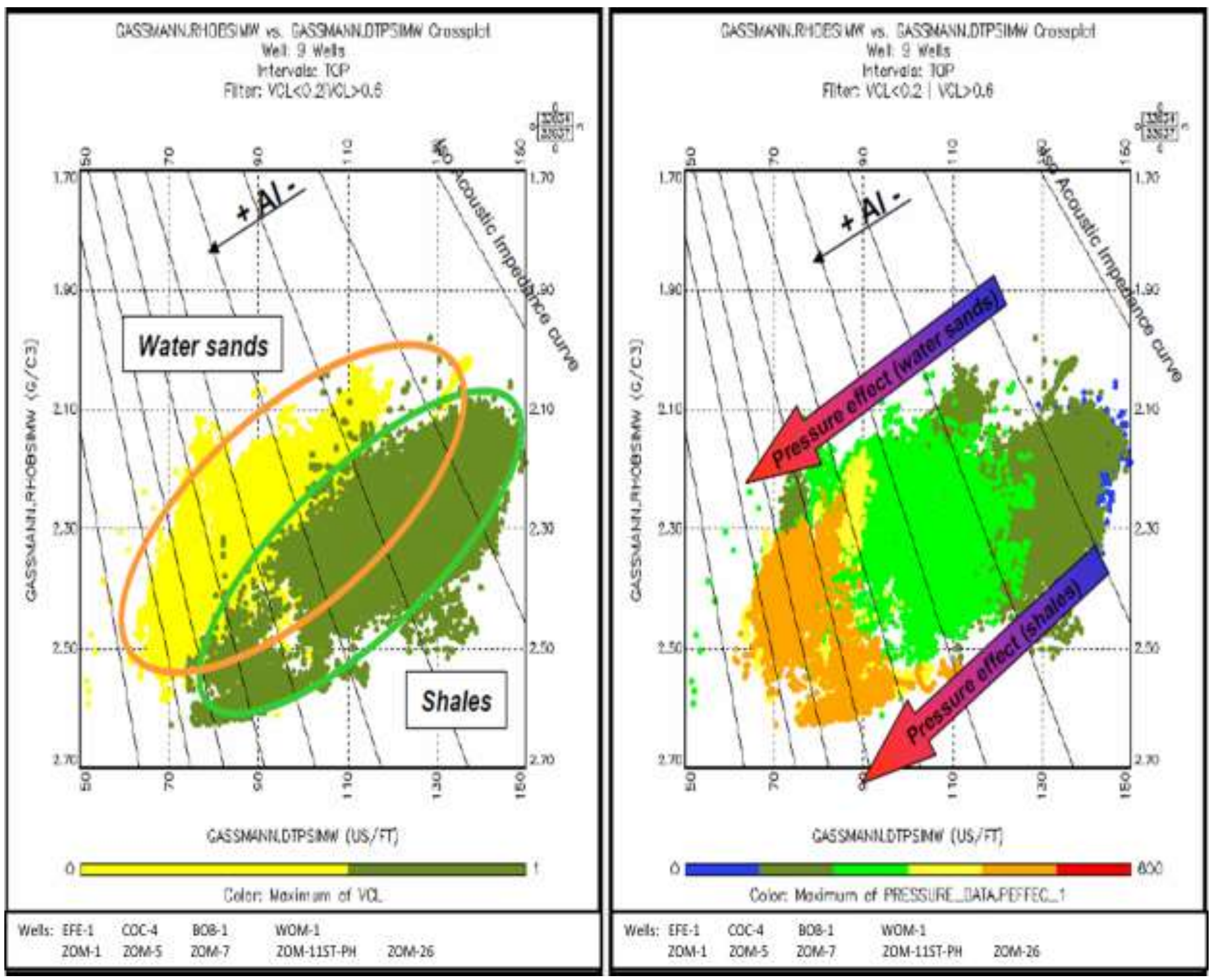

Figure 5.13: Cross-plots of density versus P sonic over all the 9 considered wells (except KUY-1E) colour coded by lithology (left hand side) and effective pressure (right hand side). Overall good separation of water sands and shales, water sands and shales are globally in the same trend versus effective pressure.

5.9.2 Poisson's ratio (PR) vs. Acoustic impedance (IP)

Figure 5.14 presents, over all considered wells with shear sonic data, the respective positions of clean water sands and shales. Crossplots made from water substitution results. The modelled Poisson's ratio (PRSIMW) is plotted versus the modelled 'P' impedance (IPSIMW). On the left hand side, this crossplot is colour coded by lithology (sand in yellow, shales in green), and colour coded by effective pressure on the right hand side. Presented only are clean reservoirs (isolated by a cut-off applied on VCL<0.2) and shaly intervals (isolated by a cut-off applied on VCL>0.6). Results from the analysis of these crossplots are:

- Overall rather good organization of all reservoirs and shales along a common trend for each lithology.
- Clean reservoirs have a normal scattering regarding the fluid content (water or oil bearing sands).
- The majority of sands is iso-impedant to shales or slightly more impedant than shales for a given value of effective pressure, whatever the effective pressure (i.e., roughly, whatever the burial, except for overpressured zones).
- Clean reservoirs and shales are aligned along two trends very close one from the other. From a Poisson's ratio point of view, less under compacted sands (i.e. with small effective pressure) have a Poisson's ratio of the order of the one of shales, while sands whose effective pressure is more important have a Poisson's ratio following a homogeneous trend rather parallel, but superior to the one of shales. These sands are globally softer than shales, but follow the same kind of compaction law. Such sands should give AVA anomalies.

To conclude with, the global behaviour of shales is rather homogeneous on all the wells. This is encouraging since it provides us a reference which will be valid for the whole study.

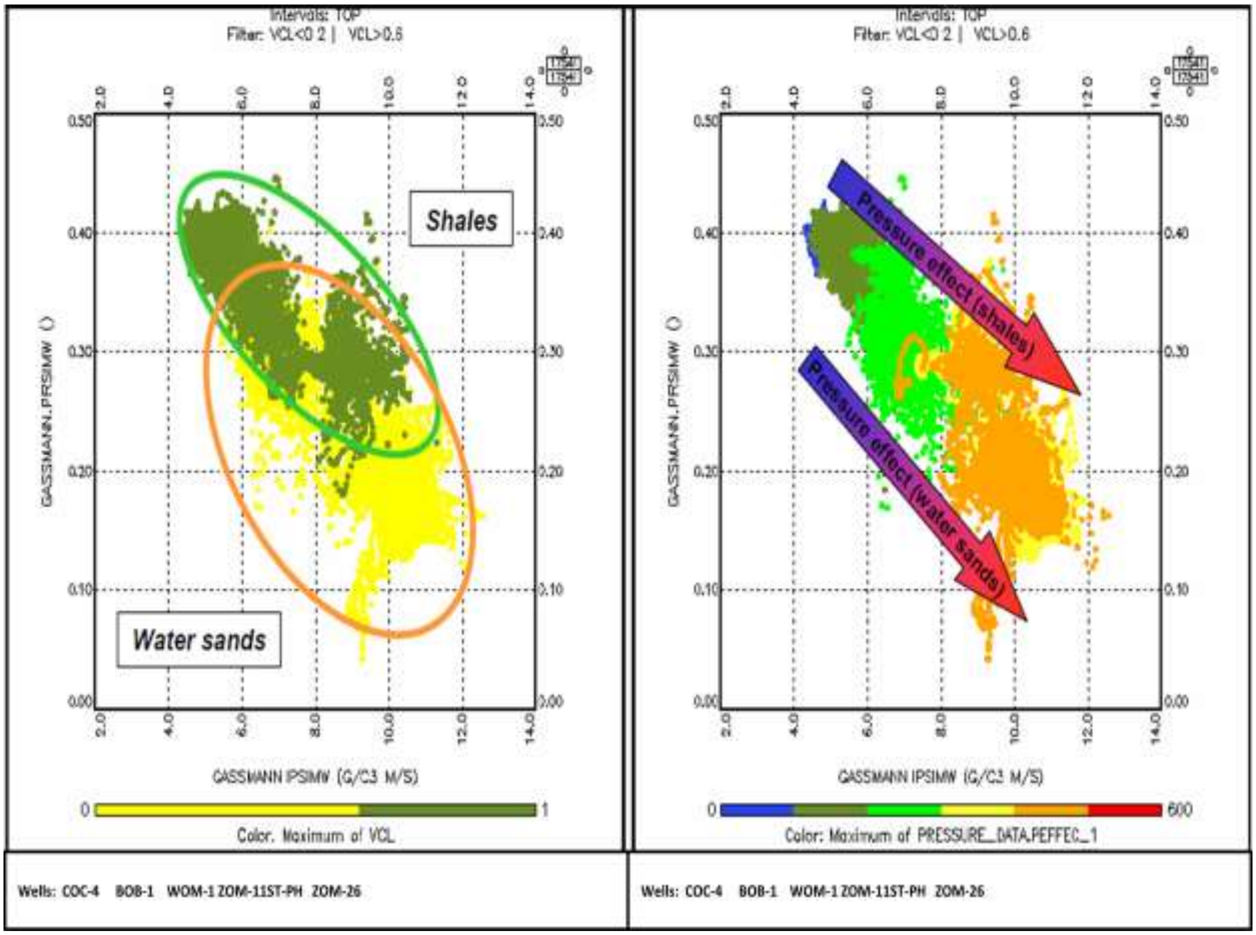

Figure 5.14: Cross-plot of P impedance versus Poisson's ratio for all the wells with sonic data. Overall good separation of water sands and shales, water sands and shales are globally in the same trend versus effective pressure.

5.10 Application of this Rock Physics Model (PEM) on KUY-1E

Plate 10 presents the modelling results on KUY-1E (actual measurements correspond to black curves, modelled logs with the Rock Physics Model (PEM) to red ones). The first observation shows that the modelling seems to be accurate for the density and velocities (P &S).

Generally speaking, results are relatively similar over all wells. Trends and variations of density and velocities are correctly modelled, especially in clean reservoirs (whatever the fluid). The relative deviations (modelling versus measurement) are weak: about 6% for ‘P’ velocities, about 8% for ‘S’velocities and less than 3% on density (Figure 5.15).

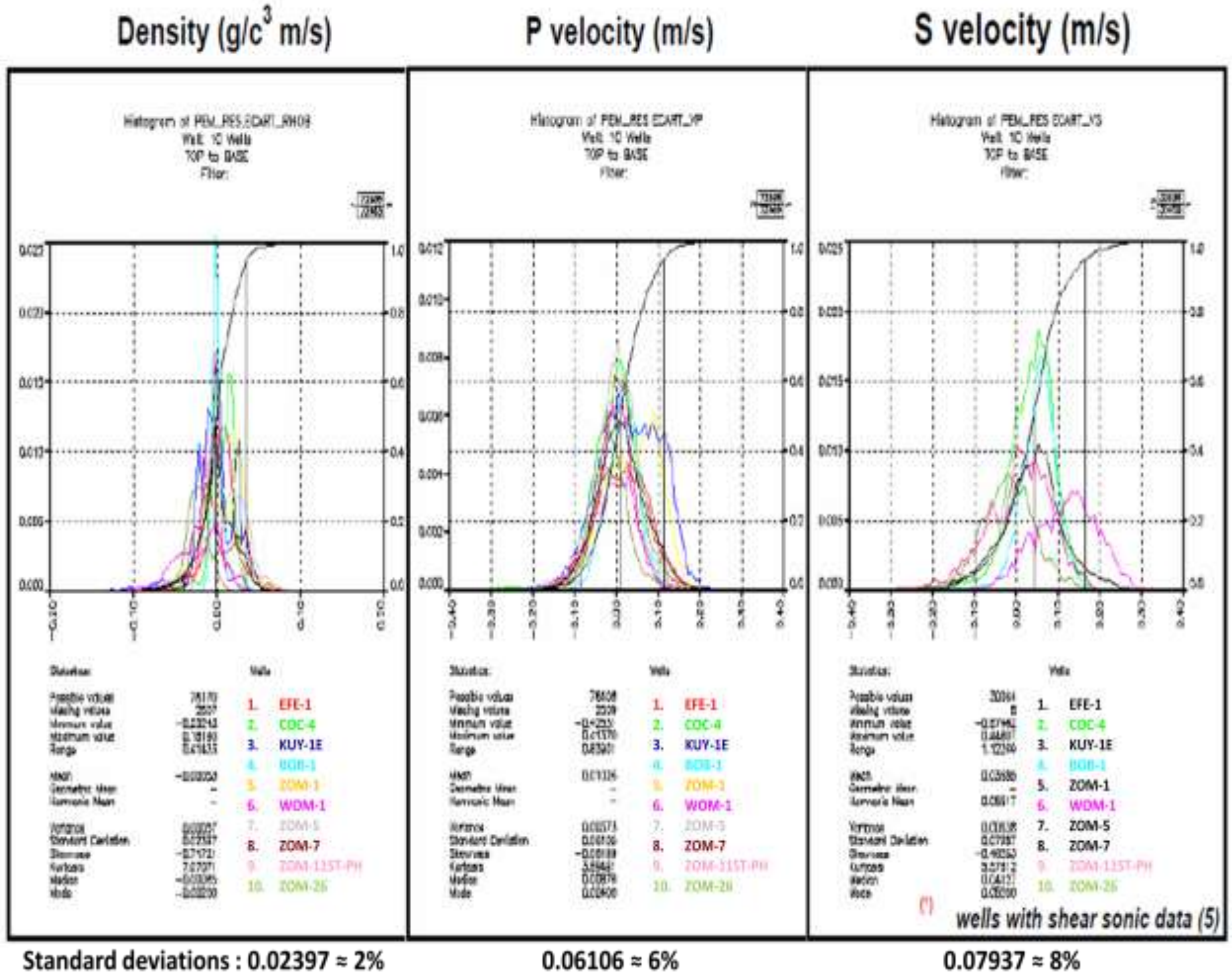

Figure 5.15: Relative deviations between modelled and measured density and velocities for all the ten wells used in this study.

5.10.1 Global Behaviour of Water Sands and Shales on KUY-1E using the Rock Physics Model (PEM)

Figure 5.16 represent, for KUY-1E well, the respective positions of clean water sands and shales. Cross-plots are made with the modelled density after water substitution (RHOBSIMW) versus the modelled ‘P’ sonic (DTPSIMW), colour coded by lithology (sand in yellow, shales in green). Presented only are clean reservoirs (isolated by a cut-off applied on VCL<0.2) filled with 100% water in order to get rid of the fluid effect and shaly intervals (isolated by a cut-off applied on VCL>0.6). Straight lines represent the iso-impedance lines. For example, any point of the straight line located in the upper right hand corner of the crossplot, exhibits an impedance of 2. The more you move to the lower left hand corner, the higher the impedance. Results from the analysis of this cross-plot shows that the behaviour of shales from this well is a bit different in that the separation between these poles (water sands and shales) is less clear compared to that from the other wells from fields in OML’s 70, 99 and 102 blocks (see section 5.9.1). Water sands and shales are seen to be overlapping making it difficult for us to discriminate our sands from shales. Main reasons for this are the presence of important washout and strong overpressures on this well that affected both the density and sonic log measurements.

In spite of the difficulties encountered in the building of the Petroelastic/rock physics model (linking the petrophysical parameters to the elastic properties of the rock), there were overall good separation of sands from shales giving us confidence that AVO Seismofacies methodology could be used to characterize the reservoirs.

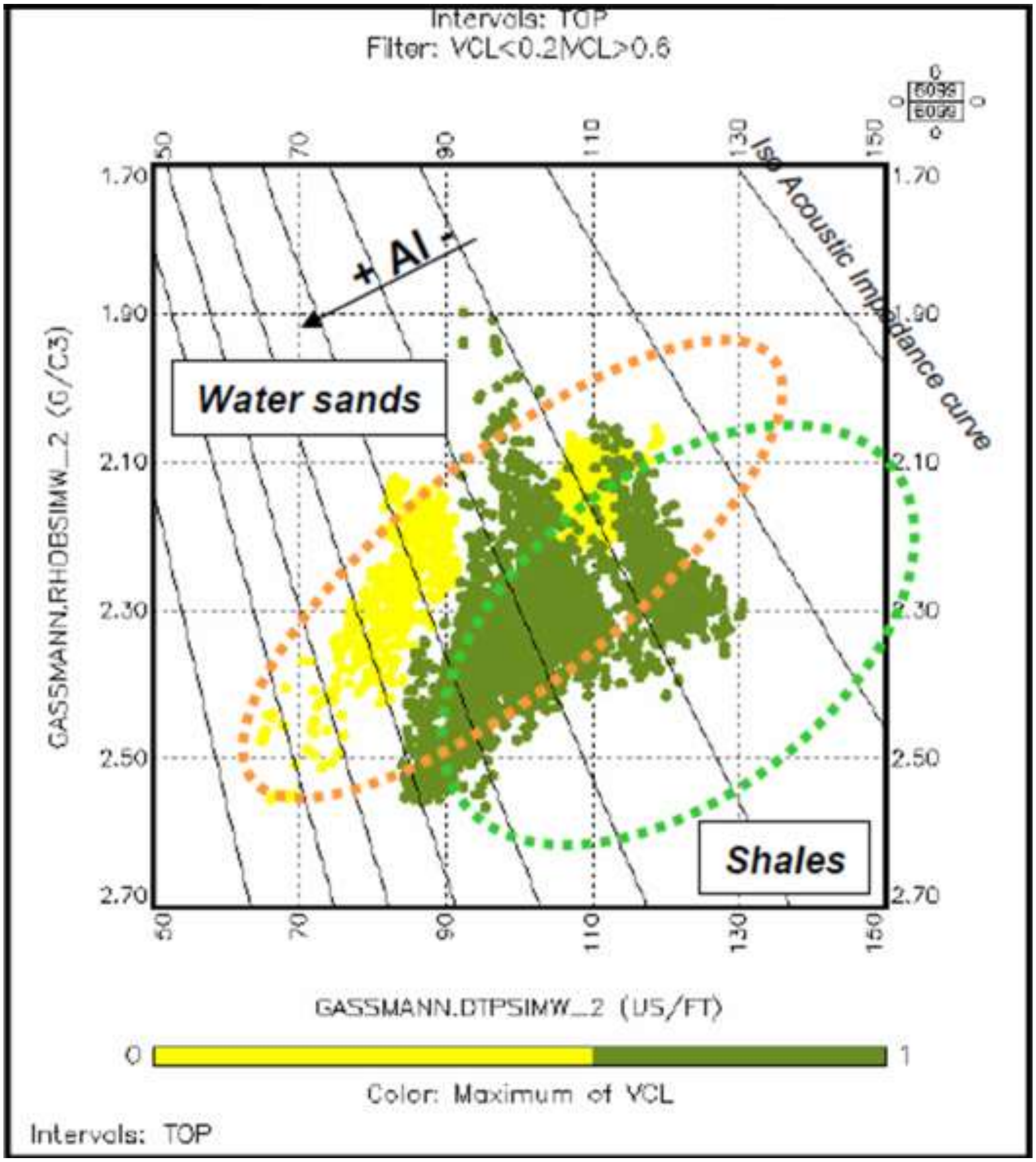

Figure 5.16: Cross-plot of modelled density versus the modelled 'P' sonic, colour coded by lithology. Water sands and shales are difficult to separate and not in the same trend than that from OML's 70, 99 and 102 wells. Density log is questionable (washouts).

CHAPTER SIX

AVO SEISMOFACIES STUDY

6.0 Introduction to AVO Seismofacies Study

AVO Seismofacies combines two angle sub-stacks to create a third cube, AVO Seismofacies cube showing the differences from a reference/background trend. It accounts for expected Amplitude Variation with Angle (AVA) effects and use information only from angle sub-stacks and does not need a petrophysical a priori that would be difficult to establish (no shear information, large missing parts of sonic and density, difficult well-to-seismic calibration). It is displayed with a specific colour scale or with values closely related to Poisson's Ratio (PR) variations; the white zones generally correspond to shale or wet sand (background/reference), a blue event shows a Poisson's Ratio (PR) decrease which can be interpreted as possible onset of an hydrocarbon bearing reservoir, a yellow-red event shows a Poisson's Ratio (PR) increase which can be interpreted as either the offset of an hydrocarbon reservoir or a fluid contact.

6.1 AVO Seismofacies Seismic Data QC

Analyzing AVO supposes to have Near and Far cubes that are not clipped and that are almost zero-phase. This is done in Sismage software using the clipping QC and the phase QC tools.

6.1.1 Clipping QC

The clipping is a cut-off artificially applied on the amplitudes of a seismic block. It occurs during the data loading while storing the samples in a reduced format structure (from 32 bits to 16 bits). The shape of the waveform is not preserved and the amplitudes are artificially truncated. It is easy to understand the impact of such a phenomenon on the AVO effect. The AVO effect can be lost or artificially boosted by truncation of amplitudes. Regarding the present study, clipping detection was computed around R11 reservoir for each angle stack in a time window ranging from 2100-3300ms TWT. The output maps showed that none of the angle stack cube was clipped.

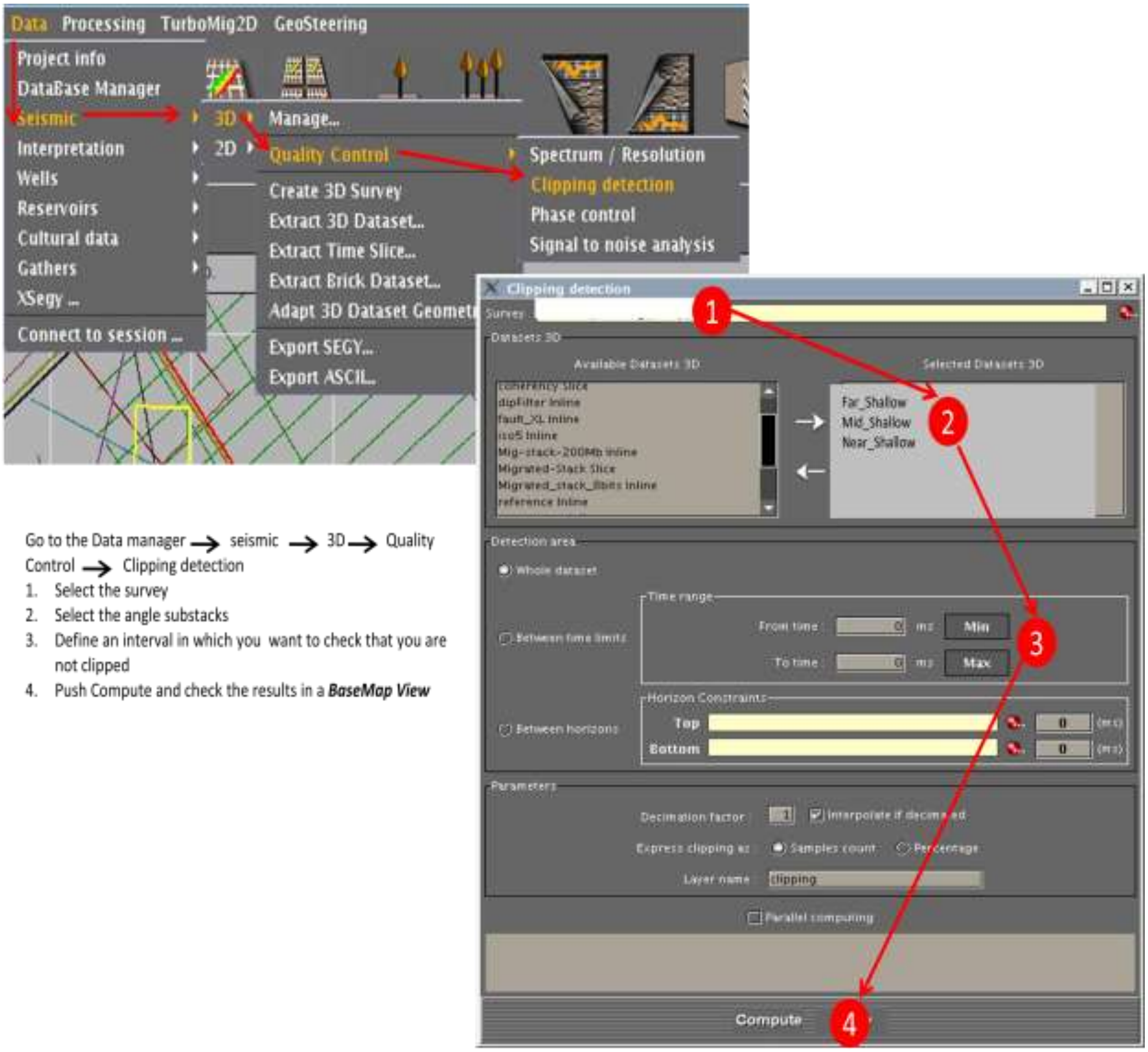

Figure 6.0: Sismage interface for clipping QC

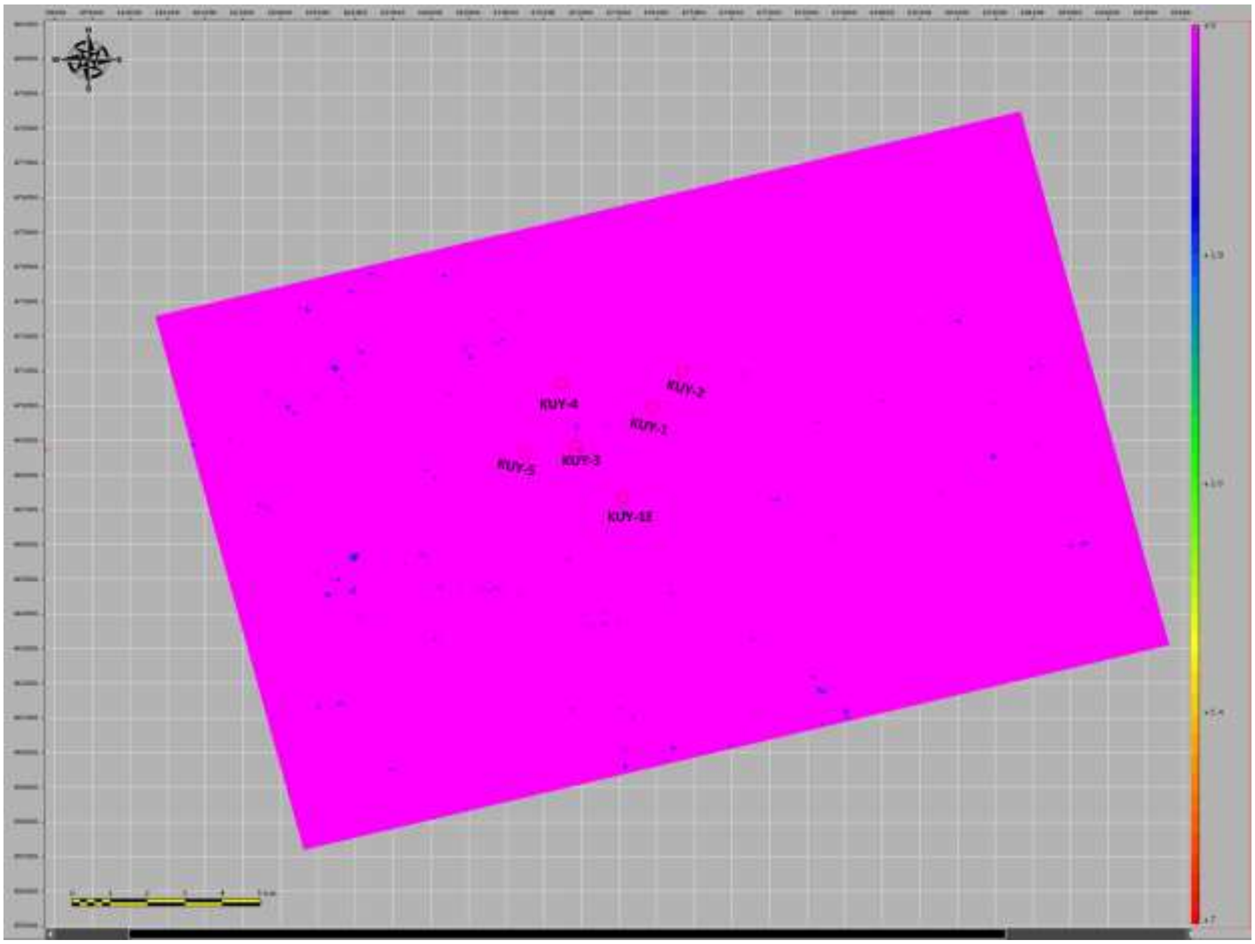

Figure 6.1: Clipping detection analyses for the Near cube

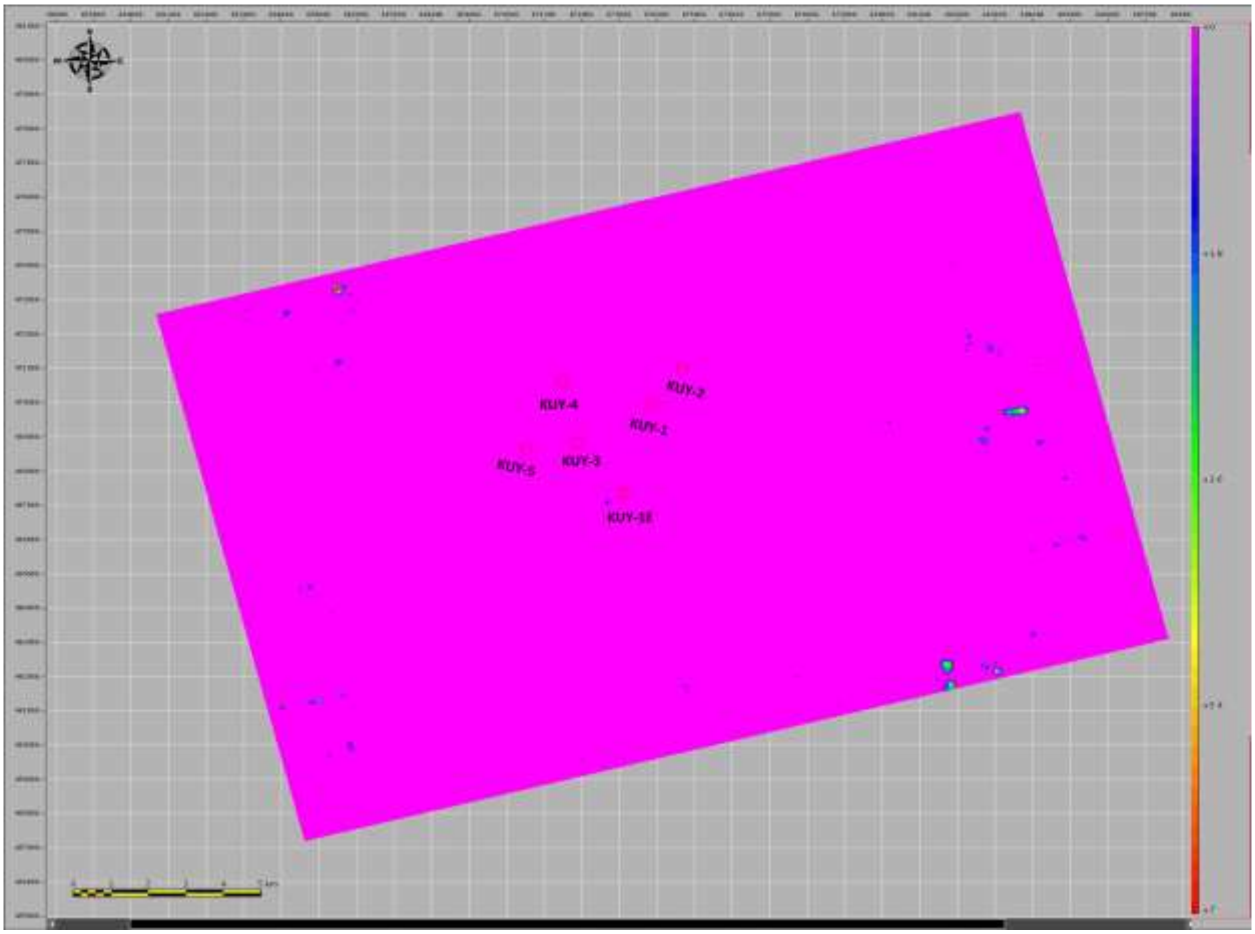

Figure 6.2: Clipping detection analyses for the Mid cube

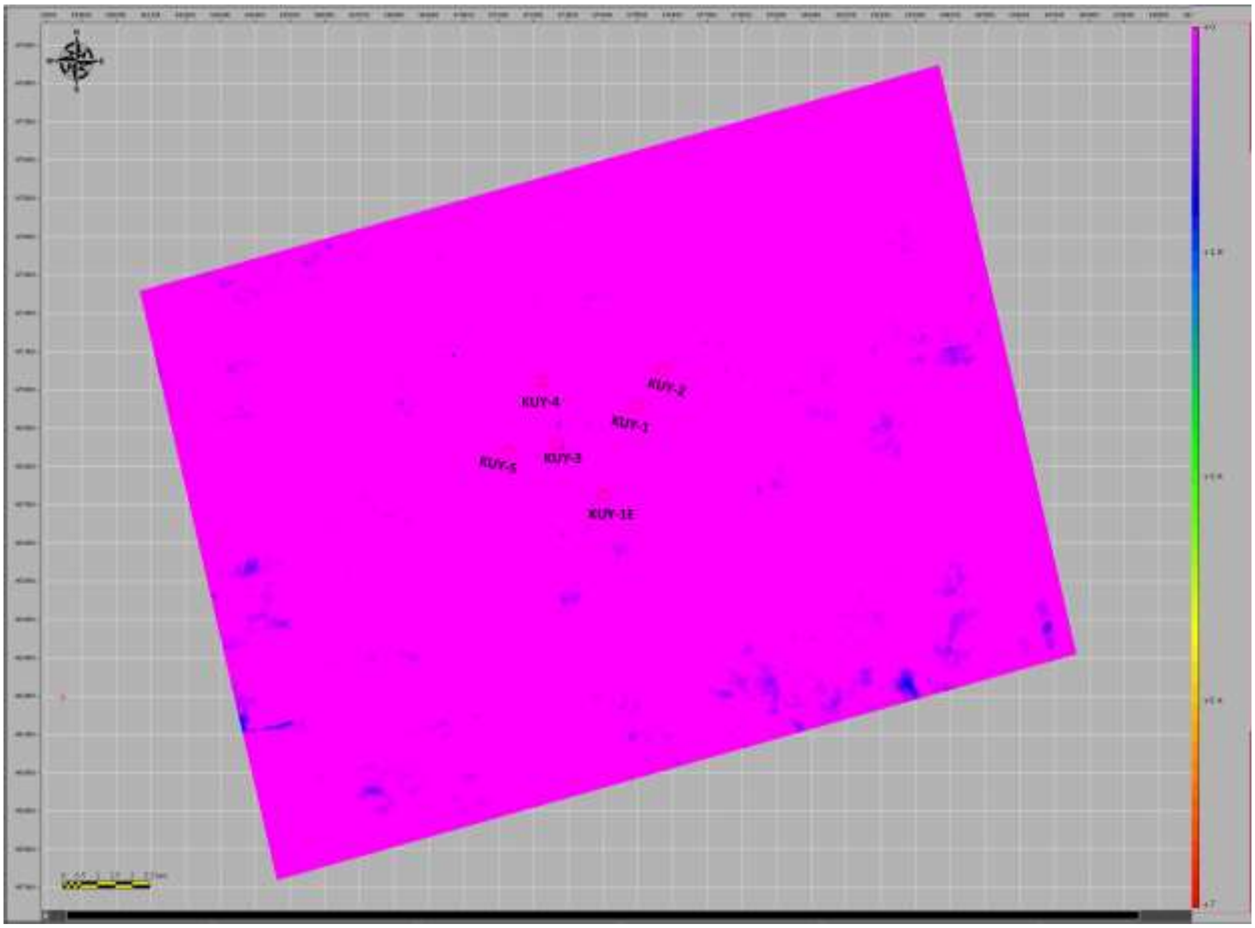

Figure 6.3: Clipping detection analyses for the Far cube

6.1.2 Phase QC

The idea here is to check that the seismic phase is almost zero-phase on both the Near and Far angle stack cubes. To do this, one can carry out some CAL5D calibration, estimate the instantaneous phase along an isolated and energetic seismic event with known polarity that is not tuned or use seabed if present. Signal is presumed to be zero - phased if computed phase is between -30^0 and $+30^0$. In our case, since seabed was not present on the data (see Figure 6.4). A well-to-seismic calibration was done on KUY-4 well not just for phase QC but also for hydrocarbon purposes on each of the angle stacks using CAL5D algorithm (Figure 6.5). The computed phase is about -25 degrees (see Table 7). This phase is not far to zero and we left it as it is.

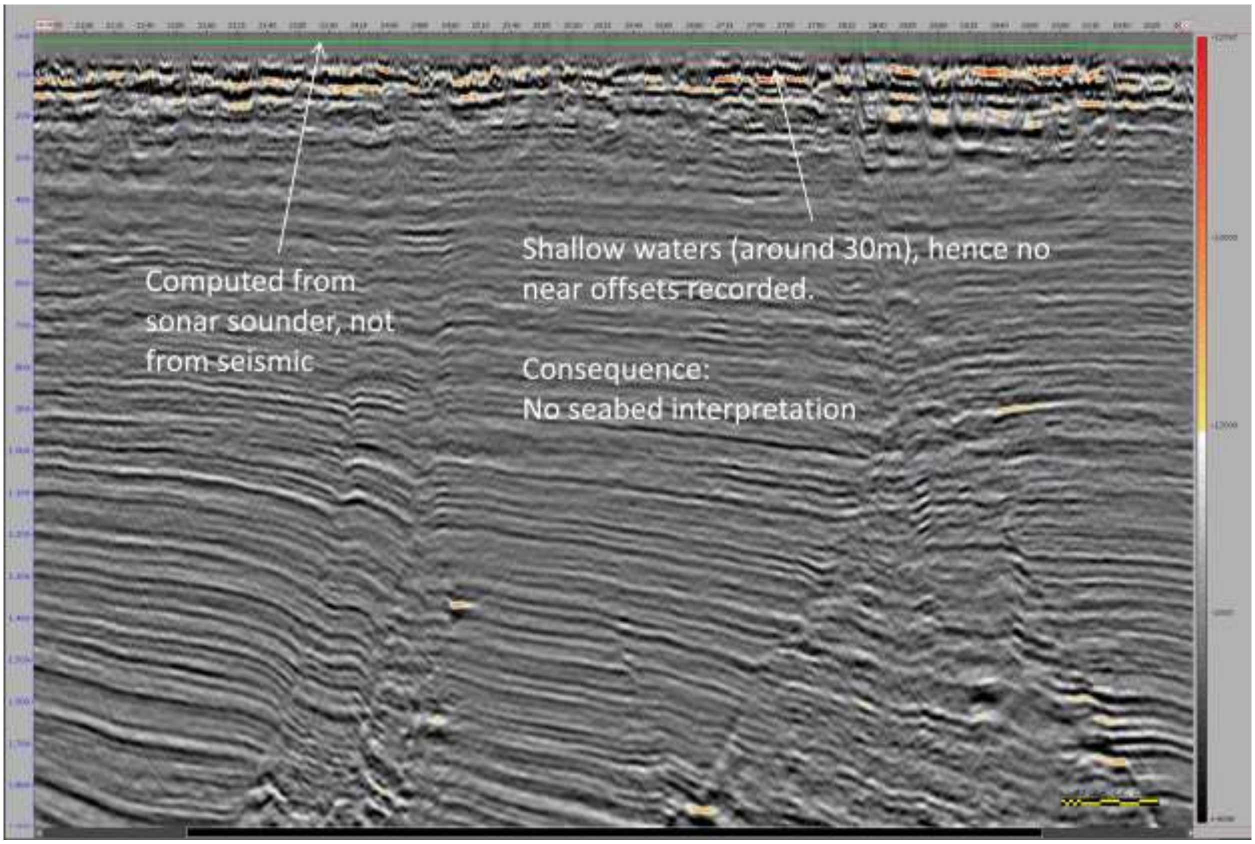

Figure 6.4: Cross section showing that seabed was not present over the studied area.

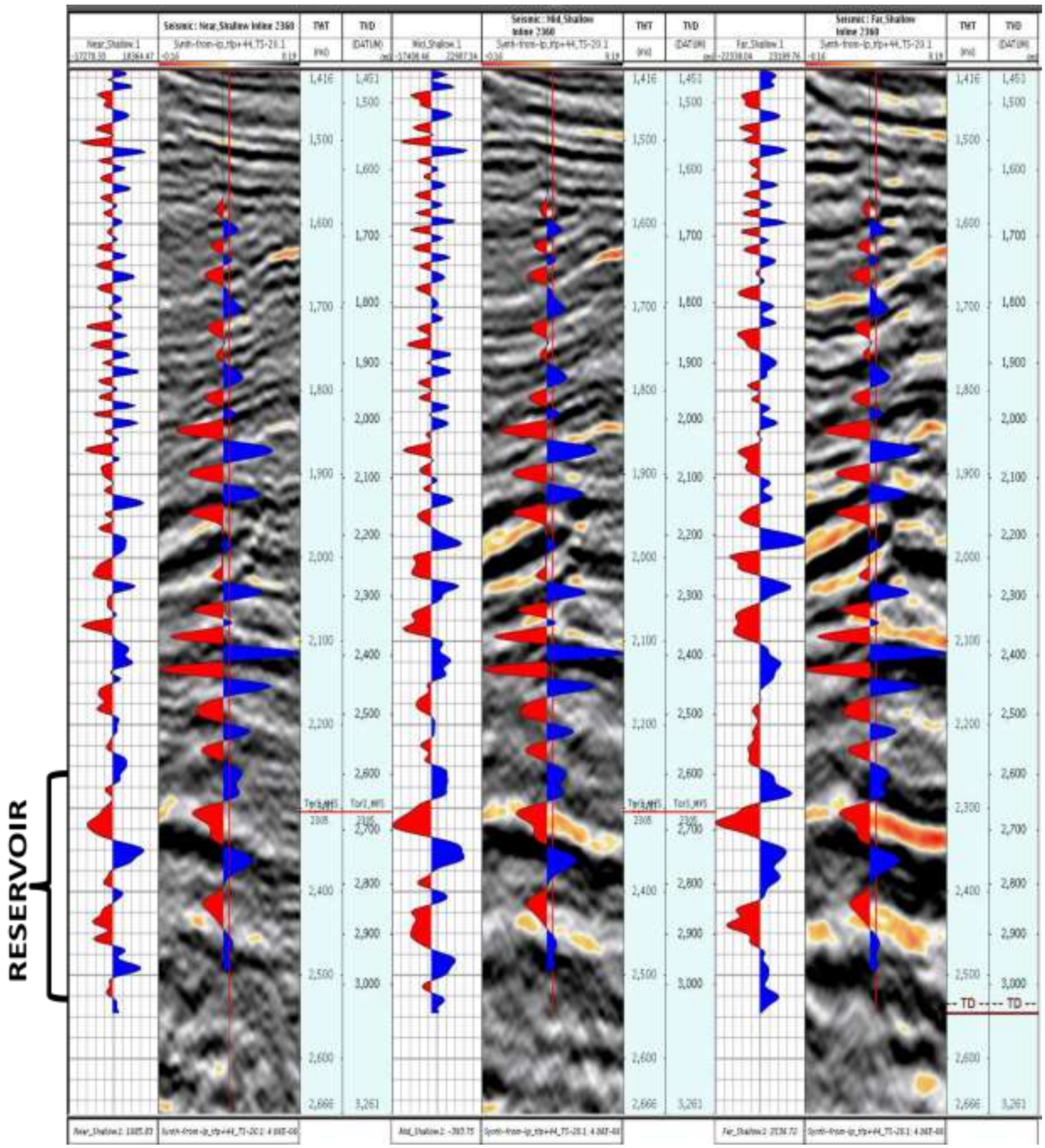

Figure 6.5: KUY-4 well-to-seismic tie on the Near, Mid and Far cubes used for phase QC.

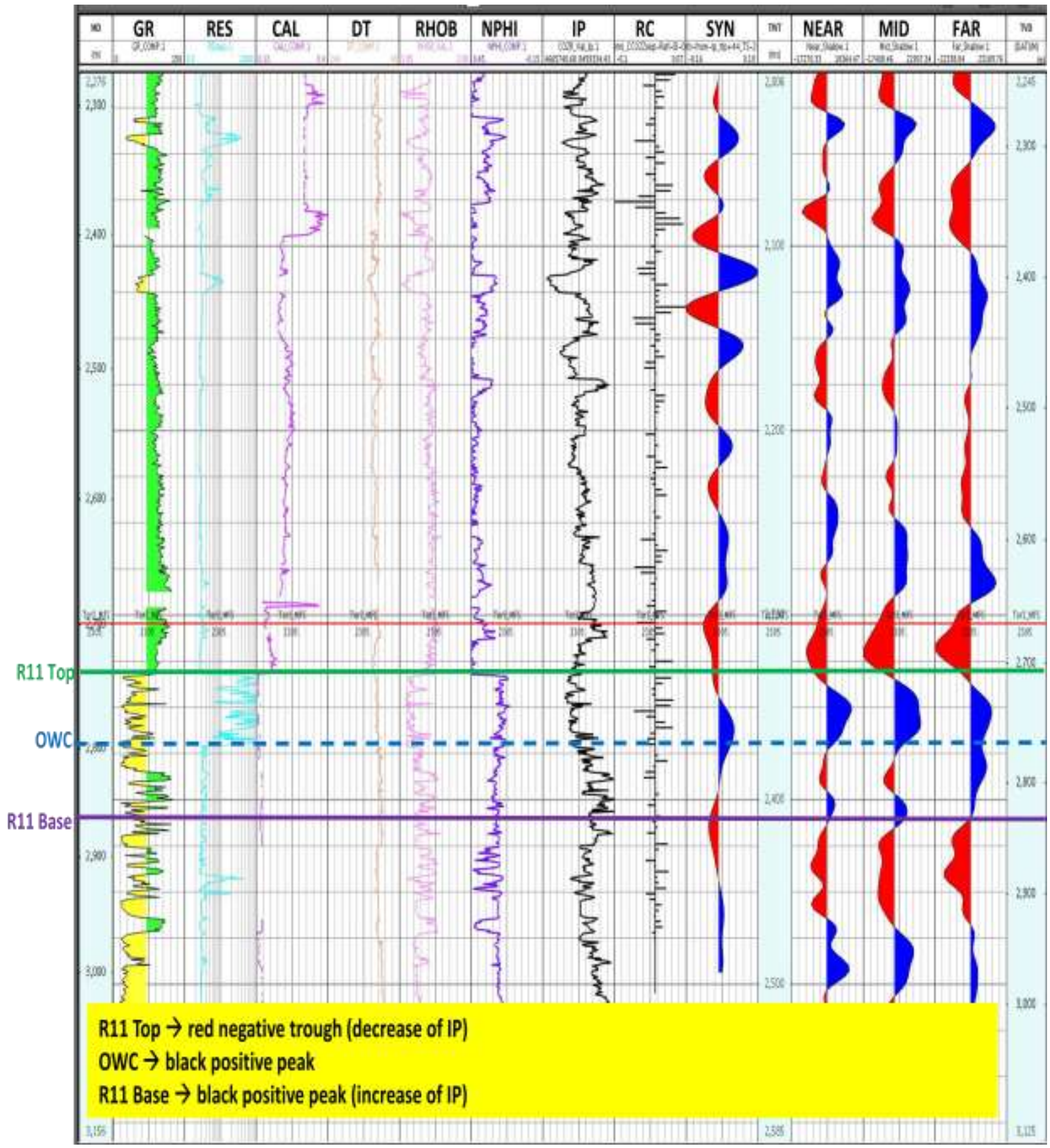

Figure 6.6: KUY-4 well logs together with the synthetic trace and angle substacks used for phase QC.

6.2 Proposed Sub-stack Pair Choice and Initial Cross-Correlation before Common Bandwidth Filtering

The idea here was to test each pair (Near-Mid, Mid-Far and Near-Far), since we have more than two available angle sub-stacks. The output is an estimate of quality control (QC) attribute maps used to compare the angle sub-stack pair. These output maps would give us an idea of the cross-correlation between Near and Far, stretch between Near and Far, resolution of Near and Far, root mean square (RMS) amplitudes of Near and Far, time and phase shifts between Near and Far. Cross-correlation maps are used to measure the confidence level of the AVO Seismofacies. If one obtains a good correlation and a time-shift map near zero for high correlation, it is not necessary to shift the Far cube. However, if one obtains a bad correlation (lower than 50%), it might be necessary to shift the Far cube to adjust it on the Near cube in order to improve the correlation.

We first computed for the original/raw pair around R11 reservoir in a time window ranging from 2100-3300ms TWT (see hereunder).

1. Insert the pair of substacks chosen (Near – Mid, Mid – Far & Near – Far).

2. Choose the interval of computation (2100 – 3300ms TWT).

3. Select the maps you want to compute (RMS amplitude Near, RMS amplitude Far, Near resolution, Far resolution and Far/Near Stretch.

4. Define the output Layer Name

5. Compute

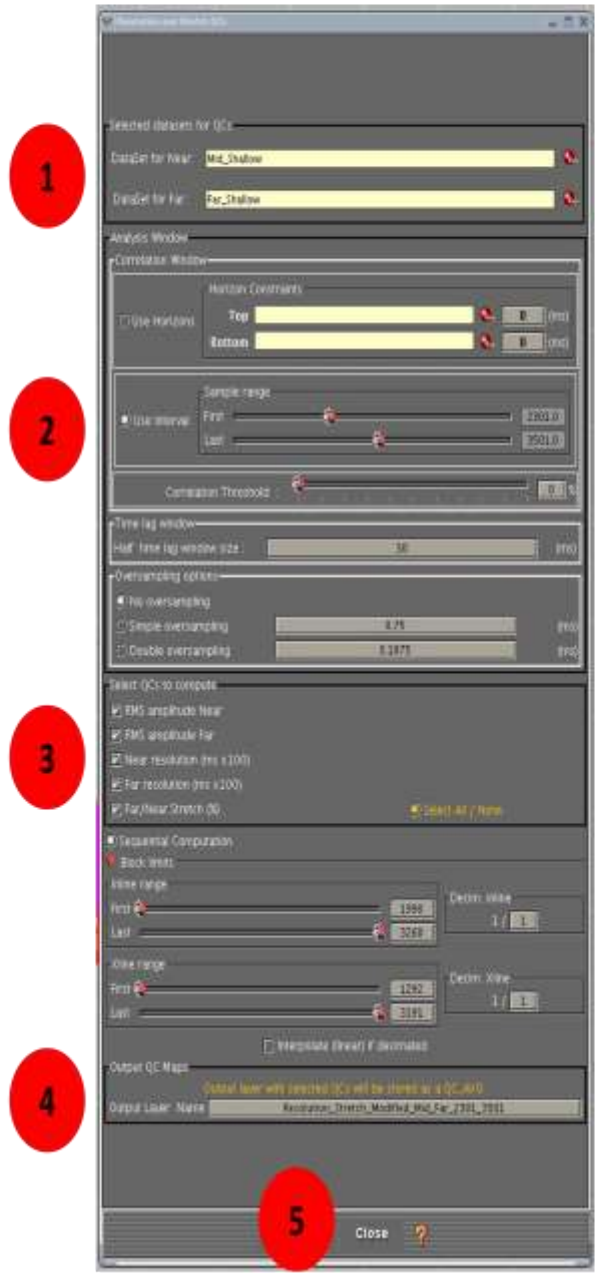

Figure 6.7: Dialog for resolution and stretch QCs

1. Insert the pair of substacks chosen (Near – Mid, Mid – Far & Near – Far).
2. Choose the interval of computation (2100 – 3300ms TWT).
3. Select the maps you want to compute (RMS amplitude Near, RMS amplitude Far, correlation envelope, phase- shift envelope and time-shift envelope)
4. Compute

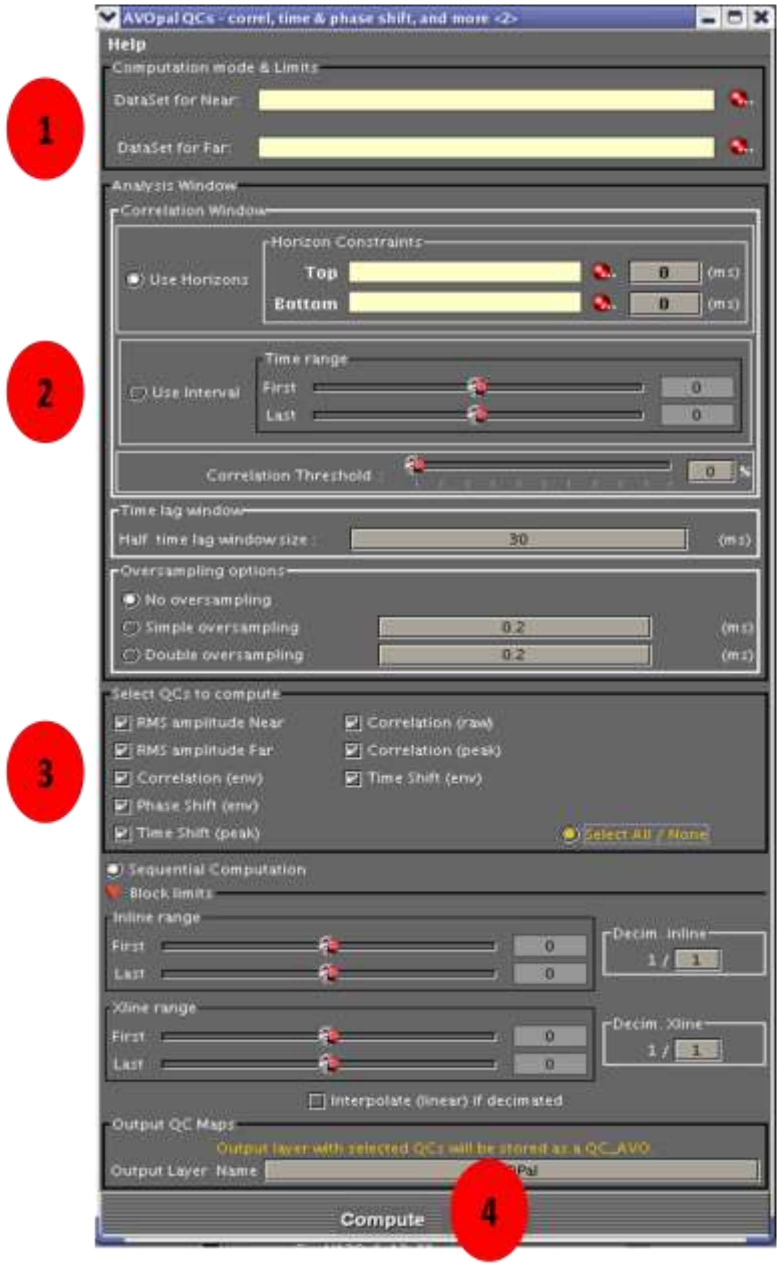

Figure 6.8: Dialog box for correlation, RMS amplitudes, time and phase shift QCs

6.2.1 Original/Raw Near - Mid Pair

An estimate of quality control attribute maps (correlation, RMS amplitudes, resolution, stretch factor, phase and time shifts) were computed around the studied AVO interval for this combination using the original/ raw Near and Mid substacks. The analysis of this result showed a satisfactory level of correlation between Near and Mid with a good homogeneity of the map. The median (average) value for correlation was 71%. There was also good homogeneity of the stretch between Near and Mid with an average stretch value of 107%. The average root mean square (RMS) amplitudes and resolution computed within the reservoir window was quite similar on the Near and Mid substacks. The computed resolution for the Near was 26ms while that of the Far was 28ms.Time and phase shifts between Near and Mid were reasonable and close to zero. No time or phase shift was needed.

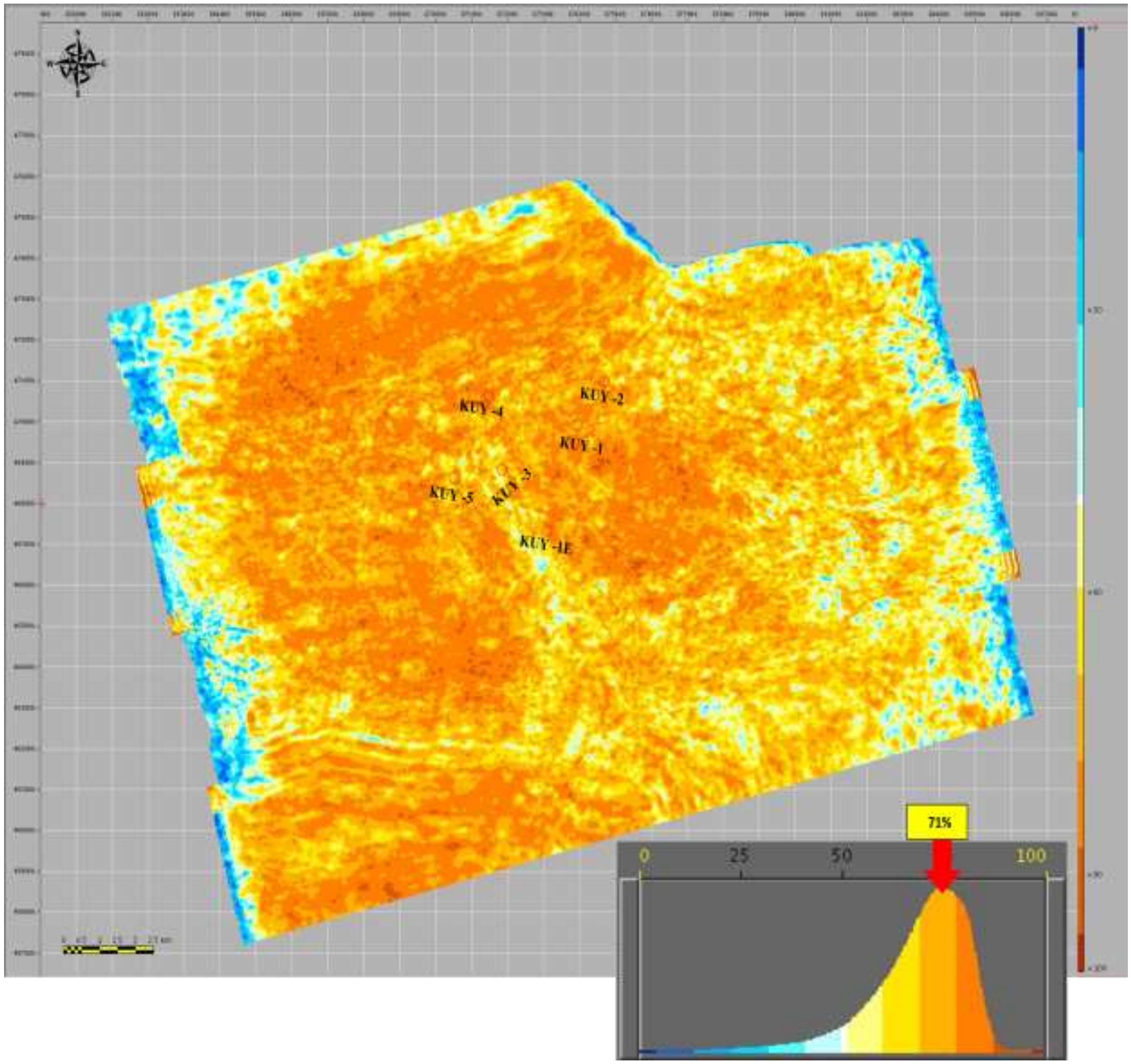

Figure 6.9: Cross-correlation map of Near-Mid pair

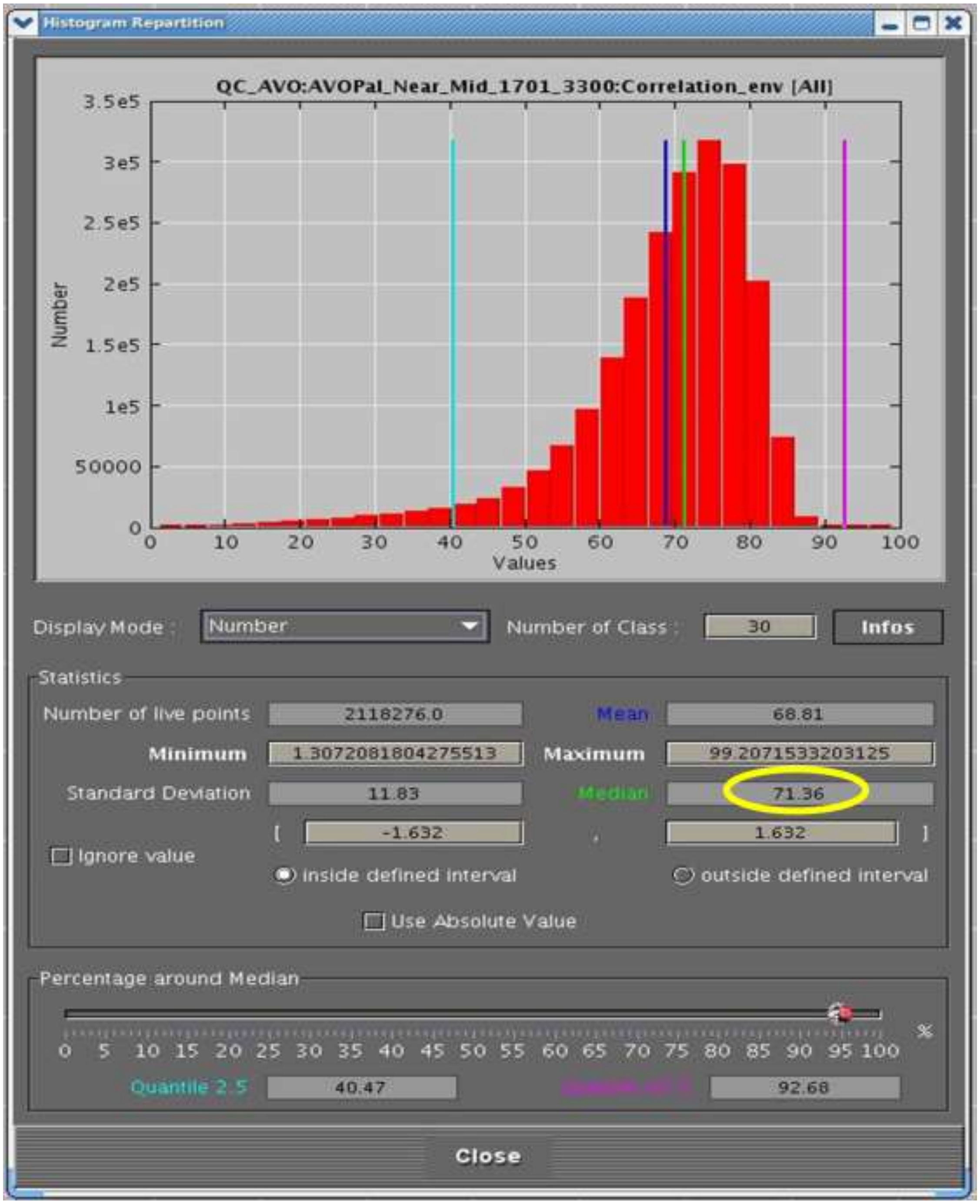

Figure 6.10: Histogram of cross-correlation for Near - Mid pair (in yellow circle)

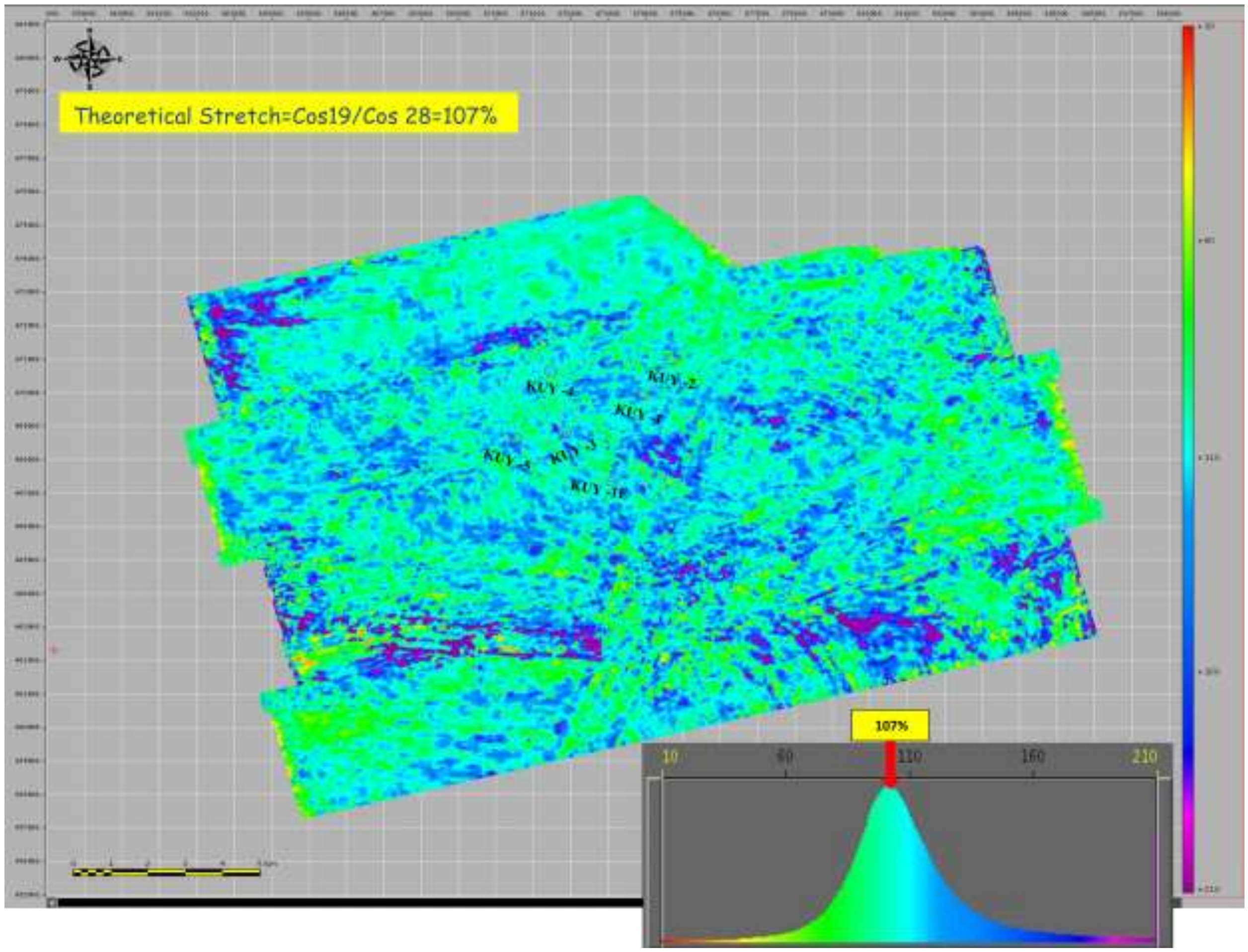

Figure 6.11: Stretch map of Near-Mid pair. Stretch occurs when a Normal Moveout (NMO) correction is applied to a seismic data during processing. Normal Moveout (NMO) stretch is the alteration of a wavelet's period by application of the Normal Moveout (NMO) correction. The effect, which increases with offset, is to lower the wavelet's frequency (i.e., make the peaks "fatter") and make subtle traps even harder to find. It also affects the shape of the wavelet and the amplitude. Theoretical stretch was calculated dividing Cosine (33º-14º) by Cosine (42º-14º). Angle substack as designed are as follows: Near (14º-24º), Mid (23º-33º) and Far (32º-42º).

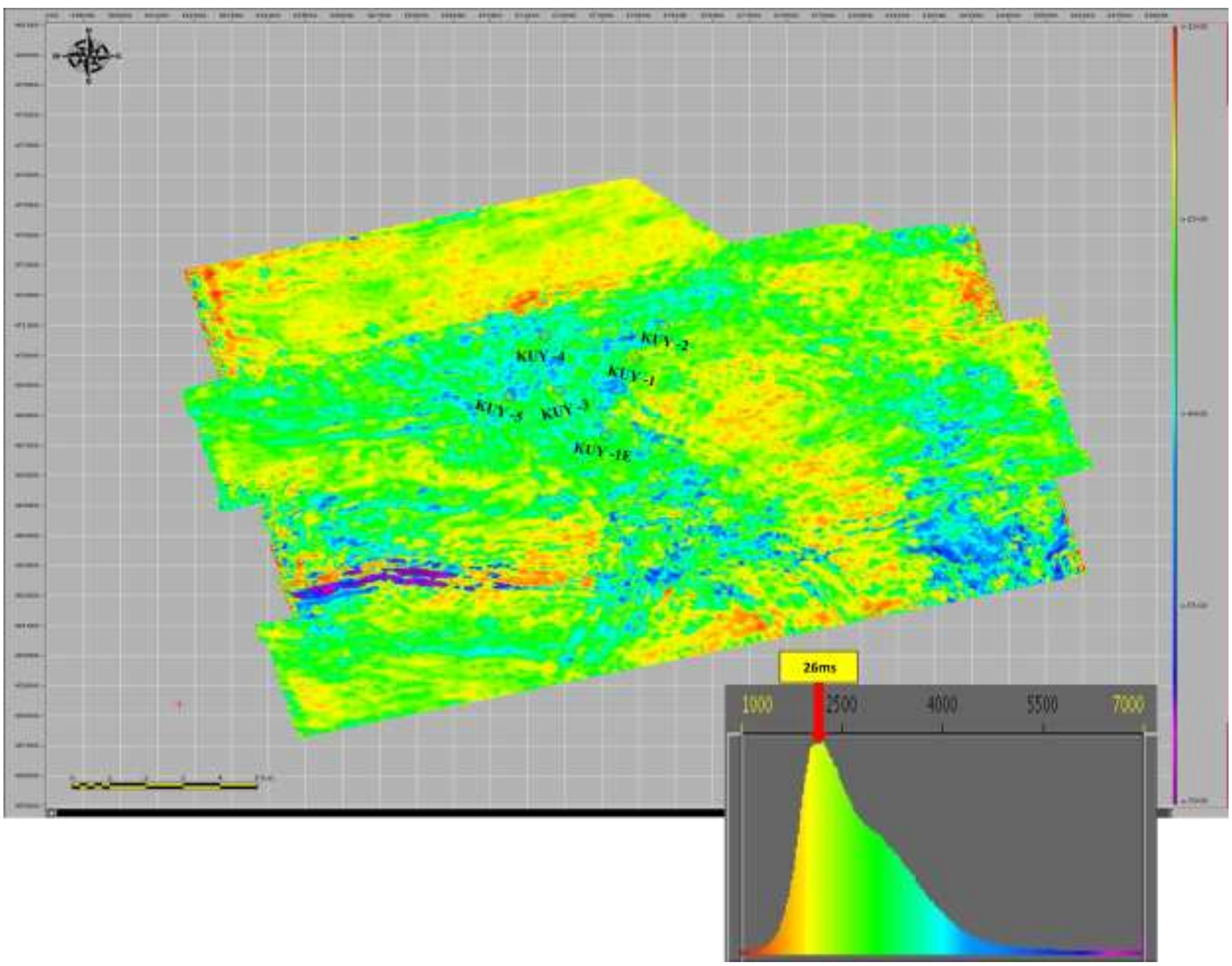

Figure 6.12: Resolution map of Near cube

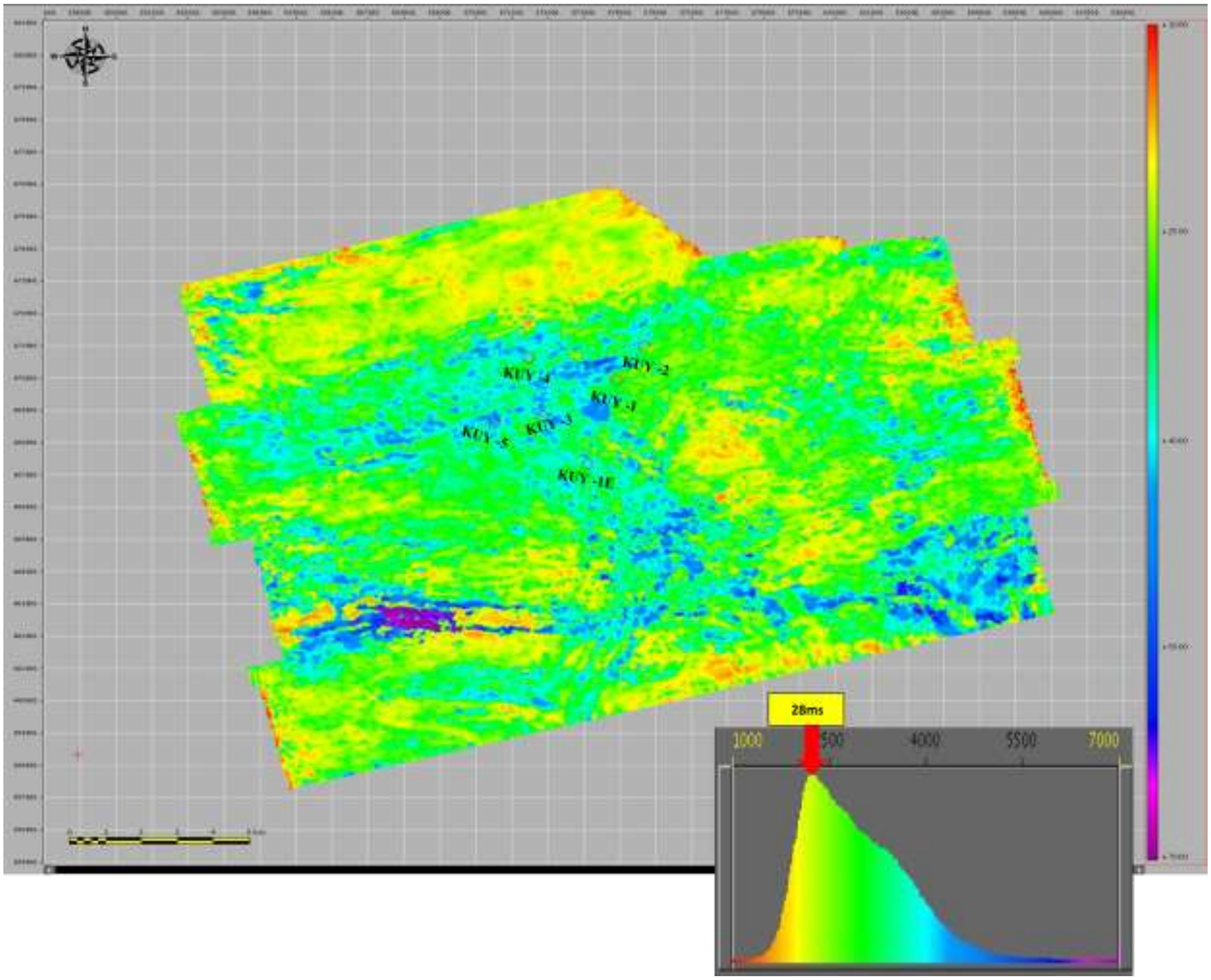

Figure 6.13: Resolution map of Mid cube

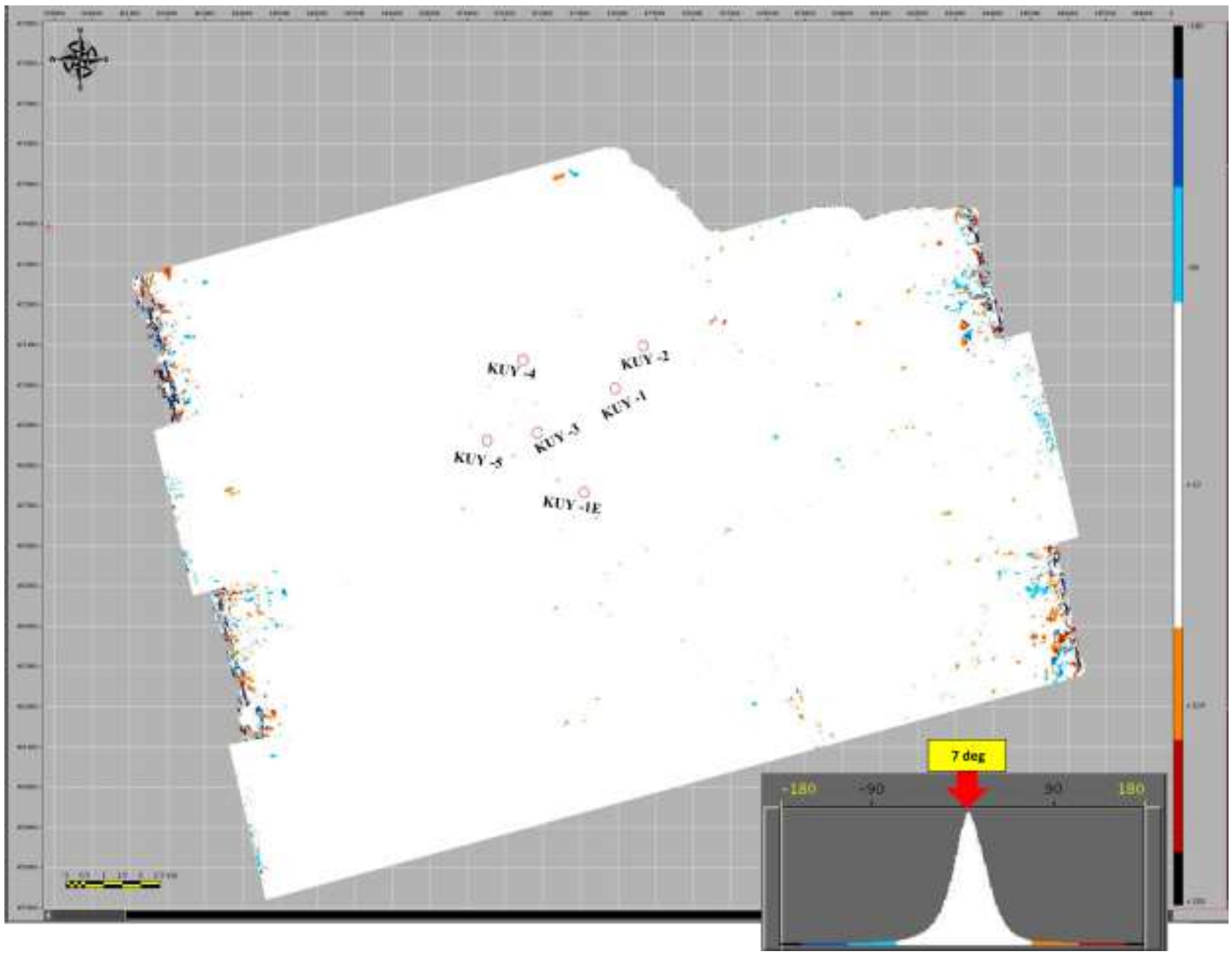

Figure 6.14: Phase shift of Near - Mid pair

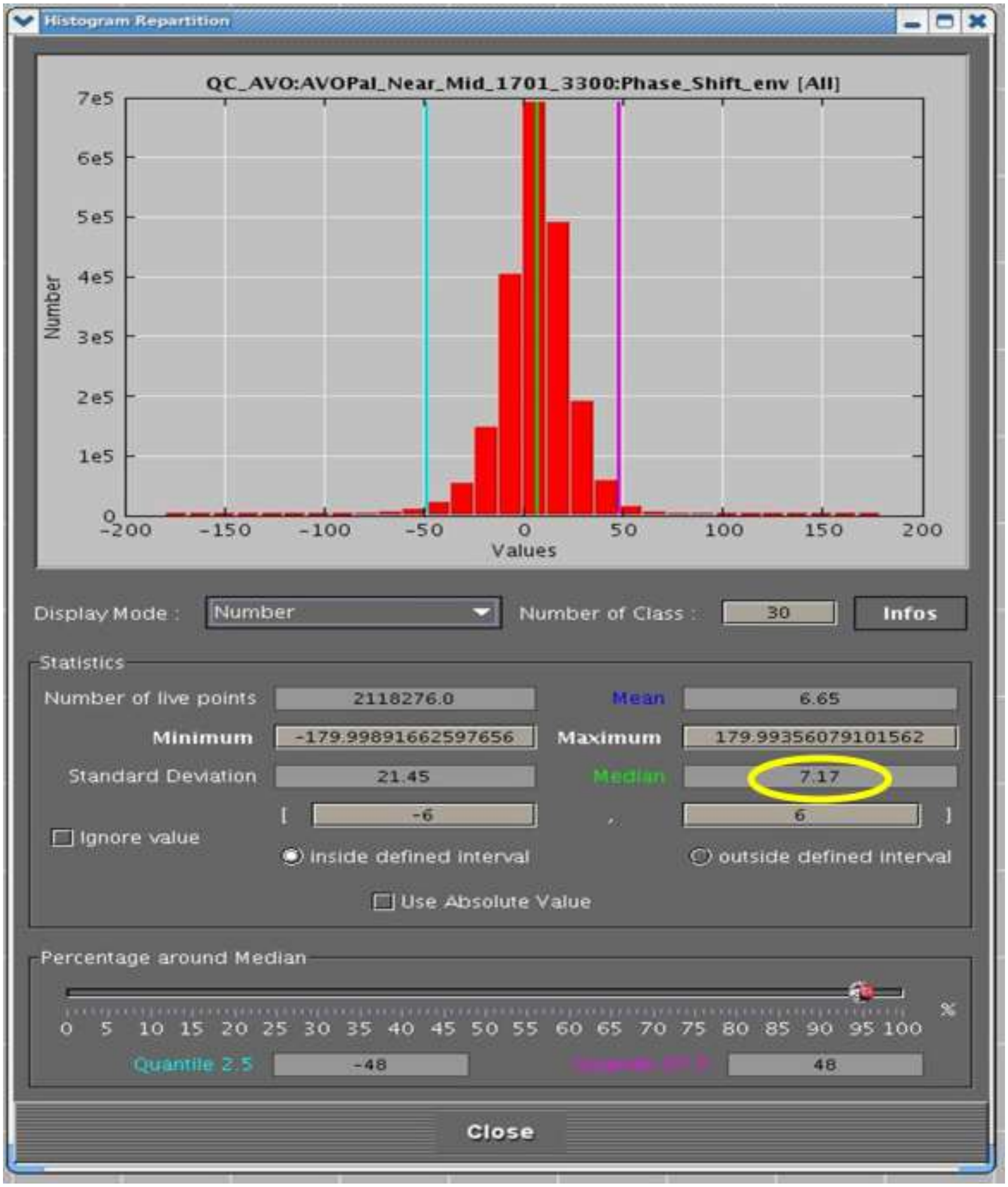

Figure 6.15: Histogram of phase shift between Near – Mid pair (in yellow circle)

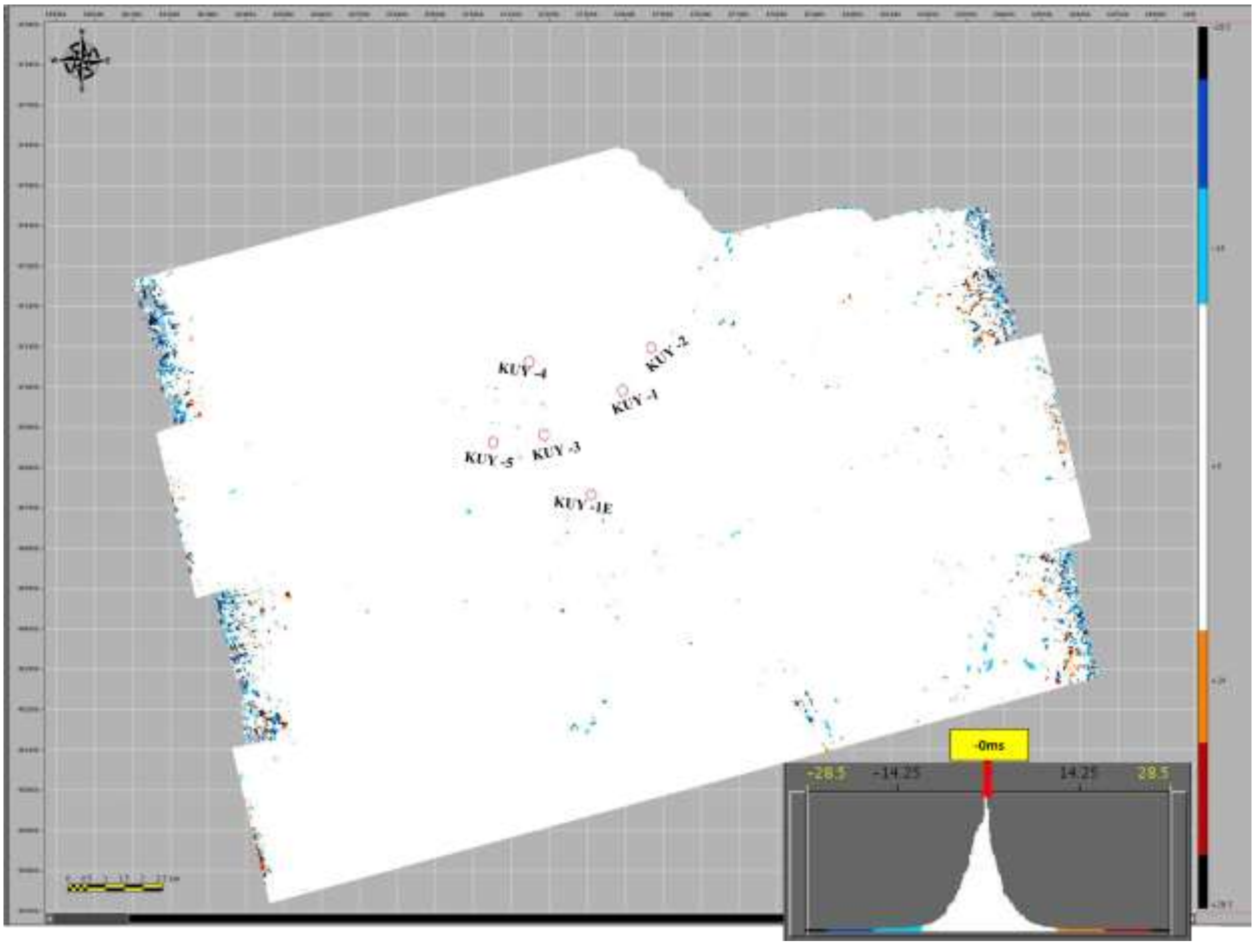

Figure 6.16: Time shift between Near and Mid pair

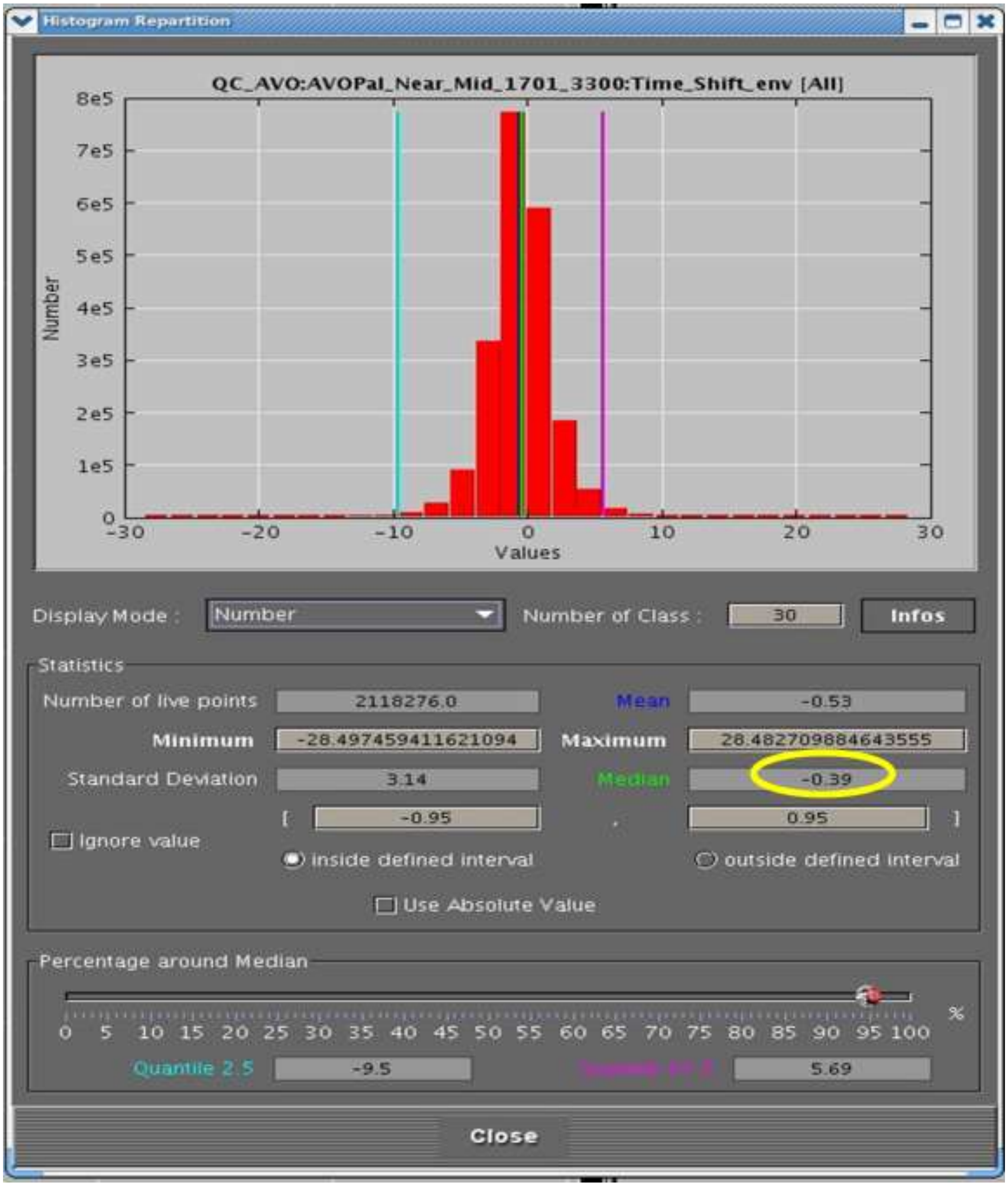

Figure 6.17: Histogram of time shift between Near – Mid pair (in yellow circle)

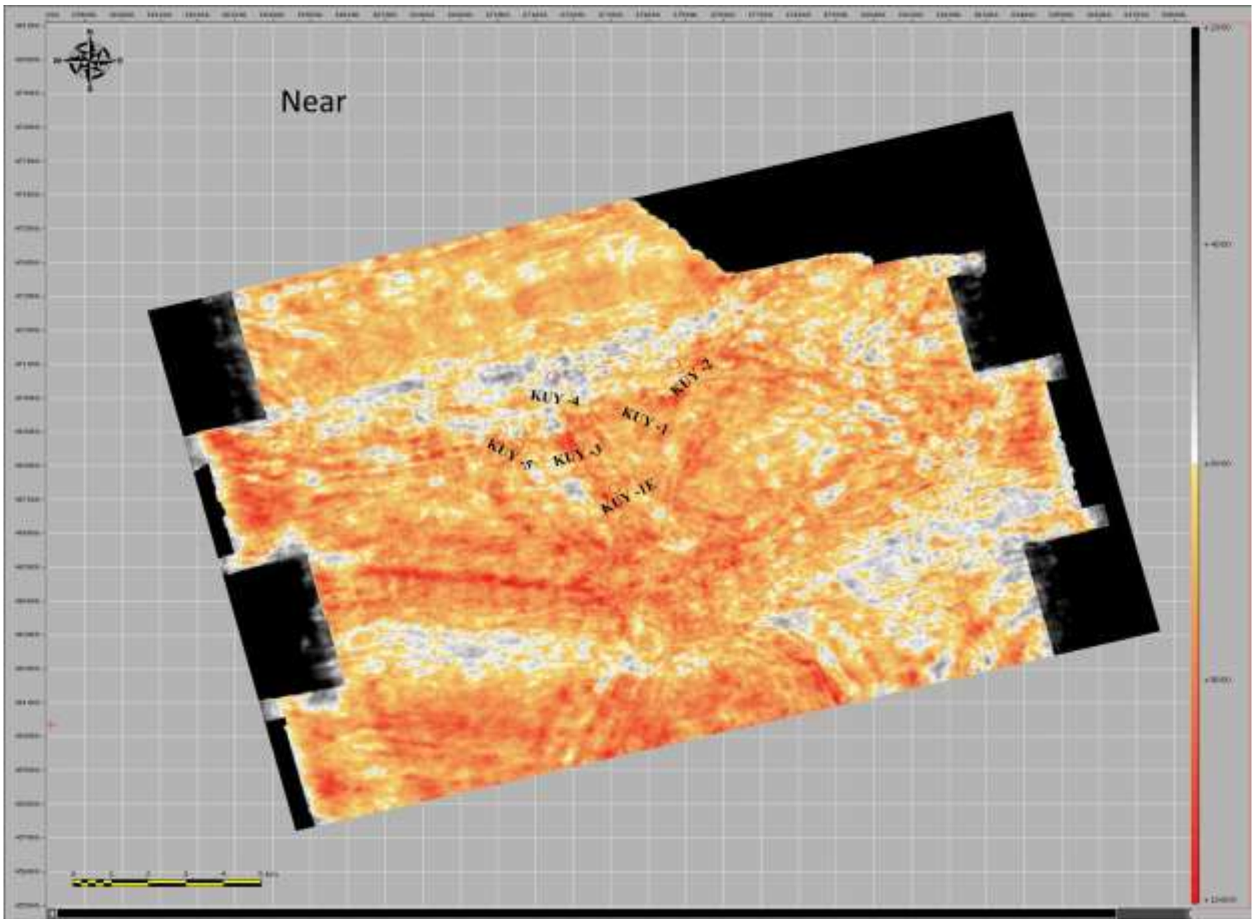

Figure 6.18: RMS amplitude map Near cube

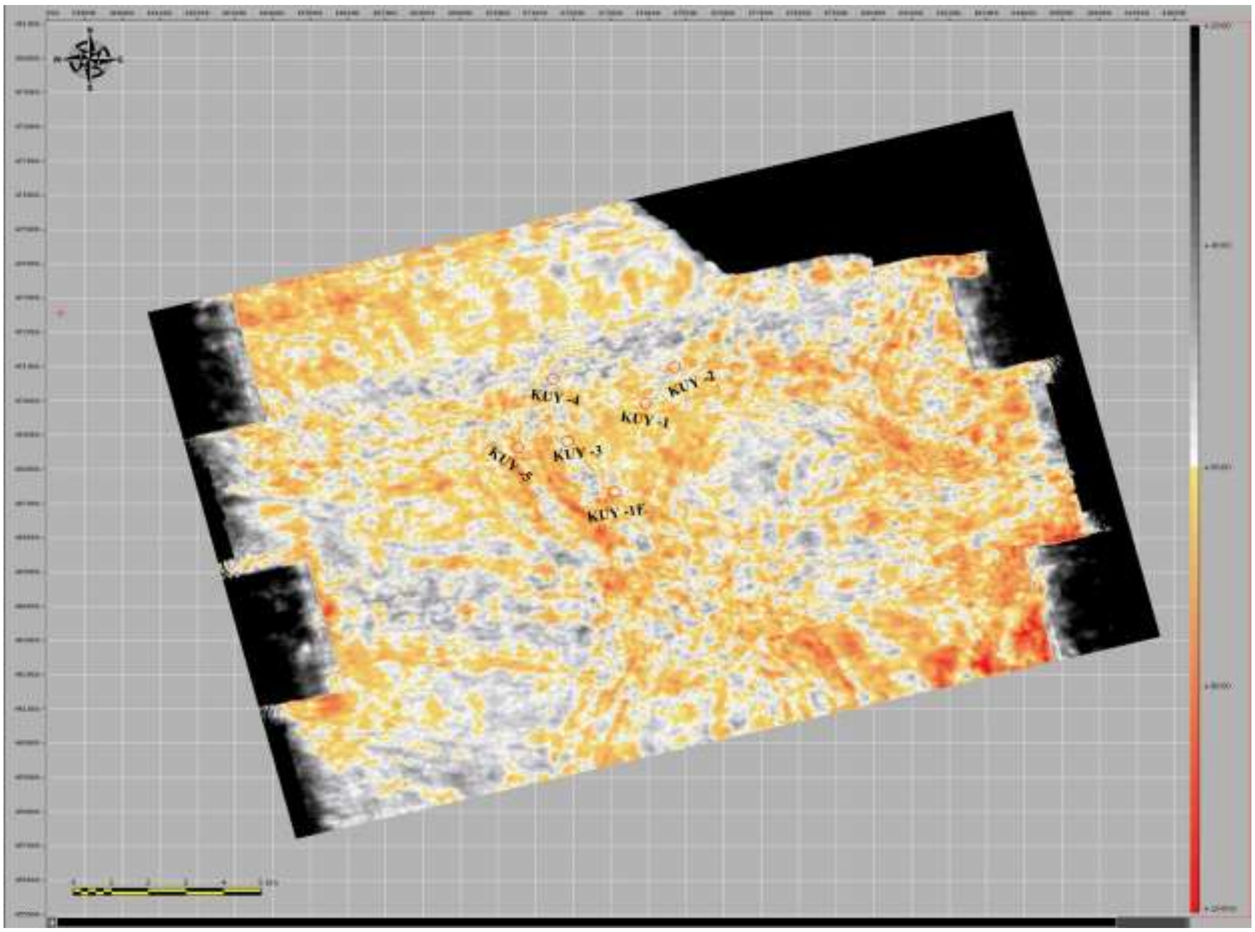

Figure 6.19: RMS amplitude map Mid cube

6.2.2 Original/Raw Mid - Far Pair

Estimate of quality control (QC) attribute maps were also computed around the studied AVO interval for this combination using the original/ raw Mid and Far substacks. The result of this analysis showed, satisfactory level of correlation between Mid and Far with a good homogeneity of the map though lower than that of the Near – Mid pair. The median correlation value was 64%. No problem of homogeneity of the stretch for both substacks beside lateral artifact far from the zone of interest. The average stretch value was 111%. Average resolution computed within the reservoir window was not too different on the Mid and Far substacks. The computed resolution for the Mid was 28ms while that of the Far was 34ms. The average root mean square (RMS) amplitudes computed within the reservoir window was quite similar on the Mid and Far substacks. Phase and time shifts between Mid and Far were reasonable and close to zero. No time or phase shift was required.

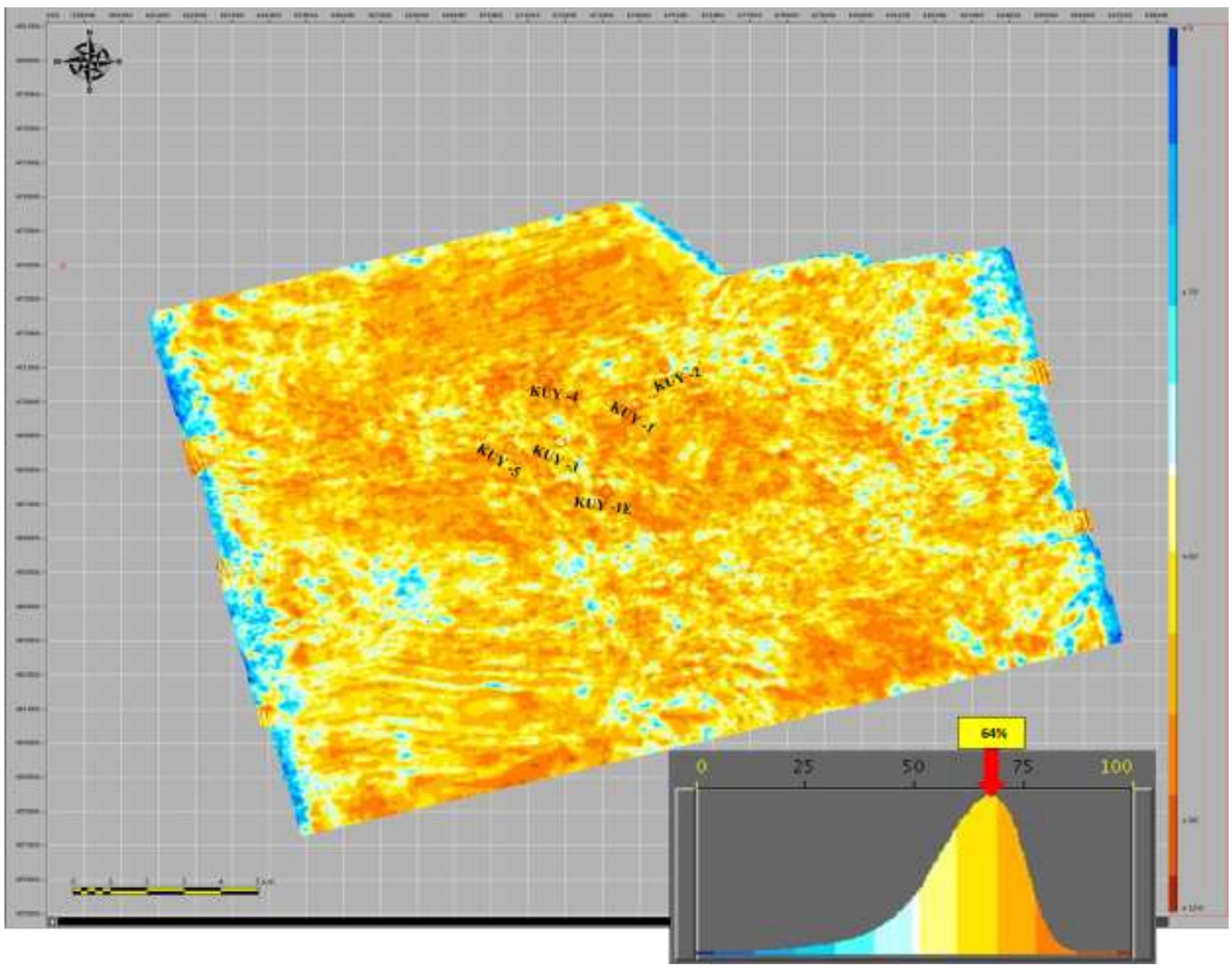

Figure 6.20: Cross-correlation map of Mid - Far pair

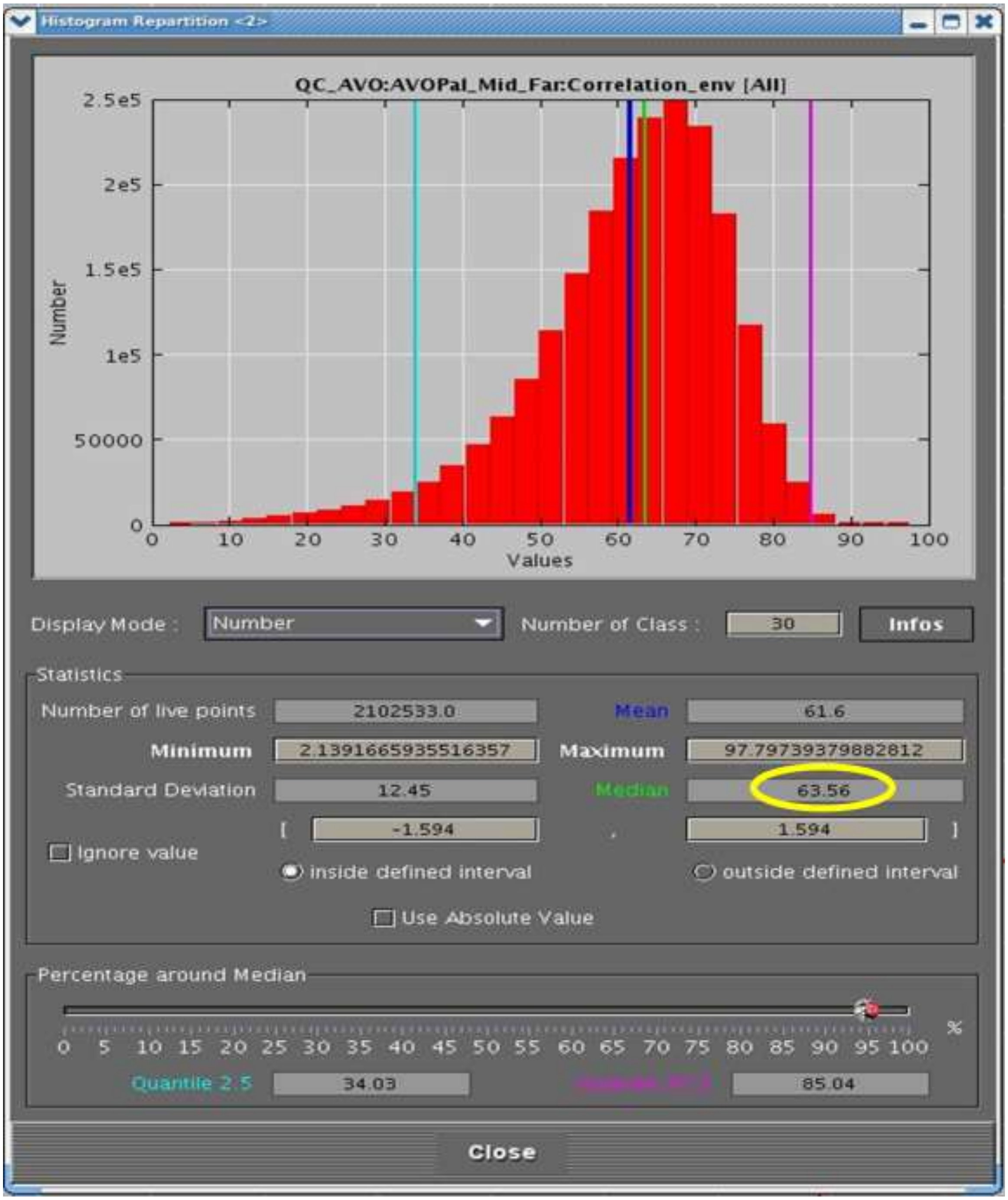

Figure 6.21: Histogram of cross-correlation between Mid – Far pair (in yellow circle)

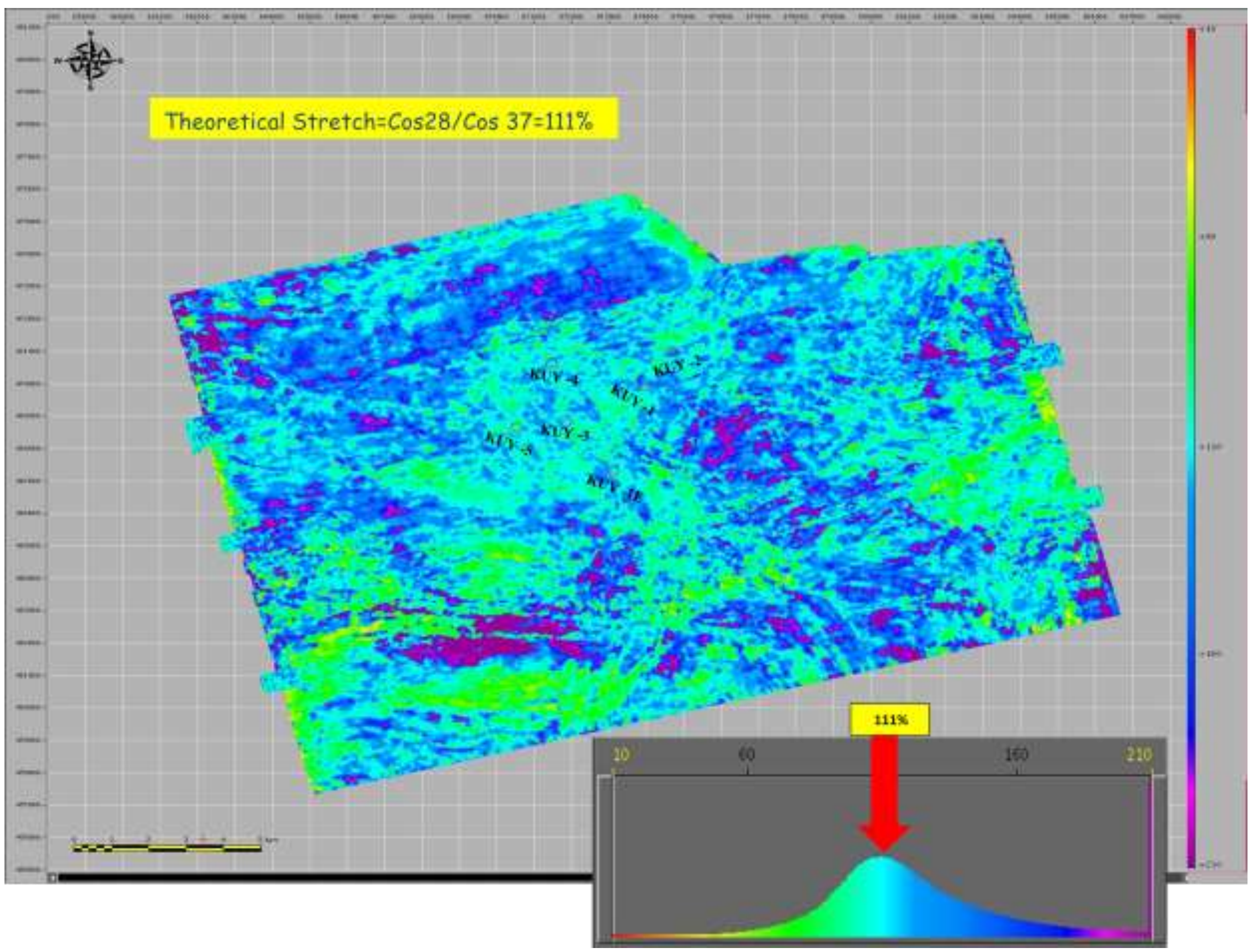

Figure 6.22: Stretch map of Mid – Far pair (see Figure 6.11 for explanation on stretch and its calculation)

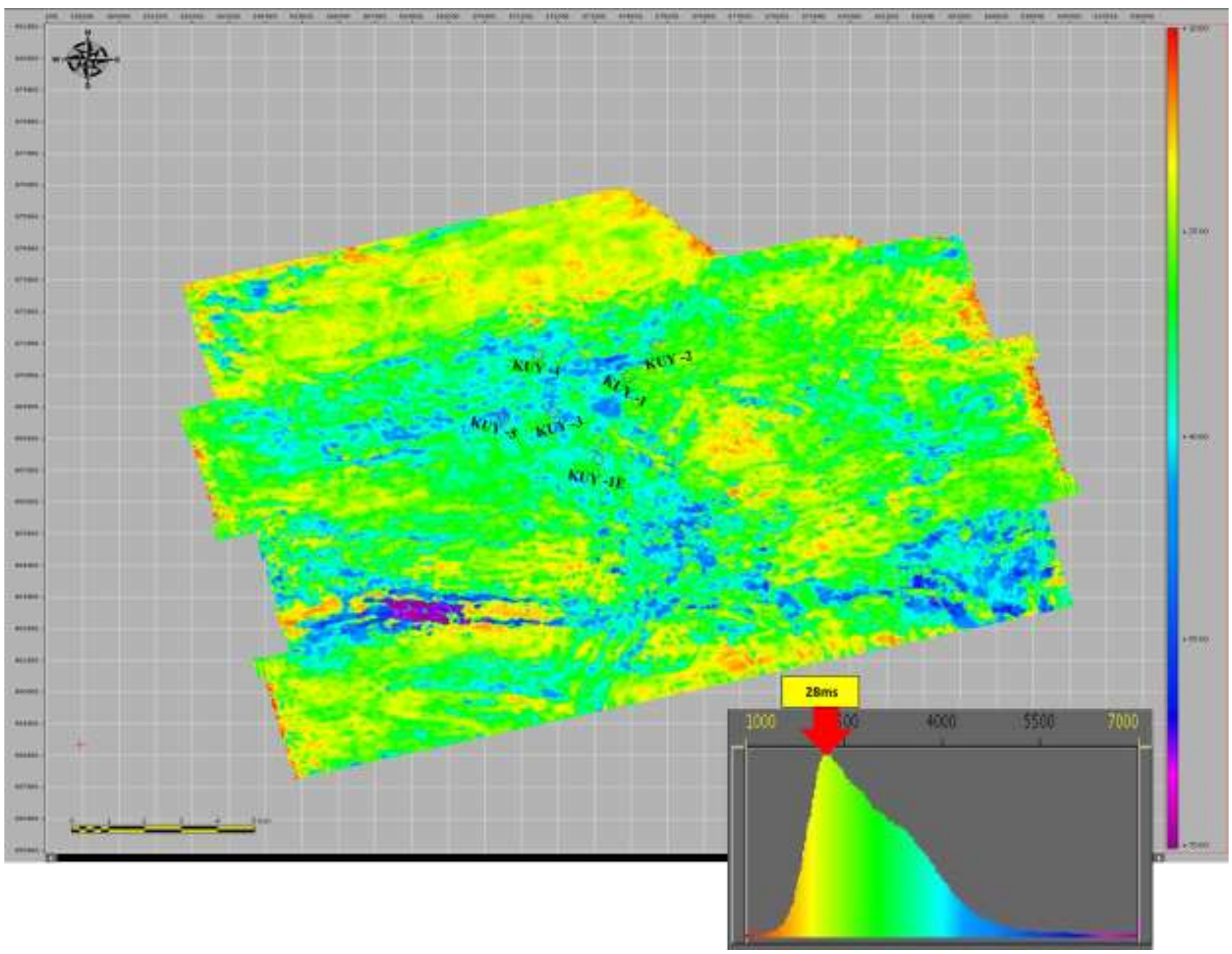

Figure 6.23: Resolution map of Mid cube

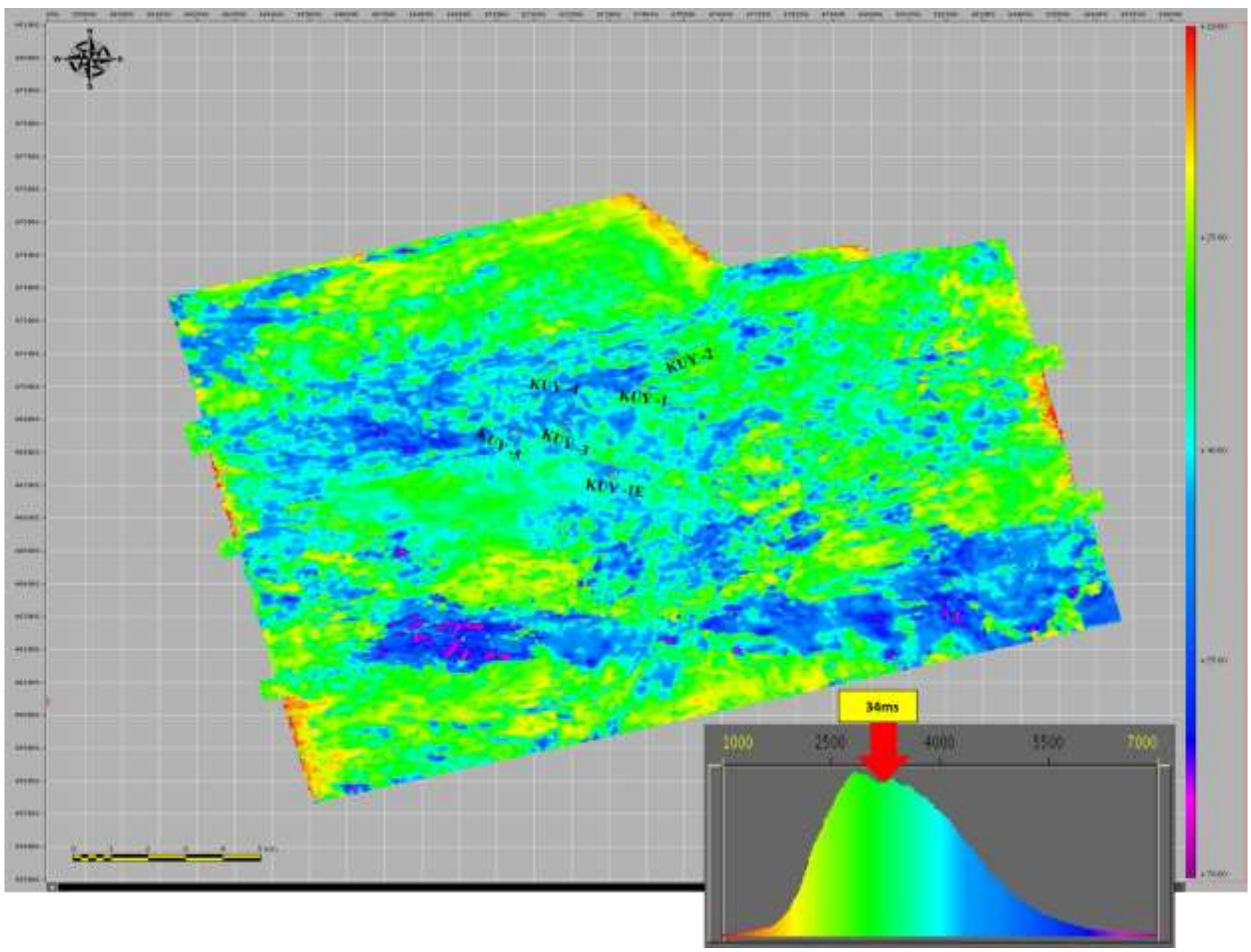

Figure 6.24: Resolution map of Far cube

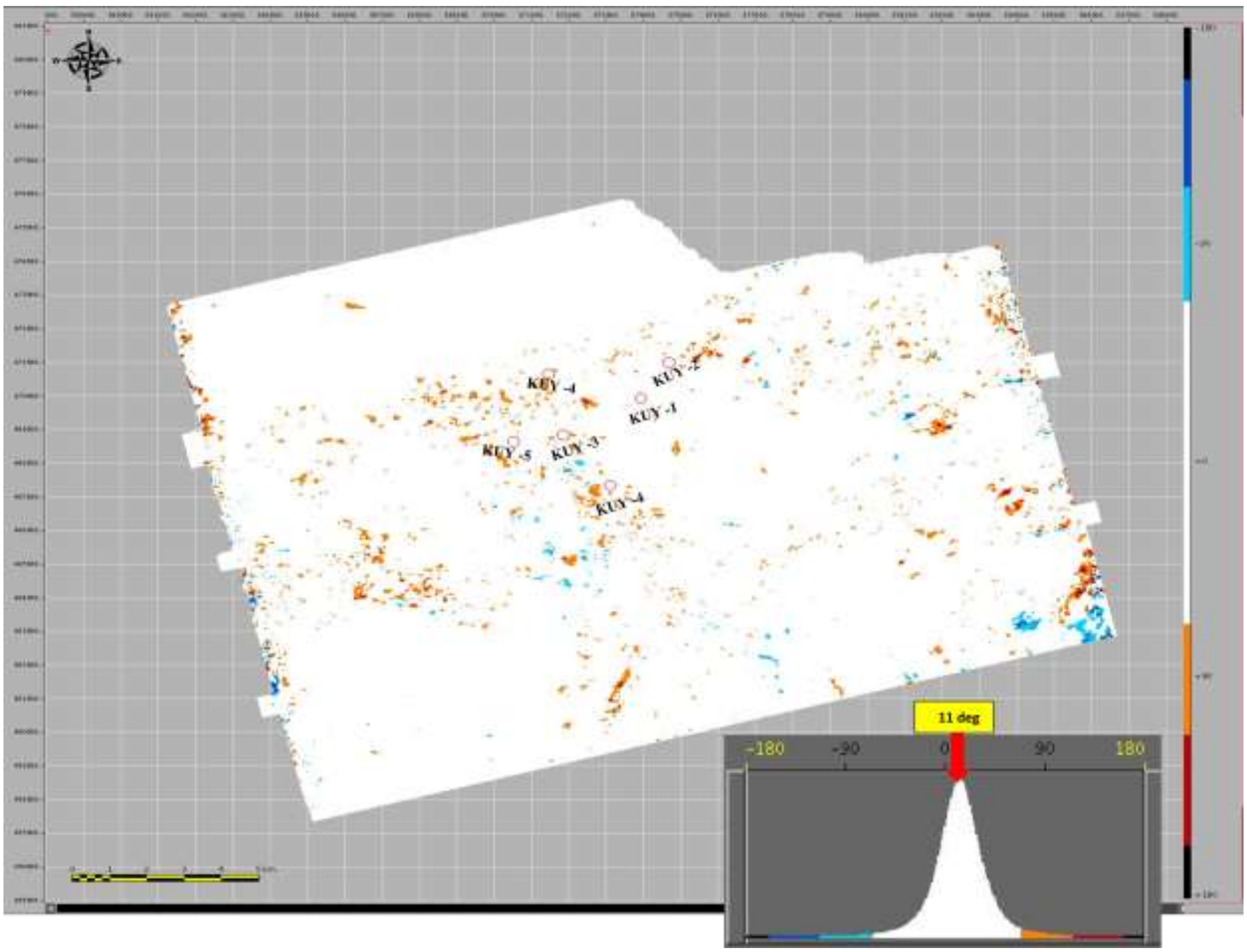

Figure 6.25: Phase shift between Mid – Far pair

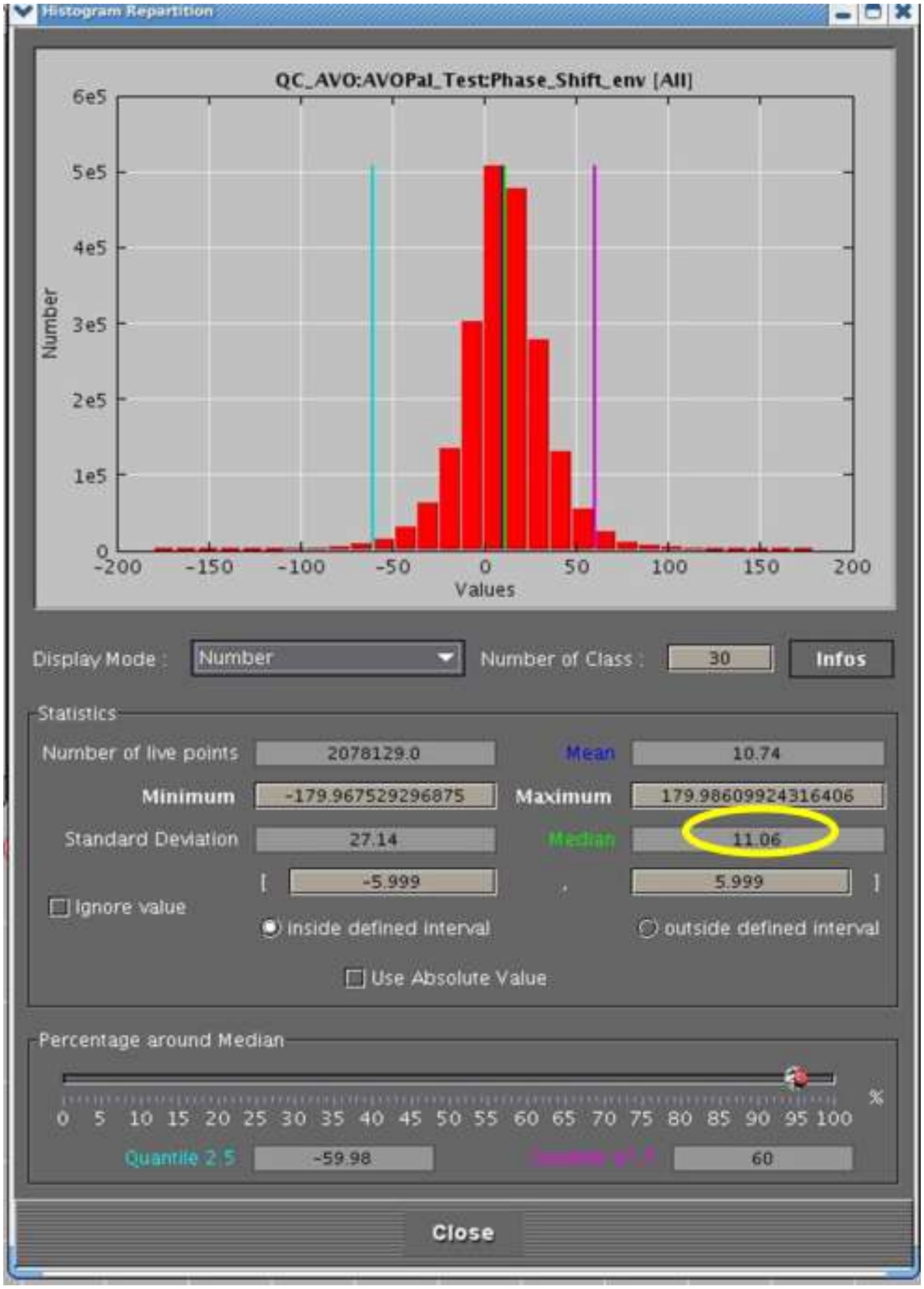

Figure 6.26: Histogram of phase shift between Mid –Far pair (in yellow circle).

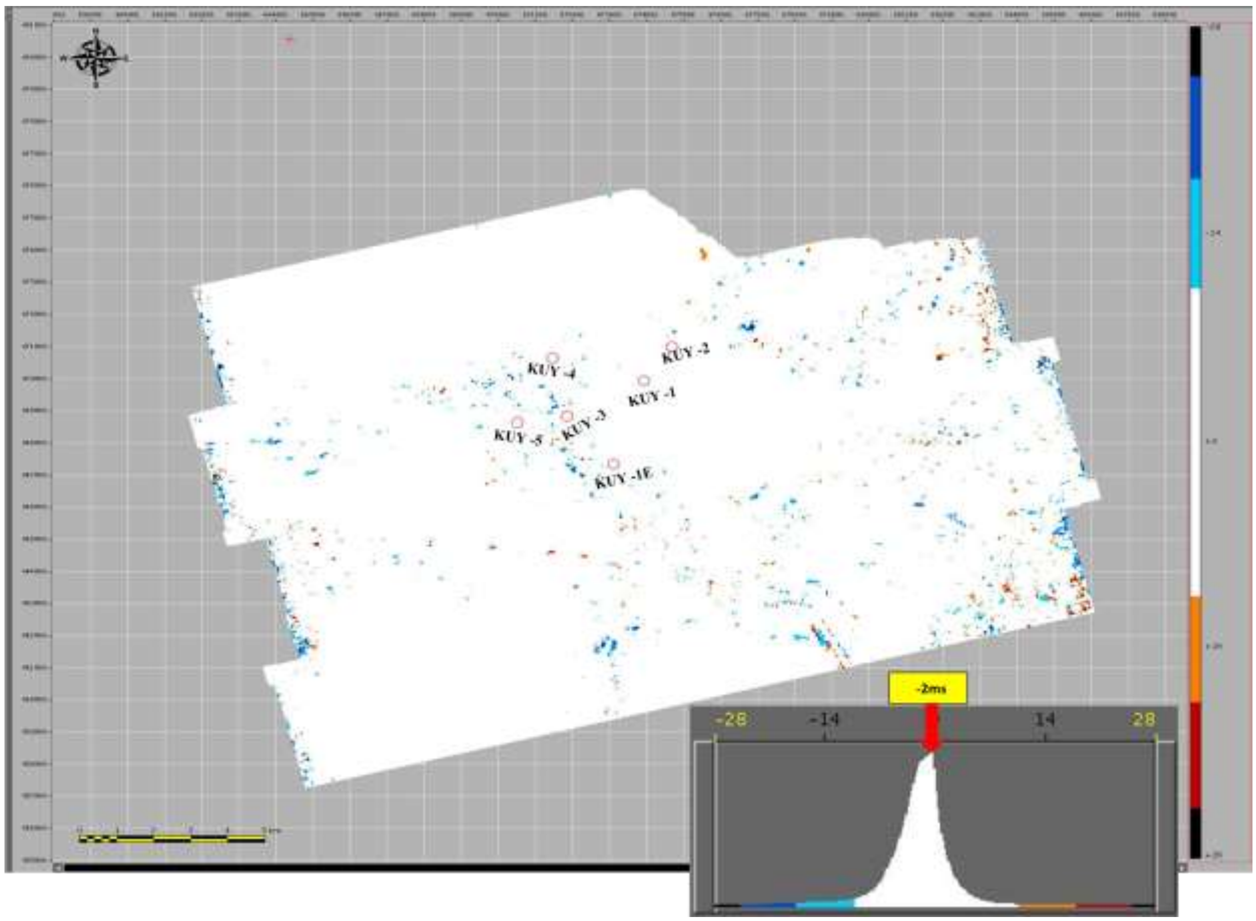

Figure 6.27: Time shift between Mid – Far pair

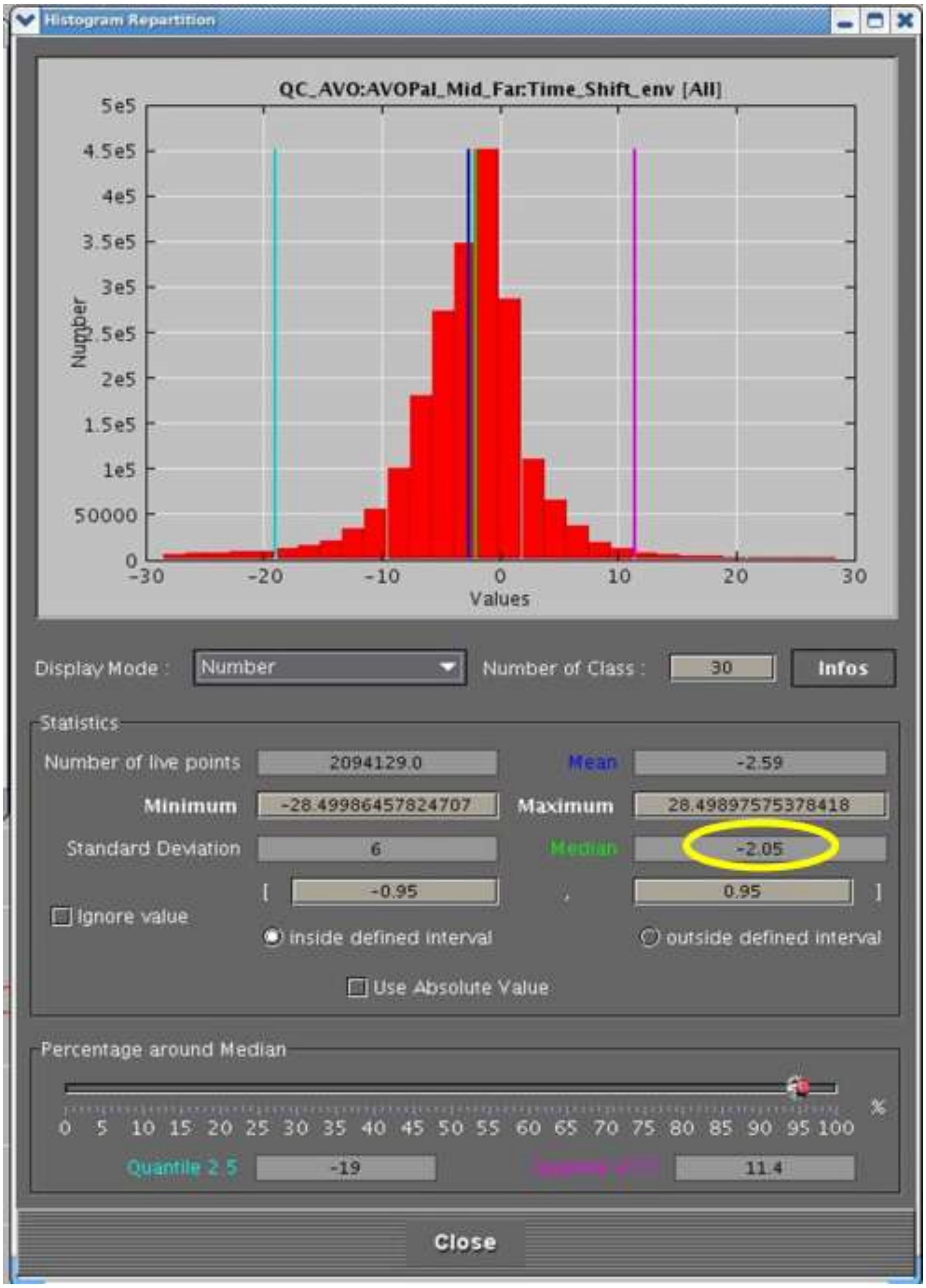

Figure 6.28: Histogram of time shift between Mid – Far pair (in yellow circle).

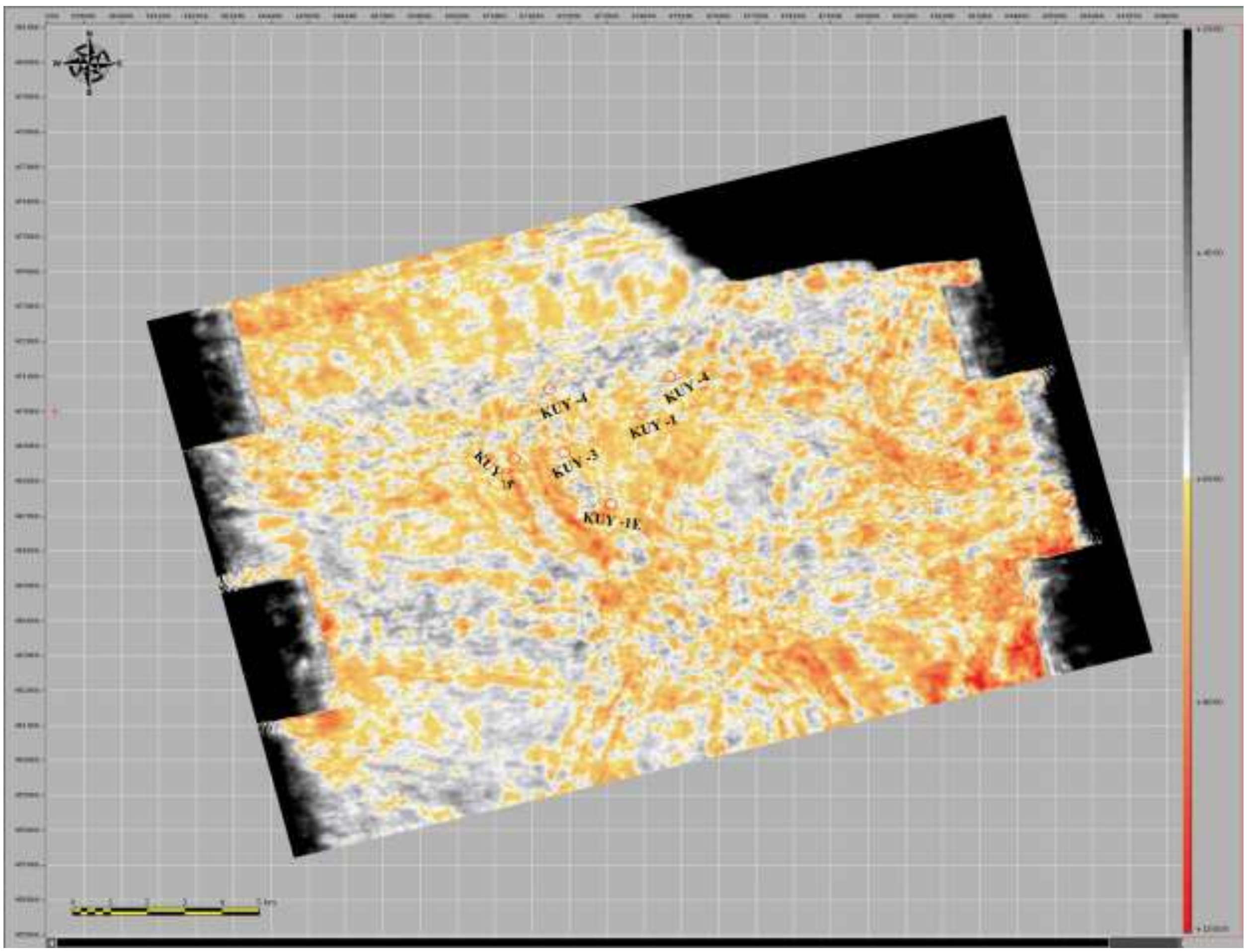

Figure 6.29: RMS amplitude map Mid cube

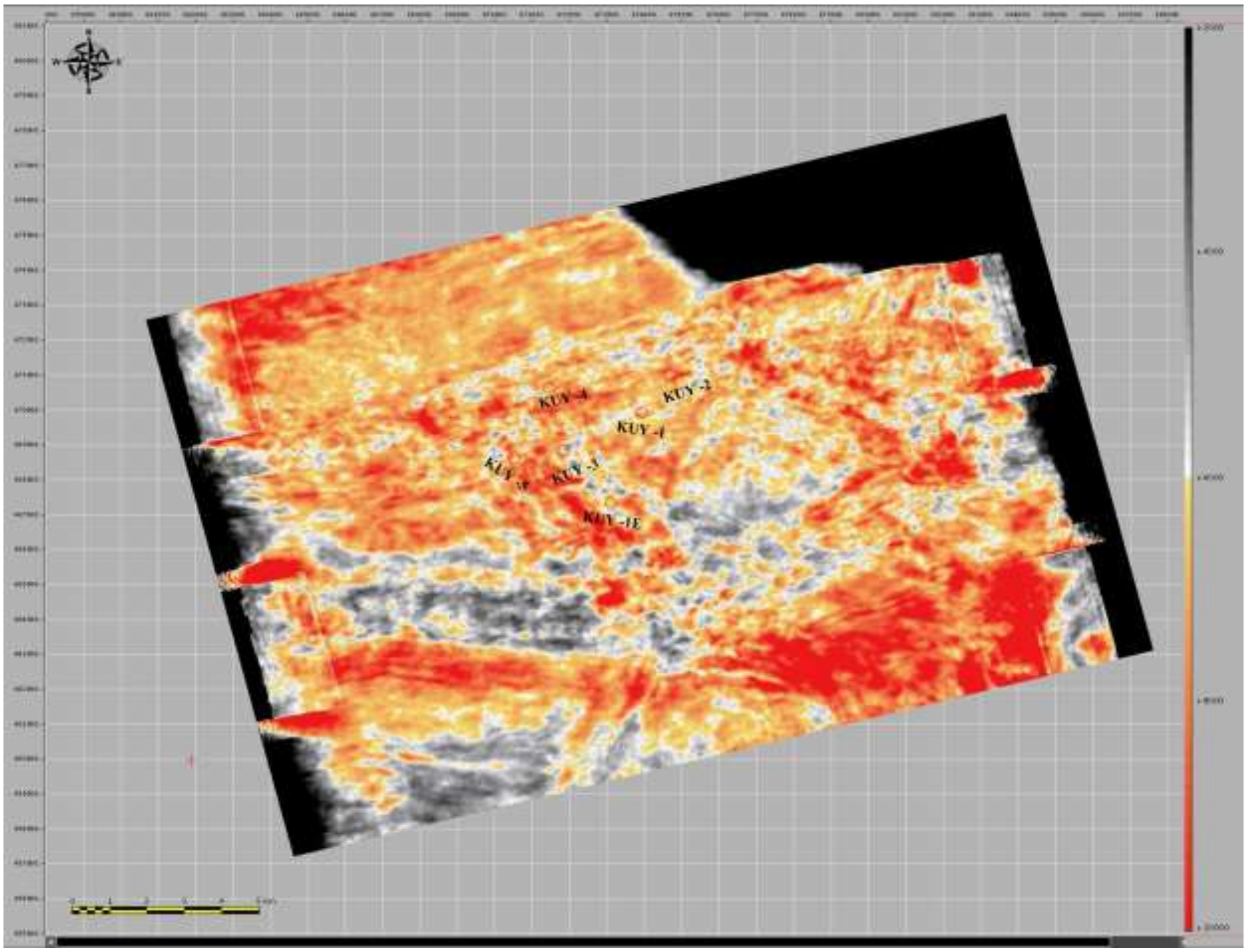

Figure 6.30: RMS amplitude map Far cube

6.2.3 Original/Raw Near - Far Pair

Quality control (QC) attribute maps were also computed around the studied AVO interval using this combination and the analysis of the results showed that the cross-correlation between Near and Far was lower than 50%. Cross-correlation between Near and Far was too low to allow an AVO analysis using this pair of substacks. There was poor homogeneity of the stretch between Near and Far with lateral artifact around the zone of interest. Computed median value of stretch was 118%. Average resolution computed within the reservoir window was too different on the Near and Far substacks. The computed resolution for the Near was 26ms while that of the Far was 34ms. Average RMS amplitudes computed within the reservoir window was quite similar on the Near and Far substacks. There were reasonable time shift between Near and Far. Phase shift was not close to zero. Time and phase shifts were required.

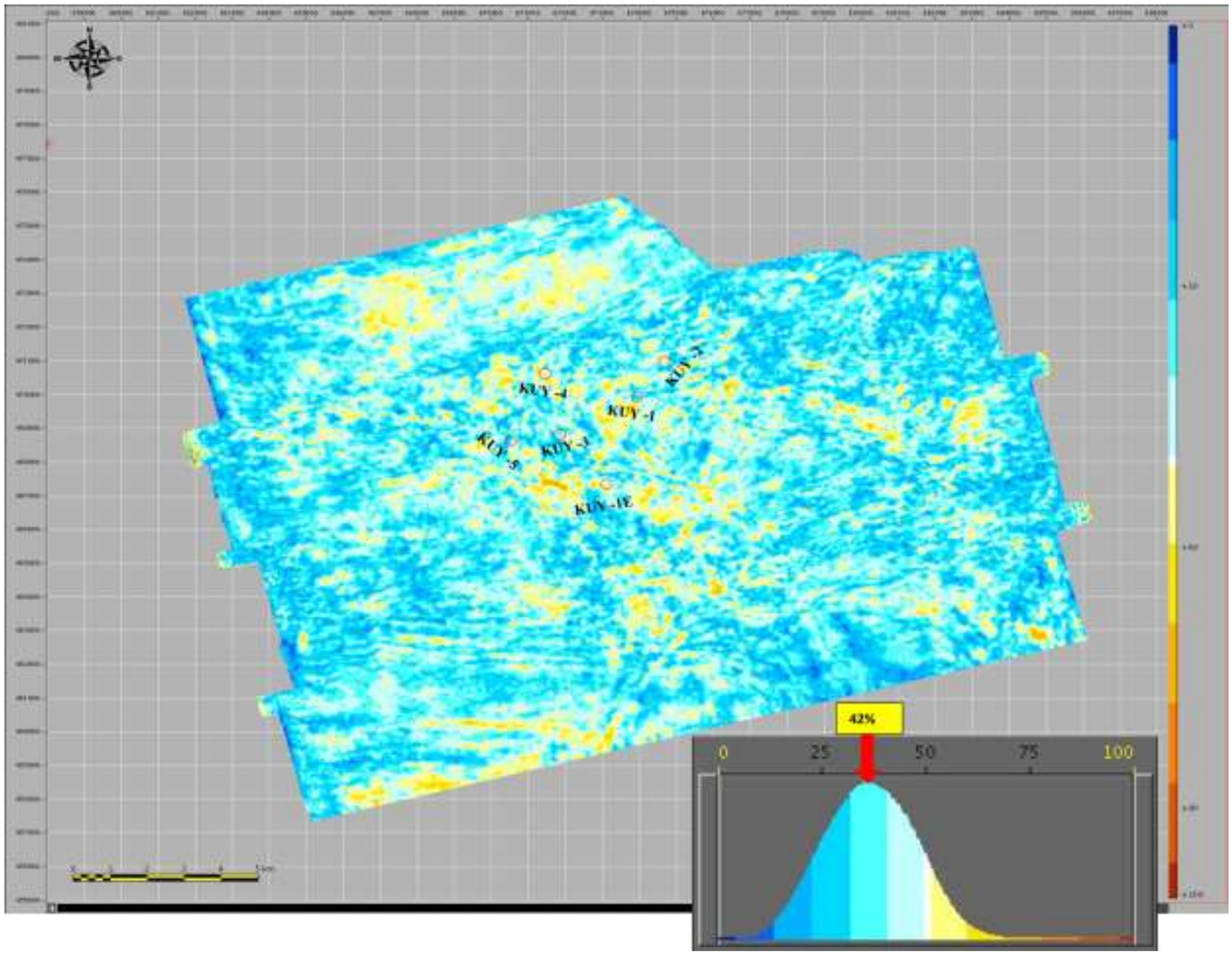

Figure 6.31: Cross-correlation map of Near - Far pair

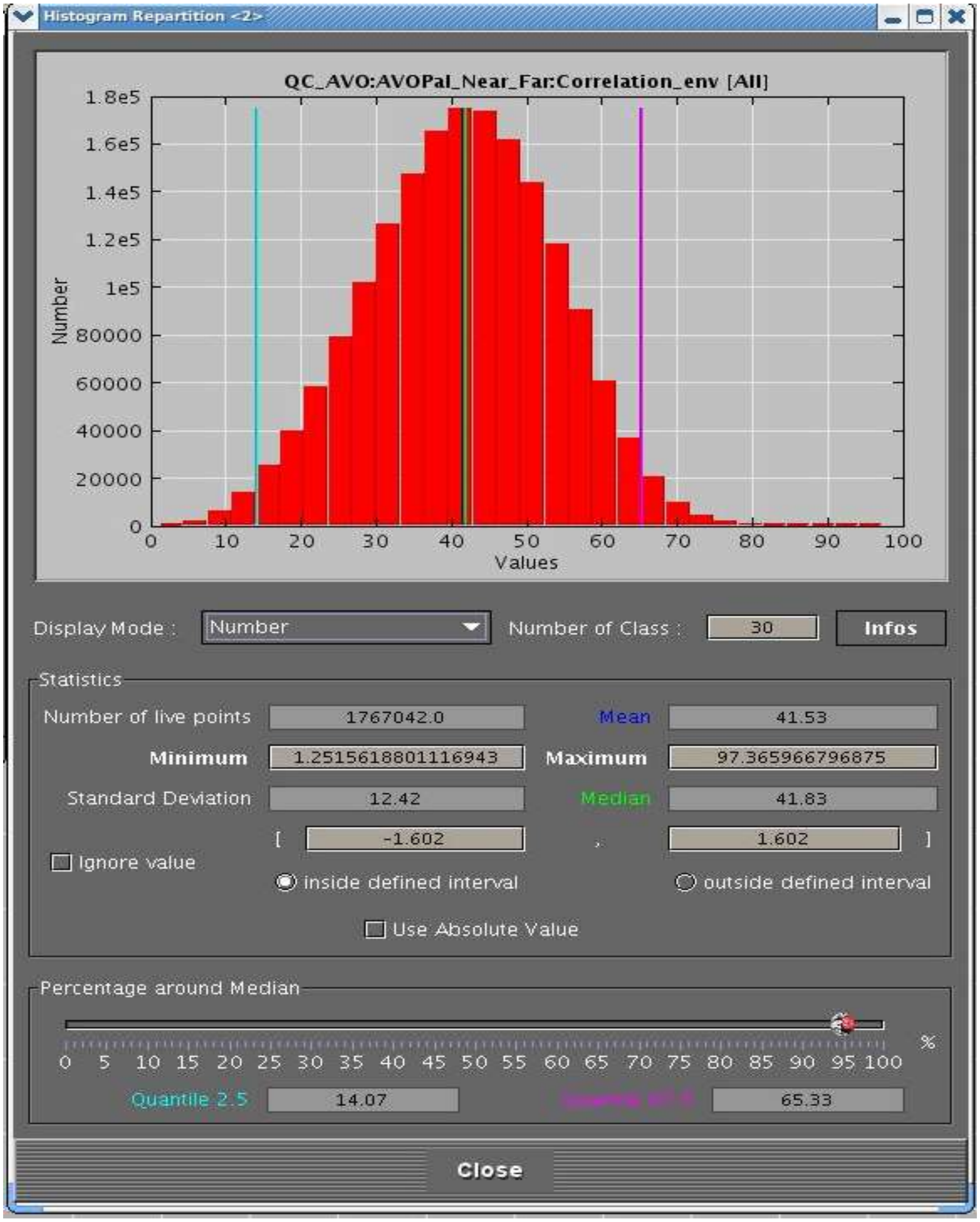

Figure 6.32: Histogram of correlation between Near – Far pair (in yellow circle)

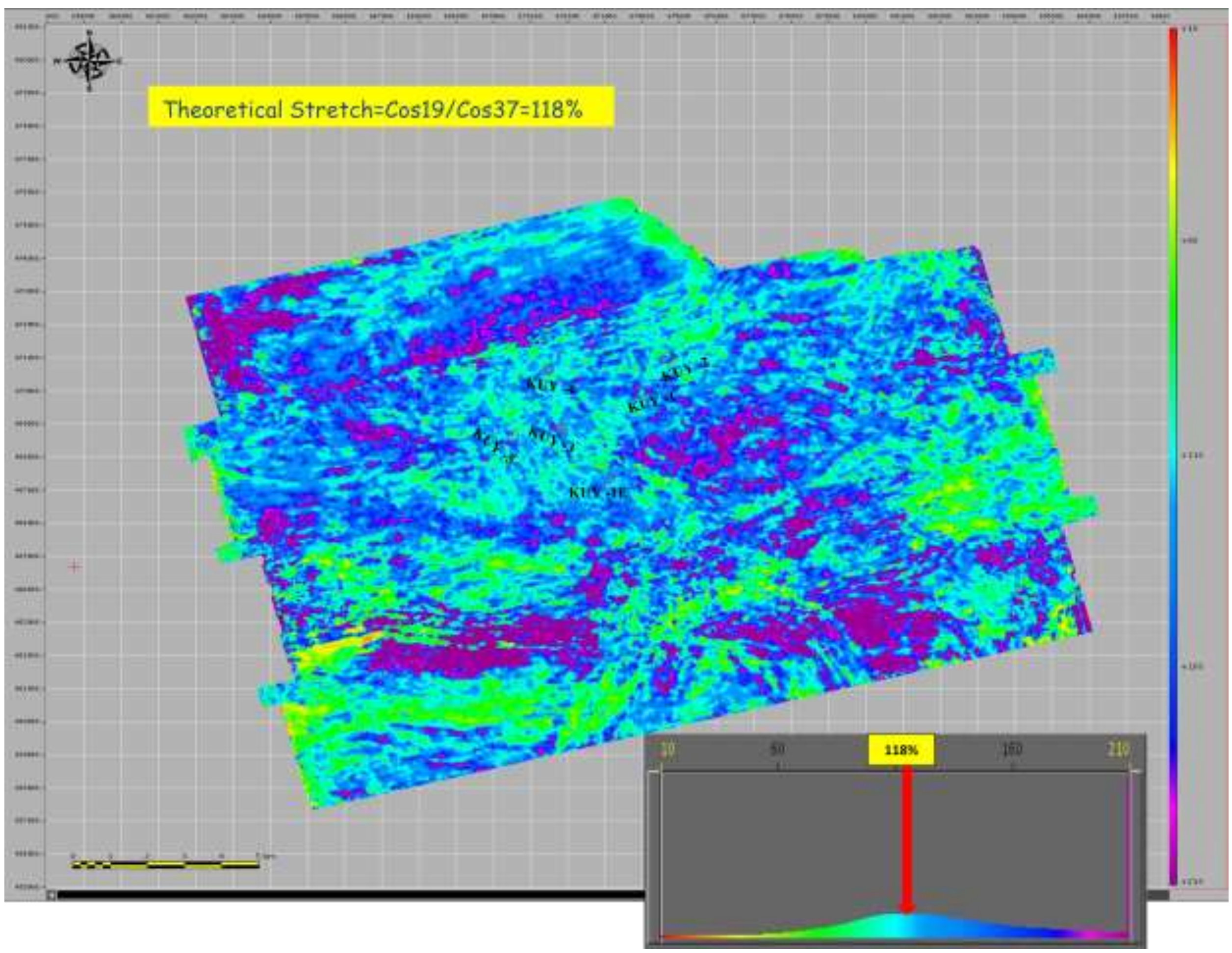

Figure 6.33: Stretch map of Near-Far pair (see Figure 6.11 for explanation on stretch and its calculation)

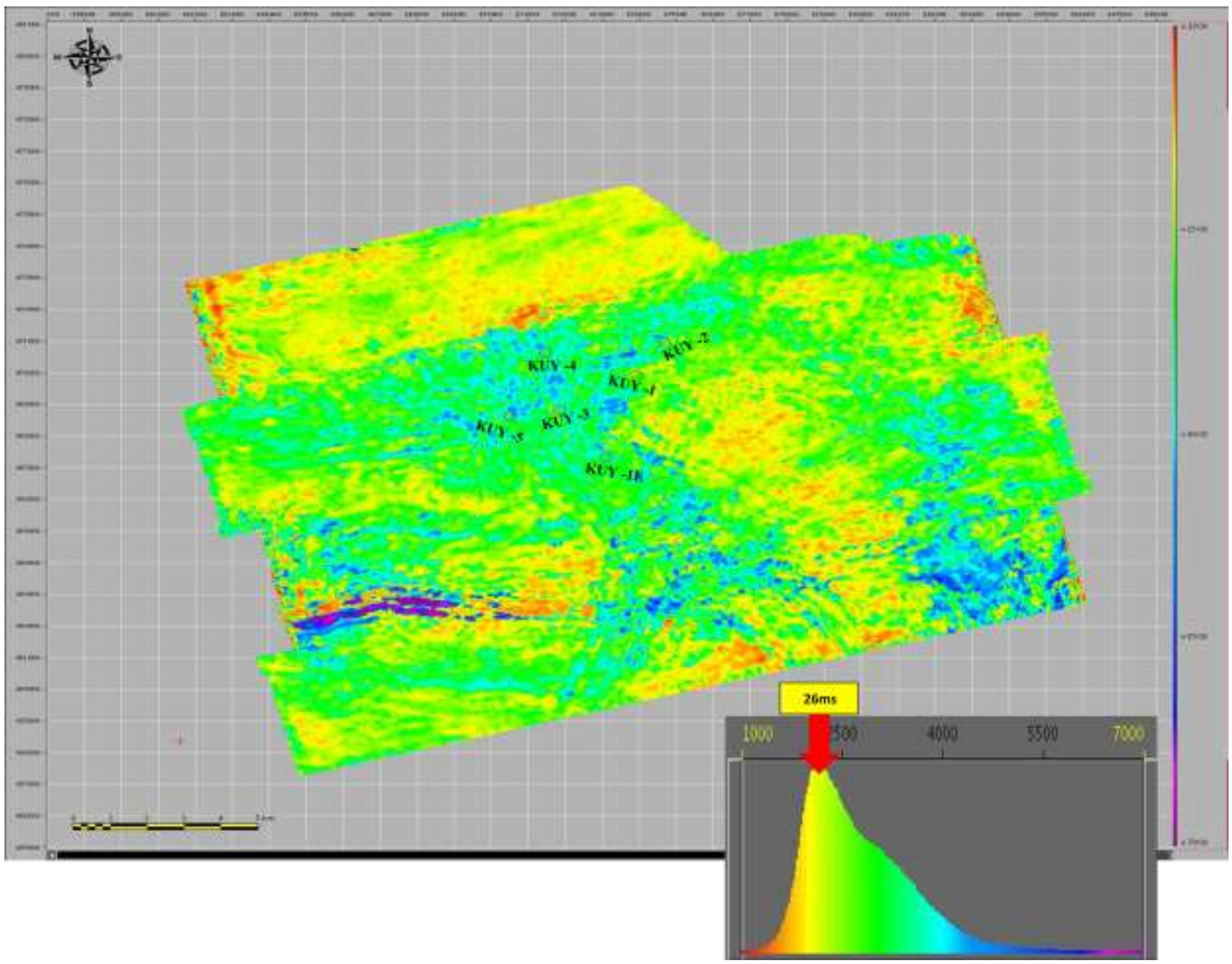

Figure 6.34: Resolution map of Near cube

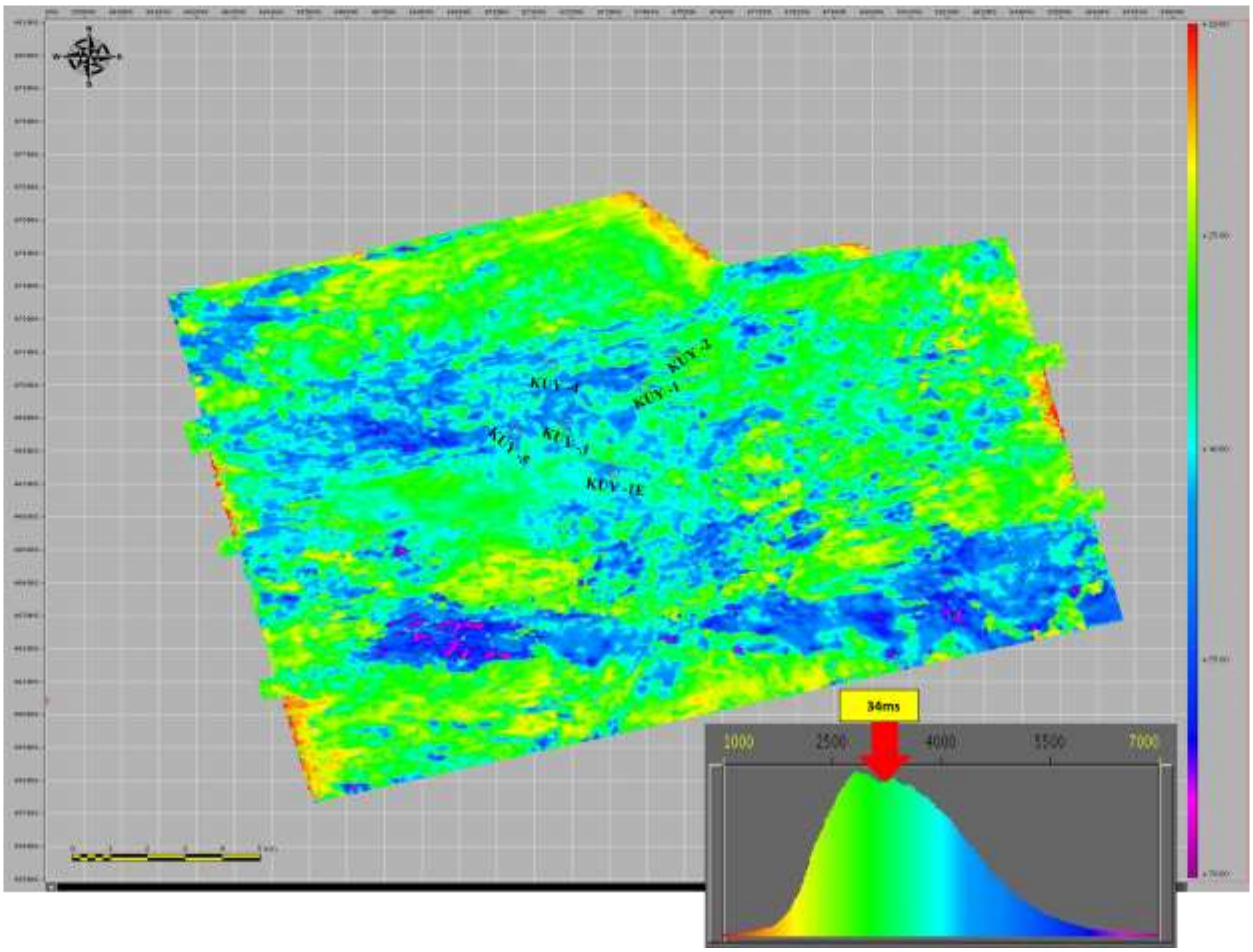

Figure 6.35: Resolution map of Far cube

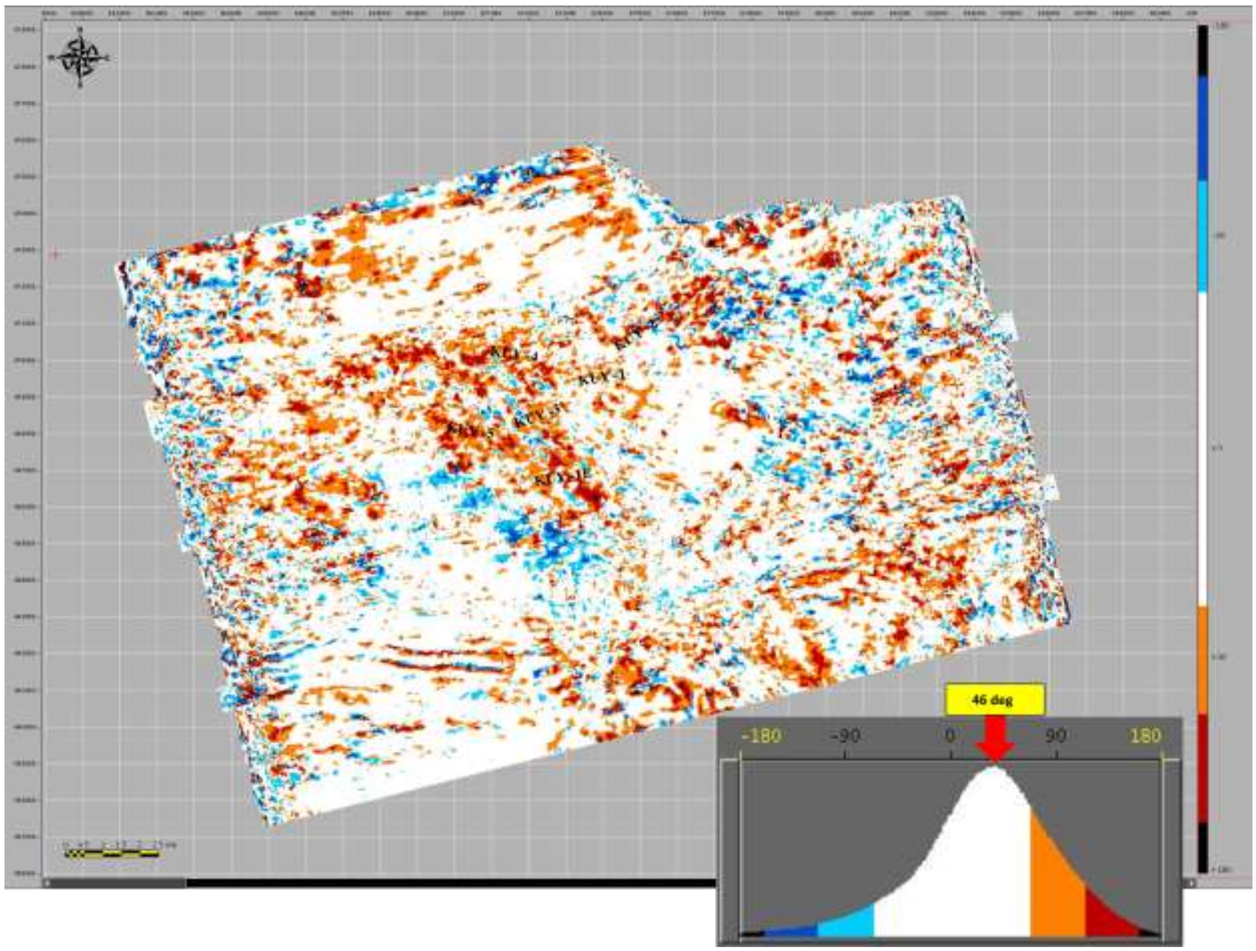

Figure 6.36: Phase shift between Near - Far pair (in yellow circle)

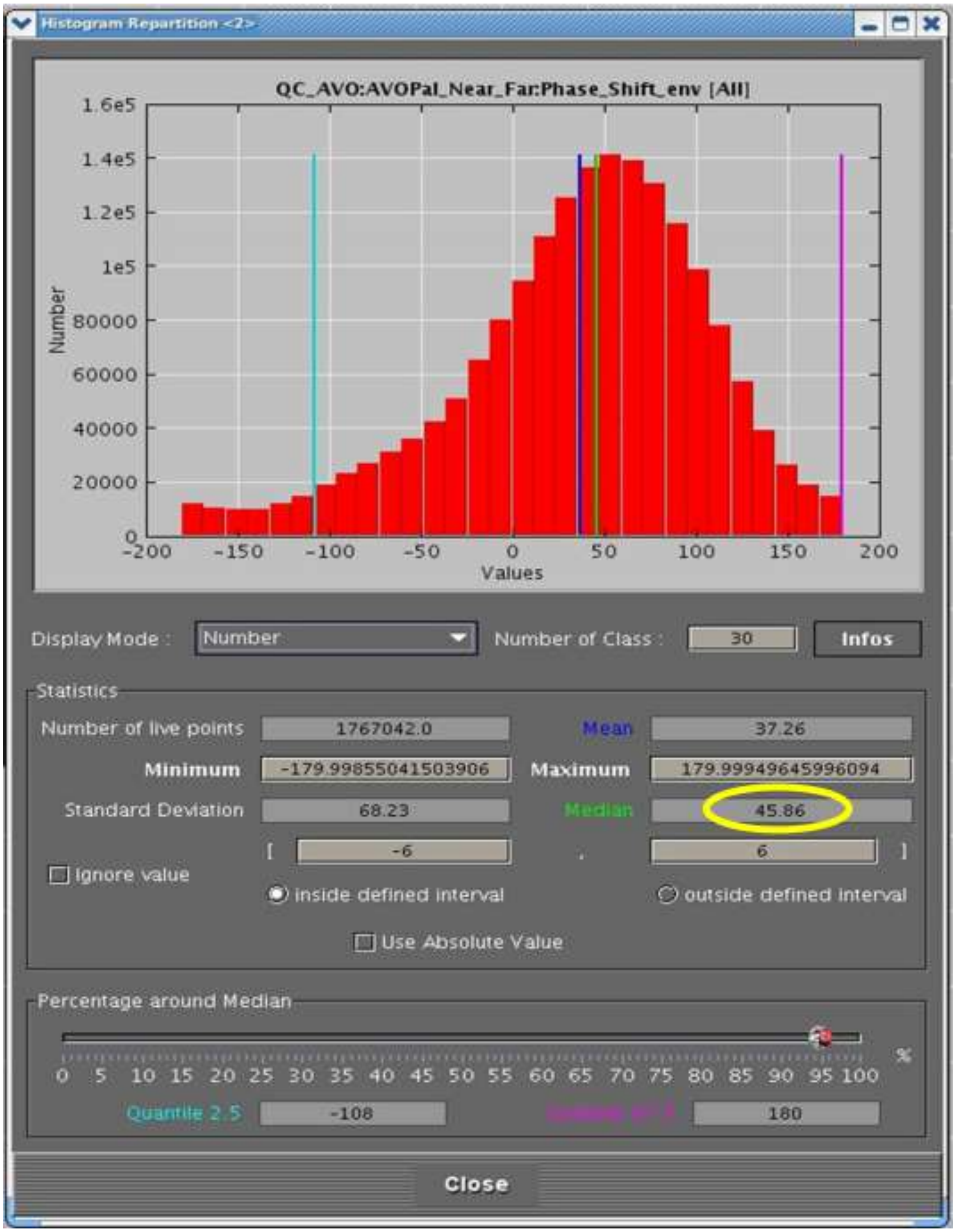

Figure 6.37: Histogram of phase shift between Near - Far pair

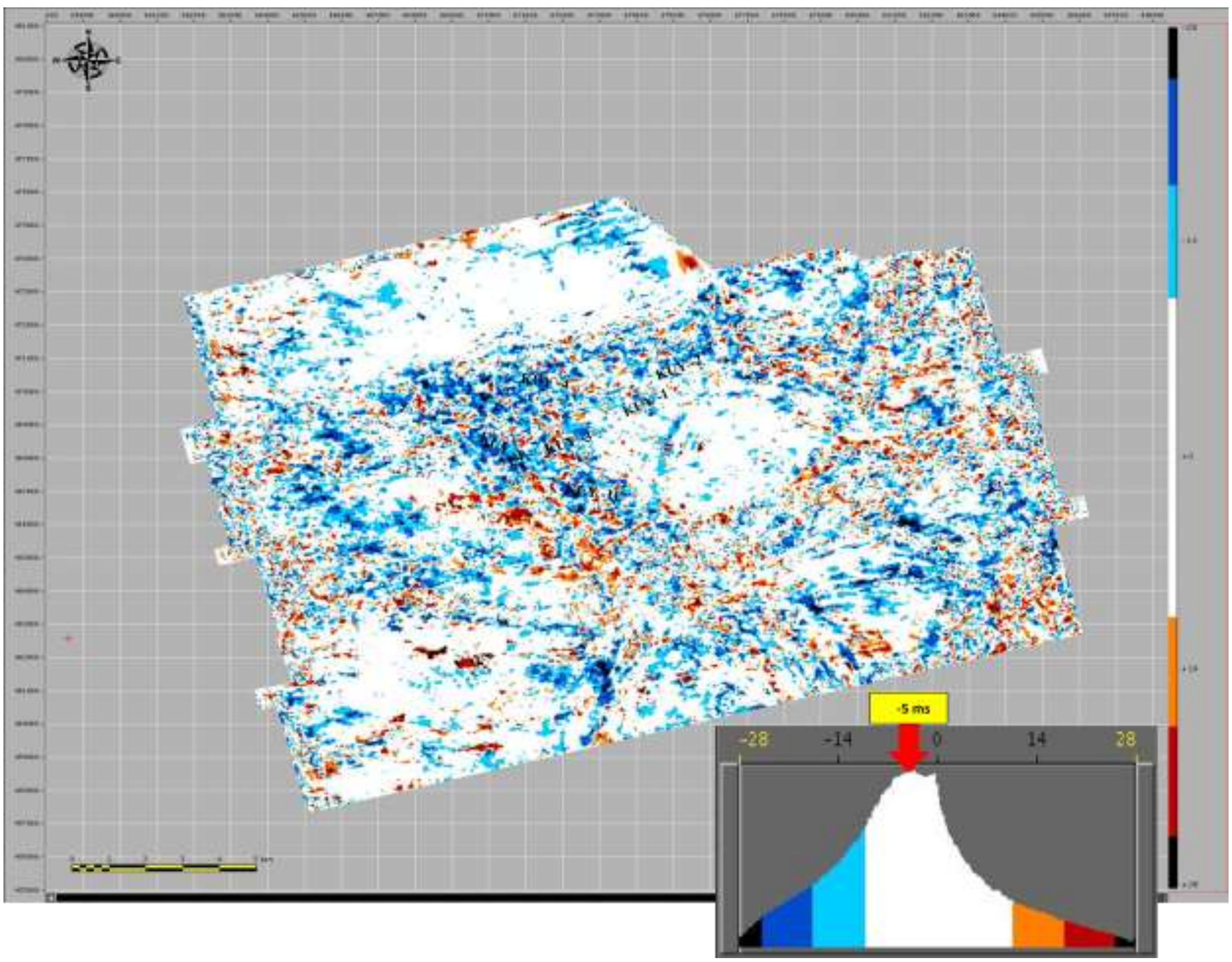

Figure 6.38: Time shift between Near – Far pair

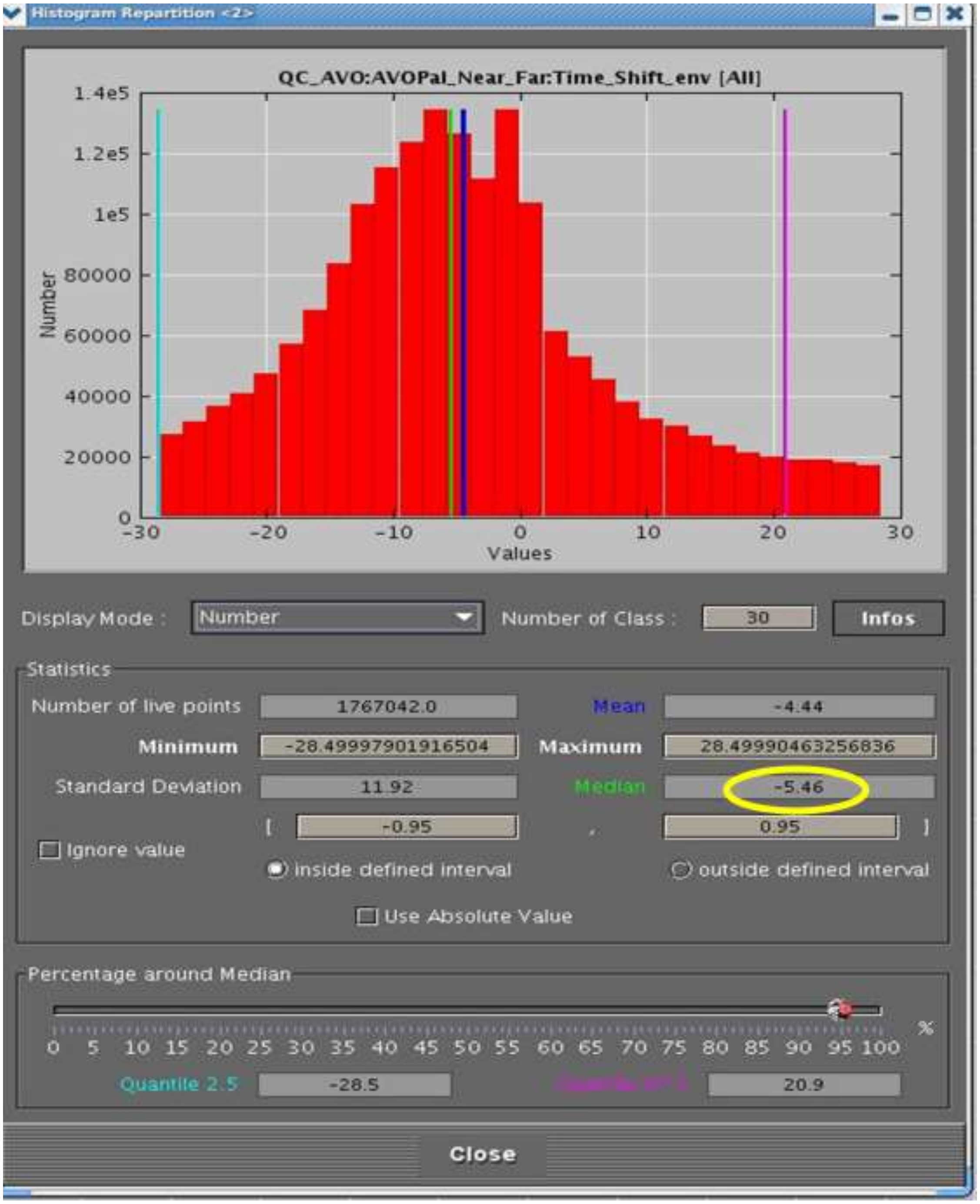

Figure 6.39: Histogram of phase shift between Near - Far pair (in yellow circle).

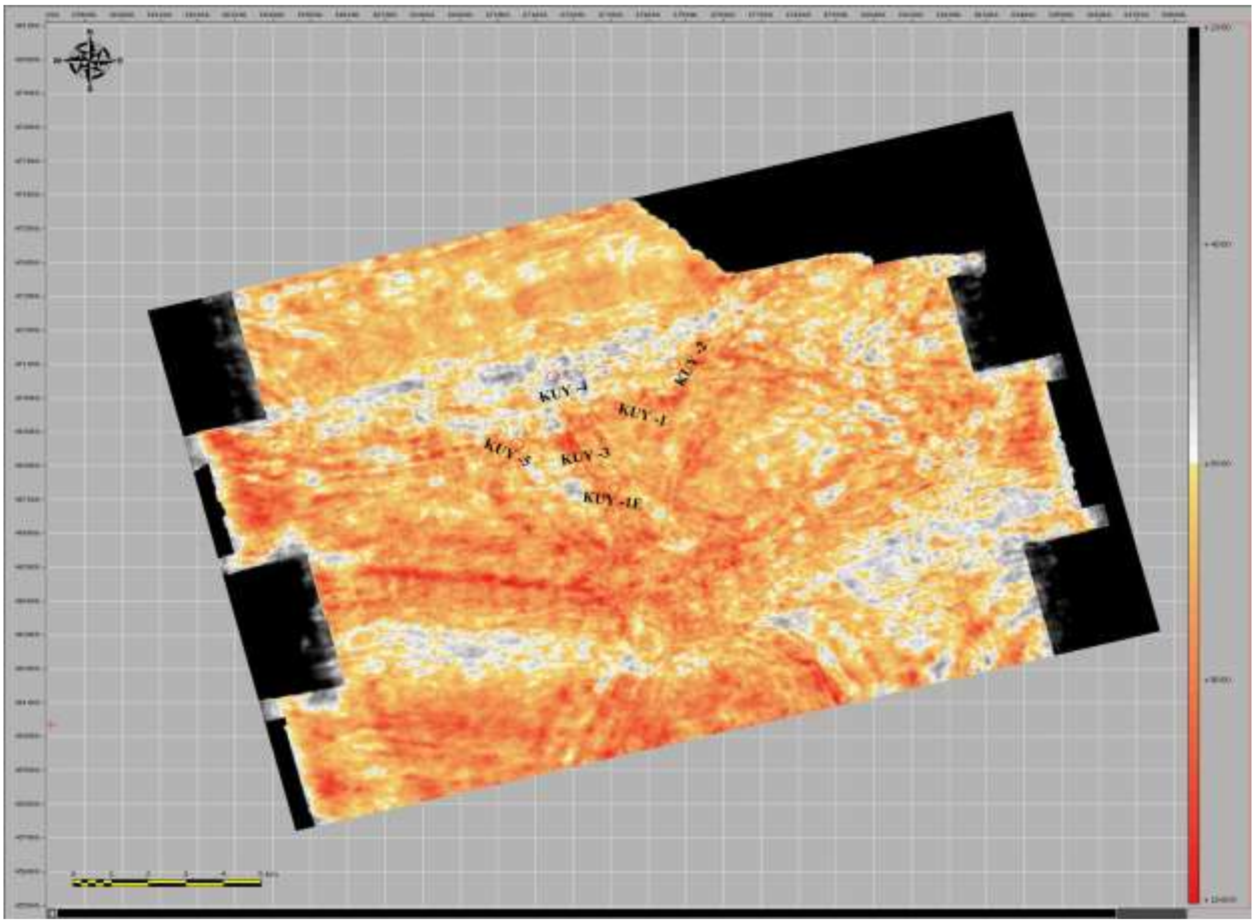

Figure 6.40: RMS amplitude map Near cube

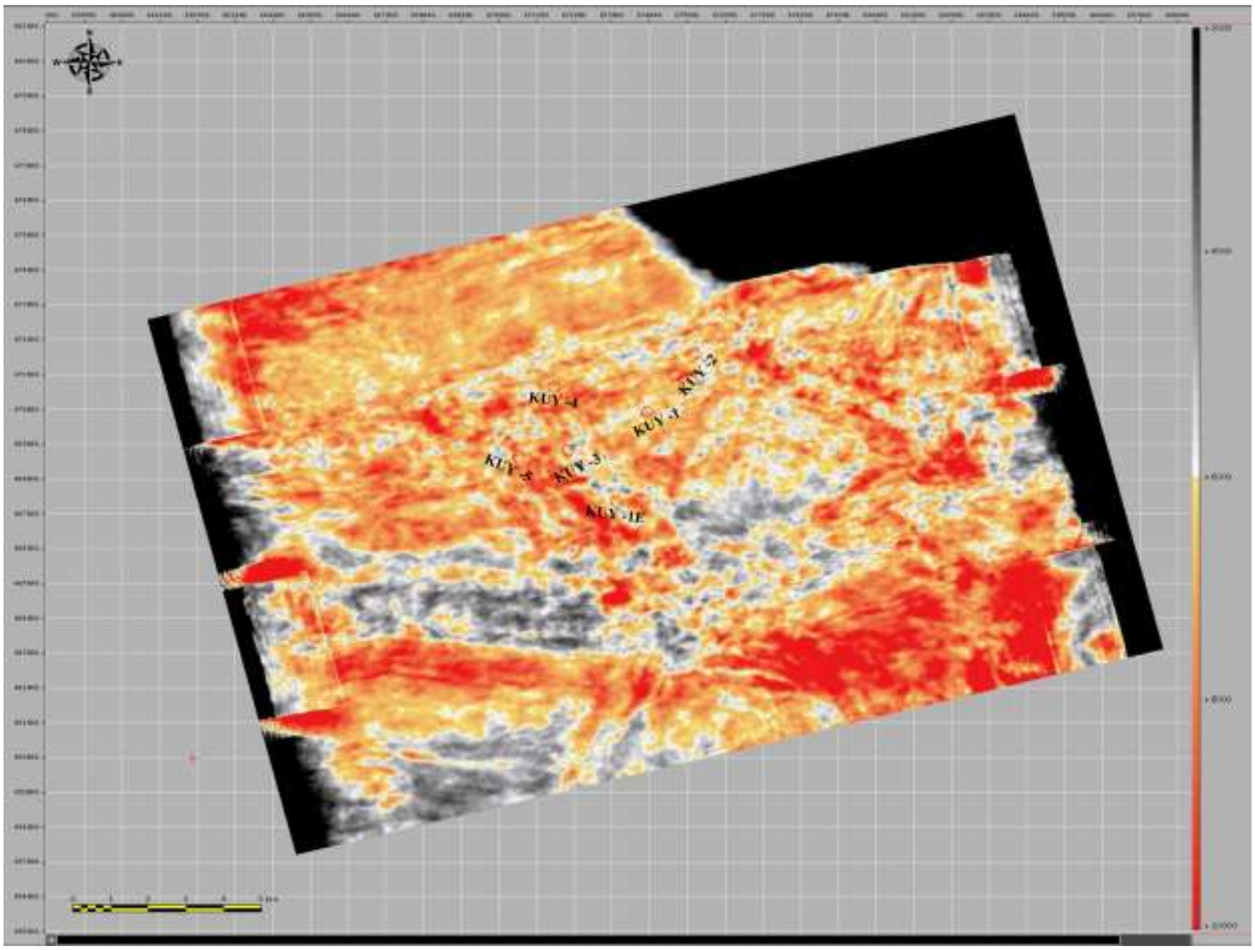

Figure 6.41: RMS amplitude map Far cube

6.3 Frequency Spectrum

The goal of this step was to display the average seismic spectrum for each substack cube and to verify the bandwidth.This would give us an idea of the bandpass filter to apply during the common bandwidth filtering. Frequency content was extracted for each substack around R11 reservoir in a time window ranging from 2100-3300ms TWT. There was good homogeneity of the frequency content between Near and Mid substack cubes while the Far substack cube showed a slight decrease of high frequencies.

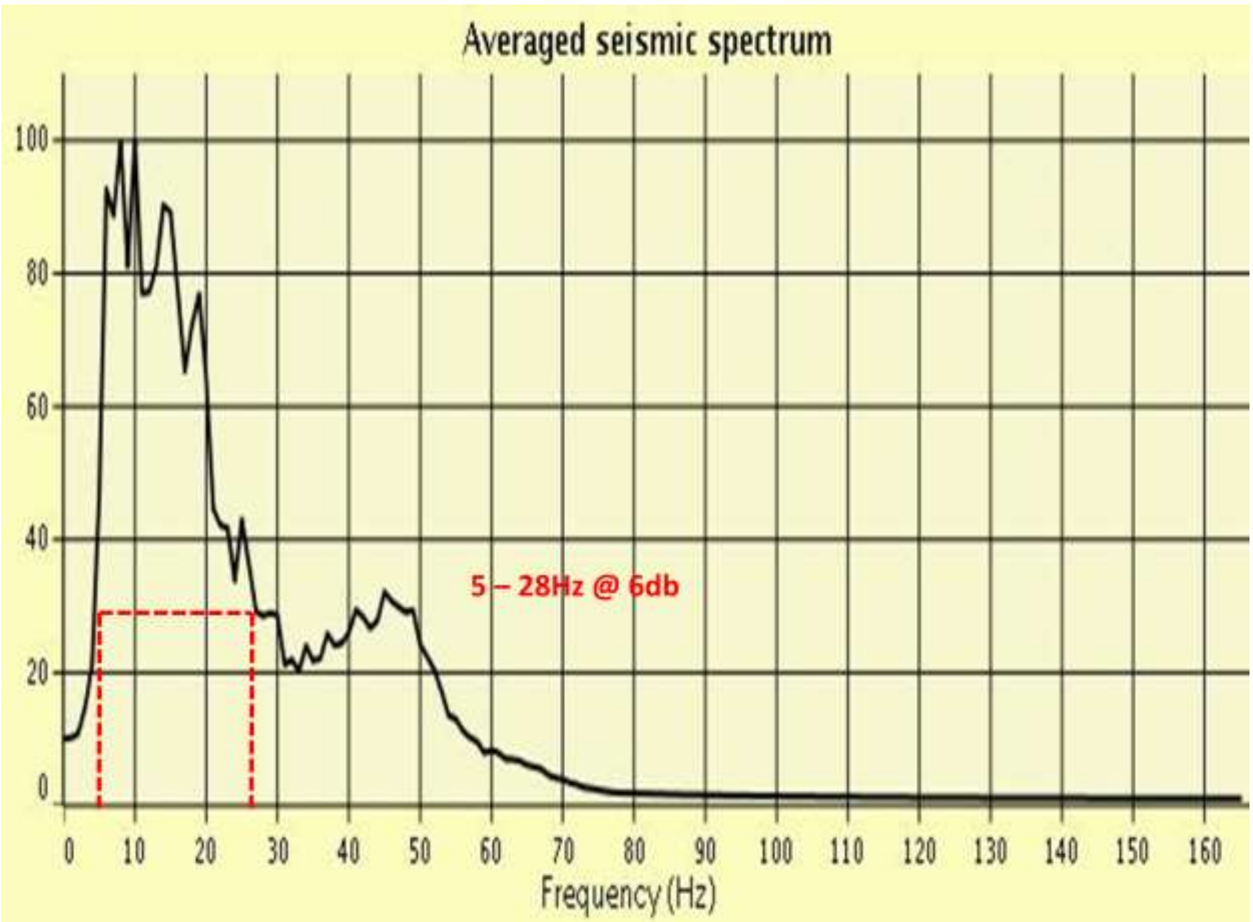

Figure 6.42: Frequency spectrum of the Near cube

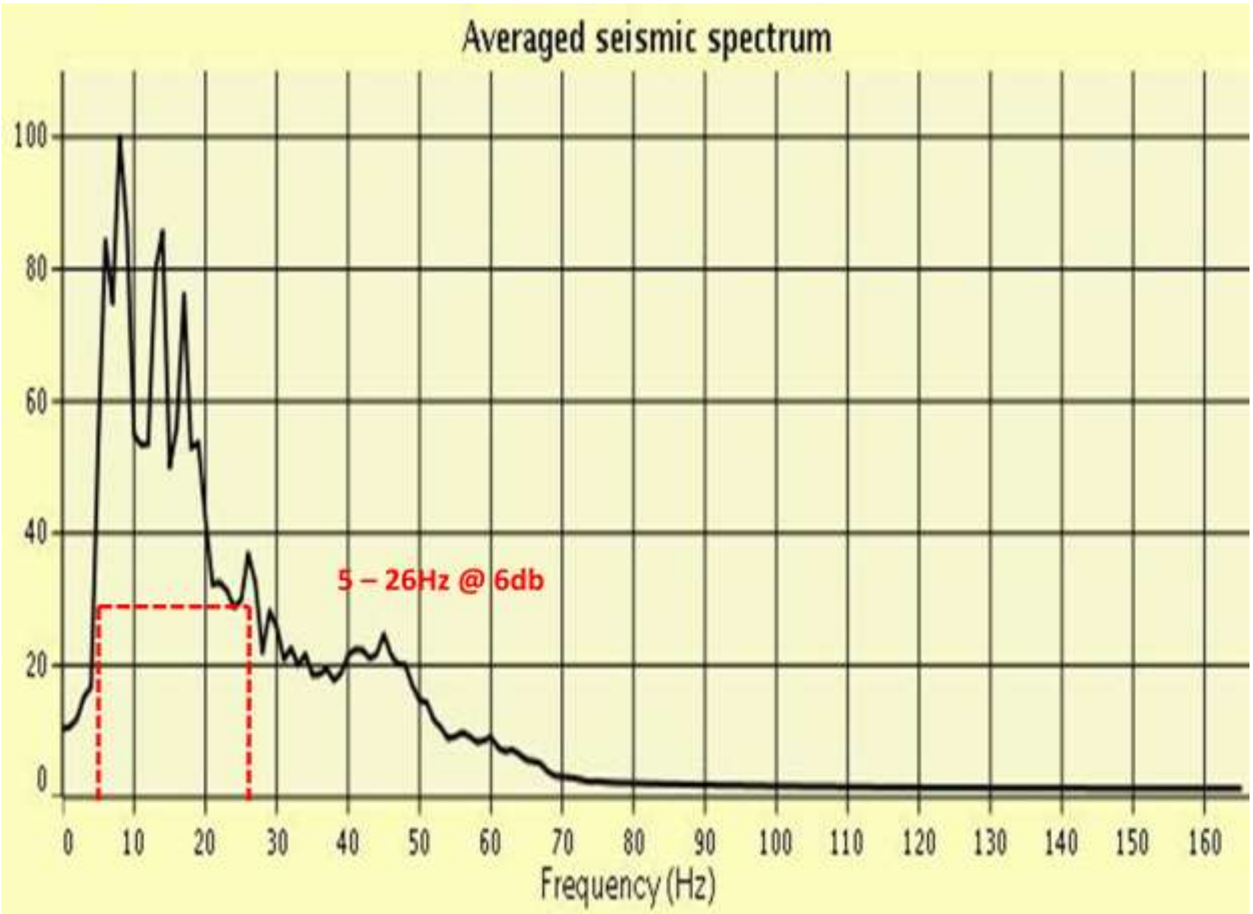

Figure 6.43: Frequency spectrum of the Mid cube

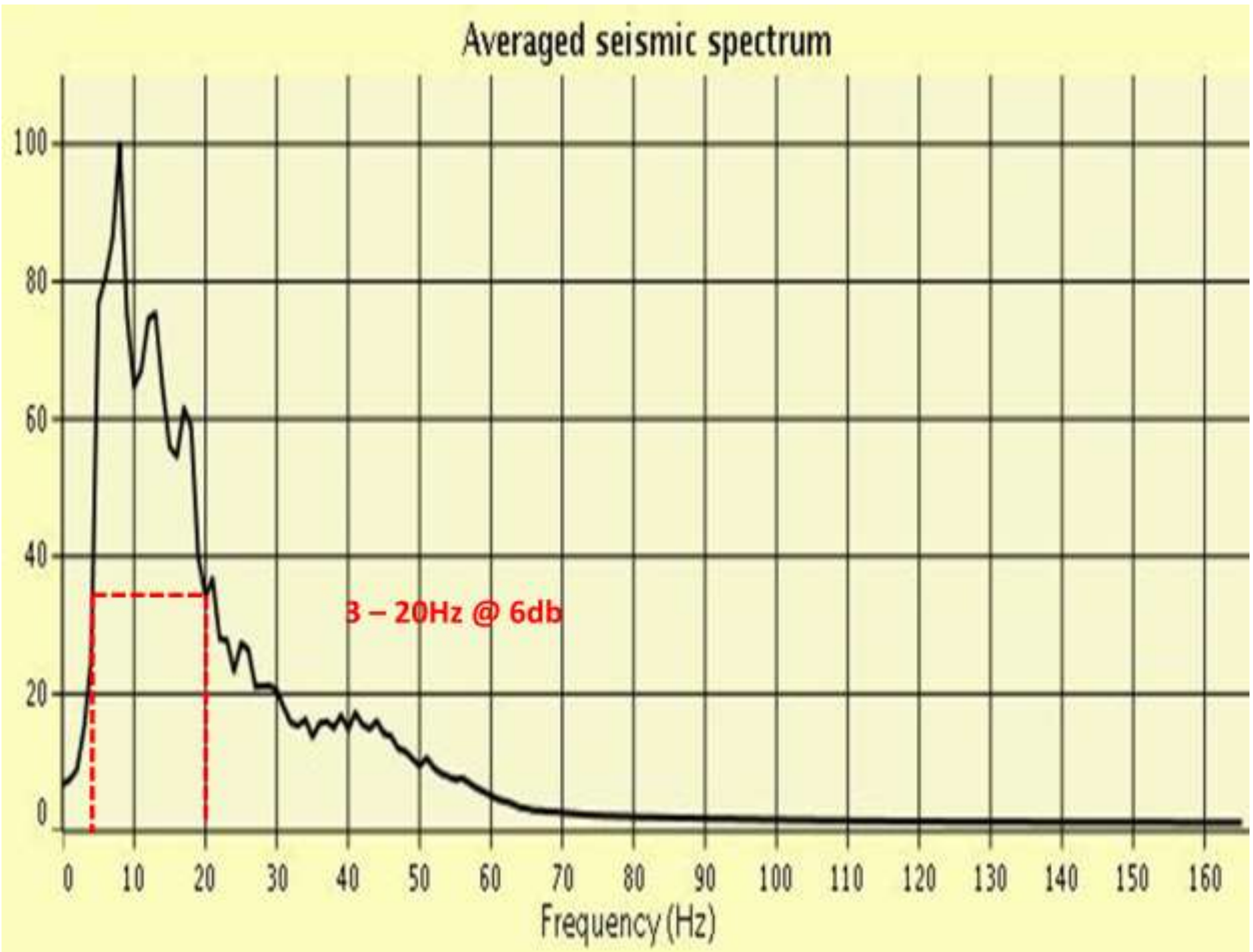

Figure 6.44: Frequency spectrum of the Far cube

6.4 Common Bandwidth Filtering

Comparing Near and Far cubes are only possible if we first balance spectra of each cube. The goal of this step is not only to work in a bandwidth with a sufficient signal to noise ratio for both cubes, but also to find and apply a common bandwidth on the Near and Far cubes to look at consistent AVO effects. The computation is divided in two phases. The first one is Preview phase. This launches a detailed analysis of both cubes, and sends results in two windows.

The first window shows analysis results superimposing elements computed for each cube separately (see Figure 6.46 for example).

1. Upper left part shows profiles of intercorrelation between one trace and its neighbouring trace. Comparing a trace with its neighbouring one is a good way to estimate the noise.
2. The upper right part, shows average of the autocorrelation profile for Near (dark blue), and the average of the autocorrelation profile for the Far (cyan blue). Comparing central peak of both shows energetic differential between cubes.
3. The lower right part shows estimated power spectra of signal and noise for each of the two cubes. It is the good place to compare bandwidths of both cubes and to evaluate what is the common bandwidth.
4. Finally, the lower left part shows statistical wavelets one for Near and one for Far. They are obtained by inverse Fourier transform of the square root of the signal power spectra described in above in number (no 3).

The second window shows, the signal processing analysis dealing with both cubes simultaneously (see Figure 6.48 for example).

1. The upper left part shows the intercorrelation profile between Near and Far block.
2. The upper right part shows the average intercorrelation signal in pink. The envelope of the intercorrelation is also shown in grey. The scale is in percentage (%) of correlation value. If the maximum of envelope is not centered at zero, it shows that a “global” time shift exists between cubes; when this observation is made across a significant part of the survey with the same value, it is compensated for as a bulk time shift. If the peak does not have its max value at the same time as the envelope, this suggests that the two cubes have a phase difference.
3. The lower right part shows again respective spectra of the Near and Far, but also the spectrum of intercorrelation between Near and Far (pink). This last spectrum is a quite good representation of the common bandwidth between Near and Far cubes.
4. Finally, the plot in the lower left part shows the RMS amplitude profiles for the Near and the Far. It allows analyzing if a great dynamic difference exists between these cubes. It is expected here that the main features (trends / major variations) are similar for both seismic cubes.

The second phase consists in building the appropriate bandpass filter to build two new Near and Far cubes sharing the same bandwidth. To do this, we play with “filter spectrum” part of the interface (yellow), and adjust the spectrum of the filter on the pink intercorrelation spectrum. Once the filter is finished, we give a name to the filtered Near cube and the filtered Far cube and then Compute. Result is checked by doing the same inline or crossline analysis after filtering and a stretch map obtained should be roughly about 100% for angle substack pair.

Common bandwidth filtering was computed around R11 reservoir in a time window ranging from 2100-3300ms TWT by first previewing the pair (Near – Mid, Mid – Far & Near – Far) to determine an appropriate bandpass filter for the Near and Far cubes. This bandpass filter was then applied on the Near and Far cubes to build two new Near and Far cubes having the same bandwidth so as to look at consistent AVO effects (see hereunder).

1. Select the original NEAR and FAR datasets:
2. Define a crossline for the analysis of both cubes
3. Select a time Interval
4. Play with filter spectrum and adjust the spectrum of the filter
5. Give a new name for the filtered cube
6. Click on preview first and later compute

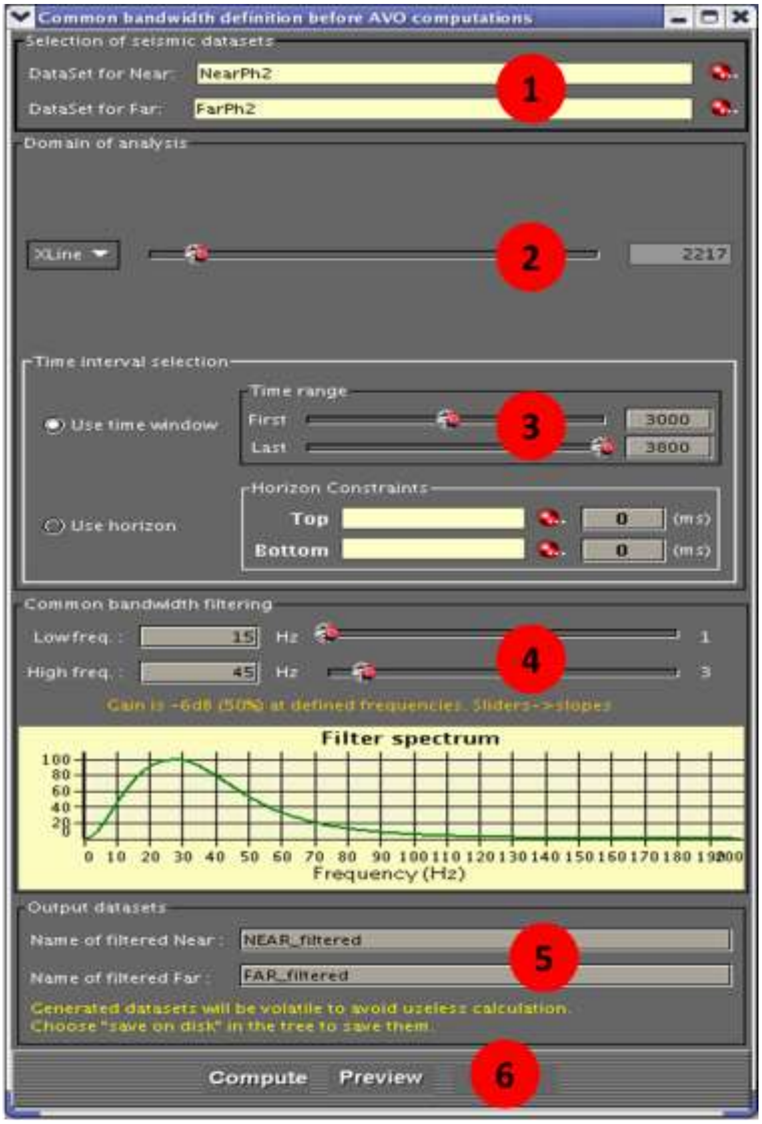

Figure 6.45: Sismage interface for common bandwidth filtering

6.4.1 Near – Mid Common Bandwidth Filtering

In order to align the cubes so as to look at consistent AVO effects for this pair, a 26Hz High-cut filter with a slope of 6 was applied to the Near stack while no filtering was applied to the Mid stack.

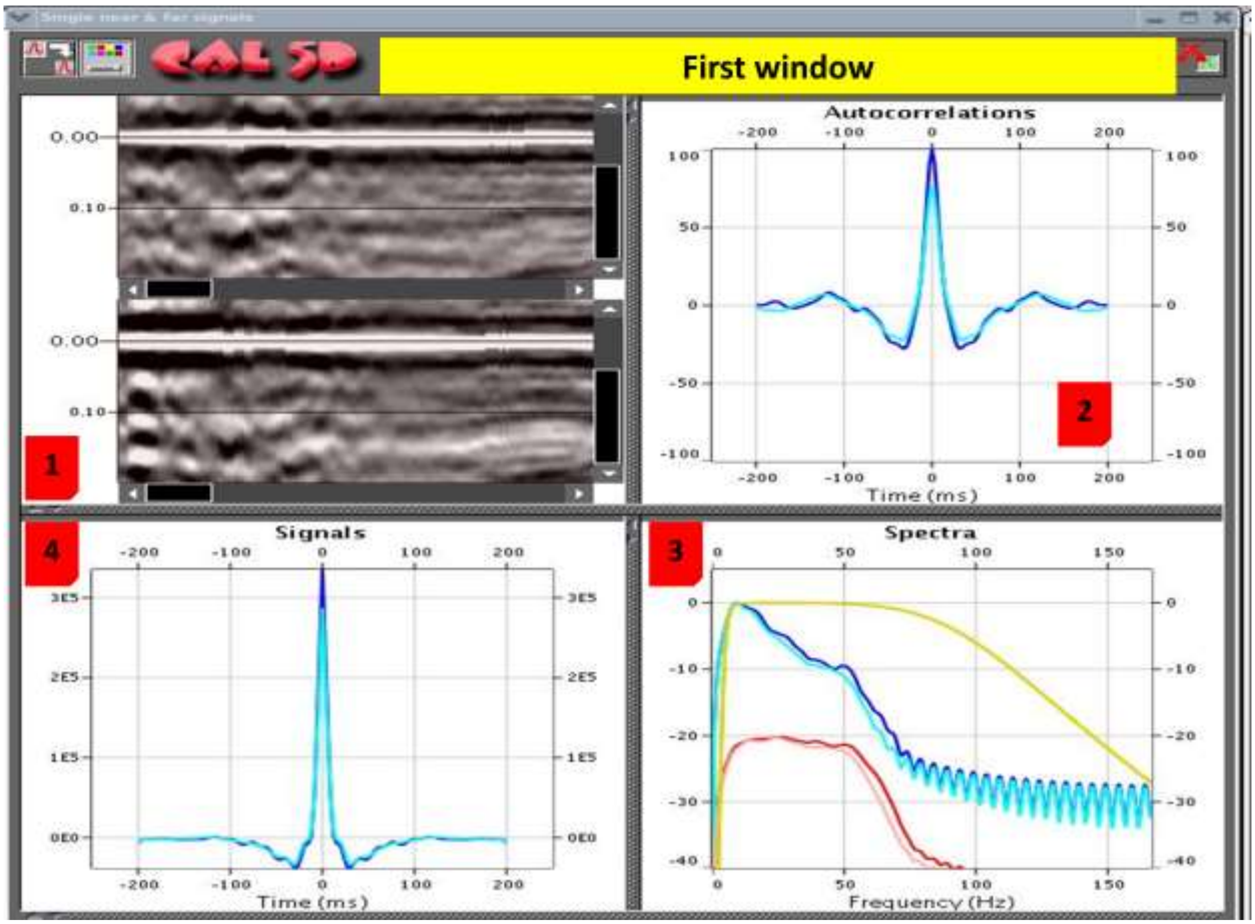

Figure 6.46: First window preview phase of Near – Mid pair before filtering. Upper left part (1) shows profiles of intercorrelation between one trace and its neighbouring trace. The upper right part (2), shows average of the autocorrelation profile for Near (dark blue), and the average of the autocorrelation profile for the Far (cyan blue). The lower right part (3) shows estimated power spectra of signal and noise for each of the two cubes. The lower left part (4) shows the RMS amplitude profiles for the Near and the Far. See section 6.4 for details.

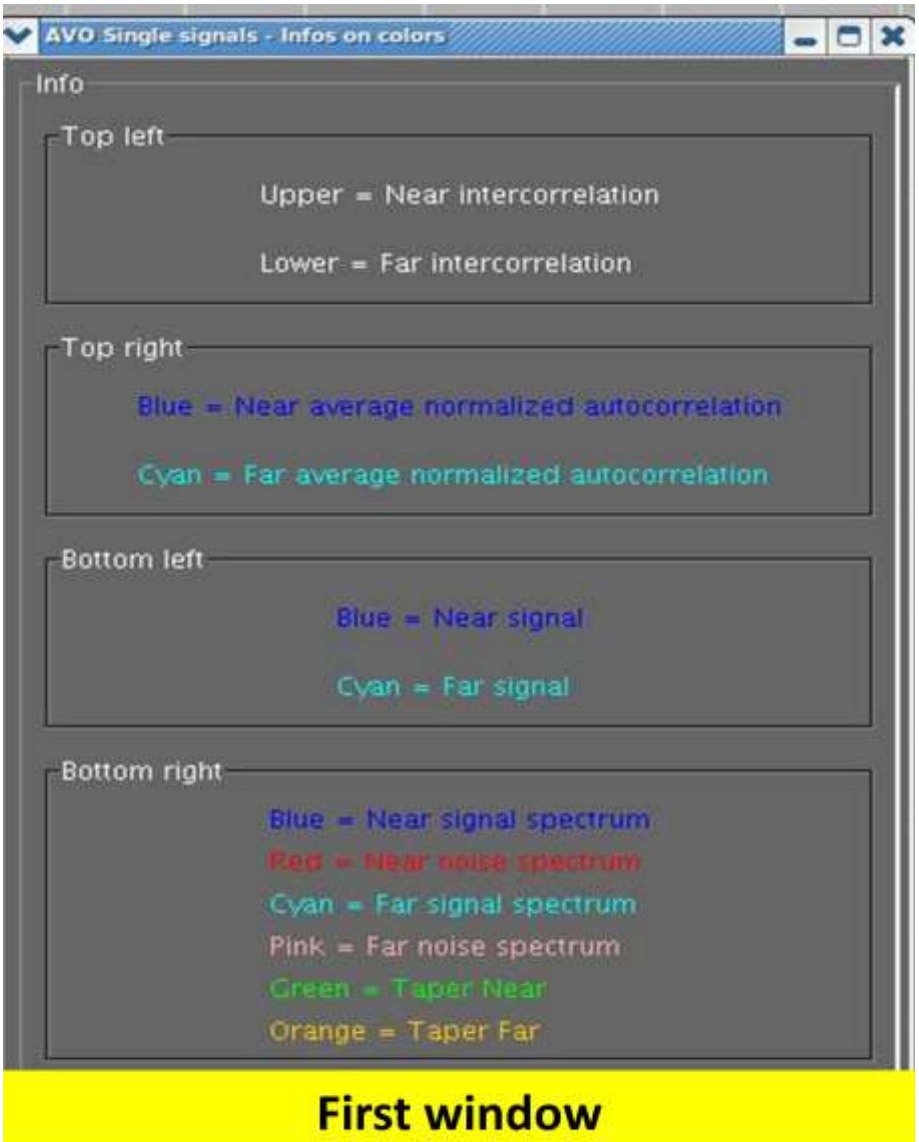

Figure 6.47: Information on colours for all first windows used in Near – Mid, Mid – Far & Near – Far combinations

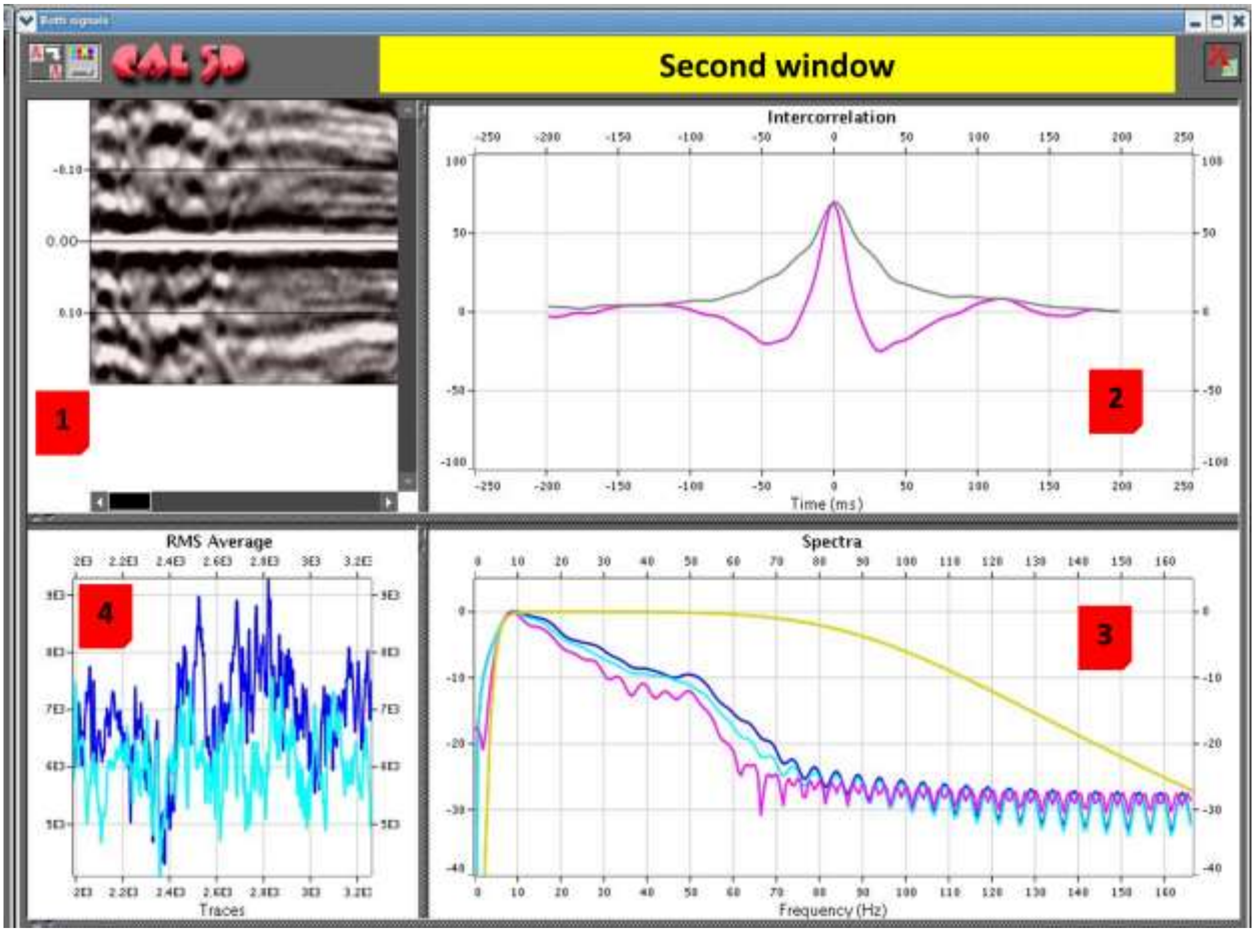

Figure 6.48: Second window preview phase of Near–Mid pair before filtering. The upper left part (1) shows the intercorrelation profile between Near and Far block. The upper right part (2) shows the average intercorrelation signal in pink. The lower right part (3) shows respective spectra of the Near and Far. The lower left part (4) shows the RMS amplitude profiles for the Near and the Far. See section 6.4 for detail.

Figure 6.49: Information on colours for all second windows used in Near –Mid, Mid – Far & Near – Far combinations

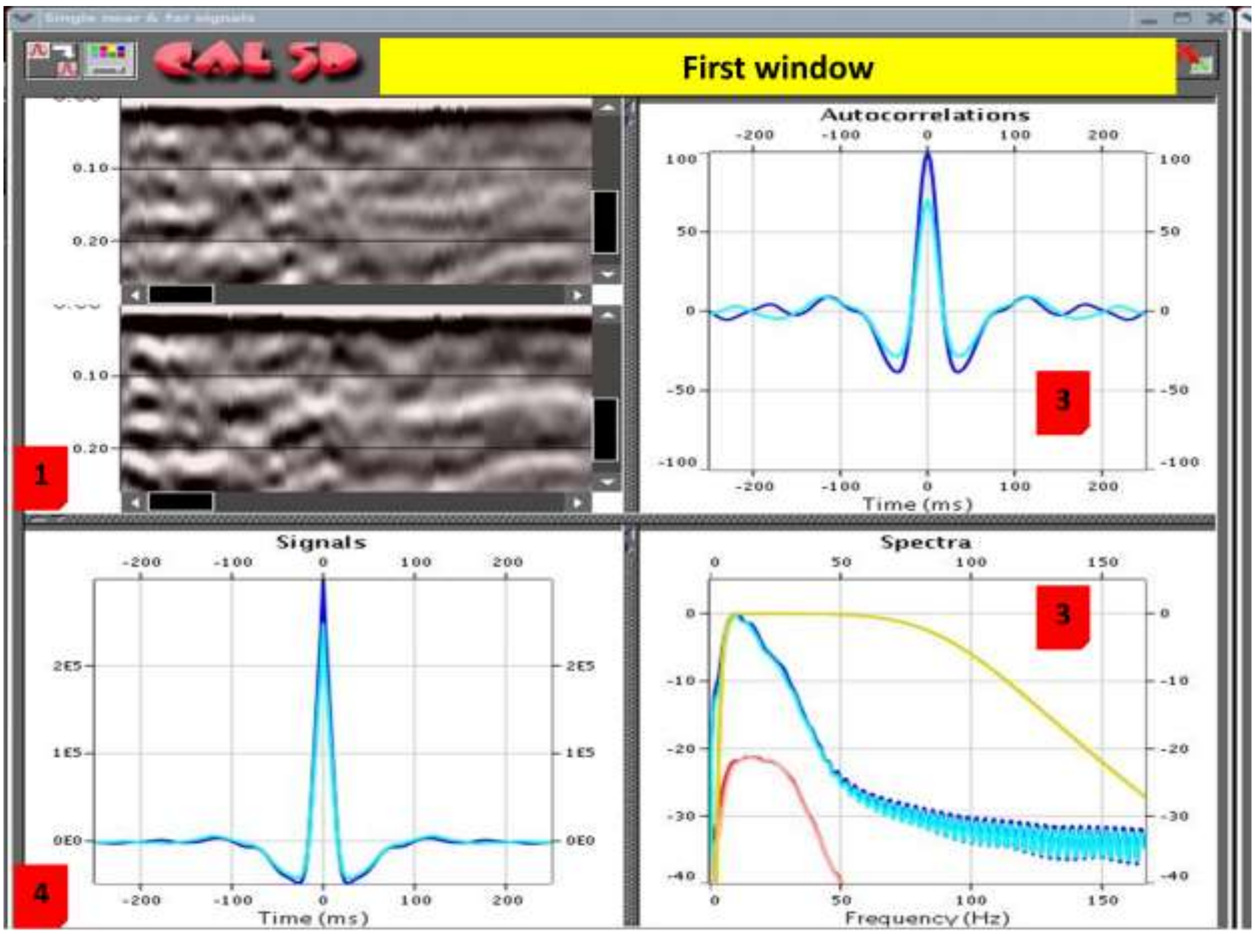

Figure 6.50: First window preview phase of Near – Mid pair after filtering. See Figure 6.46 for details on parts (upper left & right parts, lower left & right parts).

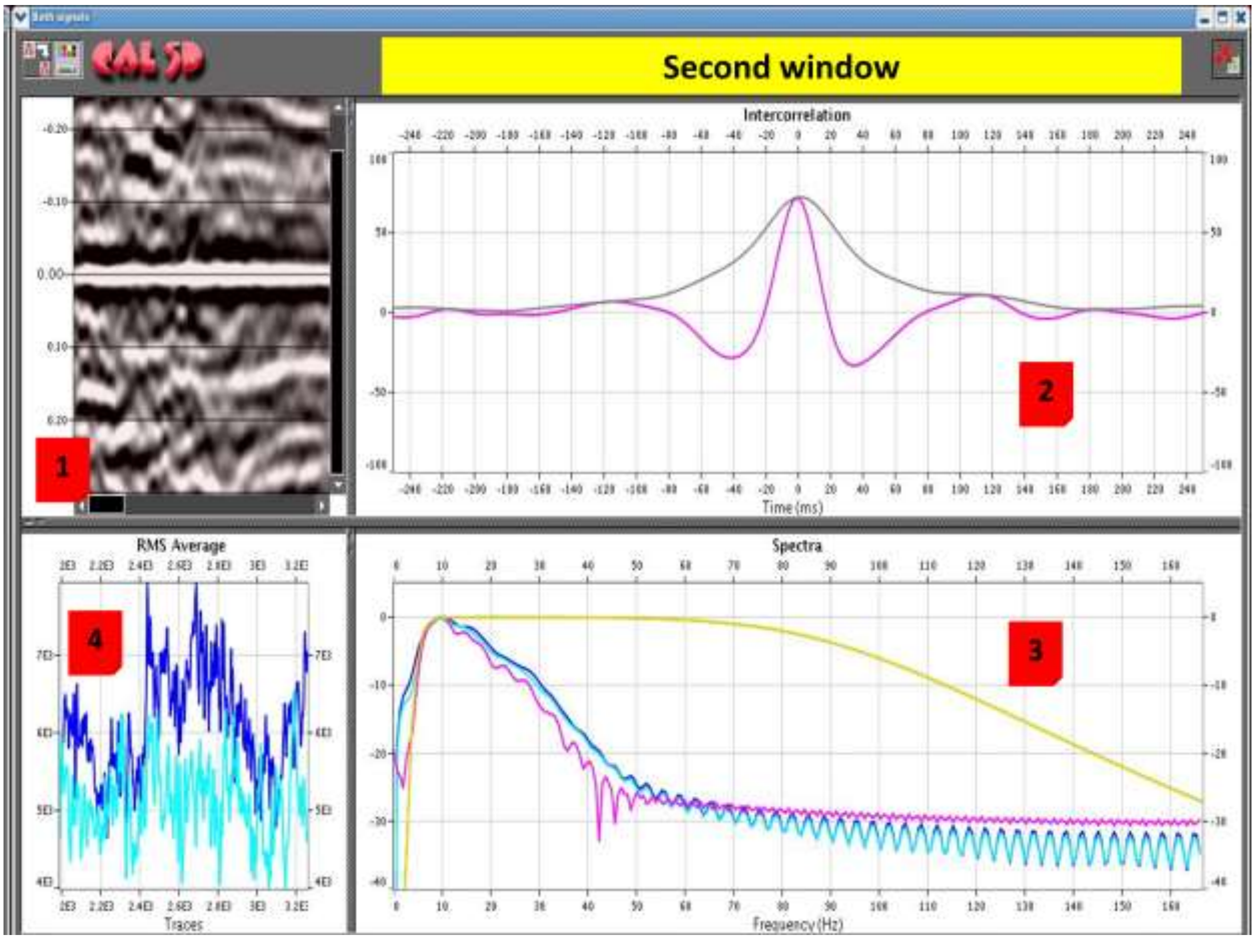

Figure 6.51: Second window preview phase of Near – Mid pair after filtering. See Figure 6.48 for details on parts (upper left & right parts, lower left & right parts).

6.4.2 Mid – Far Common Bandwidth Filtering

A 20Hz High-cut filter with a slope of 2 was applied to the Mid cube while 2Hz Low-cut filter with a slope of 3 was applied to the Far cube to align the two substacks so as to look at consistent AVO effects.

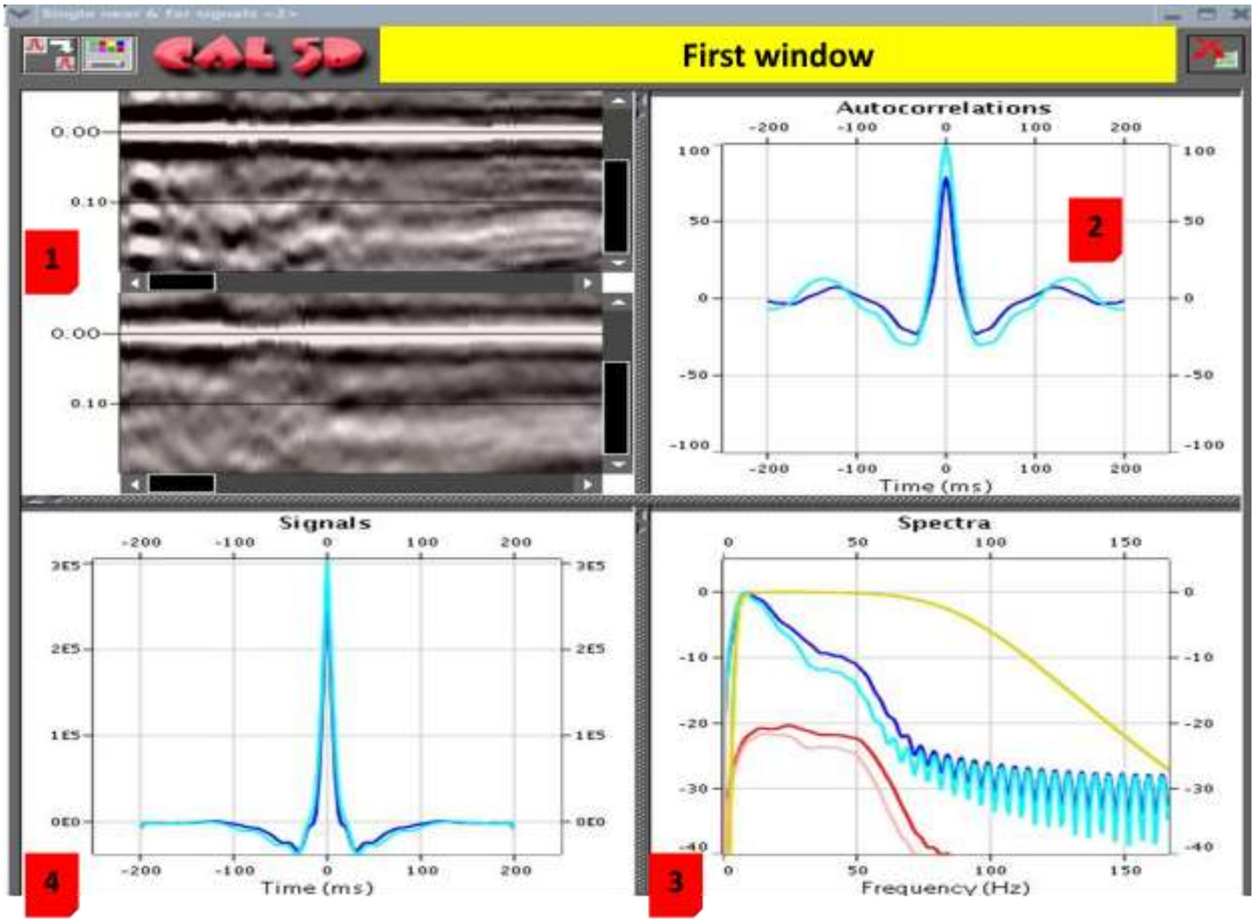

Figure 6.52: First window preview phase of Mid-Far before filtering. Upper left part (1) shows profiles of intercorrelation between one trace and its neighbouring trace. The upper right part (2), shows average of the autocorrelation profile for Near (dark blue), and the average of the autocorrelation profile for the Far (cyan blue). The lower right part (3) shows estimated power spectra of signal and noise for each of the two cubes. The lower left part (4) shows the RMS amplitude profiles for the Near and the Far. See section 6.4 for details.

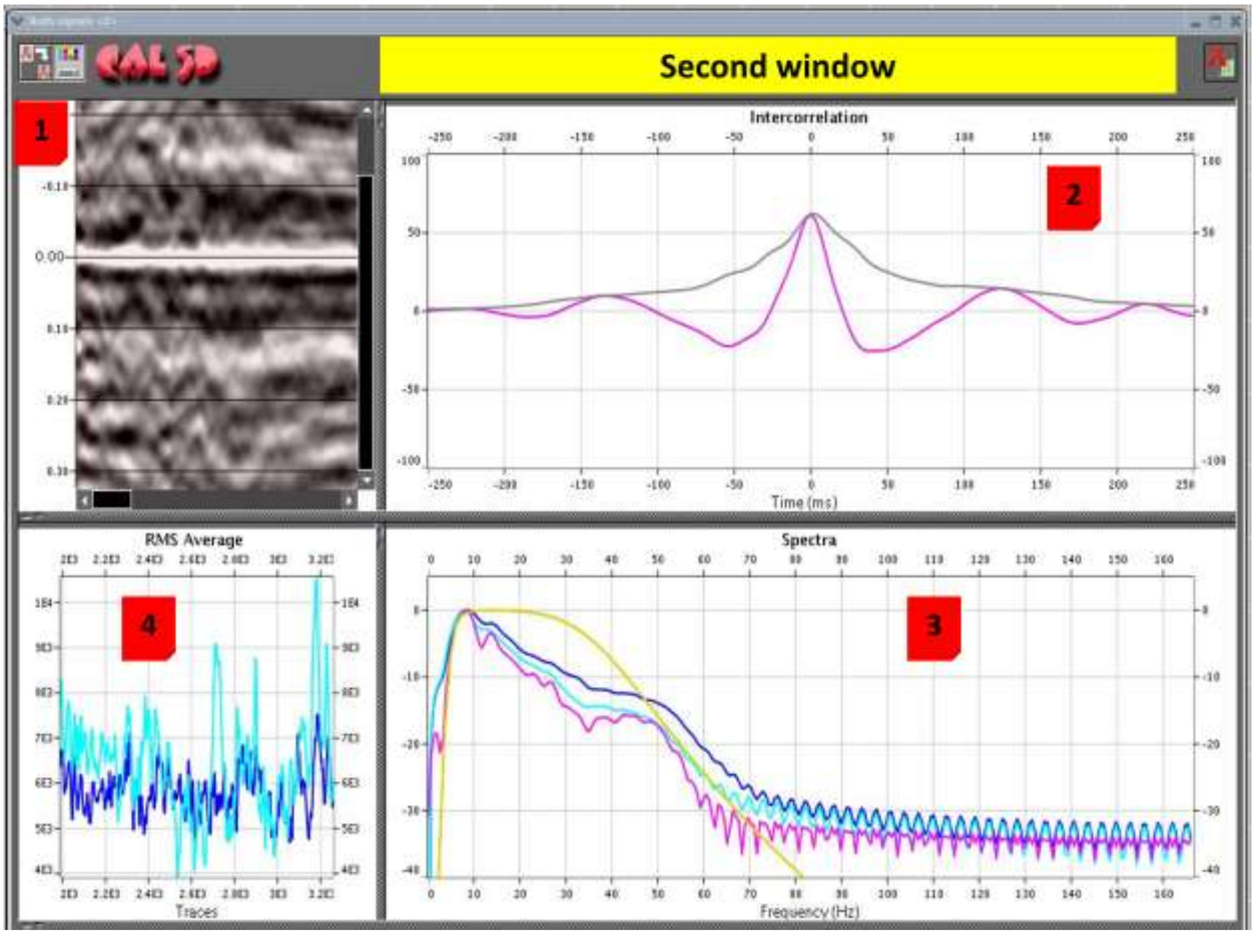

Figure 6.53: Second window preview phase of Mid–Far pair before filtering. The upper left part (1) shows the intercorrelation profile between Mid and Far block. The upper right part (2) shows the average intercorrelation signal in pink. The lower right part (3) shows respective spectra of the Mid and Far. The lower left part (4) shows the RMS amplitude profiles for the Mid and the Far. See section 6.4 for detail.

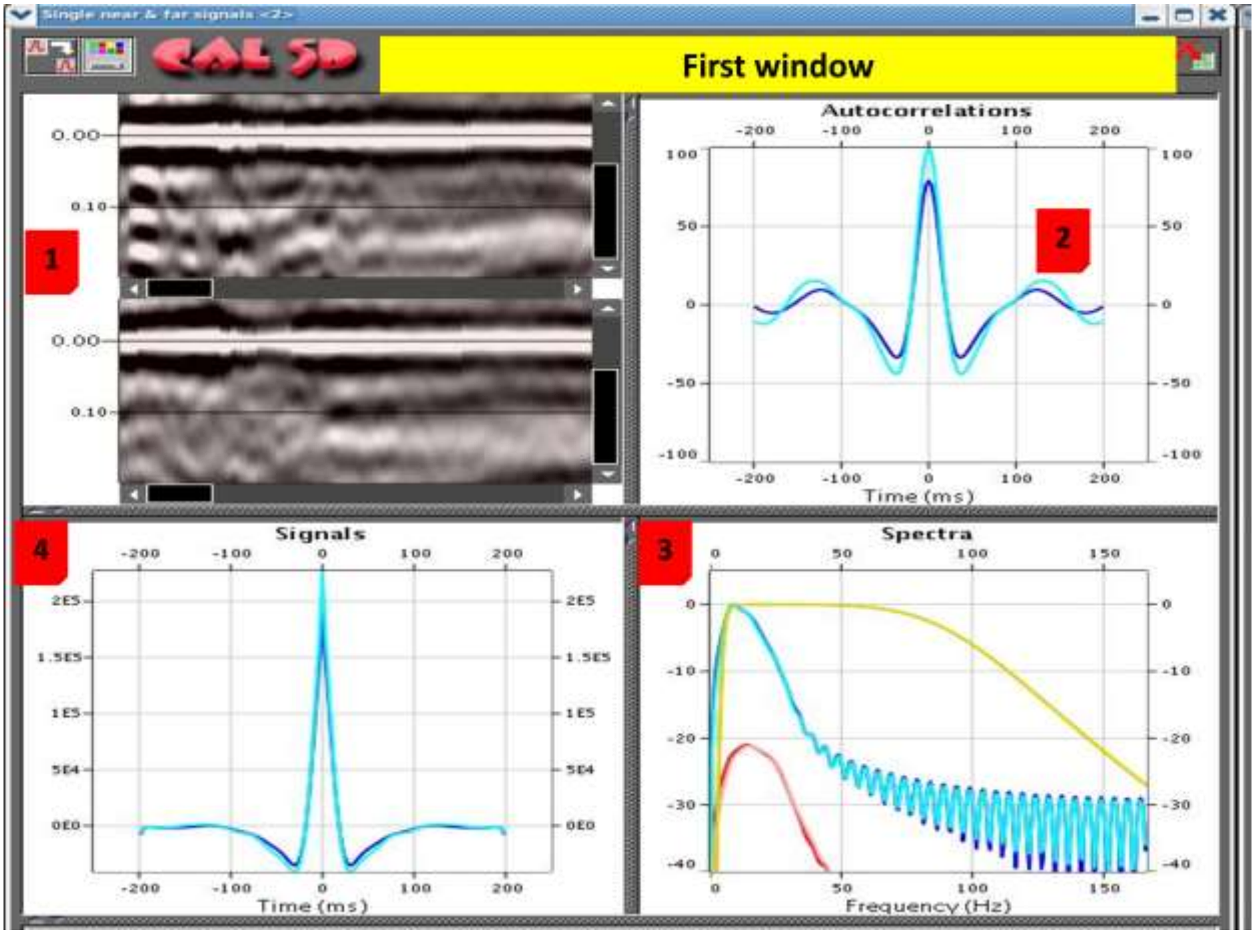

Figure 6.54: First window preview phase of Mid-Far after filtering. Upper left part (1) shows profiles of intercorrelation between one trace and its neighbouring trace. The upper right part (2), shows average of the autocorrelation profile for Mid (dark blue), and the average of the autocorrelation profile for the Far (cyan blue). The lower right part (3) shows estimated power spectra of signal and noise for each of the two cubes. The lower left part (4) shows the RMS amplitude profiles for the Mid and the Far.

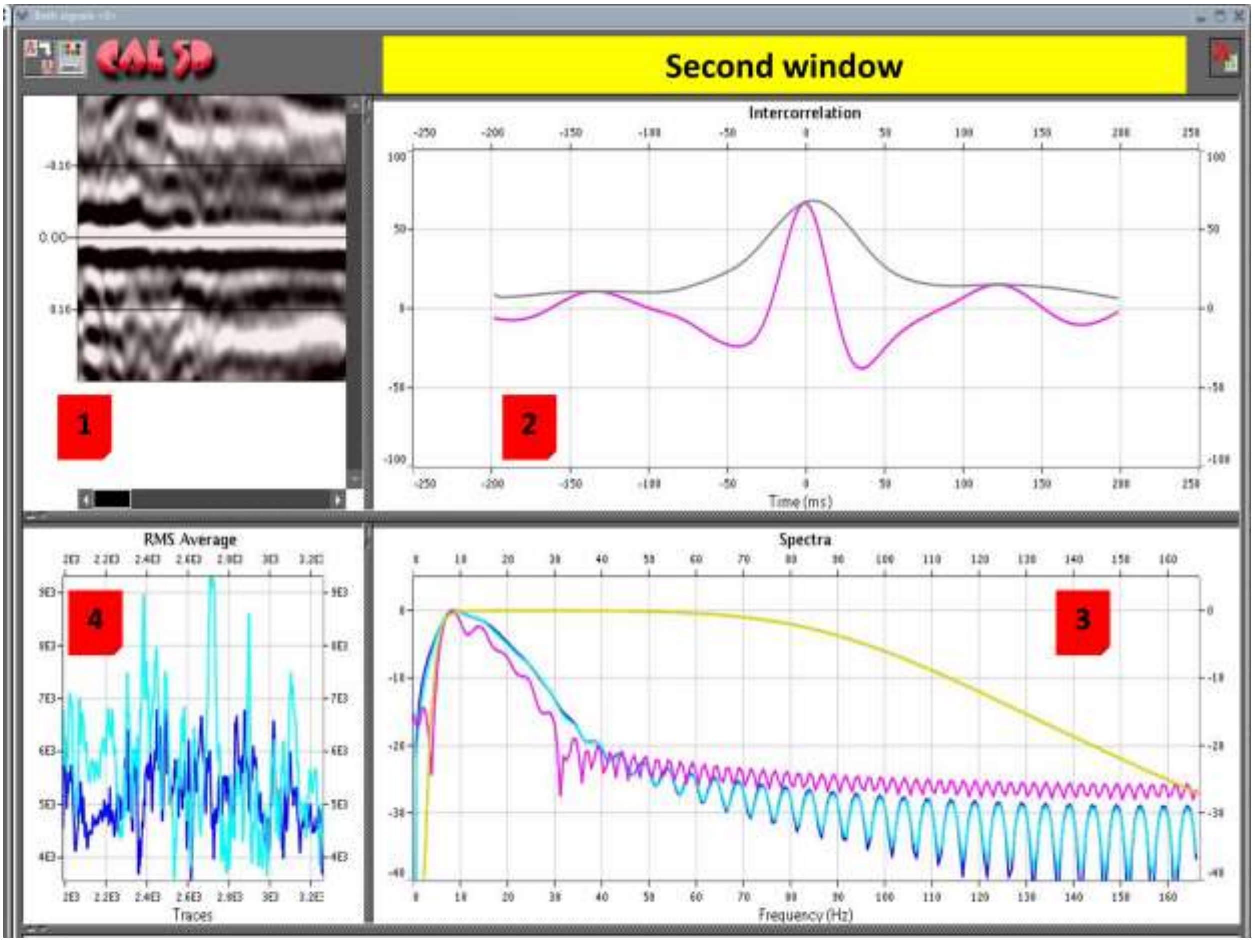

Figure 6.55: Second window preview phase of Mid–Far pair after filtering. The upper left part (1) shows the intercorrelation profile between Mid and Far block. The upper right part (2) shows the average intercorrelation signal in pink. The lower right part (3) shows respective spectra of the Mid and Far. The lower left part (4) shows the RMS amplitude profiles for the Mid and the Far.

6.4.3 Near – Far Common Bandwidth Filtering

For this pair of substack, a phase and time shifts of 46 degrees and +5ms was first applied on the original/raw Far cube to create a new Far cube. 27Hz High-cut filter with a slope of 2 was applied to the Near stack while a 2Hz Low-cut filter with a slope of 4 was then applied to the new Far stack created to align both substacks so as to look at consistent AVO effects.

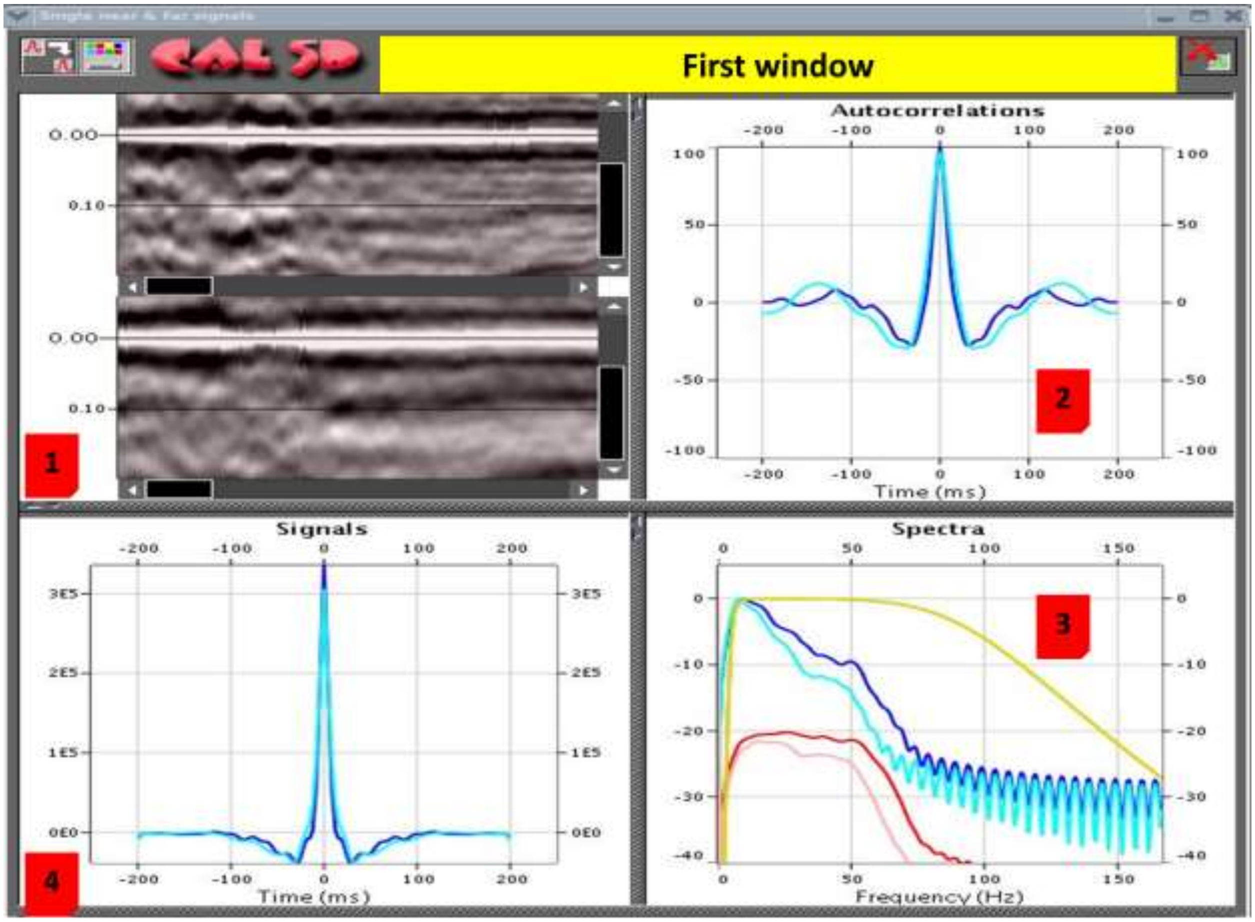

Figure 6.56: First window preview phase of Near-Far before filtering.

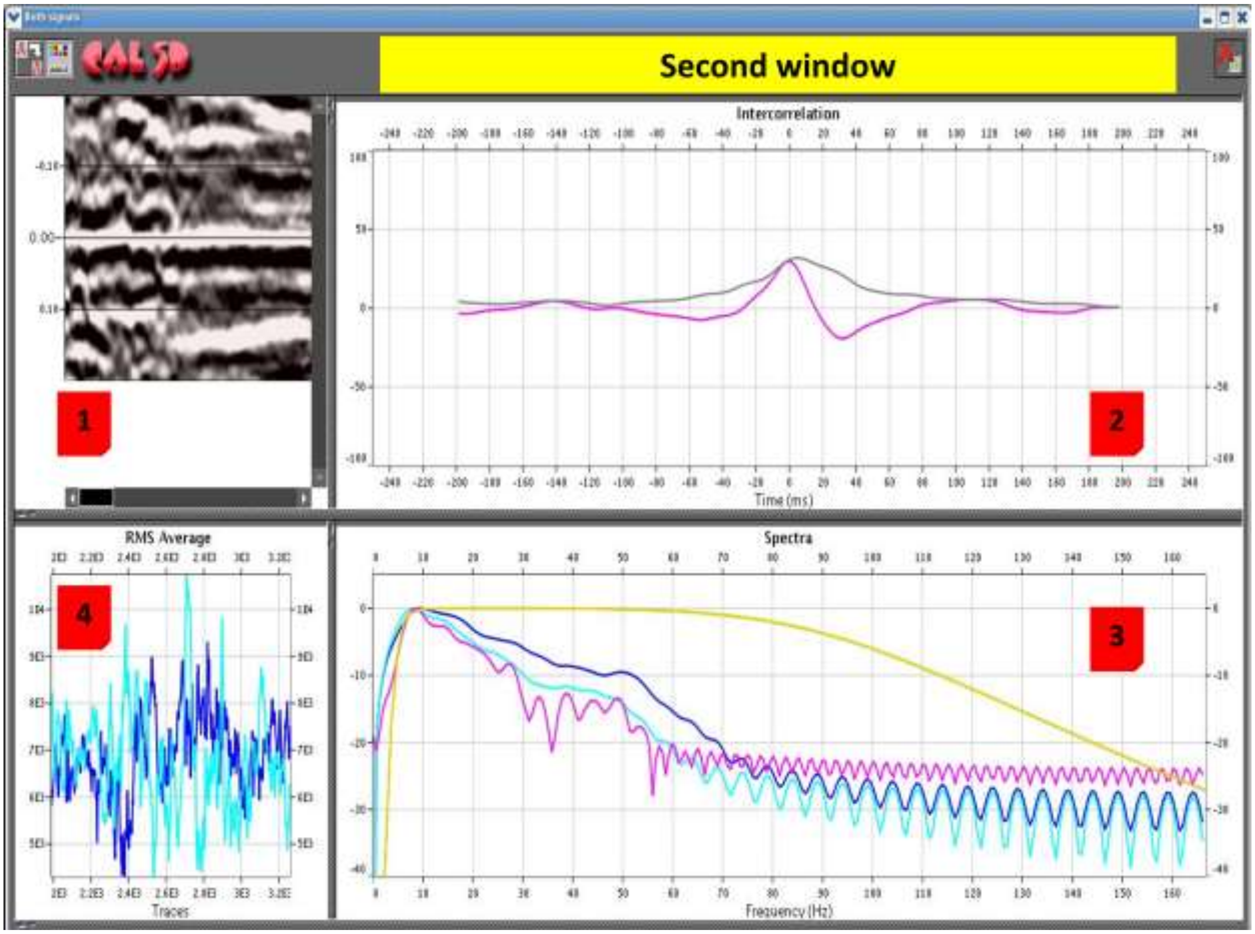

Figure 6.57: Second window preview phase of Near-Far before filtering.

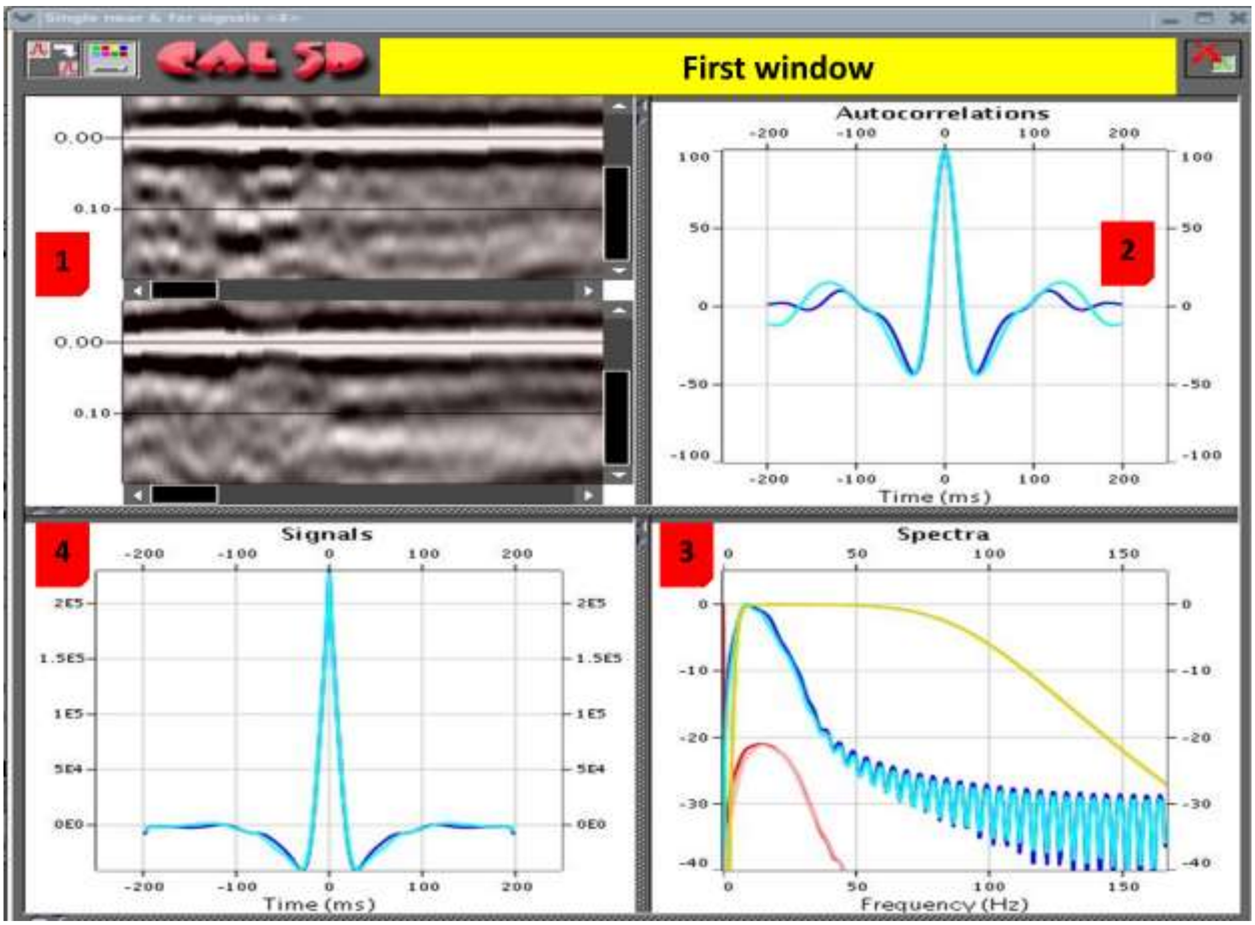

Figure 6.58: First window preview phase of Near-Far after filtering.

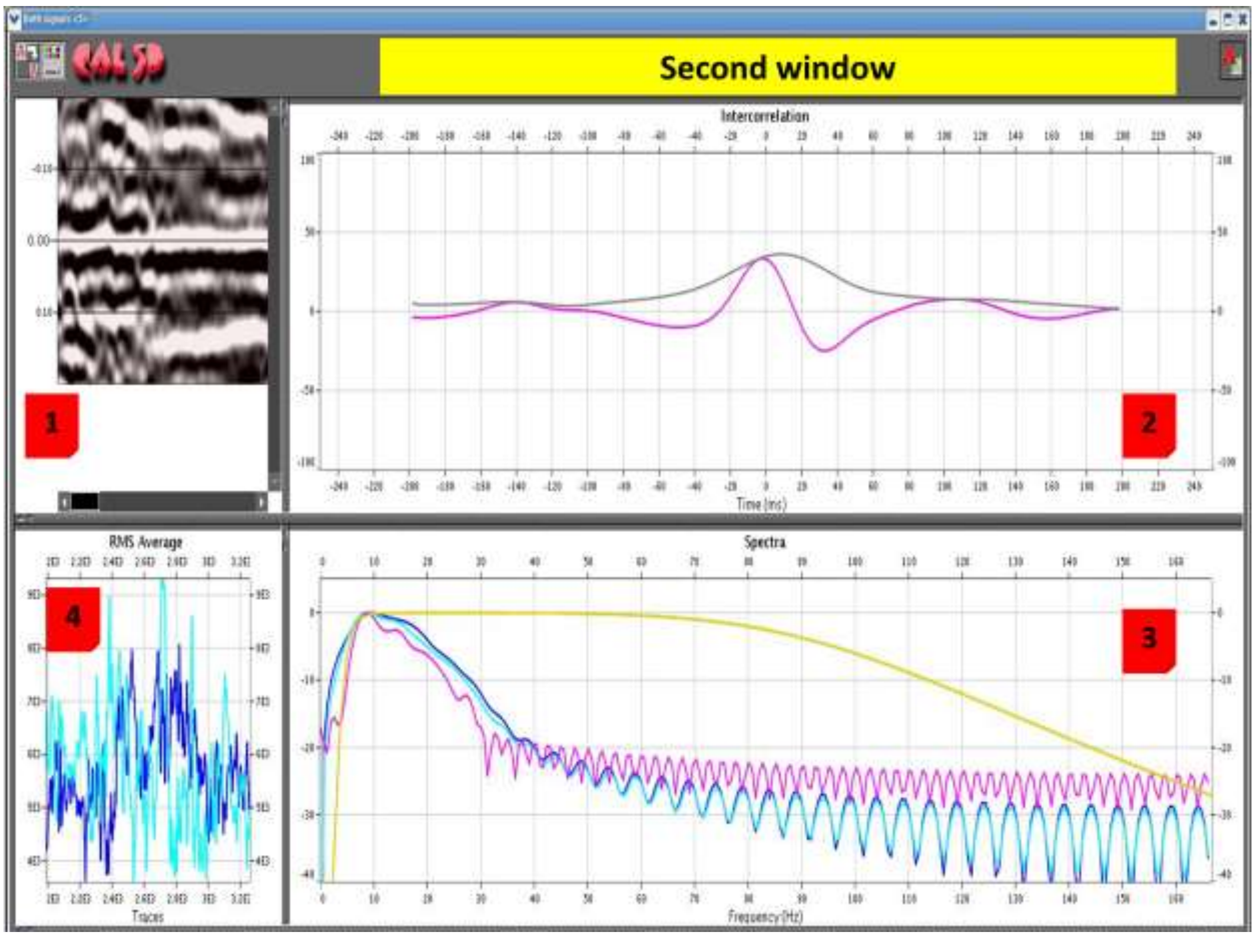

Figure 6.59: Second window preview phase of Near-Far after filtering.

6.5 Validation of Sub-stack Pair Choice after Common Bandwidth Filtering

The QC maps were recomputed around the studied AVO interval using the filtered cubes of sections 6.4.1, 6.4.2 and 6.4.3, to see how it improved on the cross-correlation maps. If average (median) cross-correlation is globally lower than 50% or higher than 90% in objective interval, the substack pair cannot be used for AVO analysis. If average (median) cross-correlation is globally higher than 50% in the objective interval, the substack pair can be used for AVO analysis.

6.5.1 Near – Mid after Filtering

The analysis of QC maps computed for this combination showed satisfactory level of correlation between Near and Mid with a good homogeneity of the map. The average (median) correlation can be seen to improve from 71% to 74%. Cross-correlation show suitable substack pair for AVO analysis. There was good homogeneity of the stretch between Near and Mid, with average stretch of 100%. The average RMS amplitudes computed within the reservoir window was quite similar on the Near and Mid substacks. Average computed resolution within the reservoir window was the same on both cubes. The computed resolution for the Near was 33ms while that of the Far was 33ms. Time and phase shifts between Near and Mid were reasonable and close to zero. No time or phase shift needed.

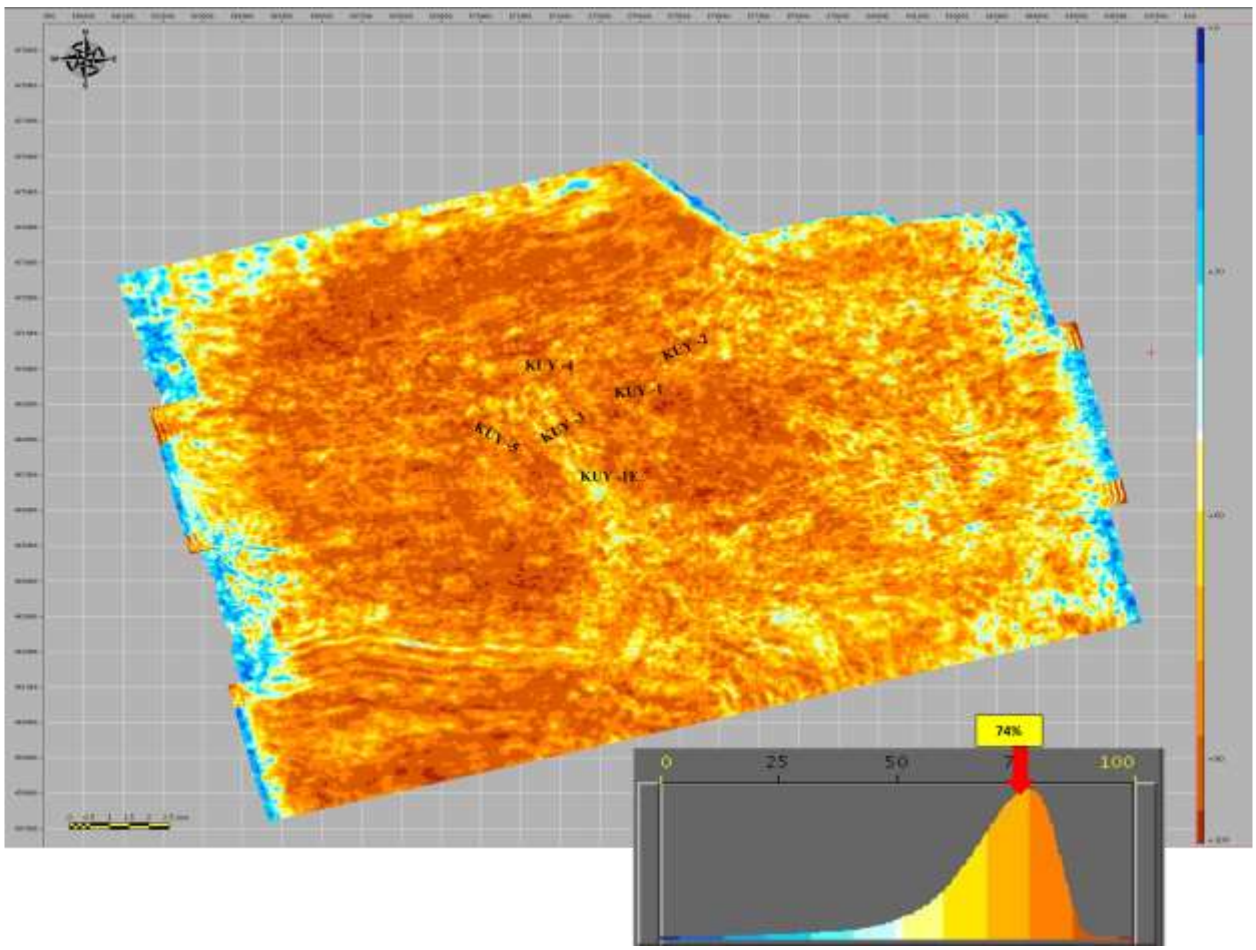

Figure 6.60: Cross-correlation map of Near-Mid pair after filtering.

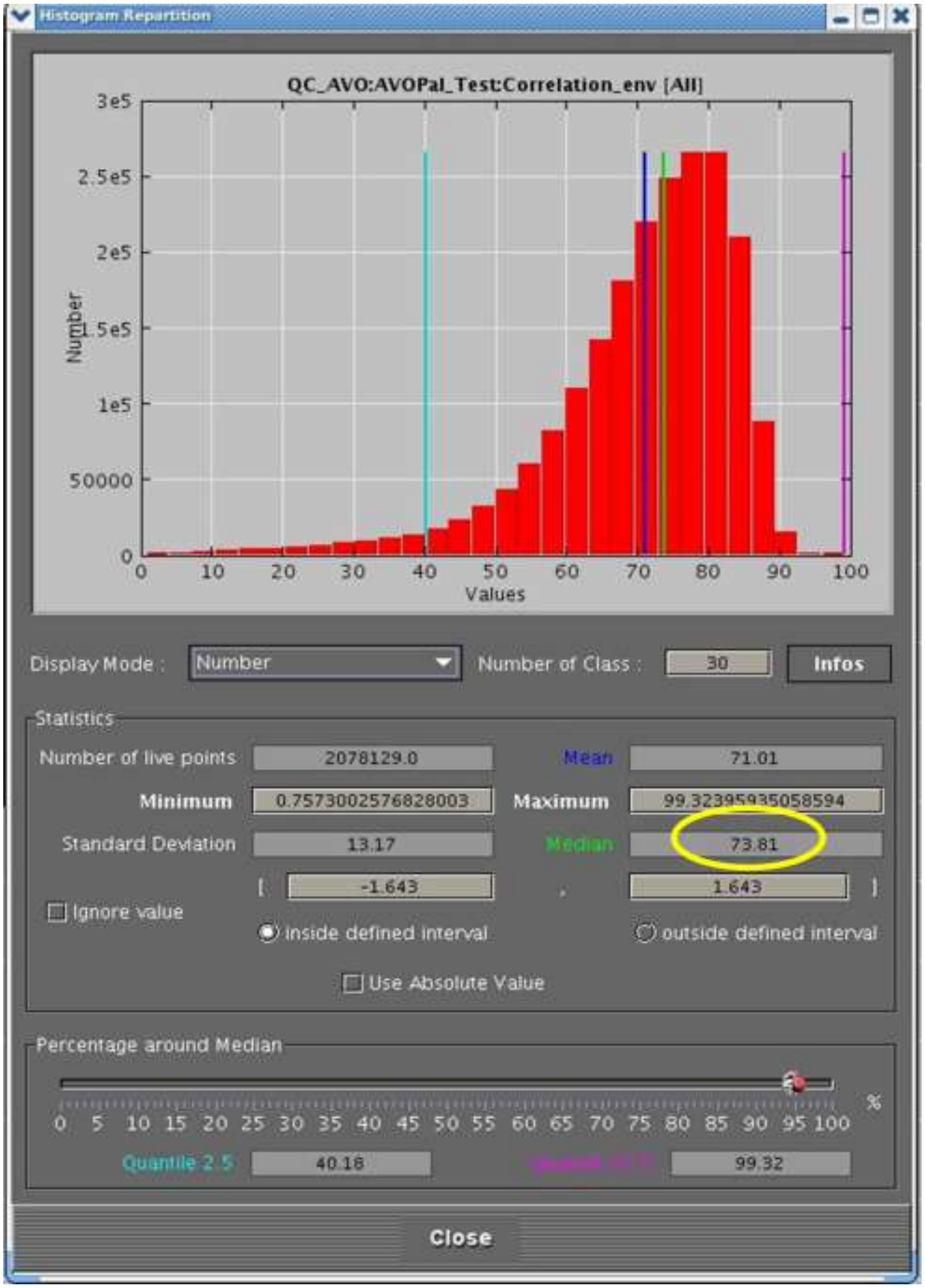

Figure 6.61: Histogram of cross-correlation for Near - Mid pair (in yellow circle) after filtering.

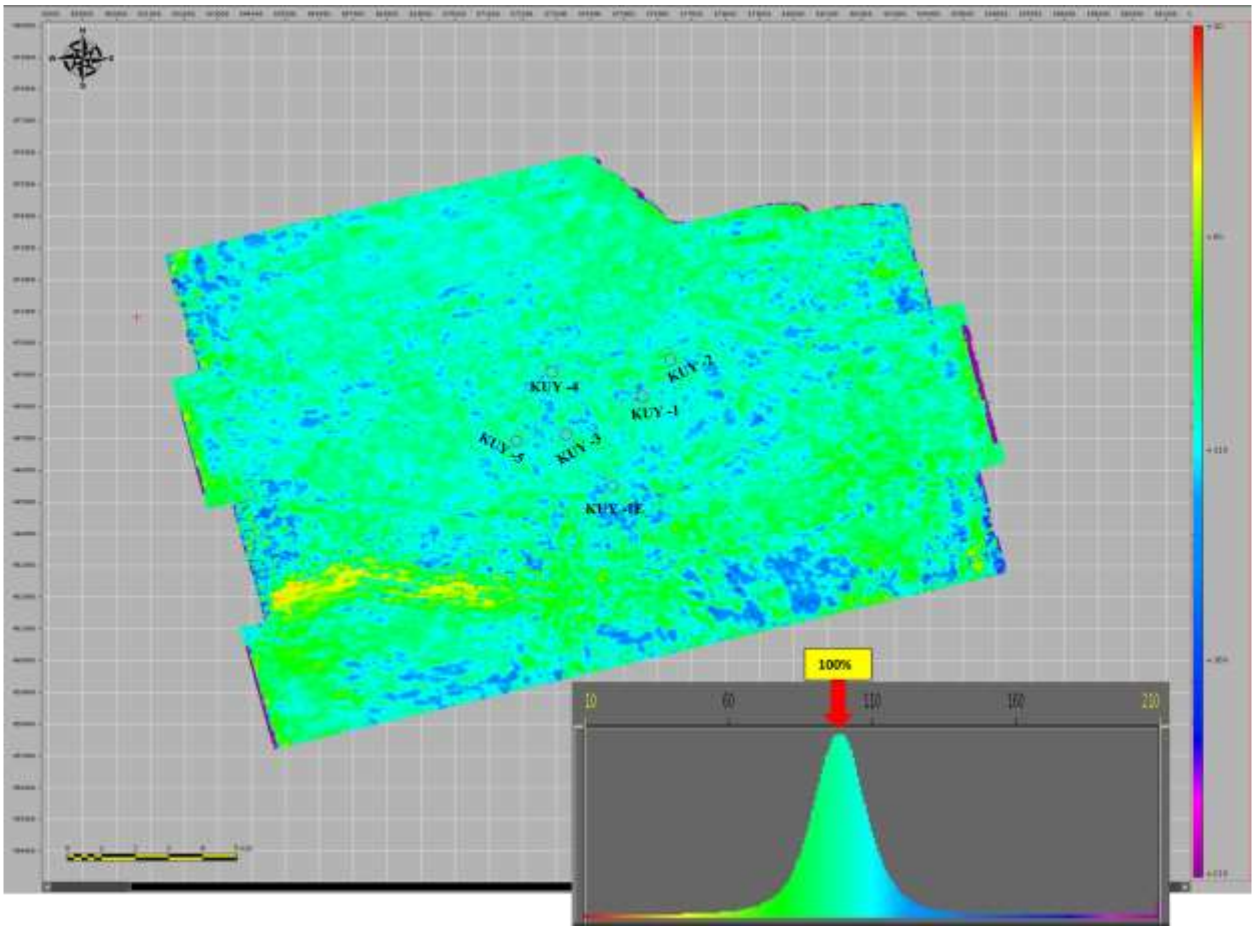

Figure 6.62: Stretch map of Near-Mid pair after filtering.

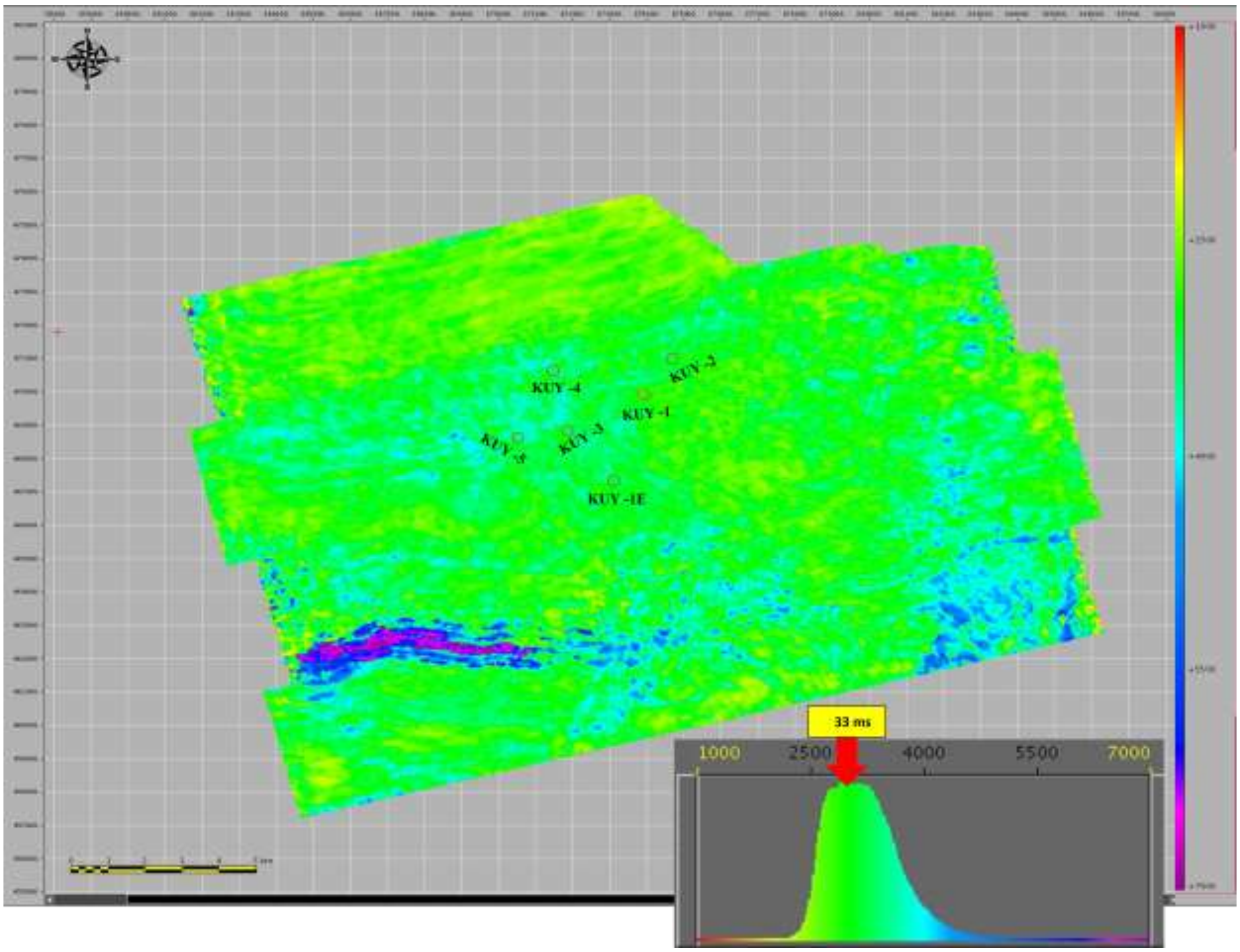

Figure 6.63: Resolution of Near cube after filtering.

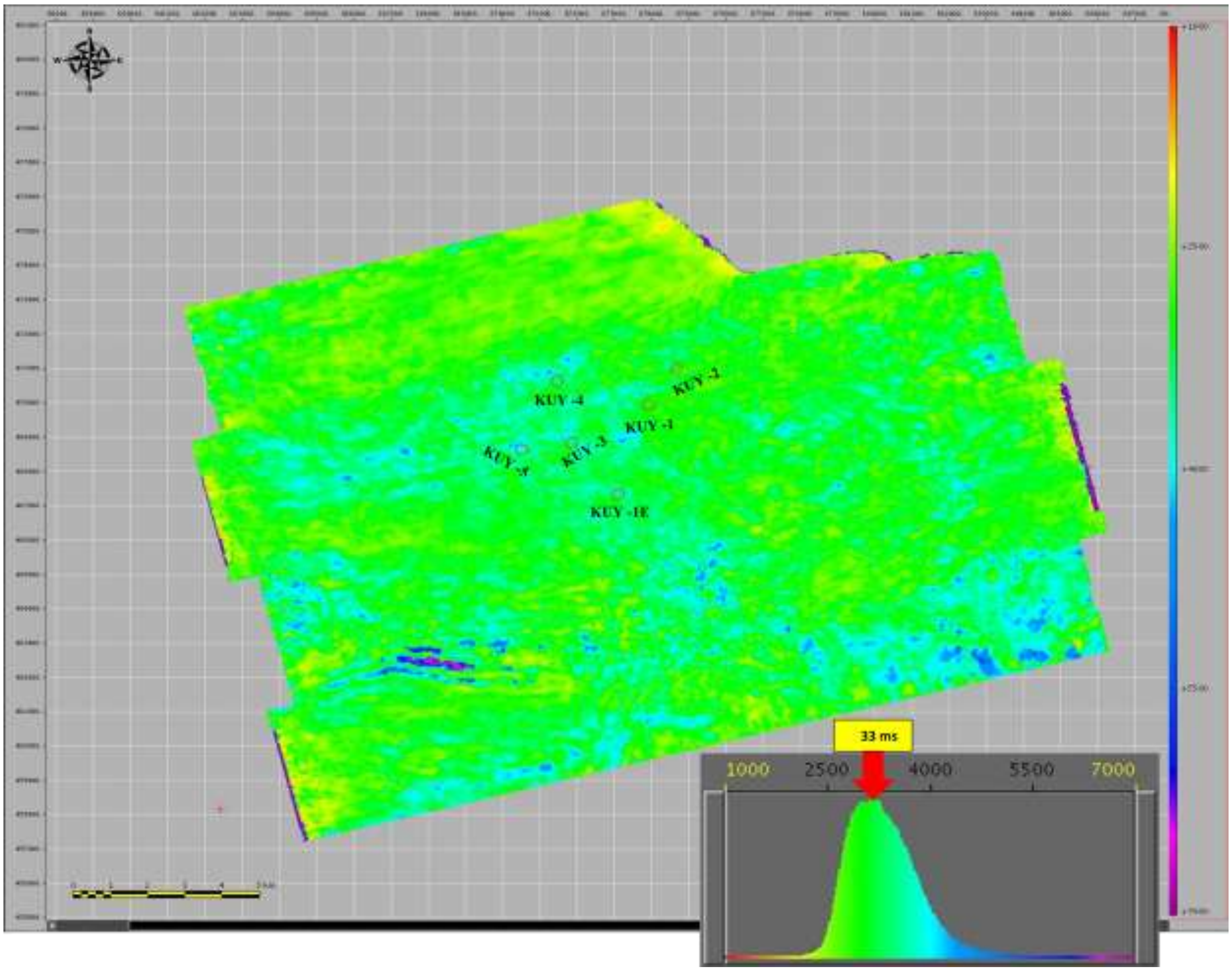

Figure 6.64: Resolution of Mid cube after filtering.

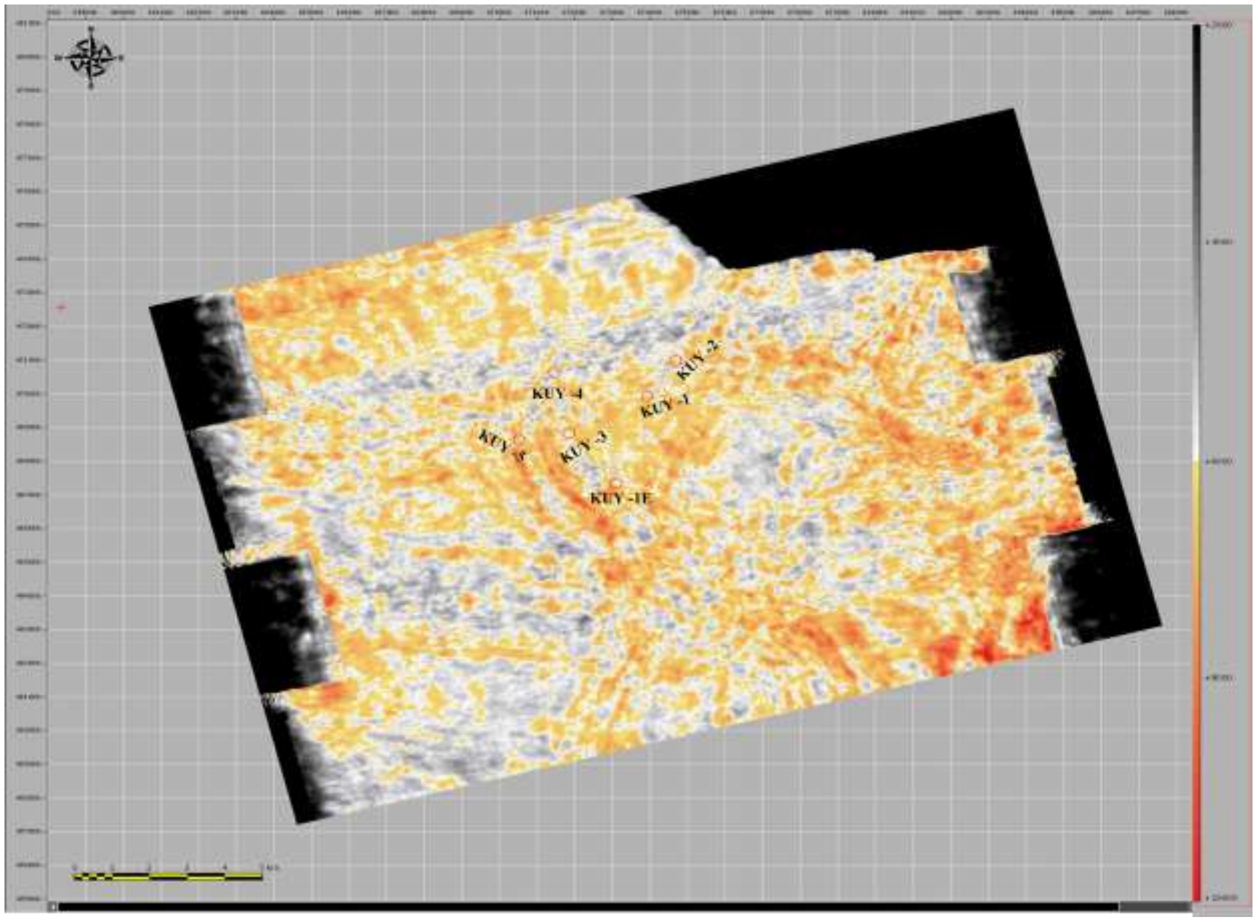

Figure 6.65: RMS amplitude map Near cube after filtering.

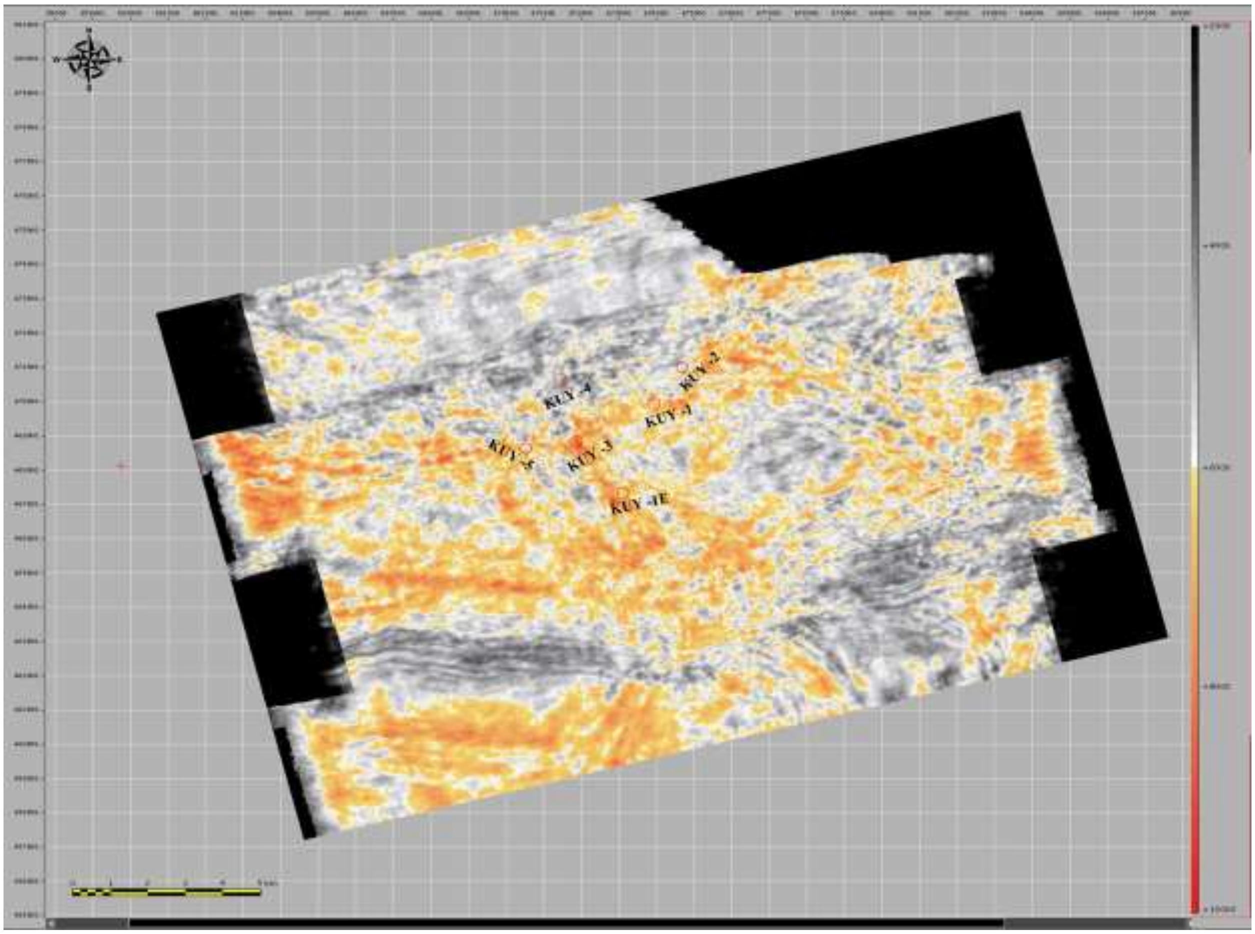

Figure 6.66: RMS amplitude map Mid cube after filtering

6.5.2 Mid – Far after filtering

The result of the analysis of QC maps computed for this pair showed satisfactory level of correlation between Mid and Far with a good homogeneity of the map. The average (median) cross-correlation improved from 64% to 69%. Cross-correlation show suitable substack pair for AVO analysis though lower than that of the Near – Mid pair. No problem of homogeneity of the stretch for both substacks. Average stretch was roughly 100%. Average resolution computed within the reservoir window was the same. The computed resolution for the Mid was 33ms while that of the Far was 33ms. The average RMS amplitudes computed within the reservoir window was quite similar on the Mid and Far substacks. Phase and time shifts between Mid and Far were reasonable and close to zero. No time or phase shift needed.

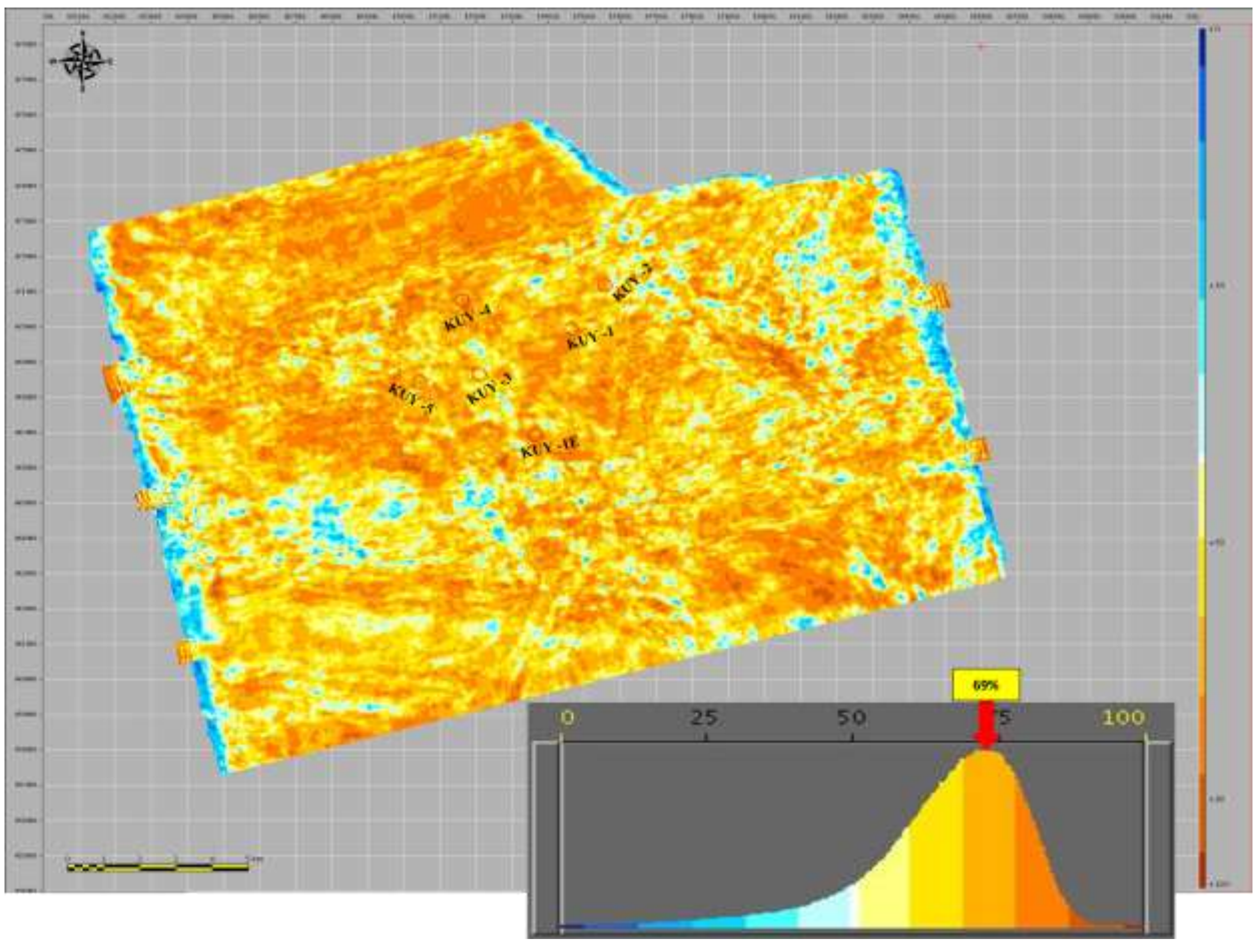

Figure 6.67: Cross-correlation map of Mid - Far pair after filtering.

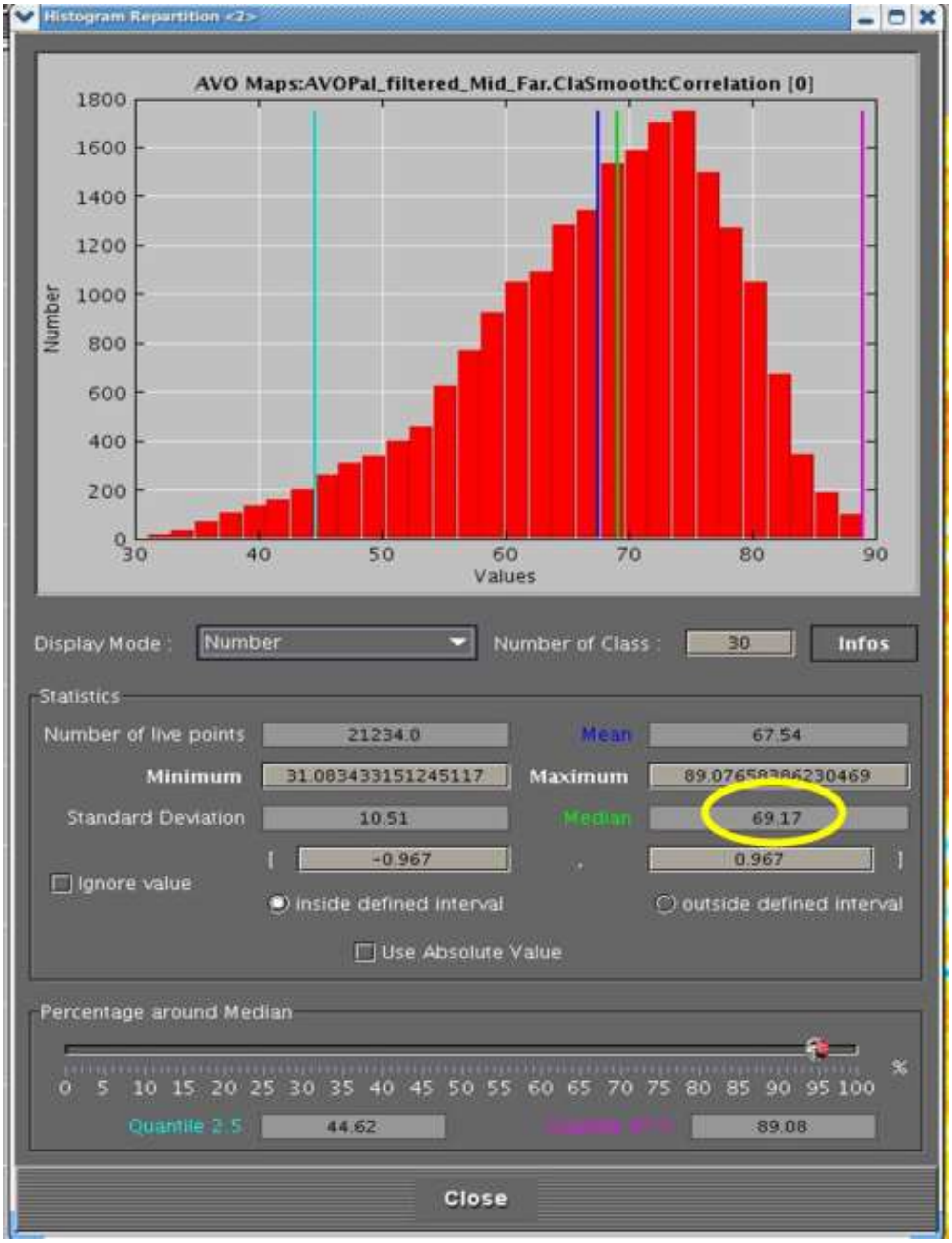

Figure 6.68: Histogram of cross-correlation for Mid - Far pair (in yellow circle) after filtering.

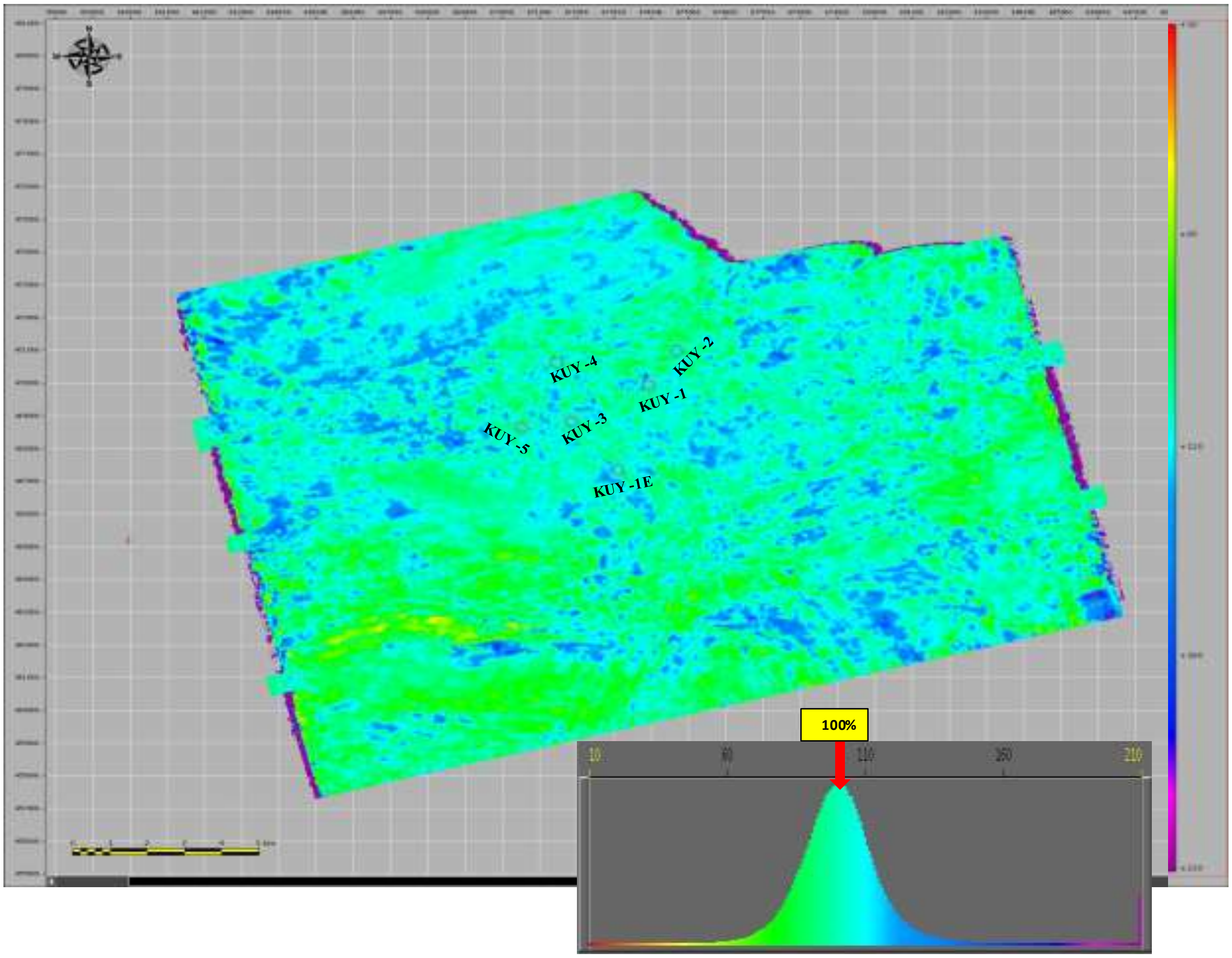

Figure 6.69: Stretch map of Mid - Far pair after filtering.

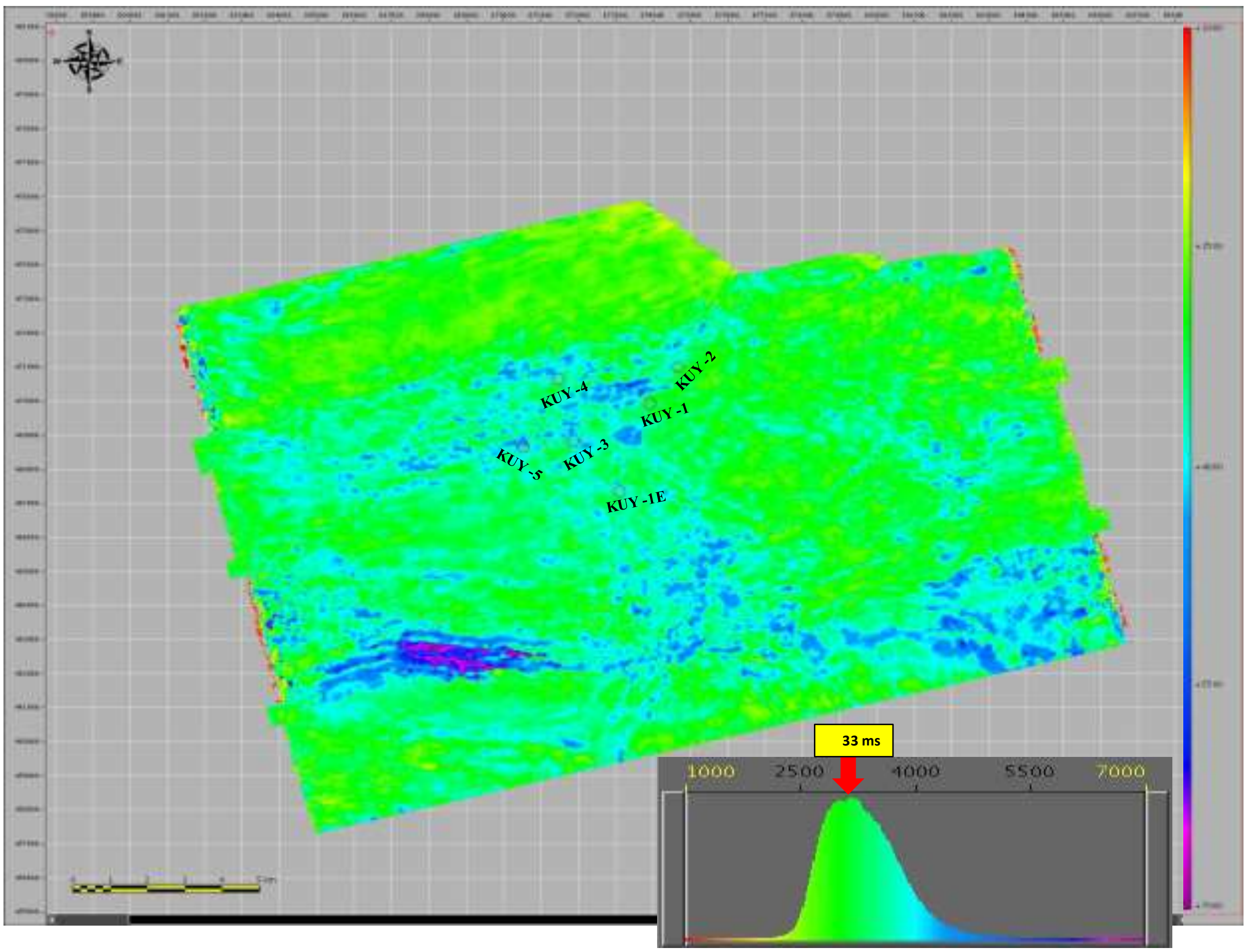

Figure 6.70: Resolution of Mid cube after filtering.

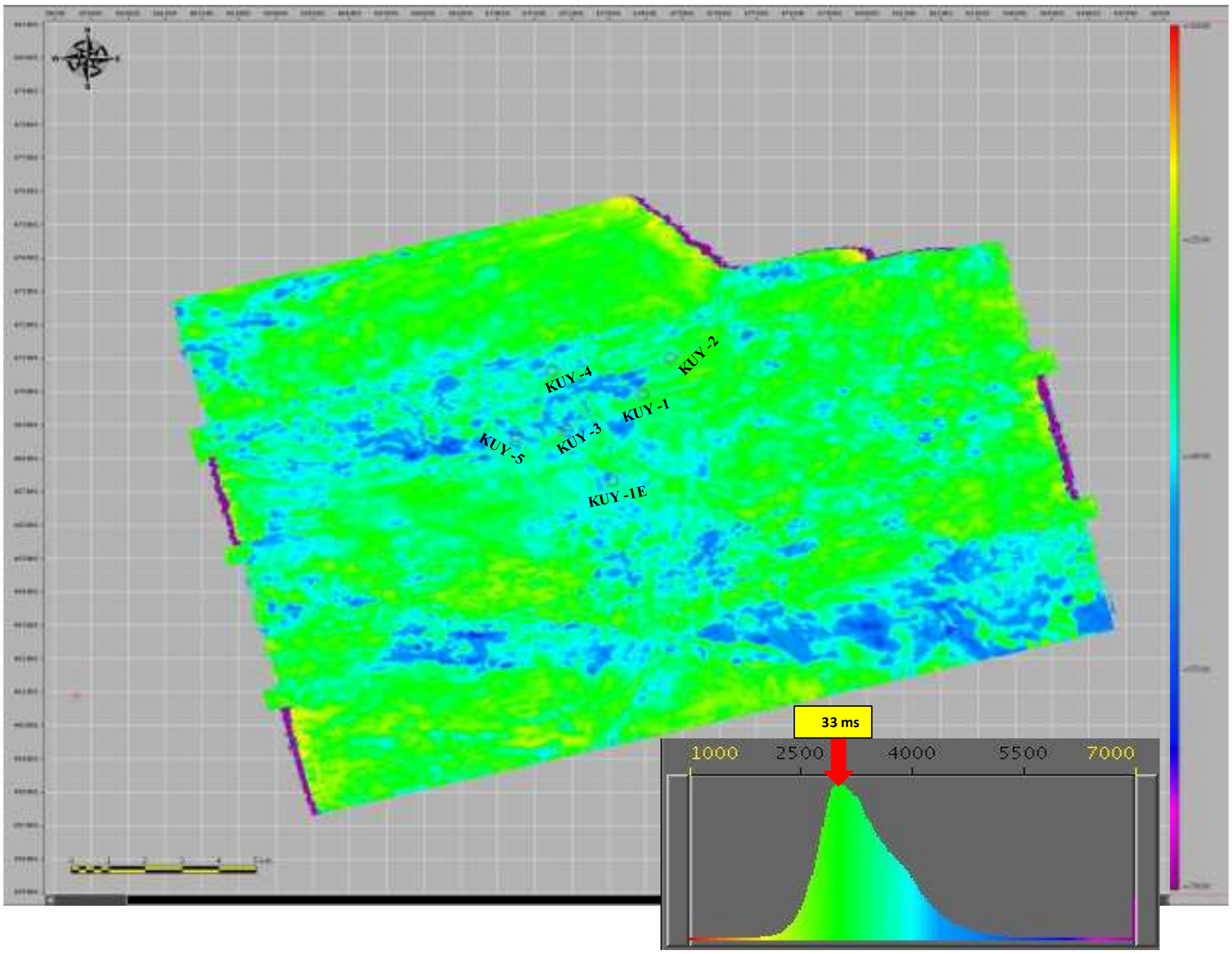

Figure 6.71: Resolution of Far cube after filtering.

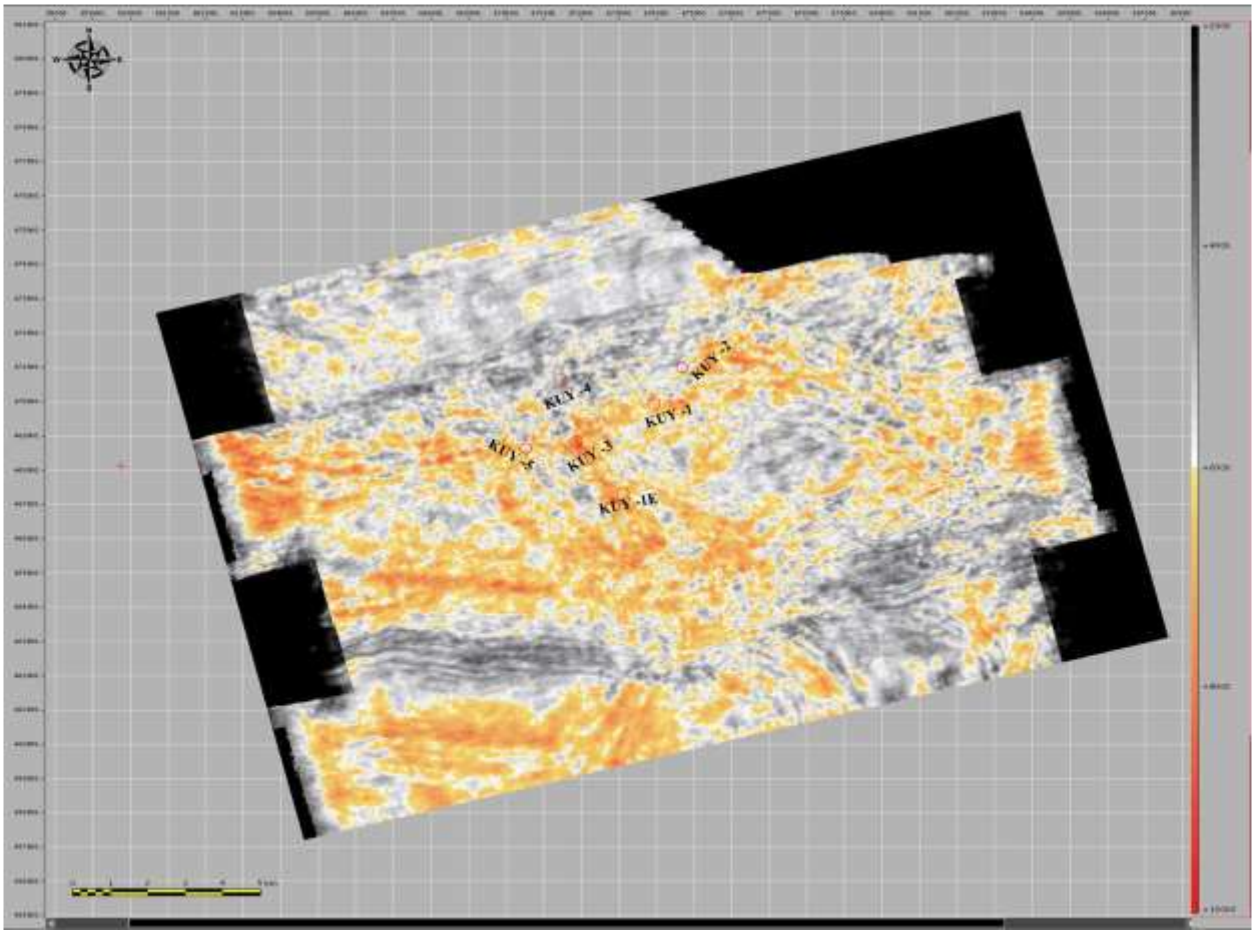

Figure 6.72: RMS amplitude map Mid cube after filtering

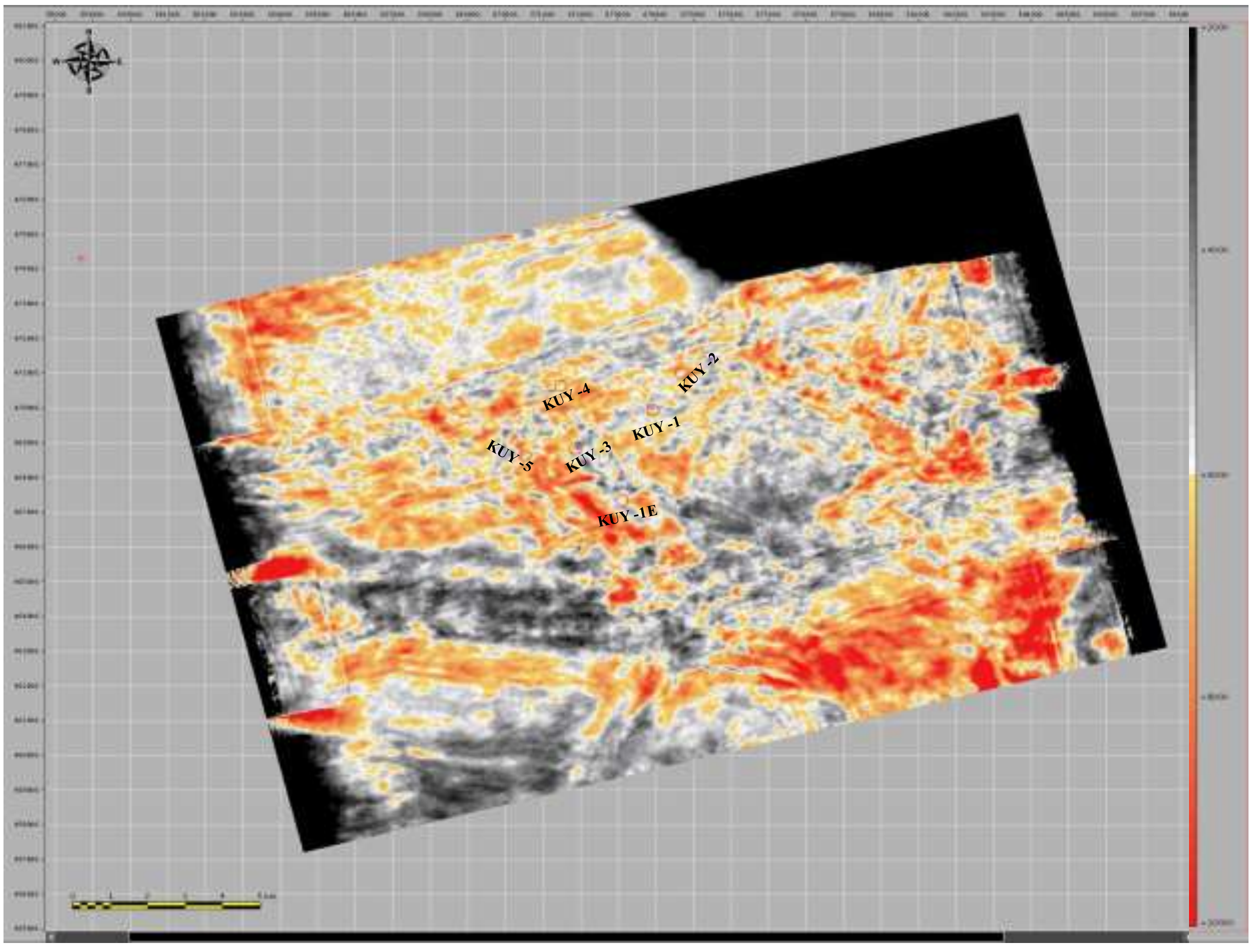

Figure 6.73: RMS amplitude map Far cube after filtering

6.5.3 Near – Far after filtering

The analysis of QC maps computed for this pair of substack showed that cross-correlation between Near and Far was lower than 50% though it improved from 42% to 46%. Cross-correlation between Near and Far are too low to allow an AVO analysis using this pair of substacks. There was poor homogeneity of the stretch between Near and Far substack with average stretch value of 104%. Average resolution computed within the reservoir window was too different on the Near and Far substacks. The computed resolution for the Near is 32ms while that of the Far is 33ms.Average RMS amplitudes computed within the reservoir window was quite similar on the Near and Far substacks. Time and phase shifts between Near and Far were reasonable and close to zero.

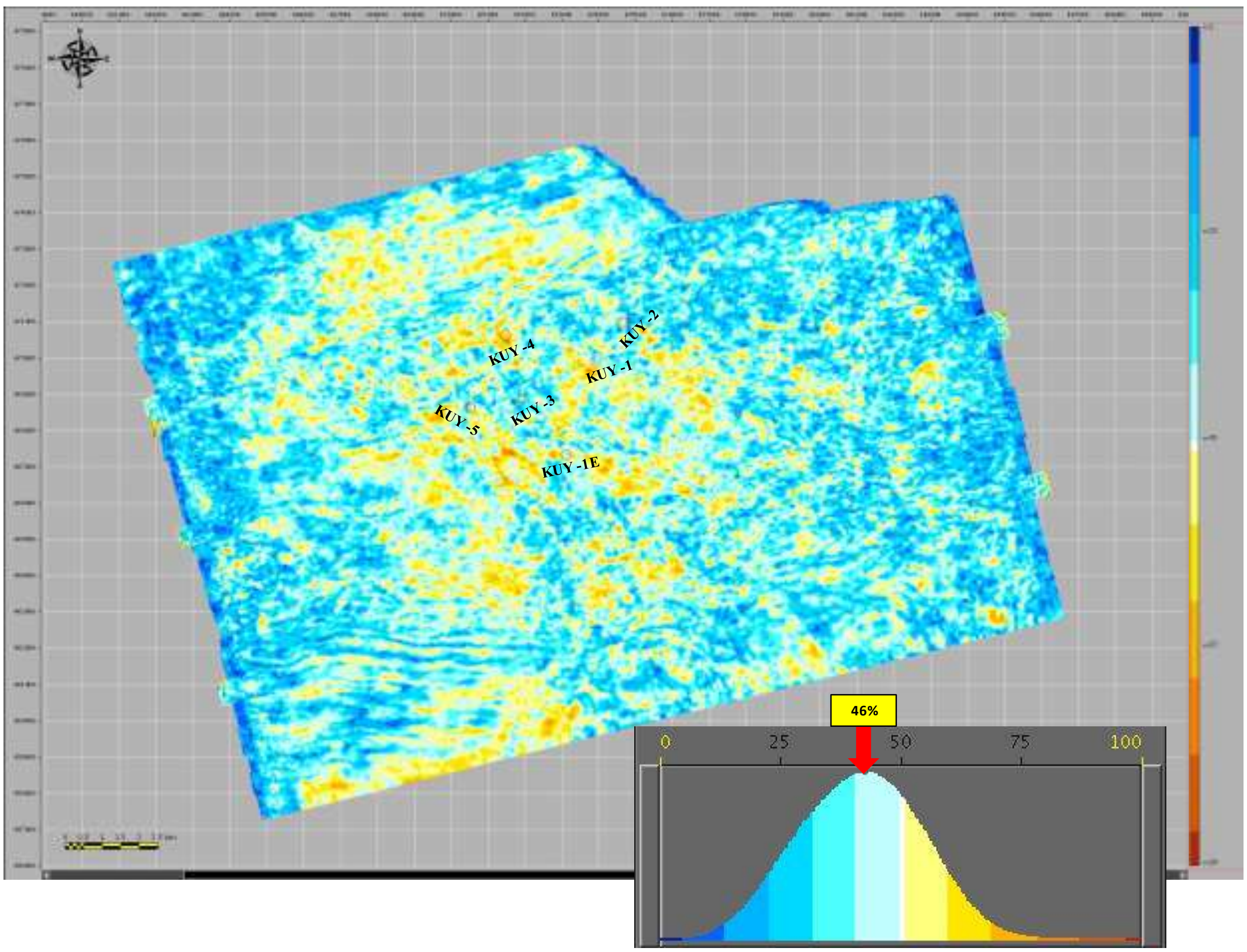

Figure 6.74: Cross-correlation map of Near - Far pair after filtering.

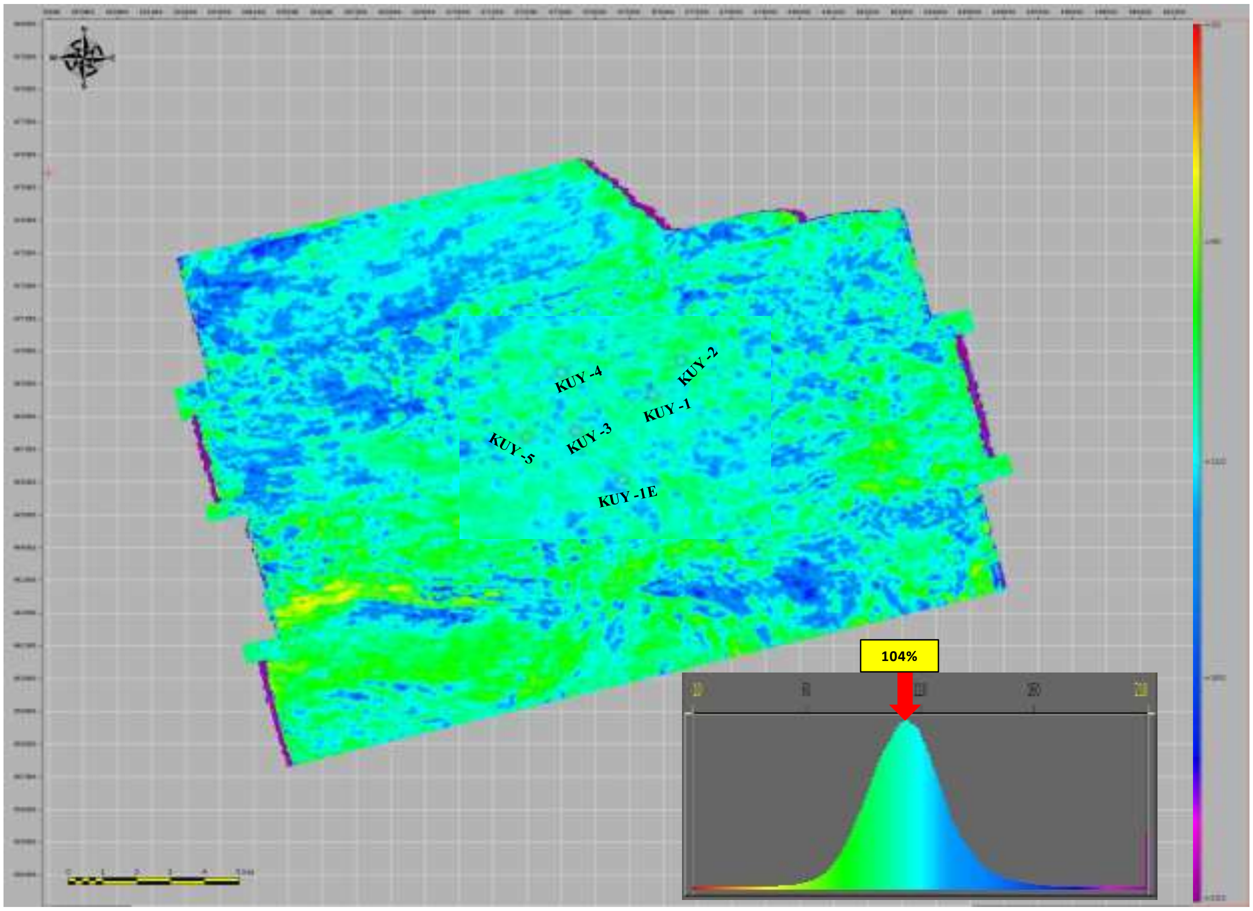

Figure 6.75: Stretch map of Near - Far pair after filtering.

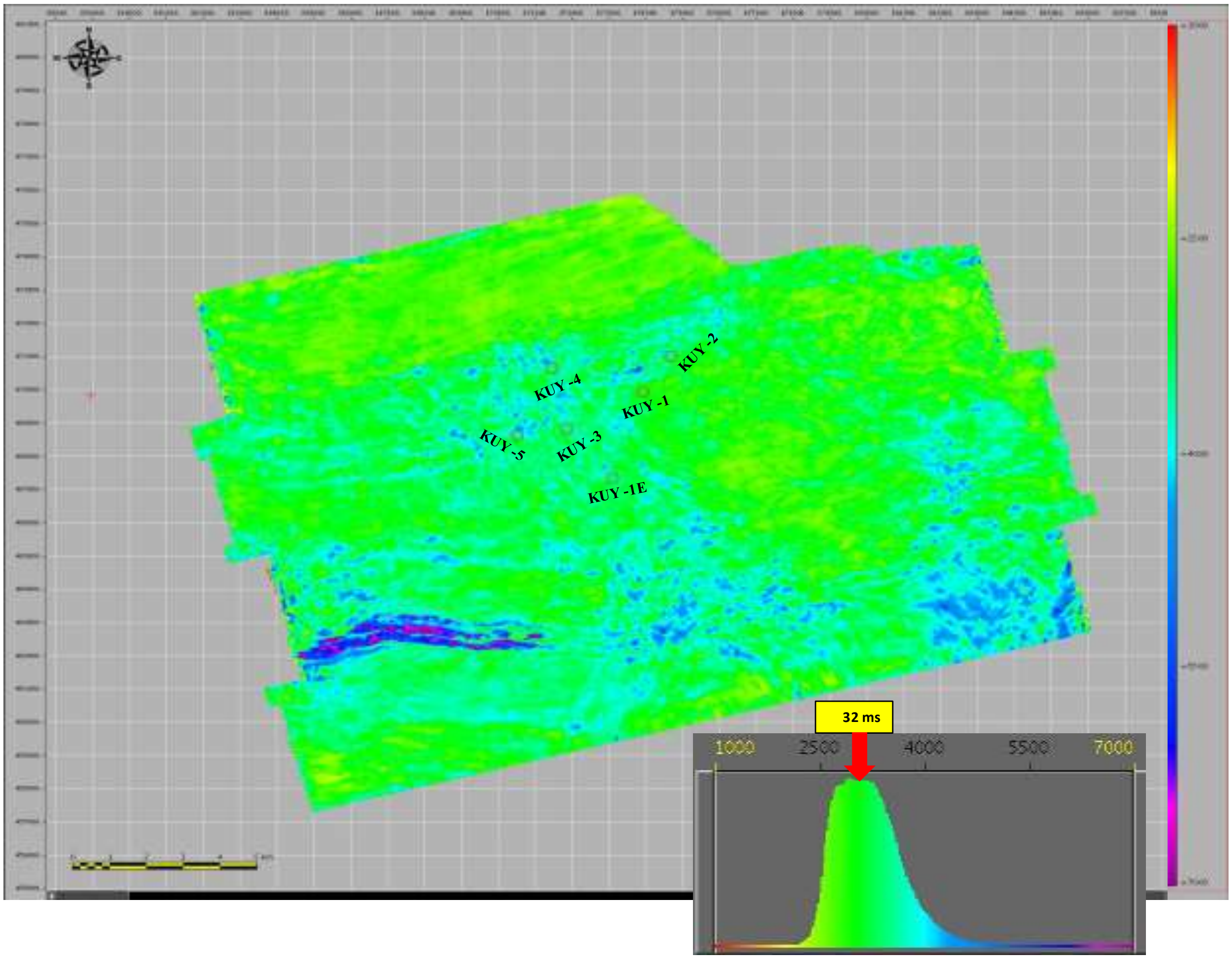

Figure 6.76: Resolution of Near cube after filtering.

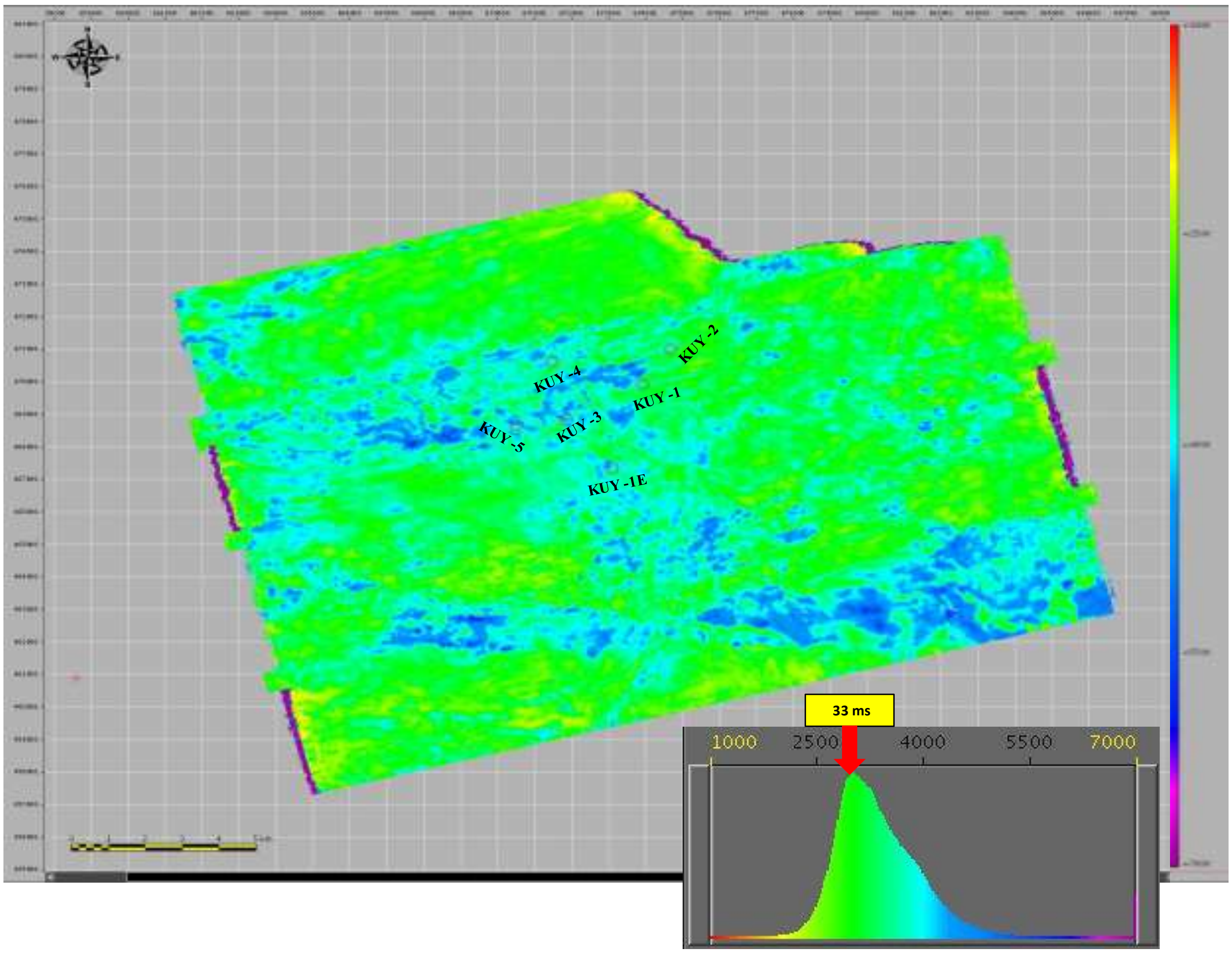

Figure 6.77: Resolution of Far cube after filtering.

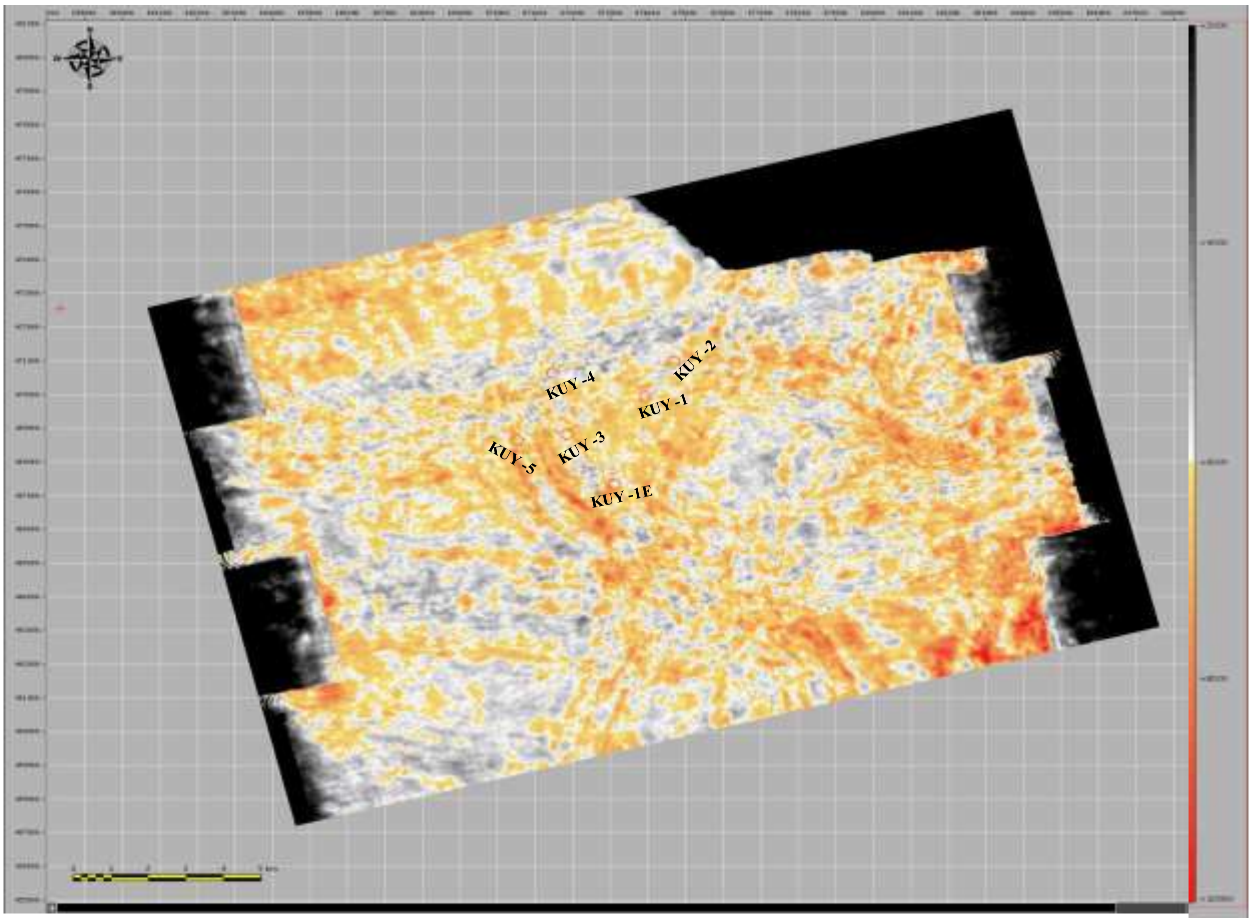

Figure 6.78: RMS amplitude map Near cube after filtering

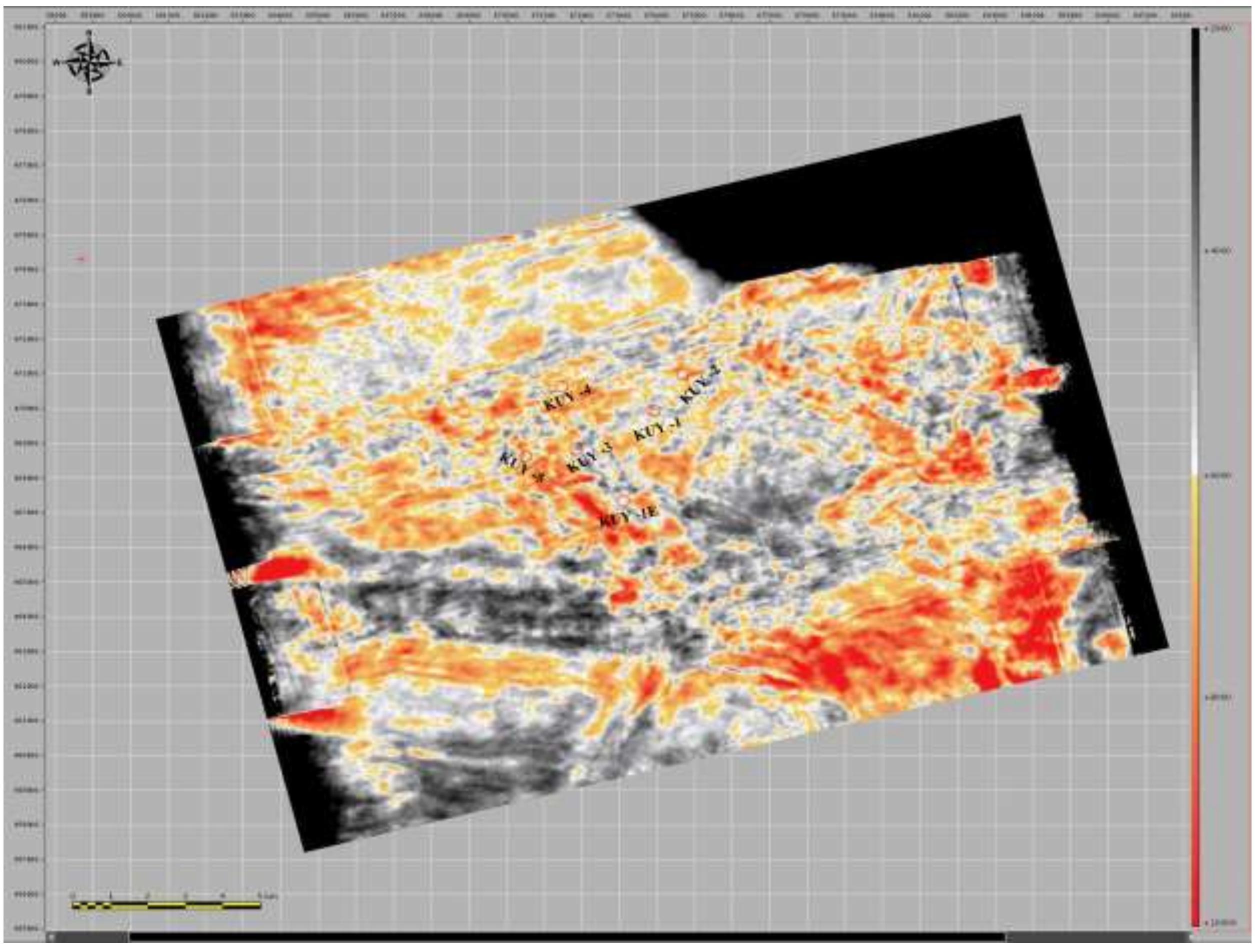

Figure 6.79: RMS amplitude map Far cube after filtering

6.6 Retained Substack Pair Choice after Filtering

The median (average) cross-correlations of Near – Mid and Mid – Far pairs can be seen to be higher than 50% and less than 90% in the studied AVO interval. Any of the Near – Mid and Mid – Far pairs can be used for AVO analysis. Cross-correlation between Near and Far is lower than 50%. Cross-correlation between Near and Far was too low to allow an AVO analysis using this pair of substacks.

In our case, we selected the Mid – Far combination/pair to be used for this study.

6.7 AVO Crossplot Analysis

AVO analysis is based on qualifying outlier points defined in a (Mid – Far) crossplot. When the background/reference trend is defined, we expect that points far from this line are maybe associated with hydrocarbon bearing reservoirs. First identify a trend statistically relating a set of reference points. This trend is known as reference trend, background trend or water line. The distance to this trend is then measured for each sample's seismic response as measured by the pair of amplitudes (Mid - Far). Then it is further scaled on statistical criteria to be able to assess how severe is the departure from the trend i.e. how "strong" is the AVO anomaly. The strategy used in Sismage AVOPal software to accomplish the above task is that, the program will carry out a virtual crossplot for each pair of Mid – Far trace position. From this crossplot, it builds a correlation coefficient, the slope of the best regression line in the scatter of points and a specific scaling range.

We first determine statistically the values of lambda and slope using maps (correlation, the slope in degrees and scaling range) in areas where we expect not to have hydrocarbon. These values are then verified on several areas at similar burial depth and within a similar stratigraphic interval on the filtered Mid and Far cubes where we also expect not to have any hydrocarbon. The average of these values will be used as inputs in Sismage to compute the final AVO Seismofacies cube.

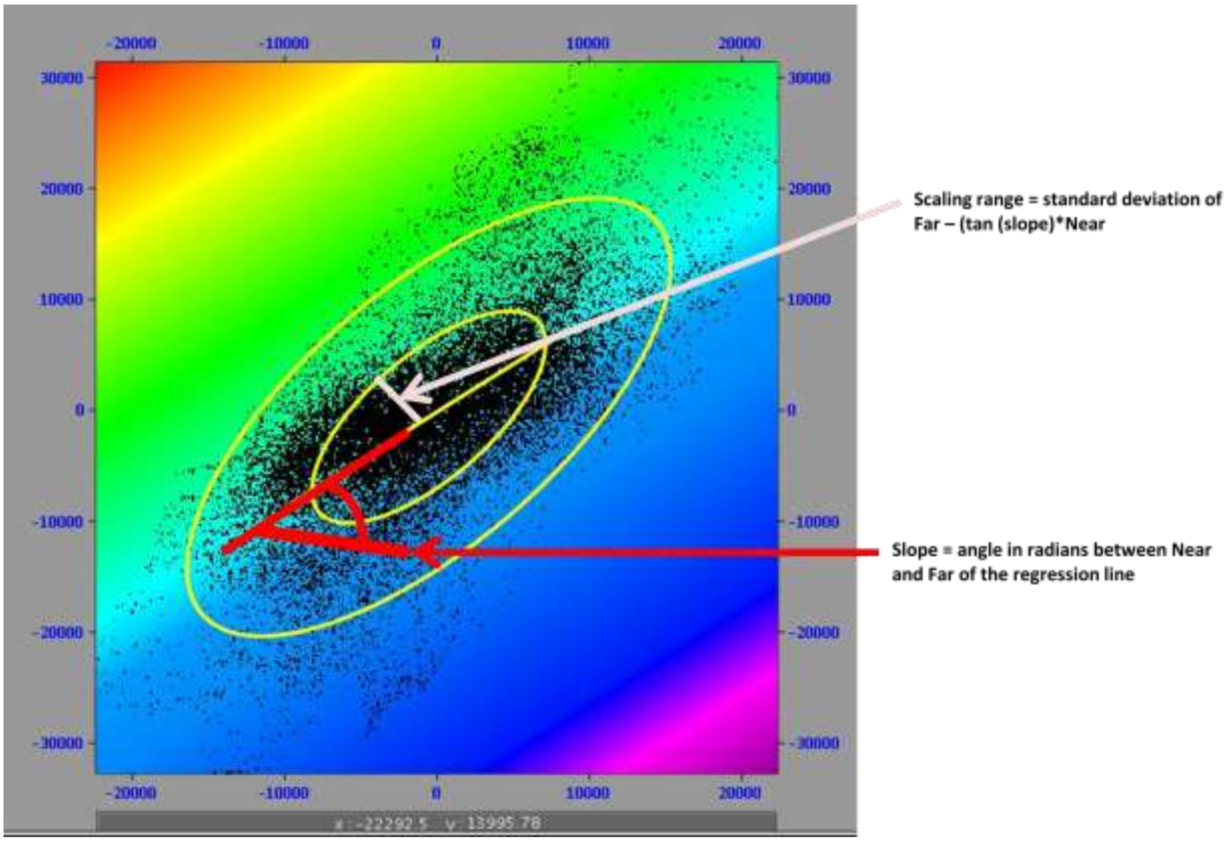

Figure 6.80: Virtual crossplot for each pair of Mid – Far trace. From this we extract three attributes, the correlation, the slope and the scaling range.

6.7.1 Computation of Lambda and Slope with Maps

Having a good knowledge of oil - water - contact (OWC) from well data over the studied area, a polygon was used to delimit areas with no hydrocarbon on the slope and scaling range maps computed using the filtered Mid and Far cubes around the studied AVO interval computed in the previous step. Average values of slope and scaling range were then extracted from the polygon on these maps through a histogram. We consider no hydrocarbon areas as areas with low RMS amplitudes on Mid and Far maps but with high correlation. The average (median) computed values of slope and scaling range were 37 degrees (37^0) and 0.24.

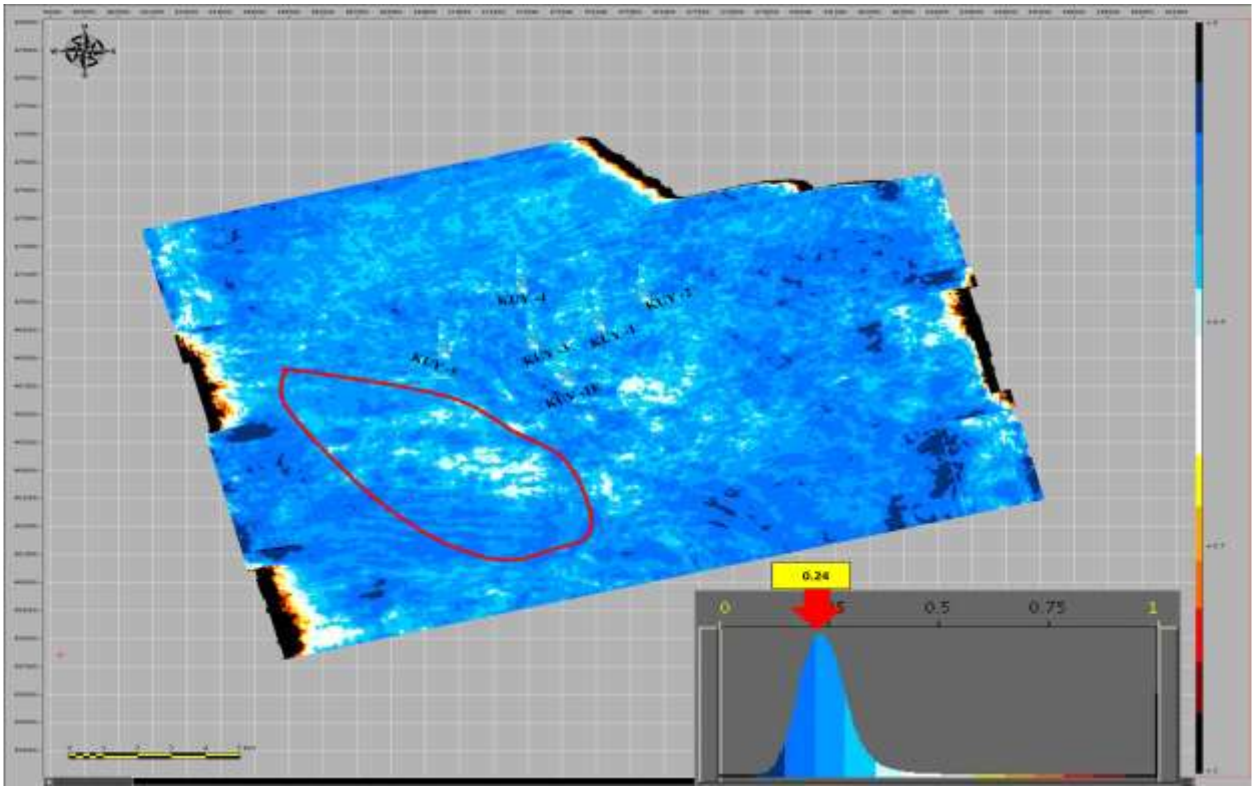

Figure 6.81A: Scaling range map of filtered Mid – Far pair. The red polygon shows area with no hydrocarbon.

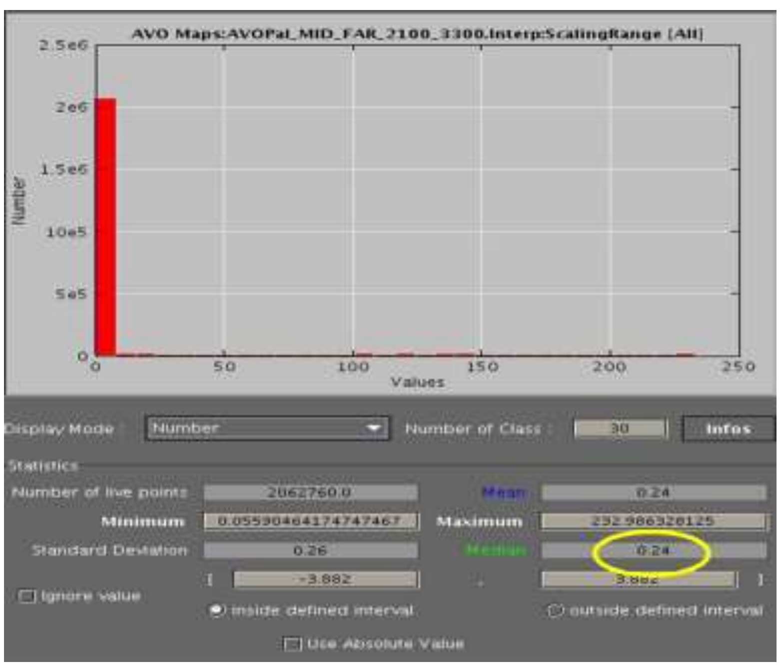

Figure 6.81B: Histogram of Scaling range map of filtered Mid – Far pair computed within the area with no hydrocarbon (polygon in red).

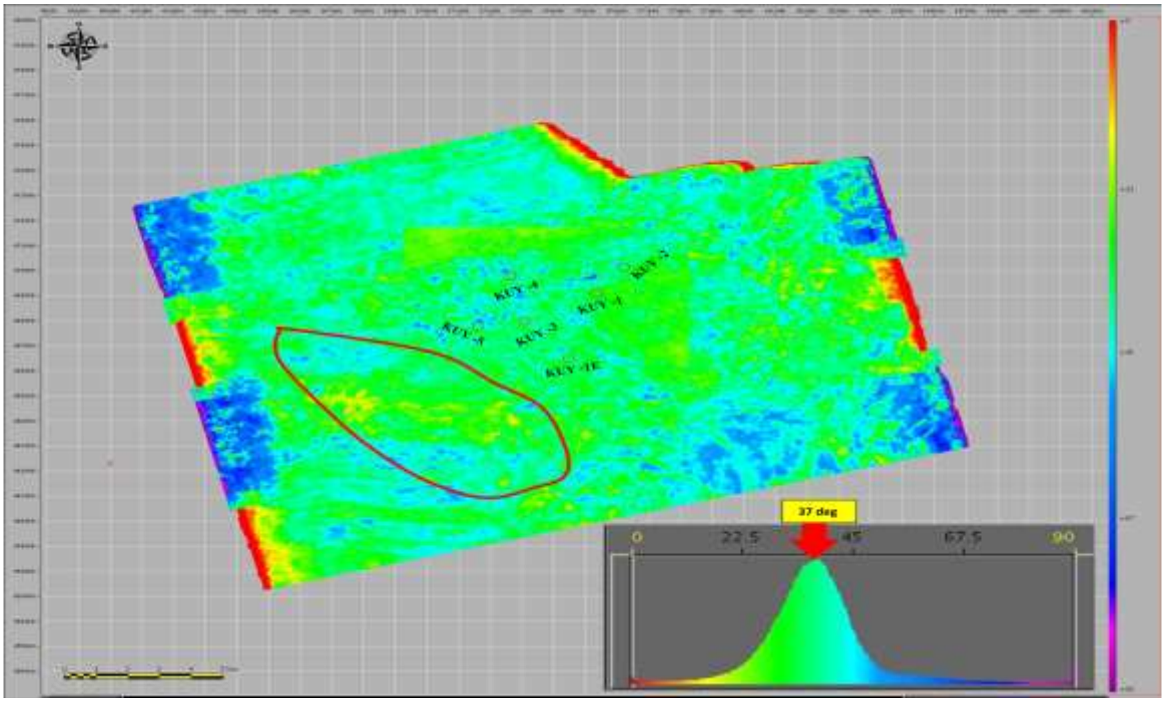

Figure 6.82A: Slope in degrees map of filtered Mid – Far pair. The red polygon shows area with no hydrocarbon.

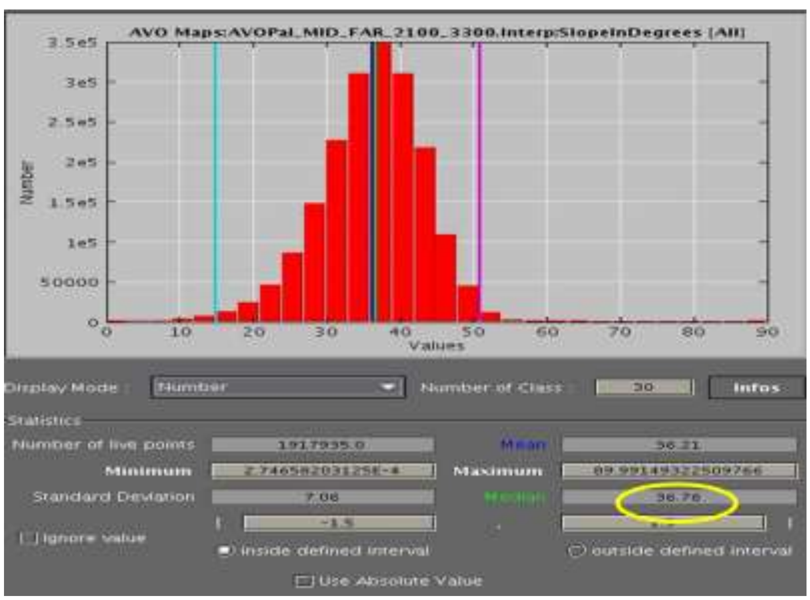

Figure 6.82B: Histogram of Slope in degrees map of filtered Mid – Far pair computed within the area with no hydrocarbon (polygon in red).

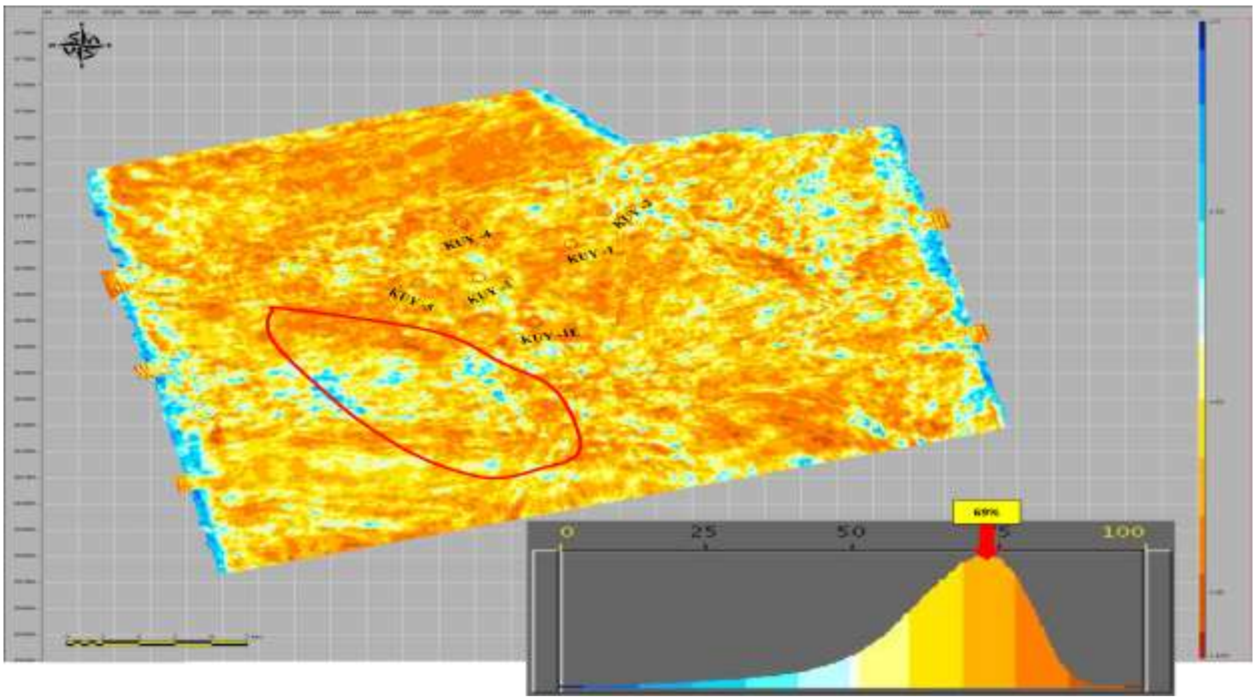

Figure 6.83: Correlation map of filtered Mid - Far pair. The red polygon shows area with no hydrocarbon.

6.7.2 Verification of Lambda and Slope Values using Cross-Sections of filtered Mid and Far Cubes in No Hydrocarbon Areas.

With the help of effective water saturation (SWE) and clay volume (VCL) logs, water sands at well was located on lines (inline, crossline & random) along well trajectories. A polygon was used to delimit areas with no hydrocarbon on the filtered Mid and Far cross - sections on several areas at similar burial depth and within a similar stratigraphic interval. An excel table was created to enter standard deviations of Mid and Far, correlation, slope and lambda values. Lambda values were then computed using the formula:

Lambda = standard deviation (Far) * square root (1-correlation* correlation)

We plotted the standard deviation (Far) * correlation against standard deviation (Mid) to evaluate by how much slope and lambda values are varying between top and bottom of the zone of interest. The slope is not modified by more than 15% otherwise we would have computed the AVO Seismofacies cube to take into account this variability.

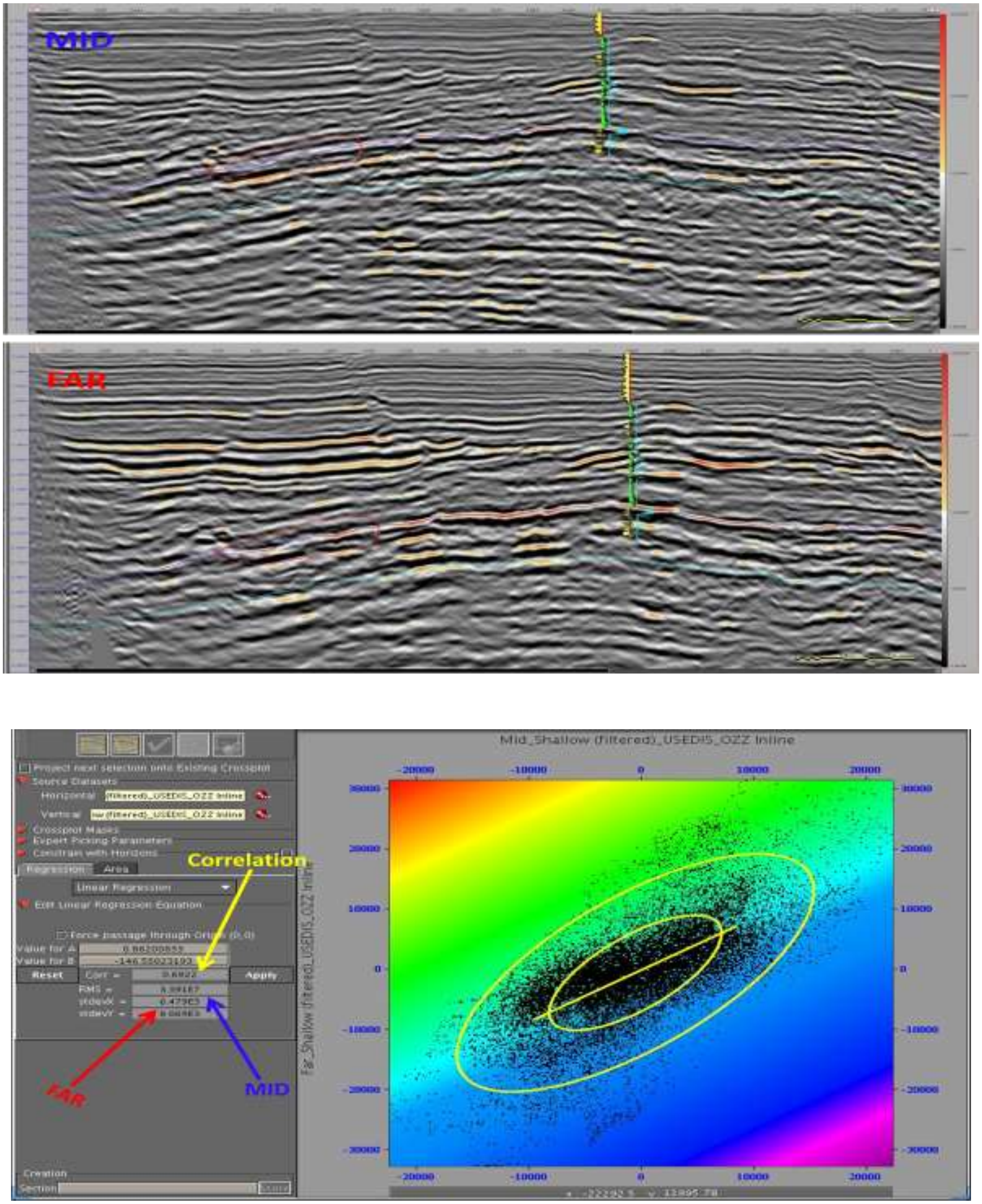

Figure 6.84: Filtered Mid and Far cross-section along inline 2360 together with the crossplot analysis. The polygon on the cross-section shows an area with no hydrocarbon.

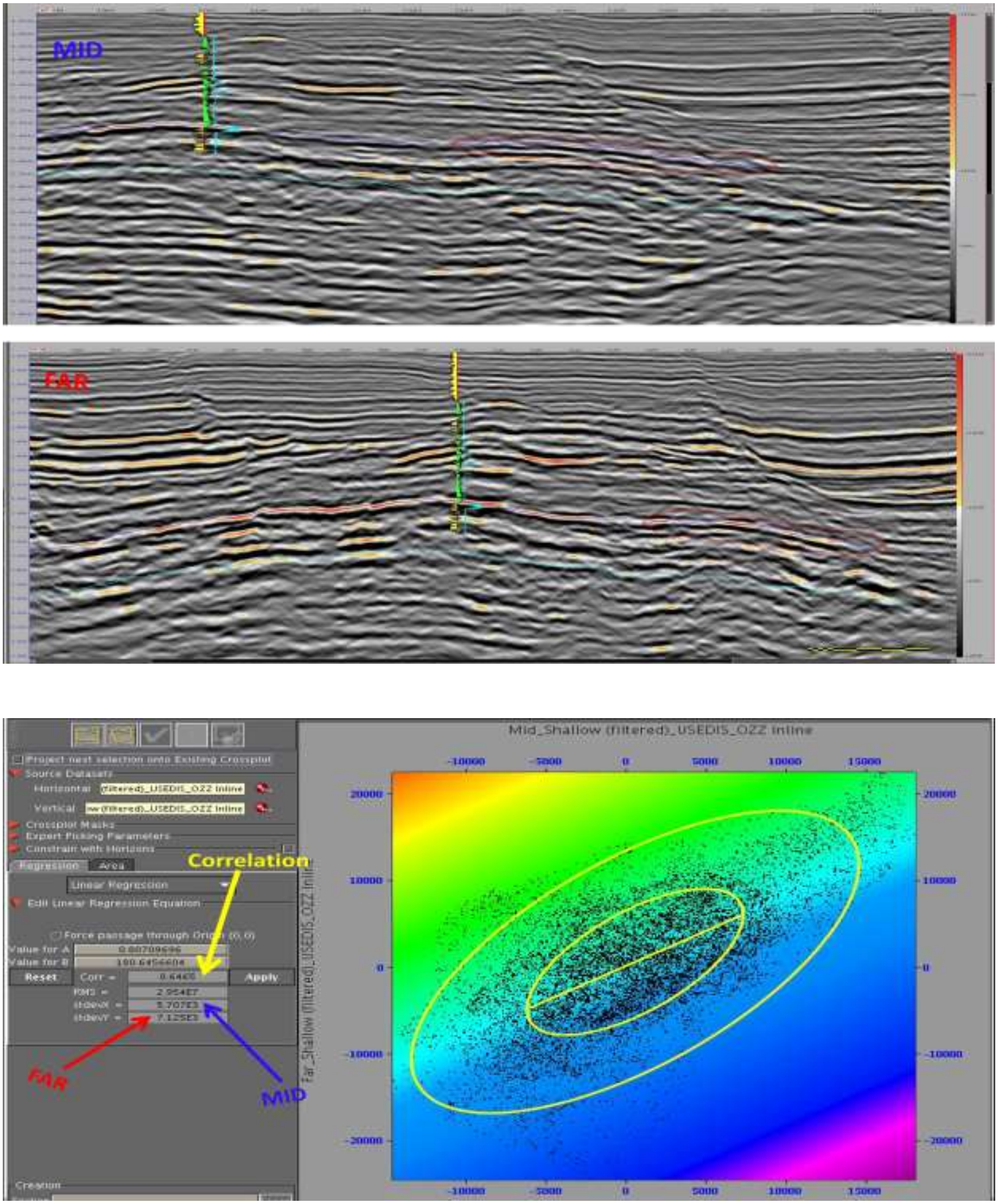

Figure 6.85: Filtered Mid and Far cross-section along crossline 2090 together with the crossplot analysis. The polygon on the cross-section shows an area with no hydrocarbon.

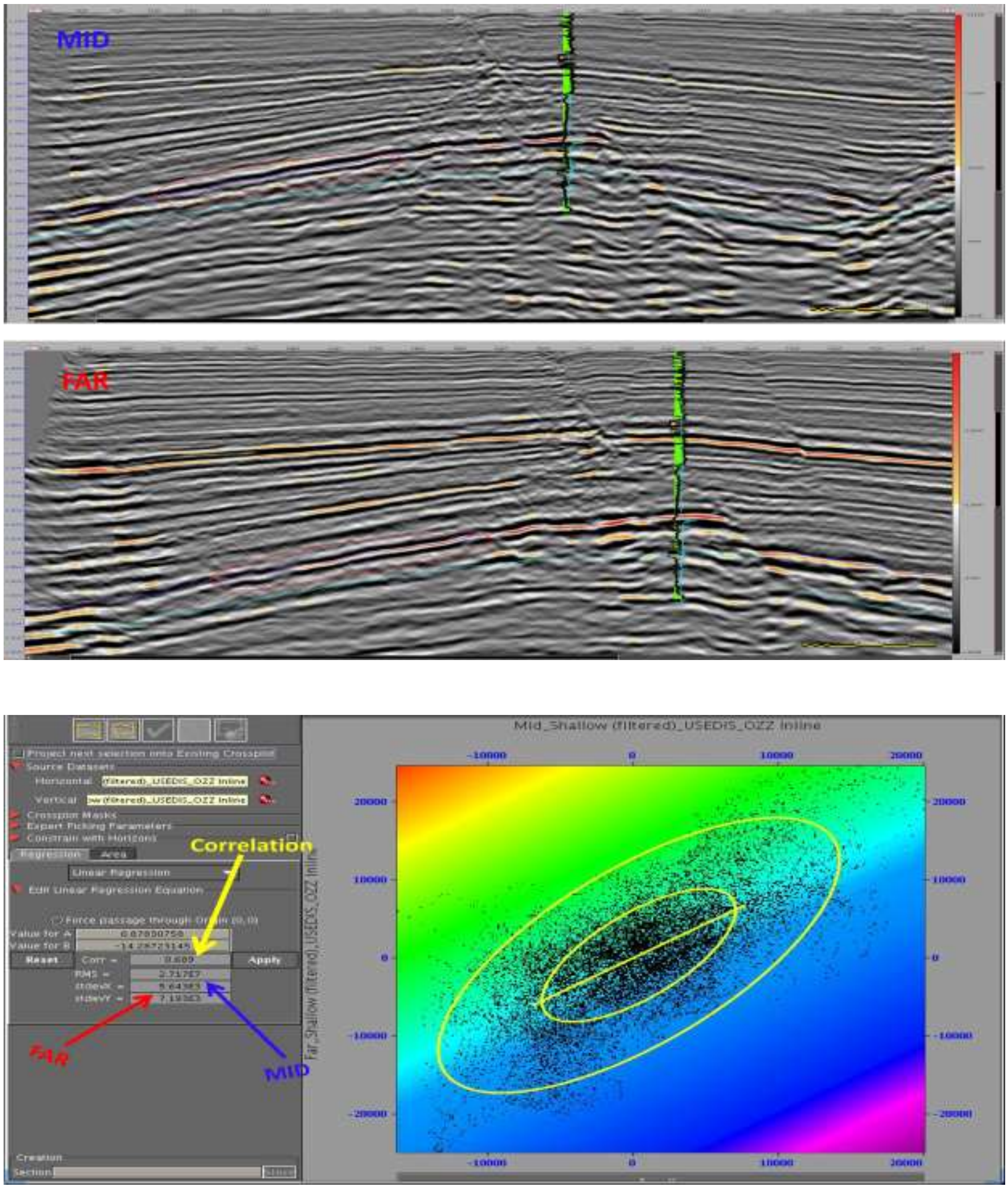

Figure 6.86: Filtered Mid and Far cross-section along inline 2648 together with the crossplot analysis. The polygon on the cross-section shows an area with no hydrocarbon.

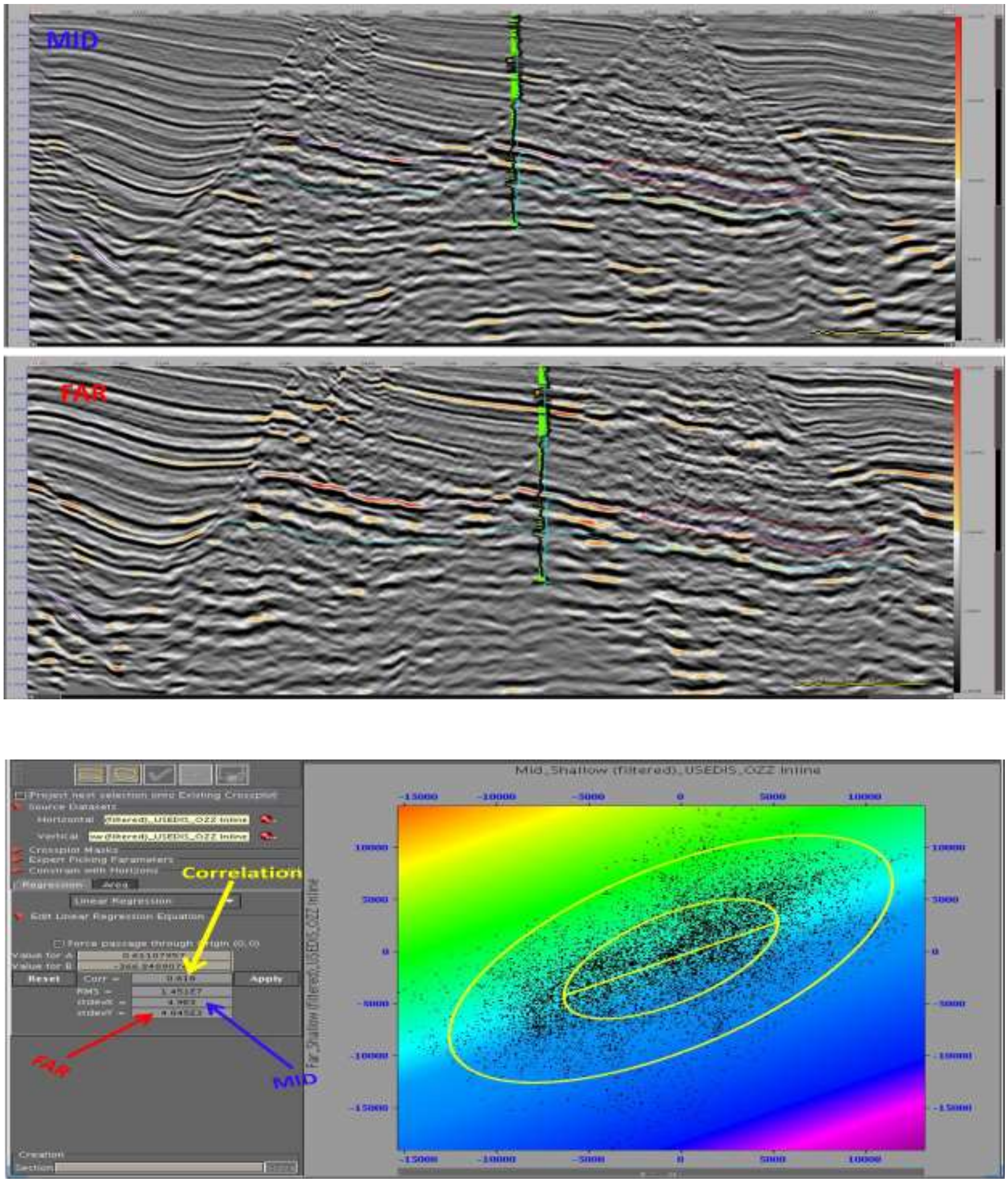

Figure 6.87: Filtered Mid and Far cross-section along crossline 2150 together with the crossplot analysis. The polygon on the cross-section shows an area with no hydrocarbon.

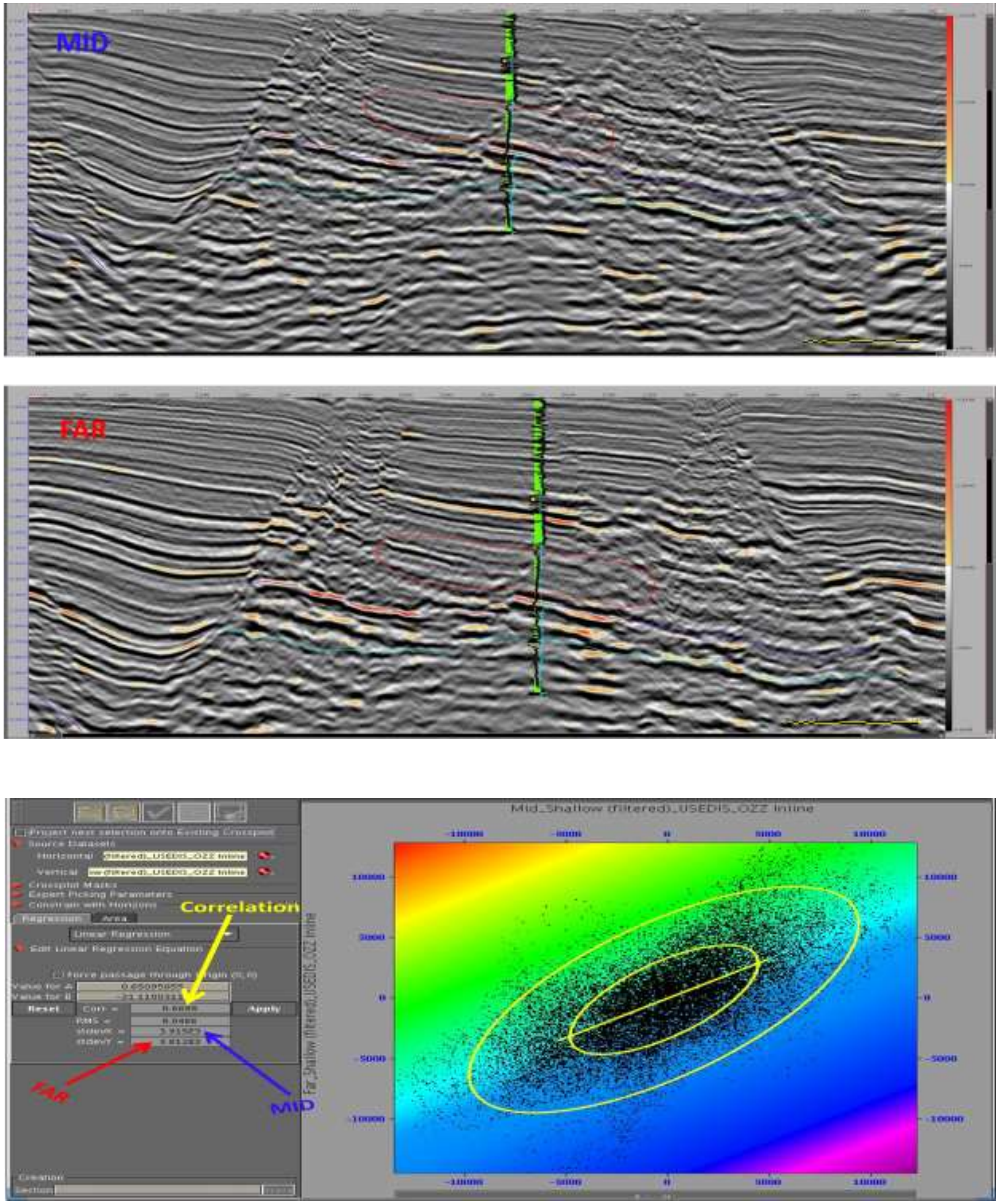

Figure 6.88: Filtered Mid and Far cross-section along inline 2374 together with the crossplot analysis. The polygon on the cross-section shows an area with no hydrocarbon.

Table 13: Excel table showing standard deviations for Mid and Far, correlation, slope, scaling range and lambda

KUYOLO AVO	Stdev(Near)	Stdev(Far)	Correlation N/M	Stdev(Far)*Correlation N/M	Slope	Slope in Degrees	Lambda	Scaling Range
Inline 2360	6479	8069	69%	5585.3618	0.8620716	40.76369	5823.4438	0.1717197
Crossline 2090	5707	7125	65%	4606.3125	0.8071338	38.90817206	5435.7624	0.1839668
Inline 2648	5643	7193	69%	4955.977	0.8782522	41.29129142	5213.2083	0.1918205
Crossline 2150	4900	4845	62%	2994.21	0.6110633	31.42757106	3809.0329	0.2625338
Inline 2374	3915	3812	67%	2548.322	0.6509124	33.06060209	2835.0306	0.3527299
					0.7619	37.3033	5666.05	0.2326

Table 14: Summary of the filtered Mid and Far crossplot analysis in an area with no hydrocarbon

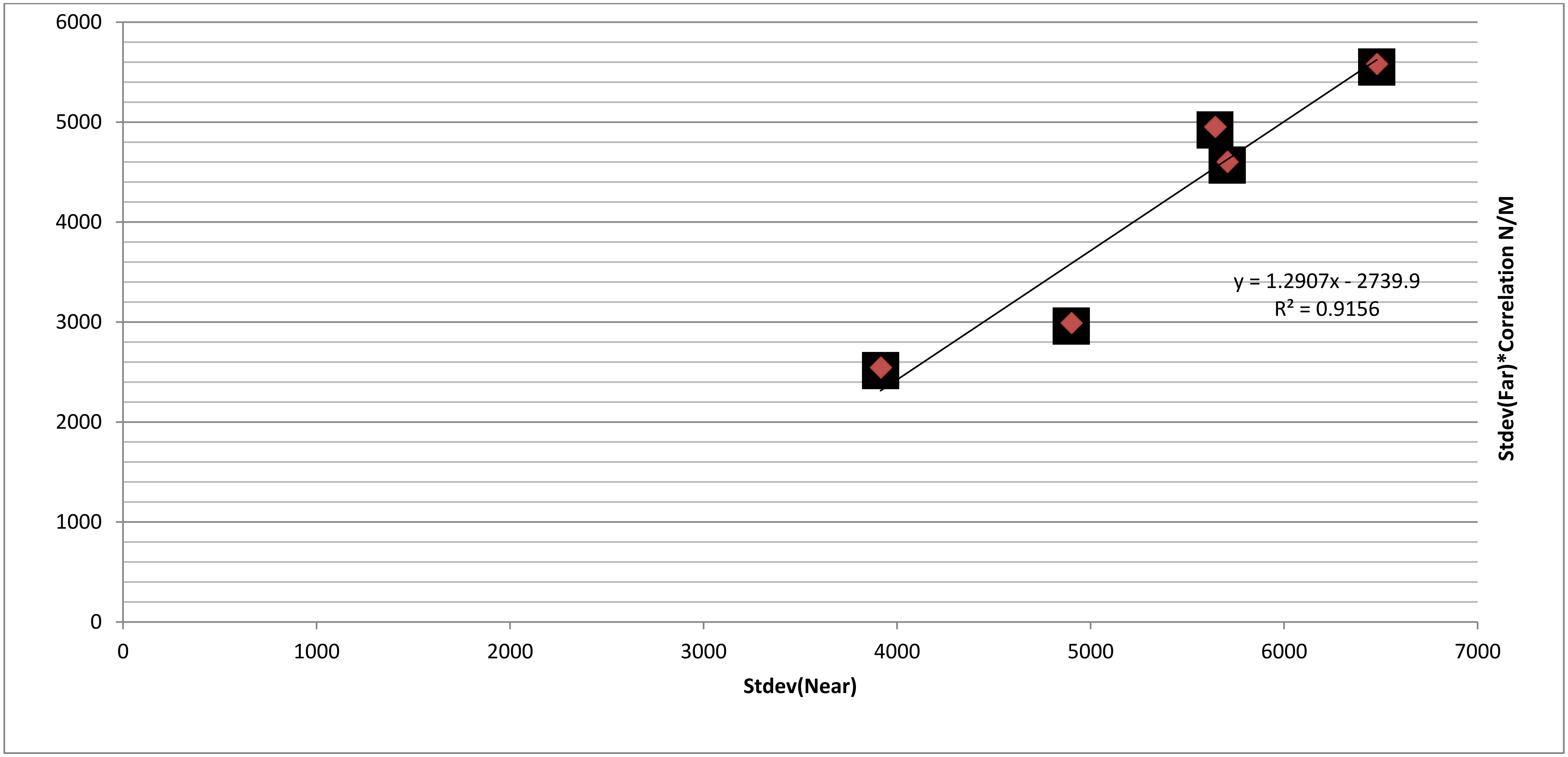

6.7.3 Final AVO Seismofacies Cube Computation

Final AVO Seismofacies cube is computed using filtered Mid and Far cubes as input and complete maps (slope, scaling range, correlation) computed in the previous step.

The final cube is computed only in the vertically defined interval (2100 -3300ms TWT). Outside of this interval, the result is set to zero. Each value of the final cube represents the vertical distance with the regression slope normalized at 1000 for one standard deviation of the AVO Seismofacies data. Results are often displayed a blue-white-red palette 

. This palette should be used as is (blue for negative and red for positive values) when seismic is zero phase with polarity such that an increase of impedance produces a positive value. With such a convention, top of a low Poisson’s ratio interval, such as one caused by the top of a hydrocarbon bearing sand, should correspond to a blue AVO Seismofacies response. A thin HC reservoir would show as a blue over red doublet; a HC related flat-spot would show as a red marker.

The dynamic range used in TOTAL is always (-9000, +9000). This range is such that the white interval represents +/-1000. In effect, this is whitening (Mid, Far) doublets distant from the background trend by less than one standard deviation: that is assumed to be non-significant or at least non discriminant to be a “derisking” observation. Hence, the computation was done in such a way that, when using the above colour palette with the above dynamic range, contrasts between shales and water sands are expected to be switched off (white), whereas anomalous AVO behaviour are enhanced by blue-red anomalies.

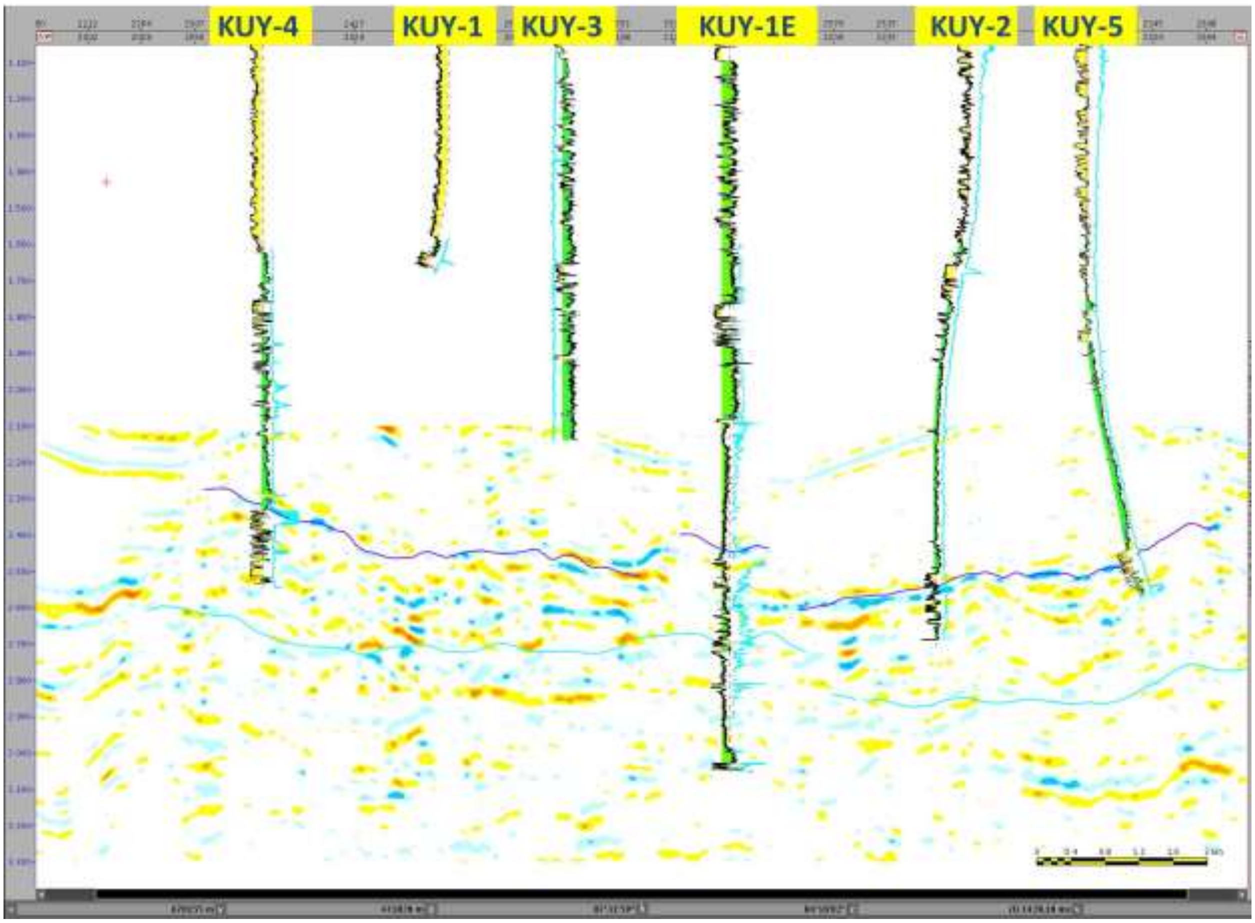

Figure 6.89: Random line through the AVO Seismofacies cube

CHAPTER SEVEN

AVO INTERPRETATION

7.0 AVO Seismofacies Interpretation

Having, computed the AVO Seismofacies cube using an adapted background trend with the data quality and validity controlled within the zone of interest, the AVO Seismofacies interpretation starts with a calibration at wells, AVO anomalies scanning, AVO analysis and interpretation and then integration with existing interpretation and evaluation. The AVO Seismofacies interpretation was done by employing the following steps in this order.

7.1 AVO Anomalies Scanning

The AVO Seismofacies cube was scanned in the target zone (where the computation is valid) using AVO Seismofacies maps (see Figures 7.5 & 7.6) extracted at horizon level (Tor3_MSF & Tor3_SB) to locate AVO anomalies. The AVO anomaly inventory was then completed by scanning the AVO Seismofacies cube in inline, crossline and random lines (see figures below). All anomalies give rather consistent AVO response ranging from weak to strong AVO amplitude.

<u>In-Line 2648</u>

This line follows the axis of the central fairway that traverses through well KUY-1E. Four AVO anomalies are seen along this line (see red circles on Figure7.0), the one on the left (west) and middle being at the edge of a structural trap has stronger response than the other two. It crosses a highly faulted area with highly dipping slopes, when the line crosses the sedimentary body, the AVO anomaly get stronger.

Cross-Line 2090

This line crosses the anomaly seen close to KUY- 4 well. Three AVO anomalies are seen alongside this line, with the one at the middle having stronger AVO response than the other two on both sides.

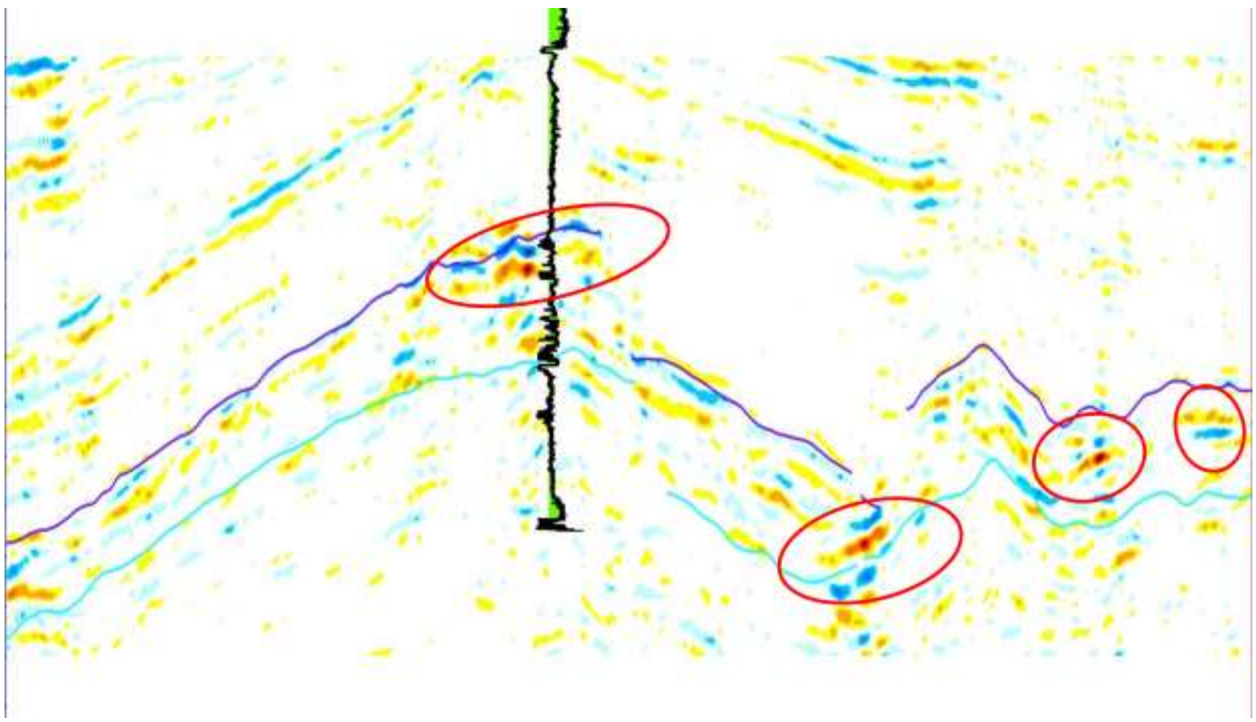

Figure 7.0: AVO Seismofacies cube scanned along Inline 2648

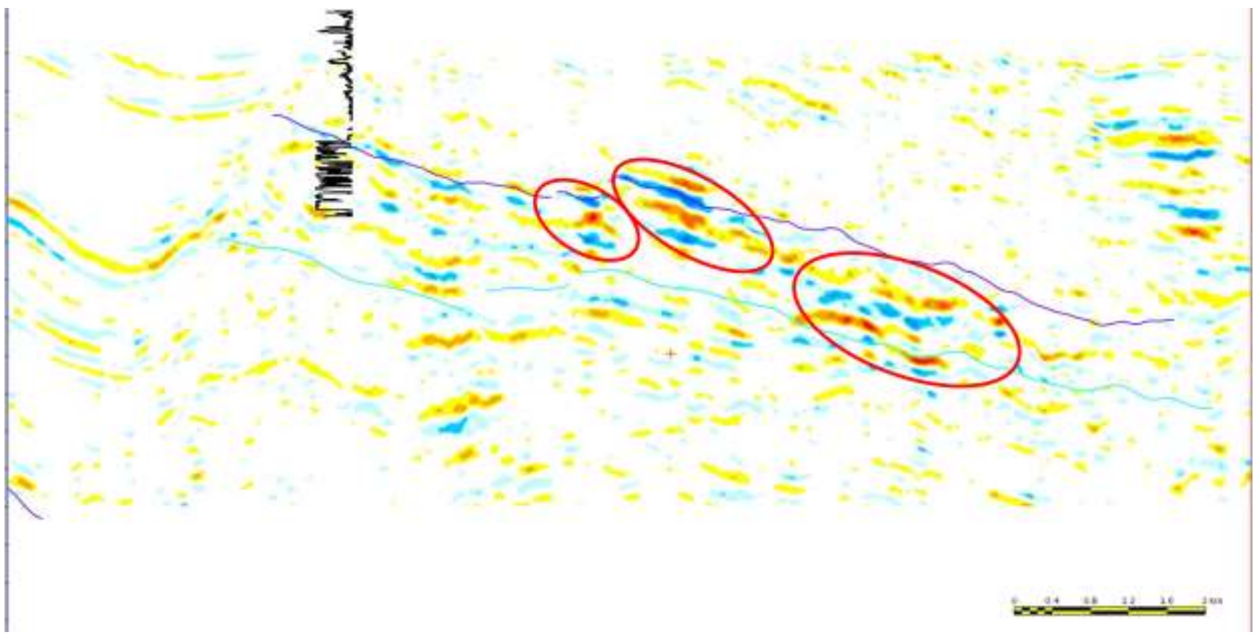

Figure 7.1: AVO Seismofacies cube scanned along Inline 2090

7.2 Calibration at Wells

The calibration of the AVO Seismofacies cube was done on the wells KUY-1E and KUY-4 (Figures 7.2 & 7.3). As can be seen, is the localization of the seismic-resolved reservoirs. The blue event showed a Poisson Ratio (PR) decrease which corresponds to the top of the hydrocarbon bearing reservoir. The yellow-red event showed a Poisson Ratio (PR) increase which could be interpreted as either the offset of a hydrocarbon reservoir or a known oil water contact.

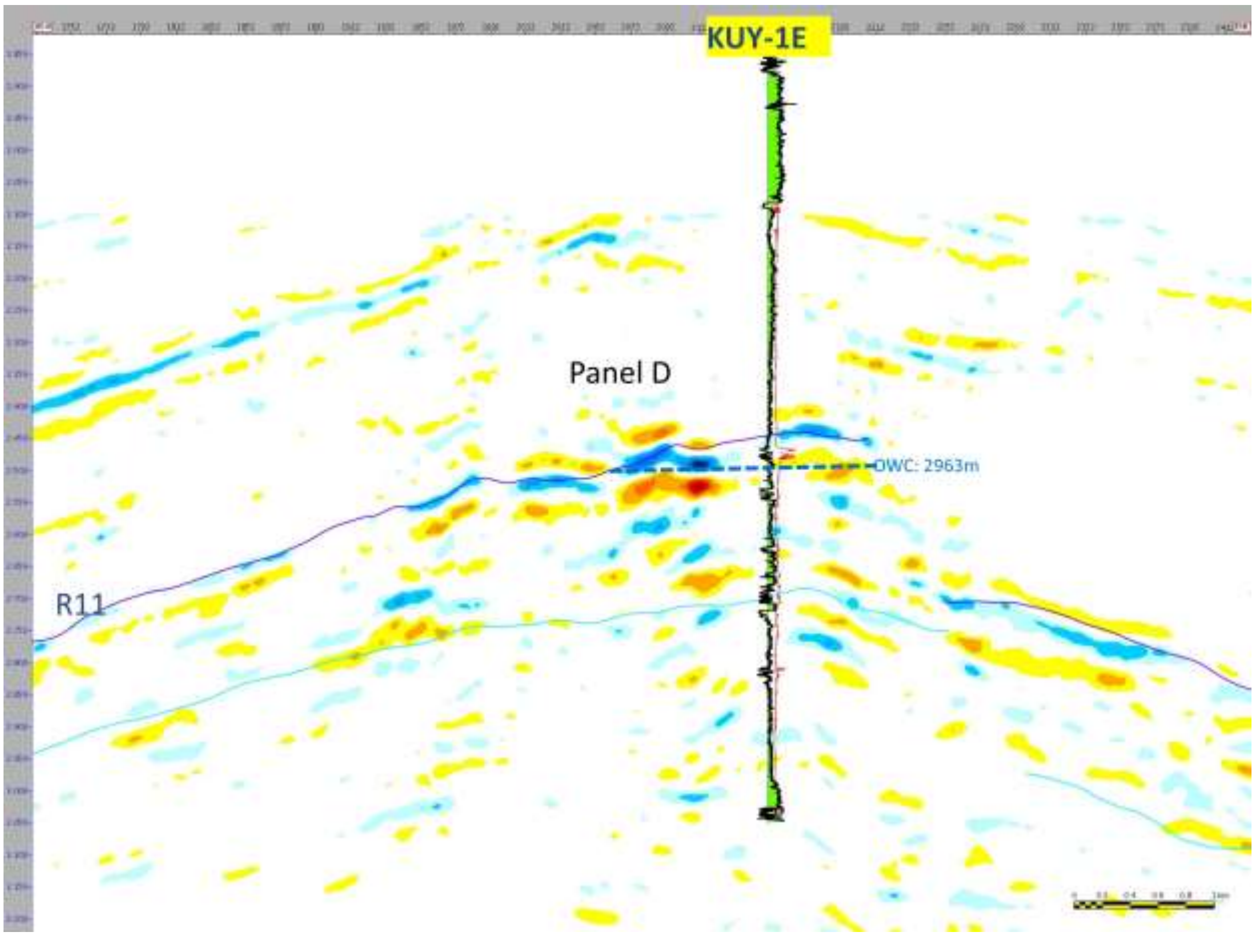

Figure 7.2: AVO Seismofacies calibration on KUY-1E well. Displayed is the volume of clay (VCL) and resistivity logs

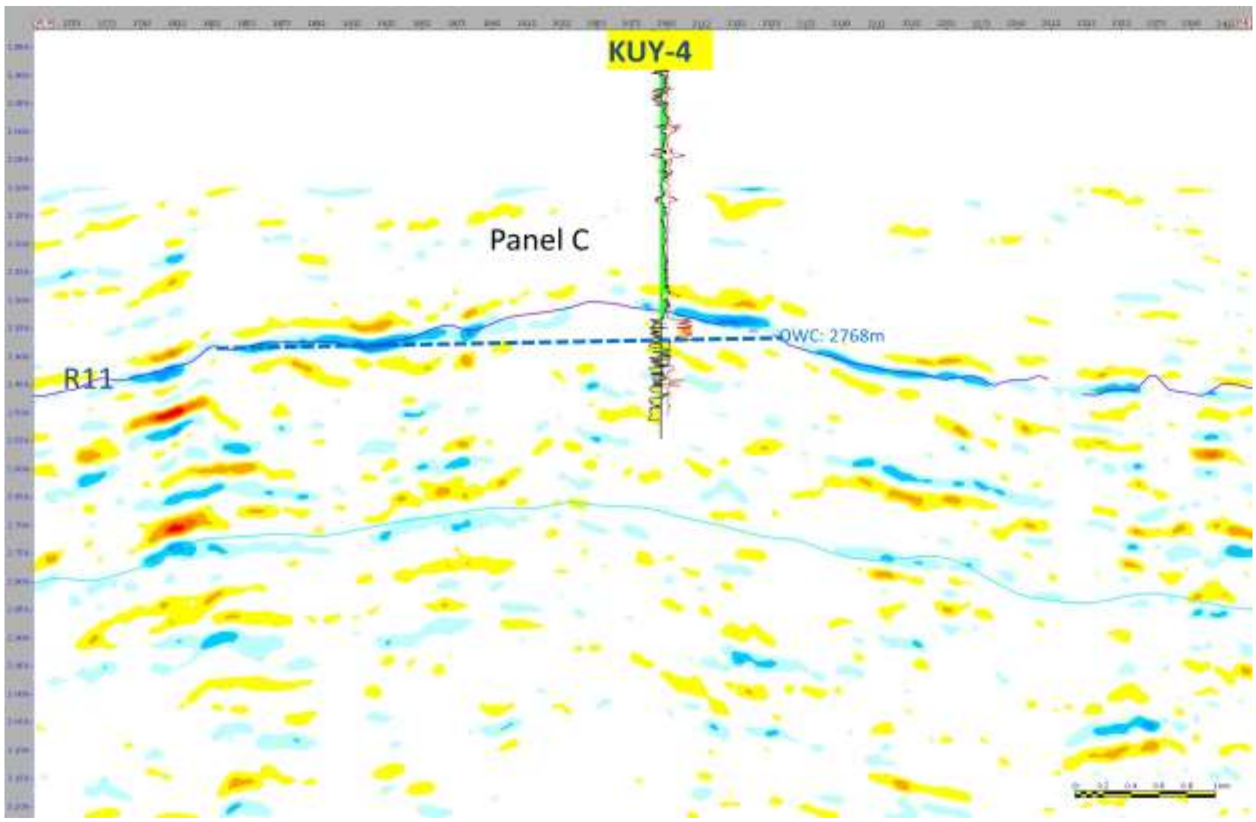

Figure 7.3: AVO Seismofacies calibration on KUY-4 well. Displayed is the volume of clay (VCL) and resistivity logs.

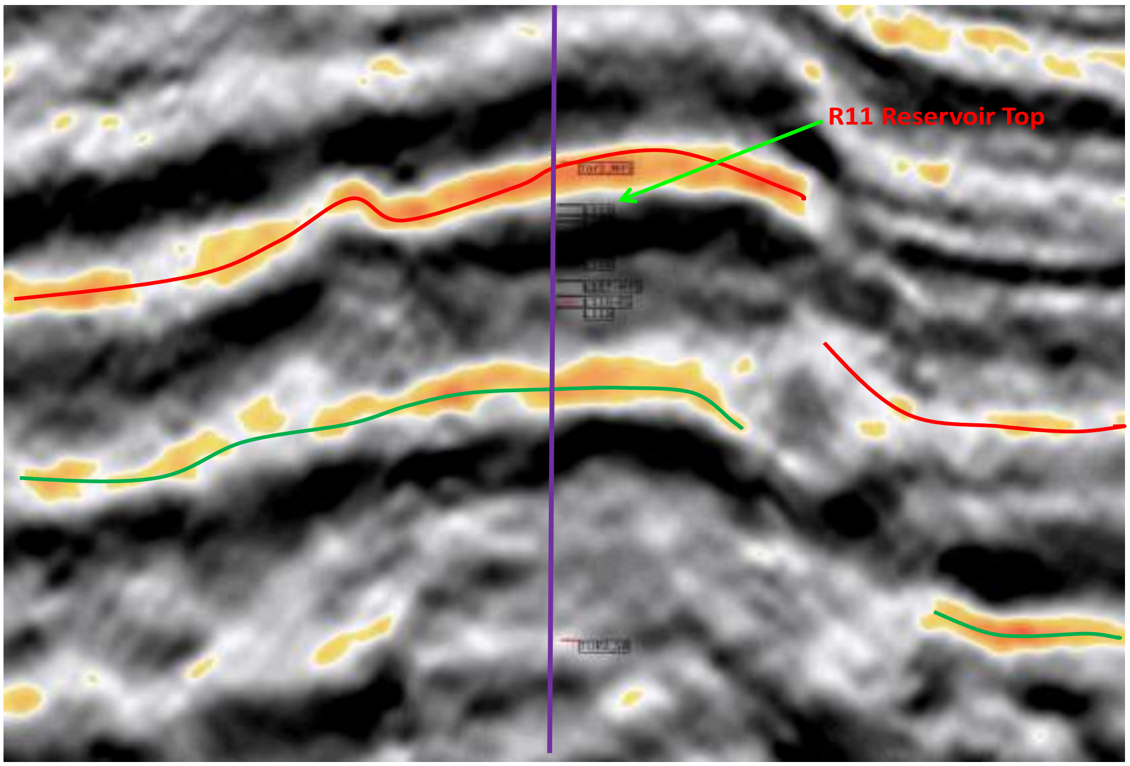

Figure 7.4: Seismic- section showing the top of R11 reservoir

7.3 AVO Analysis and Interpretation

The AVO anomalies were analyzed and compared to the AVO responses at wells to deduce what sort of fluid can be associated with the AVO response.

From the filtered Mid and Far substack several AVO maps have been realized. They are of two kinds:

- Root Mean Square (RMS) amplitude on a time slice, limited in time, in order to stack not too much anomalies. They give a global idea of the AVO anomalies location.
- Maximum negative AVO amplitude; as with our polarity convention an AVO anomaly begins with a negative amplitude (blue on seismic sections), this kind of maps highlights the shape of the top of the AVO anomalies.

The consistency of the AVO Seismofacies interpretation was evaluated with interpreters. The AVO anomaly extensions were consistent with the structural closure, fairways, the deposit system, the petroleum system and the migration paths and with the known water contacts (see Figures 7.5 - 7.8).

7.3.1 Root Mean Square (RMS) Map

Root Mean Square (RMS) map was extracted within the zone of interest and superimposed on the fault and depth maps to determine the consistency of the AVO anomalies with the structural and sedimentary interpretation. The Root Mean Square (RMS) AVO amplitude map shows some fair AVO anomalies. The yellow-red colours are high positive amplitudes. The normalized seismic amplitude map in Figure 7.5 showed a good fit-to-structure of the amplitude change at the apparent oil-water contact from seismic (see purple dotted lines is known oil-water contact at

2963m). The response is consistent with the trap geometry, the depositional model and the seismic rock properties from the well data.

7.3.2 Maximum Negative AVO Amplitude Map

Figure 7.6 showed the extracted maximum negative AVO amplitude map overlain on the depth contoured map. The map of the maximum negative AVO amplitude showed well organized anomalies fitting well with the initial interpretation. The blue colours are high negative amplitudes. The amplitude anomalies conform to the trapping geometry and estimated hydrocarbon-water contact from seismic.

7.3.3 Classification of AVO Response

The classification of AVO anomaly is based on the presence of oil and gas embedded sand (Rutherford and Williams, 1989). Class I gas sands have a positive normal-incidence reflection coefficient, lie in quadrant IV, and decrease in amplitude magnitude with increasing offset faster than the background trend. Class II gas sands have a small normal-incidence co-efficient (less than 0.02 in magnitude), but achieve a greater amplitude magnitude than the background at sufficiently high offsets. Polarity reversals are common with this type of reflector, which can lie in either quadrants II, III, or IV. Class III gas sands have a strongly negative normal-incidence reflection coefficient, which becomes even more negative with increasing offset. These sands lie in quadrant III. Class IV gas sands also have a negative normal-incidence reflection coefficient, but lie in quadrant II and decrease in amplitude magnitude with offwsset.

In order to determine the AVO class of sands for this study, amplitude values were extracted at the top of R11 reservoir from filtered Mid and Far substacks above the presumed Oil-Water-Contact (OWC). The amplitudes of the filtered Mid cube were then cross-plotted against the Far cube and the result suggested Class II sands which is in agreement with the characterization of Kuyolo sands in terms of acoustic impedance that classified the sands as Class I to Class II (see chapter four, table 10).

In summary, all analyzed AVO anomalies gave fair responses fitting rather well on the AVO maps with the structural and sedimentary interpretation, with anomaly shut-off at their base that may be interpreted as water/hydrocarbon contacts. AVO responses vary sometimes at stronger amplitudes.

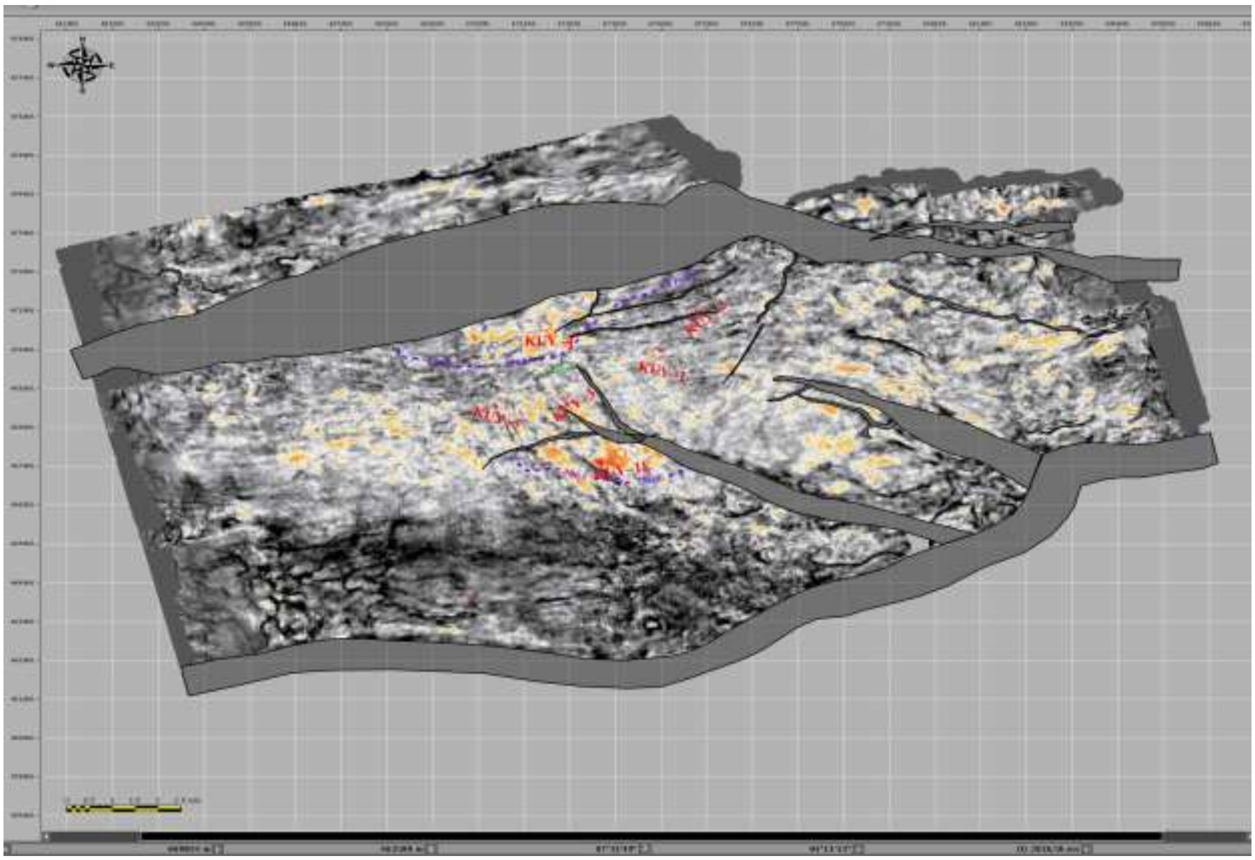

Figure 7.5 RMS (Root Mean Square) amplitude map superimposed on a fault and depth maps within R11 reservoir. The AVO amplitude anomalies (yellow-red event) are not only consistent with the structural and sedimentary interpretation but also with known water contact (purple lines).

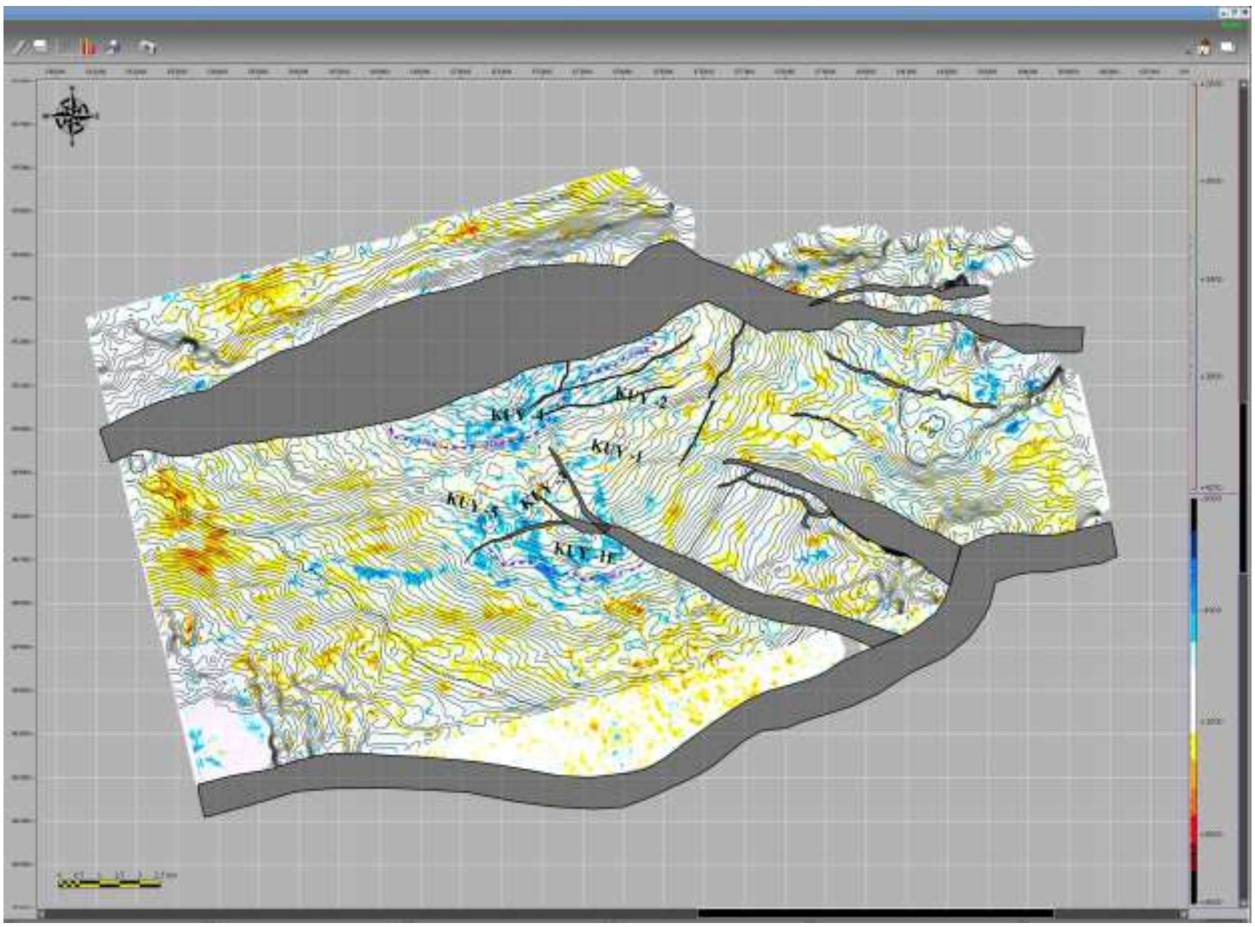

Figure 7.6 Maximum negative amplitude map superimposed on a fault and depth maps within R11 reservoir. The anomalous areas are the blue zones which is consistent with the well locations as can be seen.

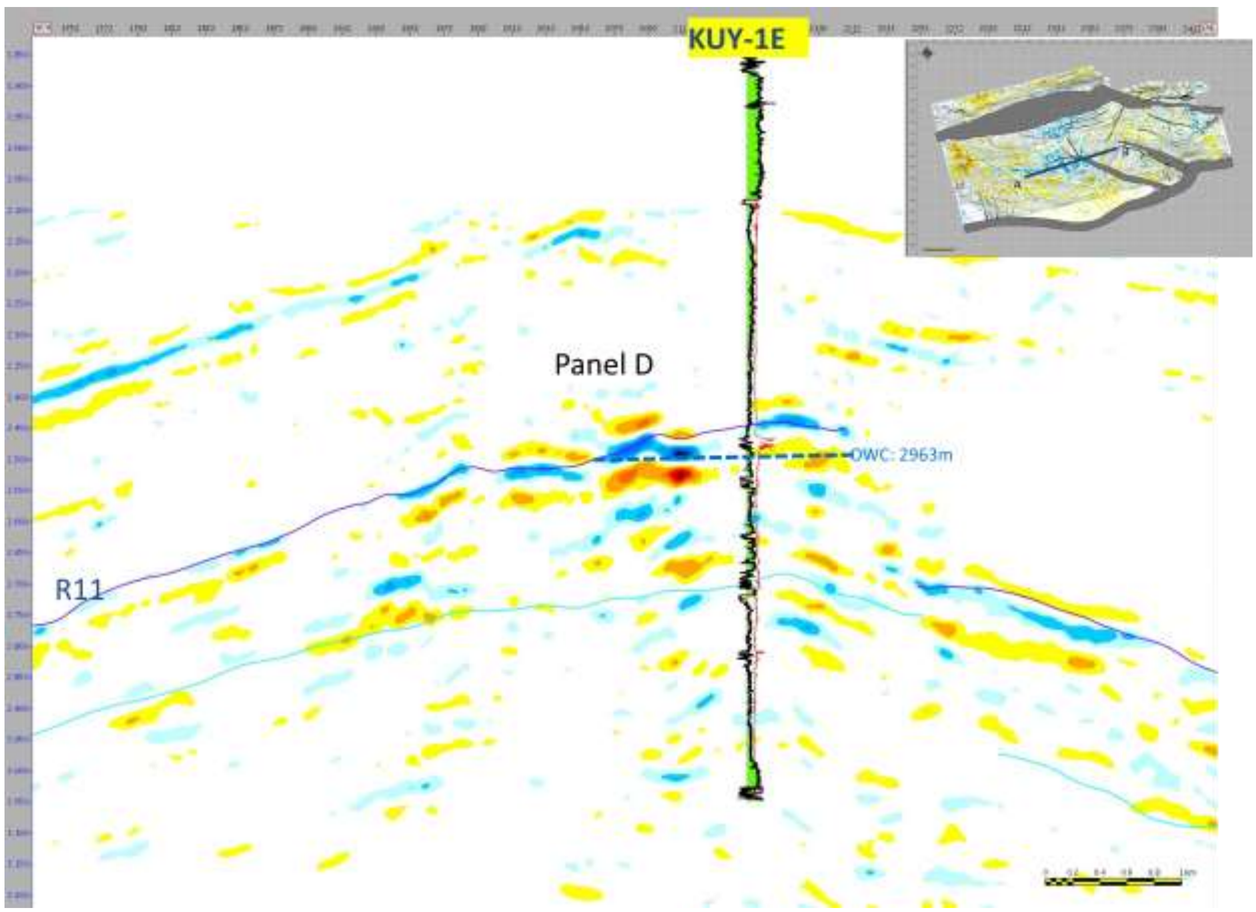

Figure 7.7 AVO Seismofacies cube on KUY-1E well with known water contact. The top of the R11 reservoir corresponds to the blue event that is accurately mapped.

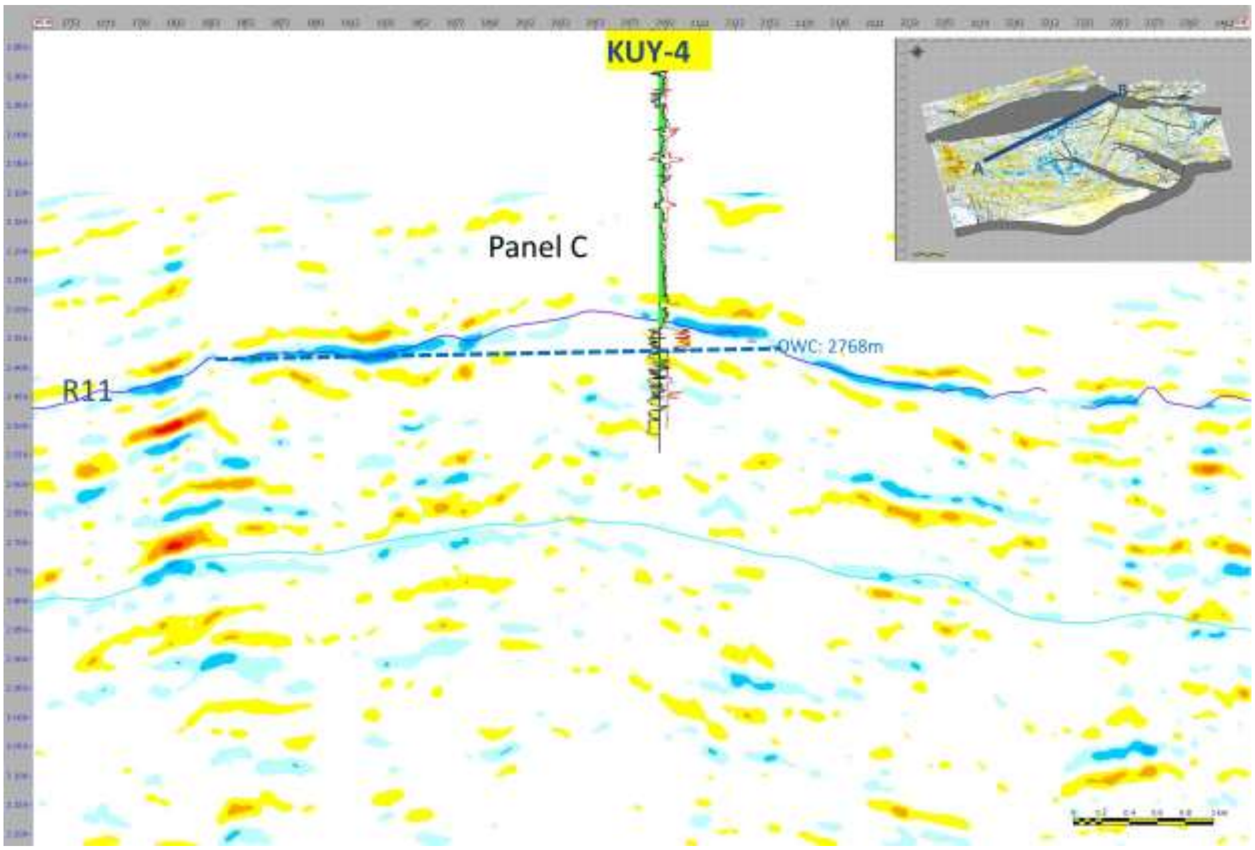

Figure 7.8 AVO Seismofacies cube on KUY-4 well with known water contact

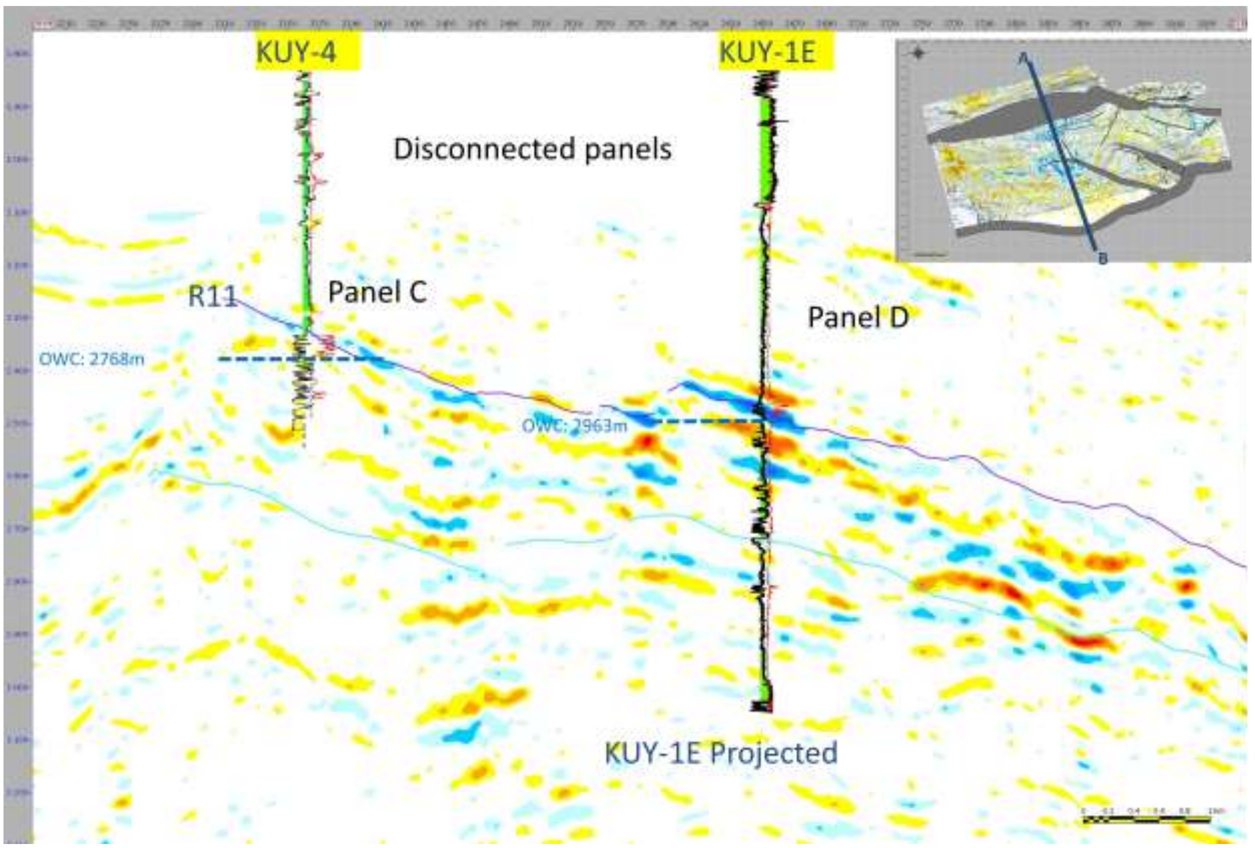

Figure 7.9 AVO Seismofacies cube on KUY-4 and KUY-1E wells with known water contact

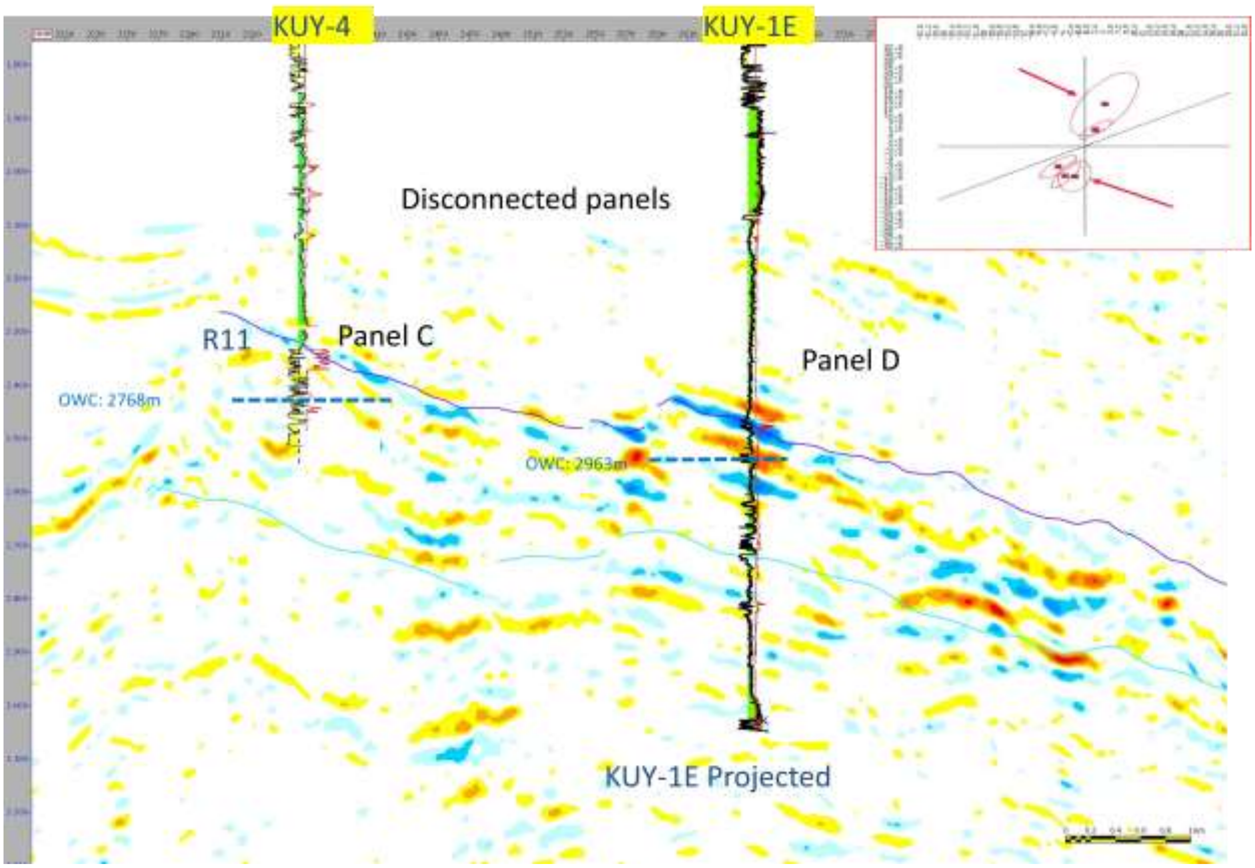

Figure 7.10 AVO Seismofacies cube with the amplitude crossplot of filtered Mid and Far stacks.

CHAPTER EIGHT

CONCLUSION AND RECOMMENDATIONS

8.0 Conclusion

In this study, AVO Seismofacies methodology based on integration of geophysical and petrophysical data was used to delineate, map and characterize the R11 reservoir of Kuyolo field, Niger Delta Basin.

The quality control analysis done on the available well and seismic data showed that though data quality was not optimum, it was nevertheless sufficient for this primary analysis of the Kuyolo field AVO anomalies.

The result of the seismic data interpretation showed excellent tie of the well and seismic data with the R11 reservoir clearly delineated and mapped with high confidence.

The shear wave data, which were not recorded, were determined empirically using the Gassmann method. Gassmann's fluid substitutions to brine, oil and gas were performed in order to model the effects of changes in pore fluids. The result of the comparison of the actual well log measurements with the modelled well logs showed that the logs were relatively similar over all wells, with the trends and variations of density and velocities correctly modelled, especially in clean sands. The analysis of the crossplots of modelled density(ρ) versus P-wave velocity (V_p) and Poisson's ratio (PR) versus acoustic impedance (IP) generated after water substitution over all the considered wells, showed overall good separation of water sands and shales giving us confidence that AVO Seismofacies methodology could be used to characterize the reservoirs.

Cross-correlation analysis showed that substack pairs of Near – Mid pair and Mid – Far pair were suitable for AVO analysis. The study revealed that cross-correlation between Near – Far pair substacks was too low to allow an AVO analysis using this pairing of substack.

Average lambda and slope in degrees values of 0.24 and 37º extracted from the crossplots of filtered Mid and Far offset substacks at several locations and depths where there was no hydrocarbon were used to compute the AVO Seismofacies cube.

All analyzed AVO anomalies gave fair responses fitting rather well on the AVO maps with the structural, sedimentary and stratigraphic interpretation, with anomaly shut-off at their base that could be interpreted as water/HC contacts. Results of crossplot analysis of the amplitude values extracted at the top of the R11 reservoir on filtered Mid and Far substacks above presumed Oil-Water-Contact (OWC) suggested class II reservoir sands.

Thus the analysis carried out in the study area enhanced the identification and delineation of the HC reservoir with high confidence. Additionally, the study has demonstrated that crossplots such as those developed and analyzed in this work helped to characterize the AVO class of reservoir sands.

8.1 Recommendations

To take full advantage of Well information in this study, it is recommended that the shear sonic should be acquired as this will help in the development phase of the field. A rock physics model or PetroElastic dedicated to Kuyolo field would also need to be constructed. In addition, the current AVO Seismofacies study should be updated taking into account expected improvements (such as better constraint of model and well position optimization) from the ongoing Dual Azimuth PreSDM reprocessing of 3D seismic from the field.

References

Aki, K. and Richards, P. G., 1980. Quantitative seismology - Theory and Methods, 1: W.H. Freeman and Co., San Francisco, 306pp.

Alkalifah, T. and Tsavankin, I., 1955. Velocity analysis for transversely isotopic media: Geophysics, vol. 60, pp.1550-1566.

Anstey, N. A., 1990. Velocity in thin section: First Break, vol. 9, pp.499-457.

Backus, M. M. and Chen, R. L., 1975. Flat spot exploration: Geophys. Prosp., vol. 23, pp.533 - 577.

Batzle, K. M. and Wang, Z., 1992. Seismic properties of fluid: Geophysics, vol.57, pp.1396-1408.

Beka, F. T. and Oti, M. N., 1995. The distal offshore Niger Delta: frontier prospects of a mature petroleum province. In: Oti, M.N., and Postma, G., (eds.), Geology of Deltas: Rotterdam, A.A. Balkema, pp. 237-241.

Biot, M. A., 1956a. Theory of propagation of elastic waves in fluid-saturated porous solid. I. Low frequency range: J. Acoustic. Soc. Am., vol. 28, pp.168-178.

Biot, M. A., 1956a, Theory of propagation of elastic waves in fluid - saturated porous solid. II. High frequency range: J. Acoustic. Soc. Am., vol. 28, pp.179-191.

Bork, J., Yin, C., Castagna, J., Karazincir, H., Wood, L. and Schneider, R., 1997. An investigation into unusual AVO signatures in the Gulf of Mexico and Trinidad: Presented at the 67th Ann. Internat. Mtg., Soc. Expl. Geophys., Expanded Abstracts, pp.199-201.

Bortfeld, R., 1961. Approximation to the reflection and transmission coefficients of plane longitudinal and transverse waves: Geophys. Prosp., vol. 9, pp. 485-503.

Bowers, G. L., 1995. Pore pressure estimation from velocity data: Accounting for over-pressure mechanisms besides under compaction: Soc. Petr. Eng., Drilling & Completion, June pp. 89-95.

Brown, A. R., 1999. Interpretation of three-dimensional seismic data, 5th ed. AAPG Memior 42 and SEG Investigations in Geophysics 9: AAPG and SEG, Tulsa, OK.

Burke, K., 1972. Longshore drift, submarine canyons, and submarine fans in development of Niger Delta: American Association of Petroleum Geologists, vol. 56, pp. 1975-1983.

Bustin, R. M., 1988. Sedimentology and characteristics of dispersed organic matter in Tertiary Niger Delta: origin of source rocks in a deltaic environment: American Association of Petroleum Geologists Bulletin, vol. 72, pp. 277-298.

Cambois, G., 1998. AVO attributes and noise: pitfalls in cross plotting: Presented at the 68th Ann. Internat. Mtg., Soc. Expl. Geophys., Expanded Abstracts, pp. 244-247.

Castagna, J.P., 1993. AVO analysis: Tutorial and review: in Castagna, J.P. and Backus, M.M., eds., Offset-dependent reflectivity - Theory and practice of AVO anomalies, Soc. Expl. Geophys. Investigations in Geophysics No. 8, pp. 3-36.

Castagna, J. P., 2000. An introduction to this special section: AVO- The next step: The Leading Edge, vol.19, pp. 1187.

Castagna, J. P., Batzle, M. L. and Kan, T. K., 1993. Rock physics - The link between rock properties and AVO response. In: Castagna, J. P. and Backus, M. M., eds., Offset-dependent reflectivity - Theory and practice of AVO anomalies, Soc. Expl. Geophys. Investigations in Geophysics No. 8, pp. 135 - 171.

Castagna, J. P., Batzle, M. L. and Eastwood, R. L., 1985. Relationships between compressional-wave and shear-wave velocities in clastic silicate rocks: Geophysics, vol.50, pp. 571-581.

Castagna, J. P. and Smith, S. W., 1994. Comparison of AVO indicators: A modeling study: Geophysics, vol. 59, pp. 1849 - 1855.

Castagna, J. P., Swan, H. W. and Foster, D. J., 1998. Framework for AVO gradient and intercept interpretation: Geophysics, vol. 63, pp. 948 - 956.

Cerveny, V. and Ravindran, R., 1971. Theory of seismic head waves: Univ. of Toronto Press, 245p.

Charles, P. U., Arnim, B. H. and Jonathan, E. D., 2007. Efficient spherical-wave AVO modeling: The Leading Edge, vol. 26, No. 12, pp. 1584- 1589.

Chesser, K., 1997. Missing data problems in forward AVO modeling: Presented at the 67th Ann. Internat. Mtg., Soc. Expl. Geophys., Expanded Abstracts, pp. 1187- 1190.

Chiburis, E. F., 1993. AVO applications in Saudi Arabia. In: Castagna, J. P. and Backus, M. M., (eds.), Offset-dependent reflectivity - Theory and practice of AVO anomalies, Soc. Expl. Geophys. Investigations in Geophysics No. 8, pp. 211 - 229.

Churlin, V. V. and Sergeyev, L. A., 1963. Application of seismic surveying to recognition of productive part of gas-oil strata: Geolog. Nefti I Gaza, vol. 7, pp. 363.

Connolly, P., 1999. Elastic impedance: The Leading Edge, vol. 18, pp. 438 - 452.

Corredor, F., J. H. Shaw, and J. Suppe, 2005. Shear fault-bend fold, deep-water Niger Delta, in J. H. Shaw, C. Connors, and J. Suppe, (eds.), Seismic Interpretation of Contractional Fault-related Folds: AAPG Studies in Geology vol. 53, pp. 87-92.

Disiena, J. P., Parsons, B. E. and Hilterman, F. J., 1995. Two-term inversion from AVO to detect the combined effect of porosity and gas in a Cretaceous sand reservoir: Presented at the 65th Ann. Internat. Mtg. Soc. Expl. Geophys., Expanded Abstracts, pp. 111 - 114.

Domencio, S. N., 1974. Effect of water saturation on seismic reflectivity of sand reservoirs encased in shale: Geophysics, vol. 39, pp. 759 - 769.

Doust, H. and Omatsola, E., 1990. Niger Delta. In: Edwards, J. D. and Santogrossi, P.A., (eds.), Divergent/passive Margin Basins, AAPG Memoir 48: Tulsa, American Association of Petroleum Geologists, pp. 239-248.

Dutta, N. C. and Levin, F. K., 1987. Geopressure: Soc. Expl. Geophys. Geophysics Reprint Series No. 7.

Ejedawe, J.E., 1981, Patterns of incidence of oil reserves in Niger Delta Basin: American Association of Petroleum Geologists, vol. 65, pp. 1574-1585.

Ejedawe, J.E., Coker, S.J.L., Lambert-Aikhionbare, D.O., Alofe, K.B. and Adoh, F.O., 1984. Evolution of oil-generative window and oil and gas occurrence in Tertiary Niger Delta Basin: American Association of Petroleum Geologists, vol. 68, pp. 1744-1751.

Ekwe, A. C. and Onuoha, K. M., 2014. Pore Fill and Lithology Discrimination from Cross-Plots of Elastic Rock Parameters: An Example from the Onshore Niger Delta Basin, Nigeria. Proceedings of the Nigerian Academy of Science, Vol. 7, No. 1, pp.67-85

Ekweozor, C. M. and Daukoru, E.M, 1984. Petroleum source bed evaluation of Tertiary Niger Delta--reply: American Association of Petroleum Geologists Bulletin, vol. 68, pp. 390-394.

Ekweozor, C. M. and Daukoru, E.M, 1994. Northern delta depobelt portion of the Akata-Agbada(!) petroleum system, Niger Delta, Nigeria. In: Magoon, L.B., and Dow, W.G., (eds.), The Petroleum System--From Source to Trap, AAPG Memoir 60: Tulsa, American Association of Petroleum Geologists, pp. 599-614.

Ekweozor, C. M., Okogun, J.I., Ekong, D.E.U. and Maxwell J.R., 1979. Preliminary organic geochemical studies of samples from the Niger Delta, Nigeria: Part 1, analysis of crude oils for triterpanes: Chemical Geology, vol. 27, pp. 11-28.

Ekweozor, C.M. and Okoye, N.V., 1980. Petroleum source-bed evaluation of Tertiary Niger Delta: American Association of Petroleum Geologists Bulletin, vol. 64, pp. 1251-1259.

Evamy, B.D., Haremboure, J., Kamerling, P., Knaap, W.A., Molloy, F.A. and Rowlands, P.H., 1978. Hydrocarbon habitat of Tertiary Niger Delta: American Association of Petroleum Geologists Bulletin, vol. 62, pp. 277-298.

Fatti, J. L., Smith G.C., Vail P. J., Strauss P. J. and Levitt P. R., 1994. Detection of gas in Sandstone Reservoirs using AVO Analysis: A 3D Seismic History using the Geostack Technique: Geophysics, vol. 59, pp. 1362 – 1376, doi: 10.1190/1.1443695

Forrest, M., 2000. Bright ideas still needed persistence: AAPG Explorer, vol. 21, No. 5, pp. 20 - 21.

Gardner, G. H. F. and Forel, D., 1987. Connections between rock properties and seismic data: Refresher course in geophysics, Univ. of Houston, Allied Geophysical Laboratories, 125pp.

Gardner, G. H. F., Gardner, L. W. and Gregory, A. R., 1974. Formation velocity and density - The diagnostic basics for stratigraphic traps: Geophysics, vol. 39, pp. 770 - 780.

Gassmann, F., 1951. Uber die elastizitat poroser medien: Viertejahrsschr. Der Naturforsch. Gesellschaft Zurich, vol. 96, pp. 1- 21.

Geerstma, J., 1961. Velocity-log interpretation: The effect of rock bulk compressibility. Soc. Petr. Eng. J., vol. 1, pp. 235 - 248.

Gidlow, P. M., Smith, G. C. and Vail, P. J., 1992. Hydrocabon detection using fluid factor traces: A case history: Presented at the Joint Soc. Expl. Geophys. /EAEG Summer Research Workshop on "How useful is amplitude-versus-offset (AVO) analysis?" pp. 78-89.

Goodway, B., Chen, T. and Downton, J., 1997. Improved AVO fluid detection and Lithology discrimination using Lame petrophysical parameters: Ir, mr & I\m fluid stack, from P and S inversions: Presented at the 67th Ann. Internat. Mtg., Soc. Expl. Geophys., Expanded Abstracts, pp.183 -186.

Graul, J. M., 1999. Amplitude variations with offset: AVO - Seismic Lithology: unpublished course notes for Soc. Expl. Geophys. Countinuing Education Course, 57pp.

Greenberg, M. L. and Castagna, J. P., 1992. Shear-wave velocity estimation in porous rocks: Theoretical formulation, preliminary verification and applications: Geophys. Prosp., vol. 40, pp. 195 - 210.

Gregory, A. R., 1977. Aspects of rock physics from laboratory and log data that is important to seismic interpretation. In: Payton, C. E., ed., Seismic Stratigraphy- Applications to Hydrocarbon Exploration, AAPG Memoir vol. 26, pp. 15 - 46.

Greve, G. M., 1997. Seismic quality - Let's tell it like it is: The Leading Edge, vol. 16, pp.145-148.

Hamilton, E. L., 1979. VP/VS and Poisson's ratio in marine sediments and rocks. In: Nur, A.M. And Wang, Z., (eds.), Seismic and acoustic velocities in reservoir rocks, vol. 1, Experimental Studies, Soc. Expl. Geophys. Reprints Series, vol.10, pp. 272 - 280.

Han, D.H., 1986. Effects of porosity and clay content on acoustic properties of sandstones and unconsolidated sediments: Ph.D dissertation, Stanford University, 234p.

Han, D.H., Nur, A. and Morgan, D., 1986. Effects of porosity and clay content on wave velocities in sandstones: Geophysics, vol. 51, pp. 2093 - 2107.

Hatchell, P.J., 2000. Fault whispers: Transmission distortions on prestack seismic reflection data: Geophysics, vol. 65, pp. 377- 389.

Herbert, W. S., 2007. Automatic compensation of AVO background drift: The Leading Edge, vol. 26, No. 12, pp. 1528- 1536.

Hendrickson, J. S., 1999. Stacked: Geophys. Prosp., vol. 47, pp. 663- 706.

Hill, R. W., 1952. The elastic behavior of crystalline aggregate: Proc. Physical Soc. London, A65, pp. 349- 354.

Hilterman, F. J., 1975. Amplitude of Seismic waves - A quick look: Geophysics, vol. 40, pp. 745- 762.

Hilterman, F. J., 1982. Interpretative lessons in three- dimensional modeling: Geophysics, vol. 47, pp. 784- 808.

Hilterman, F. J., 1990. Is AVO the seismic signature of lithology? A case history of Ship Shoal - South Addition: The Leading Edge, vol. 9, No. 6, pp. 15-22.

Hilterman, F. J., Sherwood, J. W. C., Schellhorn, R., Bankhead, B. and DeVault, B., 1998. Identification of lithology in Gulf of Mexico: The Leading Edge, vol. 17, No. 2, pp. 215- 222.

Hilterman, F. J., Van Schuyver, C. and Sbar, M., 2000. AVO examples of long-offset 2-D data in the Gulf of Mexico: The Leading Edge, vol.19, No. 11, pp. 1200- 1213.

Hilterman, F. J., Verm, R., Wilson, M. and Liang, L., 1999. Calibration of rock properties for deep- water seismic: Presented at 31st Offshore Technology Conference, OTC 10844, pp. 451- 458.

Hottmann, C. E. and Johnson, R. K., 1965. Estimation of formation pressures from log-derived shale properties: J. Petr. Tech., vol. 17, pp. 717- 722.

Jakosky, J. J., 1960. Exploration geophysics, 2nd ed. Trija Publishing Company, 380pp.

Jeffrey, A. M., Mark, S. P., Ruble, C., Tom, M. and Jaime, G. P., 2007. Amplitude anomalies in a sequence stratigraphic framework: exploration successes and pitfalls in a subgorge play, Sacramento Basin, California: The Leading Edge, vol. 26, No. 12, pp. 1516- 1526.

Kathryn, T. Y. and Robert, H. T., 2007. Fluid discrimination of poststack bright spots using lambda-mu-rho (LMR) inversion in the Columbus Basin, offshore Trinidad: The Leading Edge, vol. 26, No. 12, pp. 1508- 1515.

Knott, C. G., 1899. Reflection and refraction of elastic waves with seismological applications: Phil. Mag., vol. 48, pp. 64- 97.

Koefoed, O., 1955. On the effect of Poisson's ratios of rock strata on the reflection coefficients of plane waves: Geophys. Prosp., vol. 3, pp. 381- 387.

Kozman, J. B., and Hilterman, F. J., 2000. AVO analysis of long offset 2D data in the western Gulf of Mexico: Presented at the 2000 AAPG Annual Convention, Abstracts, pp. A80.

Krief, M., Garat, J., Stellingwerff, J., and Ventre, J., 1990, A petrophysical interpretation using the velocities of P and S waves (full-waveform sonic): The Log Analyst, vol. 31, pp. 355- 369.

Kulke, H., 1995. Nigeria, In: Kulke, H., ed., Regional Petroleum Geology of the World. Part II: Africa, America, Australia and Antarctica: Berlin, Gebrüder Borntraeger, pp. 143- 172.

Kuster, G.T. and Toksöz, M. N.m 1974. Velocity and attenuation of seismic waves in two-phase media: Geophysics, vol. 39, pp. 587- 618.

Lawrence, S. R., Munday, S. and Bray, R., 2002. Regional geology and geophysics of the eastern Gulf of Guinea (Niger Delta to Rio Muni): The Leading Edge, vol. 21, No. 11, pp. 1112 – 1117.

Lambert-Aikhionbare, D. O. and Ibe, A.C., 1984. Petroleum source-bed evaluation of the Tertiary Niger Delta: discussion: American Association of Petroleum Geologists Bulletin, vol. 68, pp. 387-394.

Lin, T. L. and Phair, R., 1993. AVO tuning: Presented at 70th Ann. Internat. Mtg. Soc. Expl. Geophys., Expanded Abstracts, pp.727- 730.

MacLeod, M. K., Hanson, R. A., Bell, C. R. and McHugo, S., 1999. The Alba Field ocean bottom cable seismic survey: Impact on development: The Leading Edge, vol. 18, pp. 1306- 1312.

Mavko, G., Mukerji, T. and Dvorkin, J., 1998. The rock physics handbook - Tools for seismic analysis in porous media: Cambridge Univ. Press, 579pp.

Merlini, E., 1959. Un nouveau dispositif auxiliarie dans la recherché sismique: Geophys. Prosp. Vol. 7, pp. 129.

Necati , G., Mag, M. and Henrik, H. R., 2007. Gather flattening: The Leading Edge, vol. 26, No. 12, pp. 1538- 1543.

Neidell, N. S. and Poggiagliolmi, E., 1977. Stratigraphic modeling and interpretation-geophysical principles and techniques. In: Payton, C. E., ed., Seismic Stratigraphy-Applications to hydrocarbon exploration, AAPG Memoir vol. 26, pp. 389 - 416.

Neff, D., 1992. Estimated pay mapping using three-dimensional seismic data and incremental pay thickness modeling*in* Sheriff, R. E., (ed.), Reservoir geophysics, Soc. Expl. Geophys. Investigations in Geophysics, vol. 7, pp. 207- 214.

Nickerson, R. L. and Tuttle, S., 2000 Lower exploration risk - Using a maximum likelihood clustering and AVO analysis: Presented at the 70th Ann. Internat. Mtg. Soc. Expl. Geophys., Expanded Abstracts, pp. 110- 113.

Nur, A. M. and Wang, Z., (eds.), 1989. Seismic and acoustic velocities in reservoir rocks - Experimental studies: vol. 1. Soc. Expl. Geophys. Geophysics Reprint Series No. 10.

Nur, A., Marion, D. and Yin, H., 1991. Wave velocities in sediments. In: Hovem, J. M., Richardson, M.D., and Stoll, R.D., eds., Shear Waves in Marine Sediments, Kluwer Academic Publishers, Dordrecht, The Netherlands, pp. 131- 140.

Omudu, L.M. and Ebeniro, J.O., 2005. Cross-plotting of rock properties for fluid discrimination using well data in offshore Niger Delta: Nigerian Journal of Physics, Vol. 17, pp. 16-20.

Ostrander, W.J., 1982. Plane wave reflection coefficients for gas sands at non normal angles of incidence: Presented at the 52nd Ann. Internat. Mtg. Soc. Expl. Geophys., Expanded Abstracts, pp. 216- 218.

Ostrander, W.J., 1984. Plane wave reflection coefficients fir gas sands at non normal angles of incidence: Geophysics, vol. 49, pp. 1637- 1648.

Paige, D.S., 1973. The dark side of the bright spot: Presented at the GSH Lithology and direct detection of hydrocarbons using geophysical methods symposium.

Pan, P.P., 1969. Direct location of oil and gas by the seismic reflection method: Ph.D Thesis, Rice Univ.

Pan, P.P. and de Bremaecker, J.C., 1970. Direct location of oil and gas by the seismic reflection method: Geophys. Prosp, vol.18, pp.712- 727.

Pennebaker, E.S., 1968. Seismic data indicate depth, magnitude of abnormal pressure World Oil, vol. 171, pp. 78-82.

Pickett, G., 1963. Acoustic character logs and their applications in formation evaluation: J. Petr. Tech., vol. 15, pp. 650- 667.

Pisetski, V. B., 1997. A method for determining the presence of fluids in a subterranean formation, U.S.A. Patent Application 57274744.

Prescott, W. T., 1973. VIBROSEIS bright spot - An example: Presented at the GHS Lithology and direct detection of hydrocarbons using geophysical methods symposium.

Press, W. H., Teukolsky, S. A., Vetterling, W.T., and Flannery, B.P., 1996. Numerical recipes in Fortran 77- 2nd ed. - The art of scientic computing: Cambridge Univ. Press, 210pp.

Quakenbush, M., B. Shang, and C. Tuttle, 2006. Poisson Impedance: The Leading Edge, vol. 25, pp. 128-138, doi: 10.1190/1.2172301

Raymer, L. L., Hunt, E. R. and Gardner, J. S., 1980. An improved sonic transit time-to-porosity transform: Presented at the Soc. Prof. Well Log Analysts 21st Annual Logging Symposium, Transactions.

Reijers, T.J.A., Petters, S.W. and Nwajide, C.S., 1997. The Niger Delta Basin. In: Selley, R.C., (ed.), African Basins--Sedimentary Basin of the World 3: Amsterdam, Elsevier Science, pp. 151-172.

Resnick, J. R., 1993. Seismic data processing for AVO and AVA analysis: in Castagna, J. P., and Backus, M.M., (eds.), Offset -dependent reflectivity- Theory and practice of AVO anomalies, Soc. Expl. Geophys. Investigations in Geophysics, vol. 8, pp. 175- 189.

Reuss, A., 1929. Berechnung der Fliessgrenzen von Mischkristallen auf Grund der Plastizitãtsbedingung für Einkristalle: Zeitschrift für Angewandte Mathematik und Mechanik, vol. 9, pp. 49- 58.

Revoir, M. E., Hawkins, J. G. and Duffy, R. E., 1992. Integrating AVO modeling and processing products - An offshore Gulf of Mexico case study for the applied explorationist: Presented at the Joint Soc. Expl. Geophys./EAEG Summer Research Workshop on "How useful is amplitude-versus-offset (AVO) analysis?" pp. 140- 153.

Richards, P.G. and Fraiser, C. W., 1976. Scattering of elastic waves from depth-dependent inhomogenities; Geophysics, vol. 41, pp. 441-458.

Rosa, A. L. R., 1976. Extraction of elastic parameters using seismic reflection amplitudes with offset variations: M. S Thesis, Univ. of Houston.

Ross, C. P., 2000. Effective AVO crossplot modeling: Geophysics, vol. 65, pp. 700- 711.

Ross, C. P. and Beale, P. C., 1994. Seismic offset balancing: Geophysics, vol. 59, pp. 93- 101.

Ross, C. P. and Kinman, D. L., 1995. Nonbright-spot AVO: Two examples: Geophysics, vol. 60, pp. 1398- 1408.

Ruger, A., 1996. Reflection coefficients and azimuthal AVO analysis in anisotropic media: Ph. D thesis, Center for Wave Phenomena, Colorado School of Mines, Golden, C.O.

Russel, B., Hawkins, J. G., Lashgari, B. and Revoir, M. E., 1992. AVO modeling and inversion- An offshore Gulf of Mexico case study: Presented at the Joint Soc. Expl. Geophys. /EAEG Summer Research Workshop on "How useful is amplitude-versus-offset (AVO) analysis?” pp. 154-163.

Rutherford, S. R. and Williams, R.H., 1989. Amplitude-versus-offset in gas sands: Geophysics, vol. 54, pp. 680- 688.

Savit, C. H., 1960. Preliminary report, A stratigraphic seismogram: Geophysics, vol. 25, pp. 312-325.

Schlumberger, 1972. Log interpretation - Volume 1 - Principles: Schlumberger Ltd.

Sengbush, R. L ., 1983. Seismic exploration methods: Internat. Human Res. Dev. Corp.

Sengbush, R. L., Lawrence, P. L. and McDonal, F. J., 1961. Interpretation of synthetic seismograms: Geophysics, vol. 26, pp. 138- 157.

Sheriff, R.E., (ed.), Reservoir Geophysics, Soc. Expl. Geophys. Investigations in Geophysics No. 7, pp. 353 - 361.

Sheriff, R.E., 1989. Geophysical Methods: Prentice Hall, 80pp.

Sherwood, J.W.C., Hilterman, F.J., Neale, R. and Chen, K.C., 1983. Synthetic seismogram with offset for layered elastic medium: Presented at the 15th Offshore Technology Conference, OTC 4508, pp. 539- 546.

Shuey, R. T., 1985. A simplification of the Zoeppritz equations: Geophysics, vol. 50, pp. 609-614.

Short, K. C. and Stäuble, A.J., 1965. Outline of geology of Niger Delta: American Association of Petroleum Geologists Bulletin, vol. 51, pp. 761-779.

Simmons, J. L. Jr. and Backus, M. M., 1994. AVO modeling and the locally converted shear wave: Geophypsics, vol. 59, pp. 1237- 1248.

Smith, G. C. and Gidlow, P. M., 1987. Wighted stacking for rock property estimation and detection of gas: Geophys. Props., vol. 35, pp. 993- 1014.

Smith, G. C. and Sutherland, R. A., 1996. The fluid factor as an AVO indicator: Geophysics, vol. 61, pp. 1425- 1428.

Spratt, S., 1987. Effect of normal moveout errors on amplitude versus offset- derived shear reflectivity: 57th SEG Expanded Abstracts, pp. 634- 637.

Stacher, P., 1995. Present understanding of the Niger Delta hydrocarbon habitat. In: Oti, M.N., and Postma, G., (eds.), Geology of Deltas: Rotterdam, A.A. Balkema, pp. 257-267.

Swan, H. W., 1993. Properties of direct AVO hydrocarbon indicators. In: Castagna, J. P., and Backus, M. M., eds., Offset-dependent reflectivity- Theory and practice of AVO anomalies, Soc. Expl. Gephys. Investigations in Geophysics No. 8, pp.78- 92.

Thomsen, L., 1986. Weak elastic anisotropy: Geophysics, vol.51, pp.1954- 1966.

Tsvankin, I. and Thomsen, L., 1994. Non-hyperbolic reflection moveout in anisotropic media: Geophysics, vol. 59, pp. 1290- 1304.

Tsvankin, I. and Thomsen, L., 1995. Inversion of reflection travel times for transverse isotropy: Geophysics, vol. 60, pp. 1095- 1107.

Tucker, P. M., 1982. Pitfalls revisited: Soc. Expl. Geophys., Tulsa, OK.

Tuttle, M. L. W., Charpentier, R. R. and Brownfield, M. E., 1999. The Niger Delta Basin Petroleum System: Niger Delta Province, Nigeria, Cameroon and Equatorial Guinea, Africa; Open-File Report 99-50-H, United States Geological Survey World Energy Report, 44pp.

Ujuanbi, O., Okolie, J.C. and Jegede, S.I., 2008. Lambda-Mu-Rho techniques as a viable tool for litho- fluid discrimination- the Niger Delta example: International Journal of Physical Sciences, Vol. 2(7), pp. 173-176.

Vali, P. R., Todd, R.G. and Sangree, J. B., 1977. Seismic Stratigraphy and global changes in sea level, Part 5: Chronostratigraphic significance of seismic reflections. In: Payton, C. C., (ed.), Seismic stratigraphy - Applications to hydrocarbon exploration: Memoir 26, AAPG, pp. 99- 116.

Verm, R. and Hilterman. F., 1955. Lithology color-coded seismic sections, The calibration of AVO crossplotting to rock properties: The Leading Edge, vol. 14, pp. 847- 853.

Verm, R., Liang, L. and Hilterman, F. J., 1998. Significance of geopressure in predicting lithology: The Leading Edge, vol. 17, pp. 227- 234.

Voigt, W., 1928. Lehrbuch der Kristallphysik: Teubner, Leipzig, Germany.

Wang, Y., 1999. Approximations to the Zoeppritz equations and their use in AVO analysis: Geophysics, vol. 64, pp. 1920- 1937.

Wang, Z. and Nur, A. M., 1992. Seismic and acoustic velocities in reservoir rocks- Theoretical and model studies: vol. 2, Soc. Expl. Geophys., Geophysics Reprint Series No. 10.

Weber, K.J., 1987. Hydrocarbon distribution patterns in Nigerian growth fault structures controlled by structural style and stratigraphy: Journal of Petroleum Science and Engineering, vol. 1, pp. 91-104.

Weber, K. J. and Daukoru, E.M., 1975. Petroleum geology of the Niger Delta: Proceedings of the Ninth World Petroleum Congress, volume 2, Geology: London, Applied Science Publishers, Ltd., pp. 210-221.

Whiteman, A., 1982. Nigeria: Its Petroleum Geology, Resources and Potential: London, Graham and Trotman, 394 pp.

Widess, M.B., 1973. How thin is a thin bed?: Geophysics, vol.38, pp.1176- 1180.

Wiggins, R. K., Kenny, G. S. and McClure, C. D., 1983. A method for determining and displaying the shear- velocity reflectivities of a geologic formation: European Patent Application 0113944.

Wood, A. W., 1955. A textbook of sound: The MacMillian Co, 101pp.

Wright, J., 1986. Reflection coefficients at pore-fluid contacts as a function of offset: Geophysics, vol. 51, pp. 1858- 1860.

Wylie, M. R. J., 1963. The fundamentals of electric log interpretation, 2nd ed.: Academic Press, 111p.

Wylie, M. R. J., Gregory, A. R. and Gardner, G. H. E., 1958. An experimental investigation of factors affecting elastic wave velocities in porous media: Geophysics, vol. 23, pp. 459- 493.

Wylie, M. R. J., Gregory, A. R. and Gardner, L. W., 1956. Elastic wave velocities in heterogenous and porous media: Geophysics, vol. 21, pp. 41- 70.

Xu, S. and White, R. E., 1995. A new velocity for clay-sand mixtures: Geophys. Prosp., vol. 43, No. 1, pp. 91- 118.

Yeshpal Singh., 2007. Lithofacies detection through simultaneous inversion and principal component attributes: The Leading Edge, vol. 26, No. 12, pp. 1576- 1583.

Yong, X., and Satinder, C., 2007. Improving AVO fidelity by NMO stretching and offset dependent tuning corrections: The Leading Edge, vol.26, No. 12, pp. 1548- 1551.

Zoeppritz, K., 1919. Erdbebenwellen VIIIB, On the reflection and propagation of seismic waves: Gottinger Nachrichten, vol. I, pp. 66- 84.

PLATE 1-10

WELL: BOB-1
MEASUREMENTS and MODELLING

Vertical Scale : 1/1500 cm

Plate 4

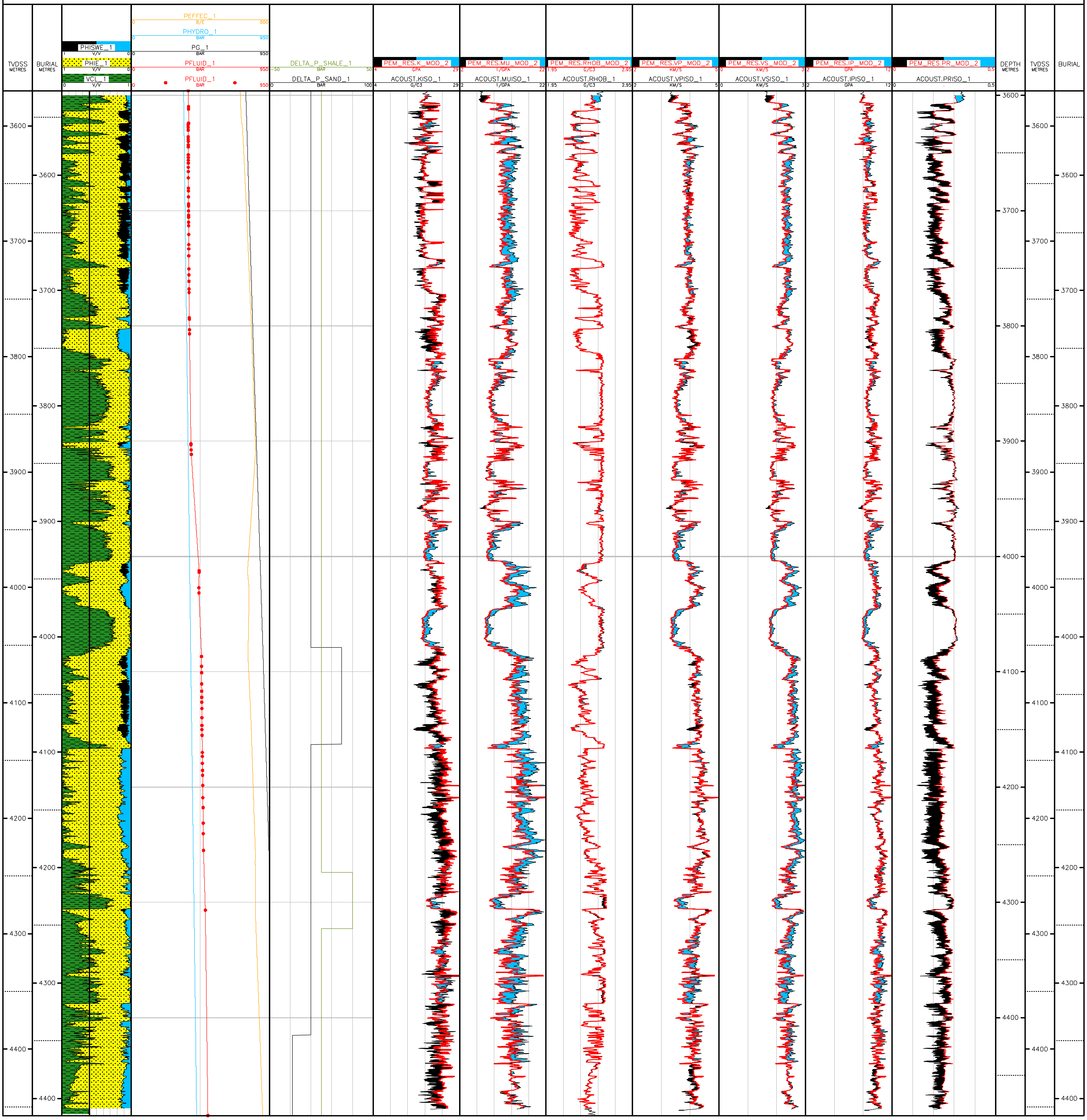

WELL: COC-4
MEASUREMENTS and MODELLING

Vertical Scale : 1/1500 cm

Plate 2

WELL: EFE-2
MEASUREMENTS and MODELLING

Vertical Scale : 1/1500 cm

Plate 1

WELL: KUY-1E
MEASUREMENTS and MODELLING

Vertical Scale : 1/1500 cm

Plate 3

WELL: WOM-1
MEASUREMENTS and MODELLING

Vertical Scale : 1/1500 cm

Plate 5

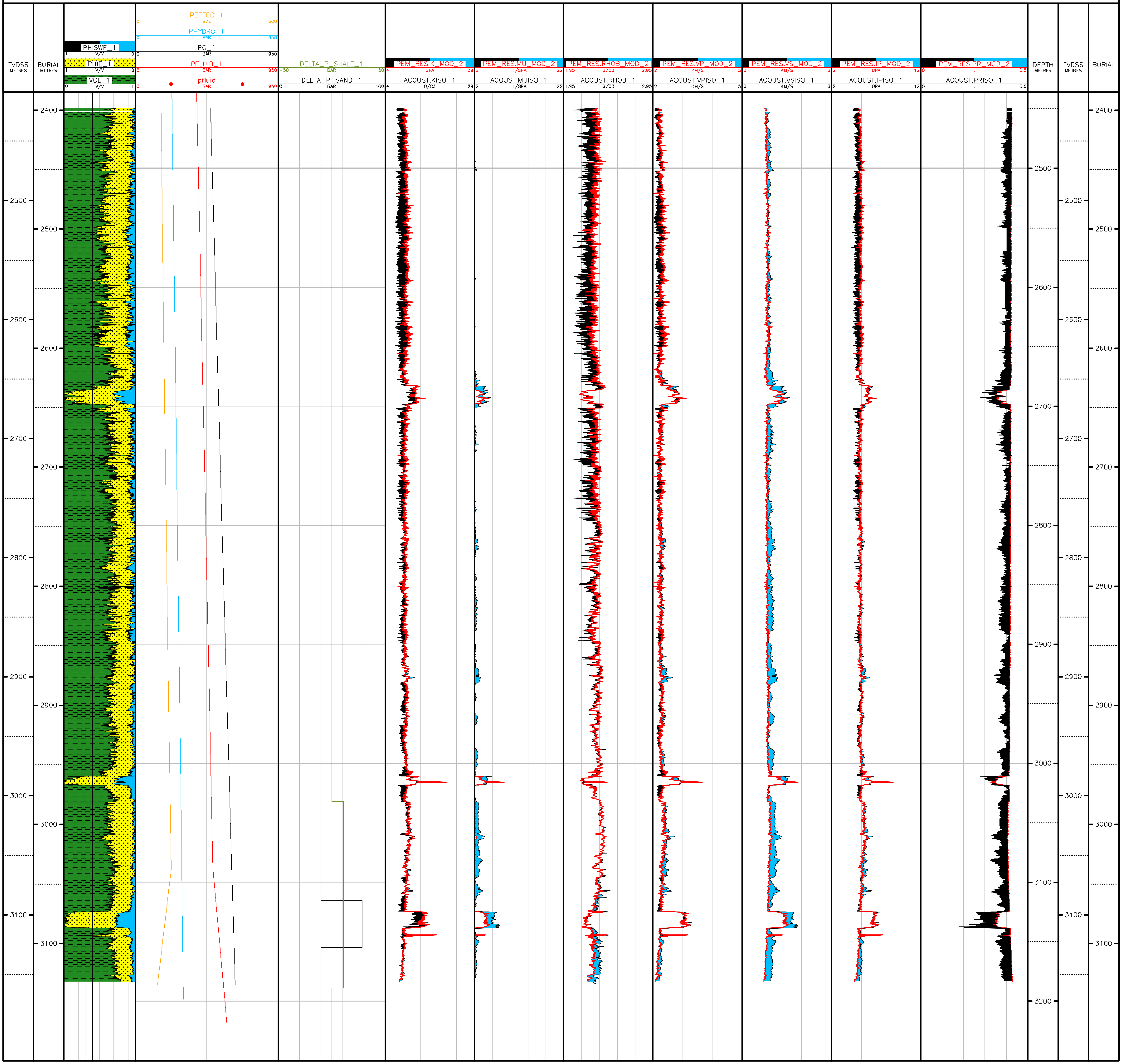

WELL: ZOM-1
MEASUREMENTS and MODELLING

Vertical Scale : 1/1500 cm

Plate 6

WELL: ZOM-5
MEASUREMENTS and MODELLING

Vertical Scale : 1/1500 cm

Plate 7

WELL: ZOM-7
MEASUREMENTS and MODELLING

Vertical Scale : 1/1500 cm

Plate 8

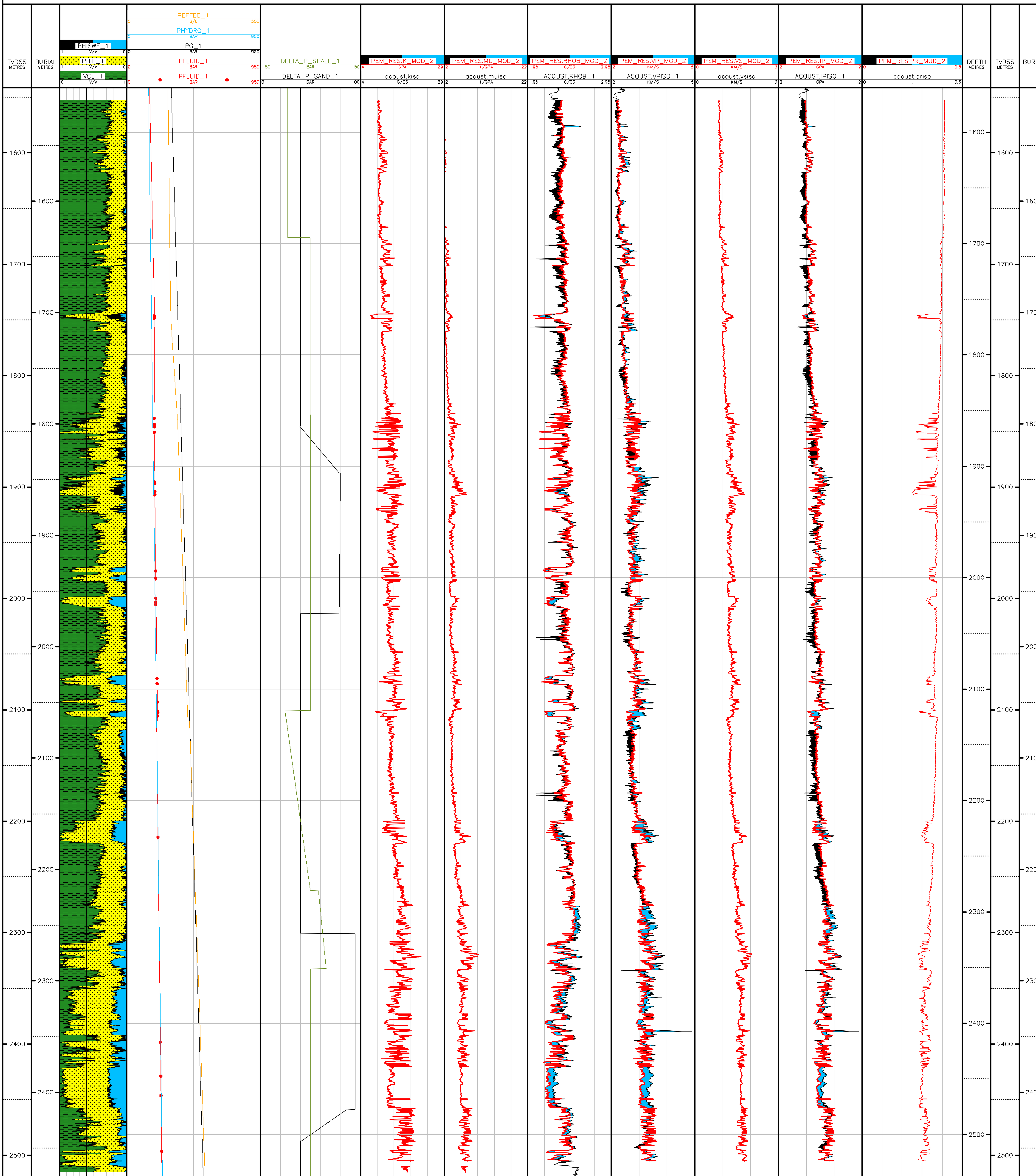

WELL: ZOM-11
MEASUREMENTS and MODELLING

Vertical Scale : 1/1500 cm

Plate 9

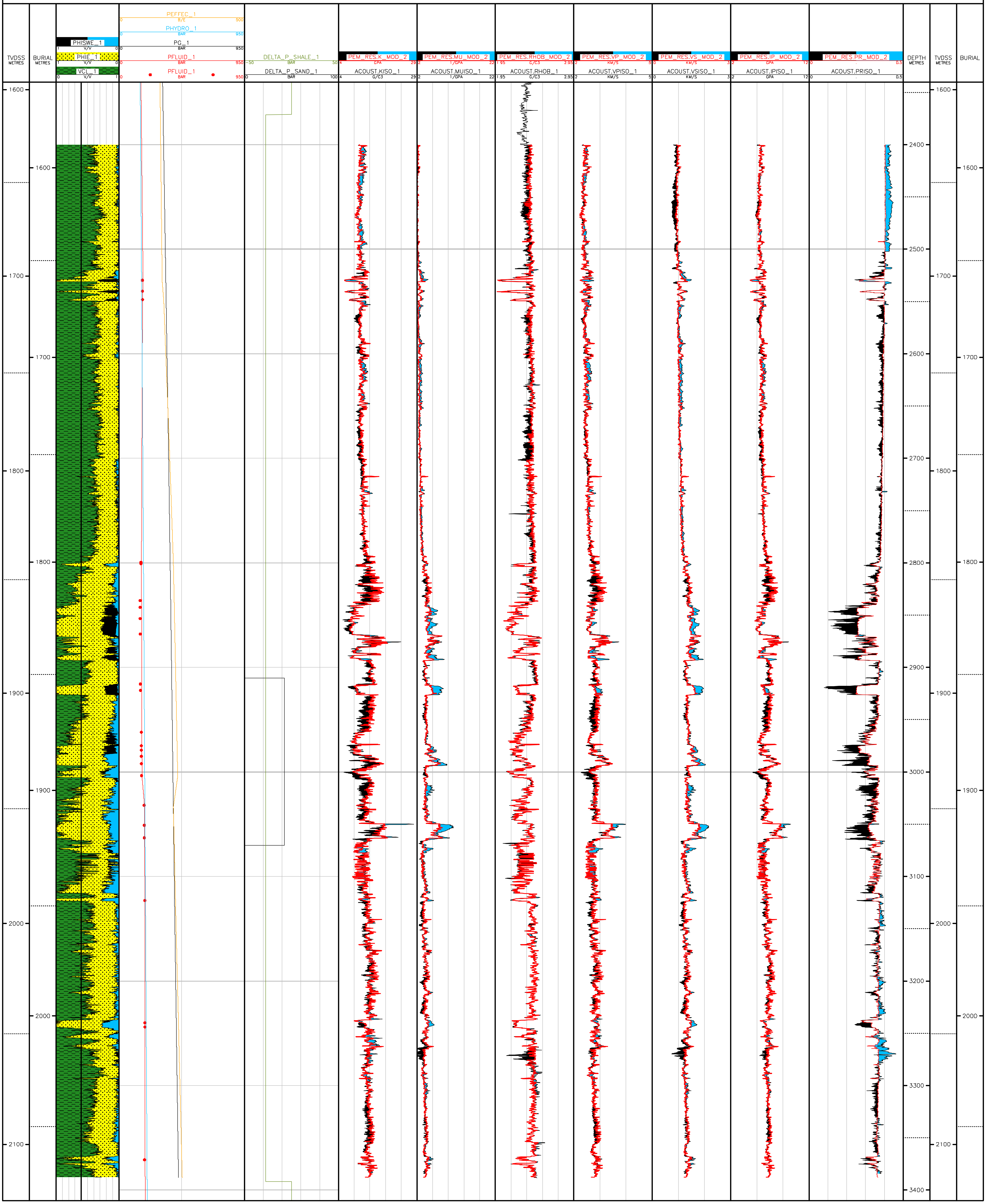

WELL: ZOM-26
MEASUREMENTS and MODELLING

Vertical Scale : 1/1500 cm

Plate 10

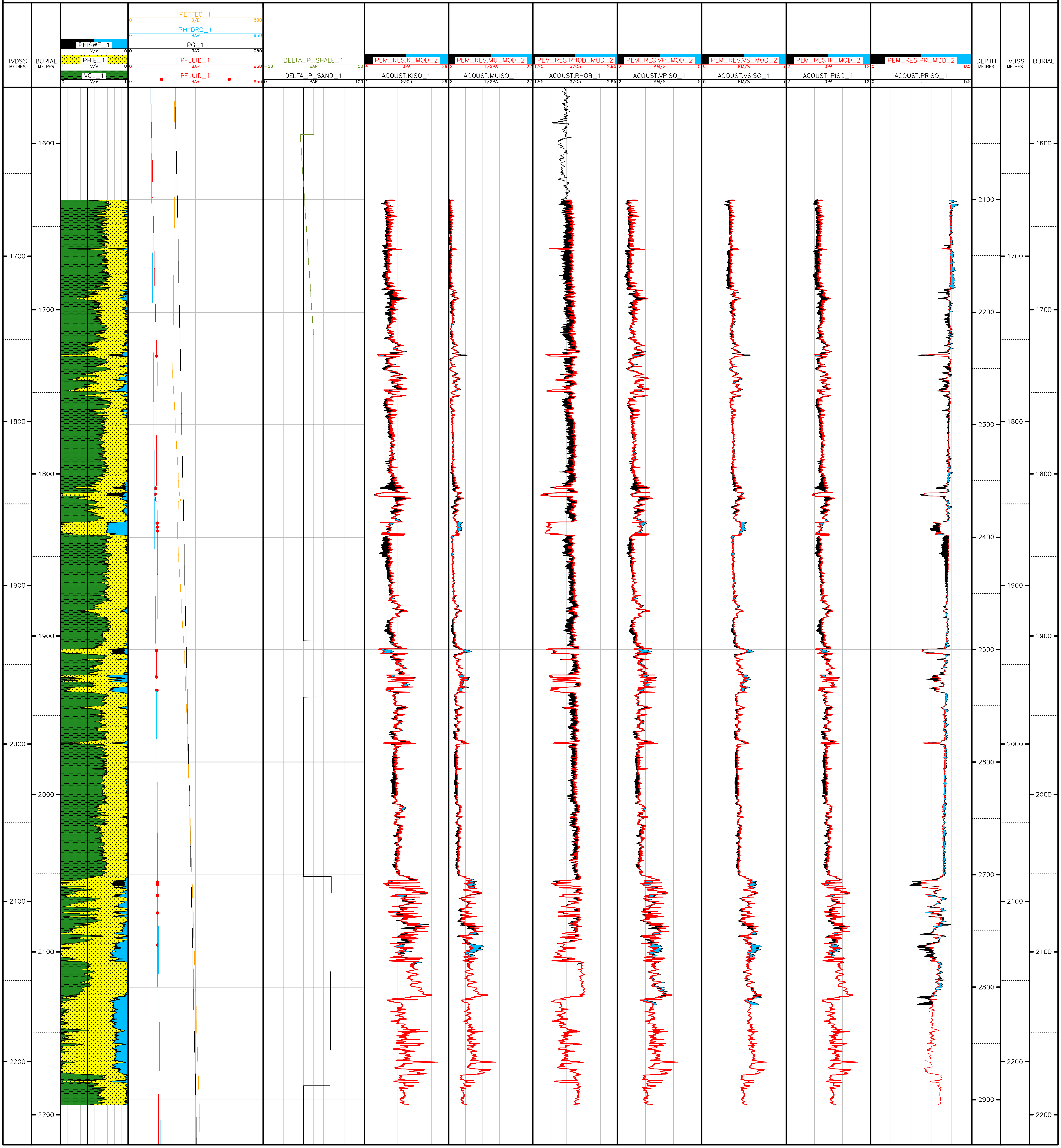

APPENDIX 1

NUMERICAL INTERPRETER PACKAGE SHOWING HOW THE PETROELASTIC/ROCK PHYSIC MODEL WAS COMPUTED

GENERALITIES & COMMENTS

/*===
/*PEM from 10 wells over OML70-99-100-102
/* COC-4 & BOB-1
/* ZOM-1; ZOM-5; ZOM- 7; ZOM-11ST-PH & ZOM-26
/* KUY-1E & EFE-2 (OML-99 & 70)
/* WOM-1
/*---
/*Following parameters are fixed:
/* Clay model is 100% laminated.
/* 25% of floating quartz grains in shales.
/* Cutoffs (CUT_VCL & CUT_PHIE) are adapted to each well.
/* Laws in sands and shales are built versus EFFECTIVE PRESSURE.
/* Pressure effect on the rock frame is taken into account.
/* 'P' & 'S' accerabilities are computed from WATER modeling (from GASSMANN's equations).
/* Water modeling determined by CUT_VCL & CUT_PHIE.
/* DeltaVP/VP (water) = DeltaVS/VS (water).
/*
/*Elastic parameters of initial fluids
/*-----------------------------------
/* KWAT = 2.385 to 2.43 GPa (COC-4 & BOB-1)
/* = 2.556 GPa for all wells
/* DWAT = 0.955 g/c3 (COC-4 & BOB-1)
/* = 0.991 g/c3 for all wells
/* KHC = 0.065 to 0.663 GPa (ZOM-1)
/* = 0.431 GPa(ZOM-7)
/* = 0.1132 to 0.3621 GPa (COC-4)
/* = 0.1236 to 0.2293 GPa (BOB-1)
/* = 0.446 to 0.466 GPa (all others)
/* DHC = 0.198 to 0.701 g/c3 (ZOM-1)
/* = 0.669 g/c3 (ZOM-7)
/* = 0.3318 to 0.5276 GPa (COC-4)
/* = 0.3586 to 0.5189 GPa (BOB-1)
/* = 0.66 to 0.677 g/c3 (all others)
/*
/*Elastic parameters (water modelling - all wells)
/*---
/* KWAT = 2.45 GPa
/* DWAT = 1.025 g/c3
/*
/*Pressure effect and depletion
/*-----------------------------------
/* A single law is used to model shales parameters. As a consequence, EFFECTIVE PRESSURE
/* is localy adapted with the so-called DELTA_P_SHALE parameter which range is (+/- 30 bars).
/* Depletion to apply is sands is egal to DELTA_P_SAND parameter.
/*==================================

Following logs are mandatory as input:

Following logs are the PEM outputs:

PEM equations:

```
VCLl_MOD=VCL-VCLd_MOD
Quartz=1.-phie-vcl
qzfl=0.25*vcl/0.75
/*-----------------------------------
/* Depletion
PEFFEC = PEFFEC + delta_p_shale
/*-----------------------------------
/* Clay elastic parametres (Effective pressure)
dclm = (2.13 + 0.00108775*PEFFEC)
kclm = (10.8+4.8*(exp((PEFFEC-250.)/160.)-exp((-PEFFEC+250.)/160.))/(exp((PEFFEC-
250.)/160.)+exp((-
PEFFEC+250.)/160.)))+0.6*((PEFFEC-250.)/160.)*(1.+(exp((PEFFEC-250.)/160.)-exp((-
PEFFEC+250.)/160.))/(exp((PEFFEC-250.)/160.)+exp((-PEFFEC+250)/160.)))
muclm = (3.2+2.7*(exp((PEFFEC-250.)/160.)-exp((-PEFFEC+250.)/160.))/(exp((PEFFEC-
250.)/160.)+exp((-
PEFFEC+250.)/160.)))+0.55*((PEFFEC-250.)/160.)*(1+(exp((PEFFEC-250.)/160.)-exp((-
PEFFEC+250.)/160.))/(exp((PEFFEC-250.)/160.)+exp((-PEFFEC+250)/160.)))
/*---------------------------------------
/* Fluid elastic parametres
if ((VCL<CUT_VCL) & (PHIE>CUT_PHIE)) then
K_FL=(phie+VCLd_mod)/(phie*SWE/KWAT + phie*(1.-SWE)/KHC + VCLd_mod/kclm)
D_FL=SWE*DWAT+(1.-SWE)*DHC
else
K_FL=KWAT
D_FL=DWAT
Endif
/*-----------------------------------
/* Modelled density
DM=VCL*DCLM+QUARTZ*2.65+D_FL*PHIE
DRESM=(QUARTZ*2.65+D_FL*PHIE)/(1.-VCL)
/*-----------------------------------
/* Pore incompressibility & shear modulus (Effective Pressure)
kphi_kminm = (0.098+0.054*(exp((PEFFEC-300.)/110.)-exp((-PEFFEC+300.)/110.))/(exp((PEFFEC-
300.)/110.)+exp((-PEFFEC+300.)/110.)))+0.0024*((PEFFEC-300.)/110.)*(1+(exp((PEFFEC-300.)/110.)-
exp((-
PEFFEC+300.)/110.))/(exp((PEFFEC-300.)/110.)+exp((-PEFFEC+300.)/110.)))
muphi_muminm = (0.052+0.028*(exp((PEFFEC-300.)/110.)-exp((-PEFFEC+300.)/110.))/(exp((PEFFEC-
```

```
300.)/110.)+exp((-PEFFEC+300.)/110.)))+0.0008*((PEFFEC-300.)/110.)*(1+(exp((PEFFEC-300.)/110.)-
exp((-
PEFFEC+300.)/110.))/(exp((PEFFEC-300.)/110.)+exp((-PEFFEC+300.)/110.)))
/*-----------------------------------
/* For sands only, initial modulii
if ((VCL<CUT_VCL) & (PHIE>CUT_PHIE)) then
PHIRES = (PHIE+VCLd_MOD)/(1.-VCLl_MOD - QZFL)
KMIN=38.
MUMIN=44.
KDRYM=kmin/(1.+(phires/kphi_kminm))
MURESM=mumin/(1.+(phires/muphi_muminm))
a=KDRYM/(kmin-KDRYM)
b=k_fl/((kmin-k_fl)*phires)
KRESM=kmin*(a+b)/(1+a+b)
```